Laser-based Additive Manufacturing of Case-hardening Steels

Laserbasierte Additive Fertigung von Einsatzstählen

Der Technischen Fakultät
der Friedrich-Alexander-Universität
Erlangen-Nürnberg

zur
Erlangung des Doktorgrades Dr.-Ing.

vorgelegt von

Dominic Bartels, M.Sc.

aus Bayreuth

Als Dissertation genehmigt
von der Technischen Fakultät
der Friedrich-Alexander-Universität Erlangen-Nürnberg

Tag der mündlichen
Prüfung: 21.03.2024

Gutachter: Prof. Dr.-Ing. Michael Schmidt
Prof. Dr.-Ing. habil. Markus Bambach

Preface

Die vorliegende Arbeit entstand im Rahmen meiner Tätigkeit als wissenschaftlicher Mitarbeiter am Lehrstuhl für Photonische Technologien der Friedrich-Alexander-Universität Erlangen-Nürnberg. Dabei entsprang die Idee aus einem industriellen Forschungsprojekt in Kooperation mit der Firma Schaeffler Technologies AG und konnte im Verlauf des BMWK-Projektes HyConnect und des Sonderforschungsbereichs 814 – Additive Fertigung weiterverfolgt werden.

Meinen Dank möchte ich dabei insbesondere meinem Doktorvater Herrn Professor Dr.-Ing. Michael Schmidt aussprechen, der mir sowohl zu Beginn als wissenschaftlicher Mitarbeiter im Bereich Additive Fertigung als auch später als Gruppenmanager das notwendige Vertrauen entgegengebracht hat. Die angeregten fachlichen und auch nicht-fachlichen Diskussionen haben mir sowohl bei meiner wissenschaftlichen als auch persönlichen Weiterentwicklung geholfen. Herrn Professor Dr.-Ing. habil. Markus Bambach möchte ich für die Übernahme des Zweitgutachtens danken. Herrn Prof. Dr.-Ing. habil. Hinnerk Hagenah und Herrn Prof. Dr.-Ing. Stefan Will möchte ich darüber hinaus für die Übernahme des Prüfungsvorsitzes bzw. des fachfremden Gutachtens danken.

Des Weiteren möchte ich mich bei Herrn Carsten Merklein (Schaeffler Technologies AG) bedanken. Carsten, deine Ideen und Anregung zur in-situ Modifikation von Einsatzstählen haben maßgeblich diese Arbeit beeinflusst. Für die gute Zusammenarbeit in den verschiedenen gemeinsamen Forschungsprojekten möchte ich mich bei der Ordinaria des Lehrstuhls für Fertigungstechnologie der FAU Erlangen-Nürnberg, Frau Professor Dr.-Ing. habil. Marion Merklein, ganz herzlich bedanken. Thomas Papke und Raphaela März danke ich für die gute und angenehme Zusammenarbeit bei der Bearbeitung der gemeinsamen Forschungsprojekte im Laufe der Jahre. Jürgen Kaiser (Neue Materialien Fürth) möchte ich ebenfalls für die Unterstützung bei der Versuchsdurchführung vor Ort an der Kombianlage danken. Den Deutschen Edelstahlwerken danke ich für die Bereitstellung der Pulvermaterialien, auch über die laufenden Forschungsprojekte hinaus, sowie den fachlichen Diskussionen.

Außerdem möchte ich meinen (ehemaligen) Arbeitskollegen am Lehrstuhl für Photonische Technologien danken. Hier sind Florian Huber, Oliver Hentschel und Michael Rasch aus der Gruppe Additive Fertigung hervorzuheben. Ihr alle habt eure Erfahrungen mit mir geteilt und habt somit

auch euren Anteil an den Erkenntnissen, die im Zuge dieser Arbeit generiert wurden. Insbesondere den Technikern möchte ich danken, die sich immer wieder die Zeit auch für die kleinsten Problemstellungen genommen haben. Vielen Dank auch an Vanessa und den morgendlichen Stammtisch, der selbst anspruchsvollste Zeiten erleichtert und die Stimmung immer wieder aufgelockert hat. Auch Clemens Roider möchte ich nicht unerwähnt lassen – die regelmäßigen Kekspausen waren eine wohltuende Ablenkung. Außerdem möchte ich allen weiteren Kollegen und Kolleginnen, mit denen ich über die Jahre zusammengearbeitet habe, meinen Dank aussprechen. Ihr habt dazu beigetragen, dass ich die Zeit am LPT genießen konnte und gerne zur Arbeit gekommen bin. Dadurch sind beinahe 5,5 Jahre bis zum Abschluss dieser Arbeit in erschreckend schneller Zeit verflogen. Darüber hinaus möchte ich mich bei allen Studierenden bedanken, die ihren Beitrag zu dieser Arbeit geleistet haben. Eure Unterstützung im Rahmen von Abschlussarbeiten oder als Hilfswissenschaftler/innen hat das Anfertigen von gemeinsamen Publikationen erleichtert bzw. teilweise erst ermöglicht und somit einen wesentlichen Beitrag zu dieser Dissertation geleistet. Hervorheben möchte ich an dieser Stelle Tobias Novotny, Moritz Albert und Miriam Heise. Für die Übernahme des Lektorats in frühen und späten Phasen dieser Arbeit möchte ich mich bei Alexander Sommereyns, Melanie Kneidl und Nora Vogg bedanken. Vielen Dank für die wertvollen Anmerkungen.

Mein allergrößter Dank gebührt meiner Familie, insbesondere meinen Eltern Anna und Karlheinz Bartels, die uns Kinder in allen Lebensabschnitten bedingungslos unterstützt haben. Ihr habt mir durch eure selbstlose Einstellung diesen Weg erst ermöglicht, daher an dieser Stelle: Vielen Dank für Alles! Auch meiner langjährigen Mitbewohnerin Julia danke ich für die vielen schönen gemeinsamen Jahre – es war eine wunderbare Zeit mit dir zusammen in Erlangen. Zu guter Letzt möchte ich nochmal meiner Freundin Nora danken, die mich stets unterstützt und zu motivieren wusste und somit maßgeblich zum Erfolg dieser Arbeit beigetragen hat. Vielen Dank für deine Unterstützung und dafür, dass auch du unsere gemeinsame Zeit geopfert hast, damit ich diese Arbeit fertigstellen konnte.

Erlangen, im November 2023 Dominic Bartels

Table of Contents

List of Symbols and Abbreviations

Symbol	*Unit*	*Description*
$d_{10\%}$	µm	Maximum Size of 10 % of all Particles
$d_{50\%}$	µm	Maximum Size of 50 % of all Particles
$d_{90\%}$	µm	Maximum Size of 90 % of all Particles
d_L	mm	Laser Spot Size
h	µm	Hatch Distance
P	W	Laser Power
R_a	µm	Mean Arithmetic Roughness
R_t	µm	Maximum Roughness of the Entire Sample
R_z	µm	Maximum Height of a Specific Profile
ρ_{rel}	%	Relative Part Density
t	µm	Layer Thickness
v	mm/s	Scanning Speed

Abreviation	*Description*
AC_3	Austenite Transformation Temperature
AM	Additive Manufacturing
AT	As-built and Tempered
BZ	Bainitized
C	Carbon
CB	Carbon Black
CCT	Continuous-Cooling-Transformation
CHD	Case-hardening Depth
CHS	Case-hardening Strategy
Cr	Chromium
DED-LB/M	Laser-based Directed Energy Deposition of Metals
DIN	Deutsches Institut für Normung
EDS / EDX	Energy Dispersive X-Ray
FZ	Fusion Zone
HAZ	Heat-affected Zone
HRC	Rockwell Hardness

Abreviation	*Description*
HTS	Heat Treatment Strategy
HV	Vickers Hardness
HV0.05	Vickers Hardness with a Nominal Load of 0.05 N
HV0.5	Vickers Hardness with a Nominal Load of 0.5 N
HV1	Vickers Hardness with a Nominal Load of 1 N
HV5	Vickers Hardness with a Nominal Load of 5 N
LBM	Laser Beamt Melting
MMC	Metal-Matrix-Composite
Mn	Manganese
Mo	Molybdenum
M_S	Martensite-Start-Temperature
N	Newton
Ni	Nickel
OES	Optical Emission Spectroscopy
OLM	Optical Light Microscopy
PBF-LB/M	Laser-based Powder Bed Fusion of Metals
ppm	Parts Per Million
QT	Quenched and Tempered
RA	Retained Austenite
RQ	Research Question
SEM	Scanning Electron Microscopy
SLM	Selective Laser Melting
TTT	Time-Temperature-Transformation
V	Vanadium
VED	Volumetric Energy Density
W	Tungsten
WC	Tungsten Carbide
Wt.-%	Weight percent
XRD	X-Ray Diffraction

List of Figures

1 Introduction

The efficient and sustainable use of the available resources is ever so important with an increasing worldwide population, which is forecasted for the upcoming years [1]. To meet the environmental challenges that arise in the future, seventeen global sustainable development goals were adopted in 2012 and came into effect as an international guideline in the beginning of 2016 [2]. The target of these goals is to assure a sustainable development on an economic, ecological, and social level. One of those seventeen goals is *Goal 12: Responsible consumption and production*, which aims at ensuring "sustainable consumption and production patterns" [3]. This goal can further be divided into several sub-goals that aim at e.g., reducing the waste throughout the life cycle of a product by prevention, reduction, recycling, and reuse. Considering the fact that an increasing desire for individualised or personalised products is observable in recent years, a transition of the production patterns needs to be expected [4]. This demand for customer-specific products will lead to an at least partial transition from a cost- and resource-efficient mass production towards a more individualized production. The latter can be seen as counterproductive since manufacturing tools would need to be generated for smaller lot sizes when aiming at generating these products through conventionally established production technologies. Therefore, alternative manufacturing processes need to be established that support the transition towards an efficient production of small lot sizes regarding the consumption of energy and critical resources like rare or hard-to-access elements.

Additive manufacturing (AM) technologies facilitate the generation of individualised products since they allow for the direct manufacturing of parts from digital data without the necessity of geometry-specific tools [5]. The selective generation of the geometry only where needed allows to reduce the material waste along the process chain compared to subtractive manufacturing technologies. Furthermore, new materials that are tailored for the final application can be generated by in-situ alloying approaches [6]. This flexibility provides the potential to further optimise the performance of the final component. However, up to now, the fabrication of high-strength steel products in laser-based additive manufacturing is very limited due to the crack tendency of carbon-rich materials. The small melt pools and the associated high cooling rates promote crack formation during processing [7]. This defect tendency hinders the application of additively manufactured products for tooling or load-optimised products e.g., in mobility.

Low-carbon case-hardening steels present a way out of this drawback for the generation of products with a high surface hardness, which is essential for avoiding excessive wear. By exposing the additively manufactured specimens to a post-process carburisation or nitriding heat treatment, the hardenability of the workpiece can be improved. Hence, it is surprising that case-hardening steels have only recently gained interest for laser-based AM despite their widespread application in conventional products and their undisputed potentials for AM.

The main goal of this work is the elaboration of a fundamental understanding on the additive manufacturing of case-hardening steels by means of laser-based powder bed fusion (PBF-LB/M) and laser-based directed energy deposition (DED-LB/M). While PBF-LB/M supports the generation of highly sophisticated geometries, DED-LB/M can be used for the efficient deposition of large volume structures and wear-resistant coatings [8]. Building on these findings, alternative approaches to the conventional carburising are analysed and evaluated regarding their potentials and limitations for adjusting the material hardness of the final workpiece. The aim of these investigations is to derive an optimised process chain for AM of case-hardening steels.

First, the correlations between the respective manufacturing process and the resulting micro- and macrostructural properties are analysed for both PBF-LB/M and DED-LB/M. The underlying material properties are determined for different thermal boundary conditions that arise when modifying e.g., the applied processing parameters or the part's geometry. Increasing the part height will encourage heat accumulation during build-up and therefore affect the transformation of the austenite upon cooling. In this instance, the effect of different heat treatment strategies on the tensile strength is studied. In the second step, the case-hardening of additively manufactured specimens is investigated to determine the influence of the process-specific material properties on the case-hardenability. Further studies focus on the in-situ modification of the material during PBF-LB/M and DED-LB/M. Therefore, the findings on the case-hardenability of additively manufactured specimens act as a benchmark. Different strategies including in-situ alloying through the addition of elemental carbon as well as in-situ particle reinforcement through the addition of hard particles like tungsten carbide (WC) are followed. These investigations aim at identifying the correlations between the chemical composition of the material system, the applied processing strategy, defect formation, and the final material properties, mainly the surface hardness.

2 State of the Art

This chapter presents the most relevant background for this work. Section 2.1 explains the microstructure formation in steels and how the thermal history affects the resulting part properties. Subsequently, the fundamentals on case-hardening steels including a description of the case-hardening heat treatment are presented in Section 2.2. Section 2.3 provides the fundamentals on laser-based AM. The influence of the thermal boundary conditions as well as the processing of case-hardening steels by means of laser-based AM is portrayed. Furthermore, alternative strategies for the modification of the surface hardness in powder-based AMprocesses are shown. Finally, in Section 2.4 the existing deficits regarding the processing of case-hardening steels in laser-based AM are derived.

2.1 Microstructure Formation in Steels

Stainless steels, tool steels, dual-phase steels and case-hardening steels - the product portfolio of steels is large [9]. The respective material properties are defined by their unique microstructure, which comprises of different constituents like grain size, grain orientation, internal voids, phase proportions, phase distributions, and precipitations [10]. The main mechanisms affecting the microstructure formation in steels can be broken down to chemical composition [11] and thermal history, whereby the latter is often defined by a post-process heat treatment [12].

Every alloying element affects the microstructure formation in a specific way by influencing the transformation behaviour [13]. Typical alloying elements include chromium (Cr), manganese (Mn), molybdenum (Mo), nickel (Ni), tungsten (W), and vanadium (V) [14]. The addition of these elements is intended for different purposes like increasing the hardenability, ultimate tensile strength, ductility, as well as corrosion or wear resistance [15]. However, among all elements, carbon can be seen as the most defining alloying element in materials design since it provides the main lever for hardening iron-based products [16]. The combination of these alloying elements in specific ratios allows to tailor the final material properties like hardness and wear resistance by forming a high-strength microstructure [17].

The thermal history of the workpiece is the second major influencing factor since the microstructure formation in steels is not only sensitive to the chemical composition but also to the thermal conditions during processing

[18]. Thereby, the thermal history comprises all applicable thermal boundary conditions like peak temperature from which the specimen is cooled down as well as cooling rate, holding temperatures, and holding times [19]. In general, the microstructure of a solidified material is formed upon cooling the workpiece, typically from temperatures above the austenitisation temperature. The austenite is thereby transformed into different microstructural constituents like martensite, bainite, ferrite, or pearlite, depending on the underlying cooling rate [20]. In general, the strength of a steel depends on the cooling conditions and decreases when lowering the cooling rates. Higher cooling rates are correspondingly favourable for the generation of high-strength materials [21]. However, a faster cooling can come at the cost of a poorer processability of the material in certain manufacturing processes due to the resulting brittle material properties [22]. High carbon contents are typically associated with a poorer weldability of the material [23]. The threshold regarding a good weldability is typically defined at approximately 0.2 wt.-% C [24]. In laser-based processing, the high cooling rates, which typically exceed 10^3 K/s [25], can result in cold cracking due to the formation of a brittle microstructure [26].

2.1.1 Time- and Temperature-dependent Transformation

The two mechanisms continuous [27] and isothermal transformation [28] need to be distinguished regarding the microstructure formation in an equilibrium state. During continuous transformation, the material is cooled from an elevated temperature to room temperature at a specific cooling rate [27]. Isothermal transformation indicates that the workpiece is cooled down to specific temperatures and held at this temperature level for a certain amount of time [28].

The chemical composition defines the temperature ranges in which the transformation into e.g., martensite [29] and bainite [30] takes place. These regions are characterised by a starting and finishing temperature for the respective microstructural constituent, commonly known as bainite and martensite start/finish temperature [31]. The time- and temperature-dependent transformation for a specific material can be obtained either from literature for established materials or by using commercially available software like JMatPro [32]. To achieve a full transformation of the austenite, these temperature thresholds need to be passed completely at defined cooling rates. If a specific region or interval is not passed completely or at an inappropriate cooling rate, non-transformed austenite remains [33]. This

retained austenite is generally undesired since it can reduce the performance (e.g., ultimate tensile strength) of highly loaded products [34] or might transform upon load [35]. Retained austenite can be avoided by e.g., undercooling during quenching [36] if the martensite finish temperature of the material was too low, or decomposed to form e.g., ferrite, by a post-process tempering at temperatures above 250 °C [37]. Furthermore, secondary phases like carbides can be precipitated when tempering the specimens [38].

Continuous Cooling Transformation

The continuous cooling transformation (CCT) describes the microstructure that is formed when cooling a workpiece from the austenitisation temperature to typically room temperature at defined cooling rates [39]. Figure 1 presents an exemplary CCT for the case-hardening steel 16MnCr5.

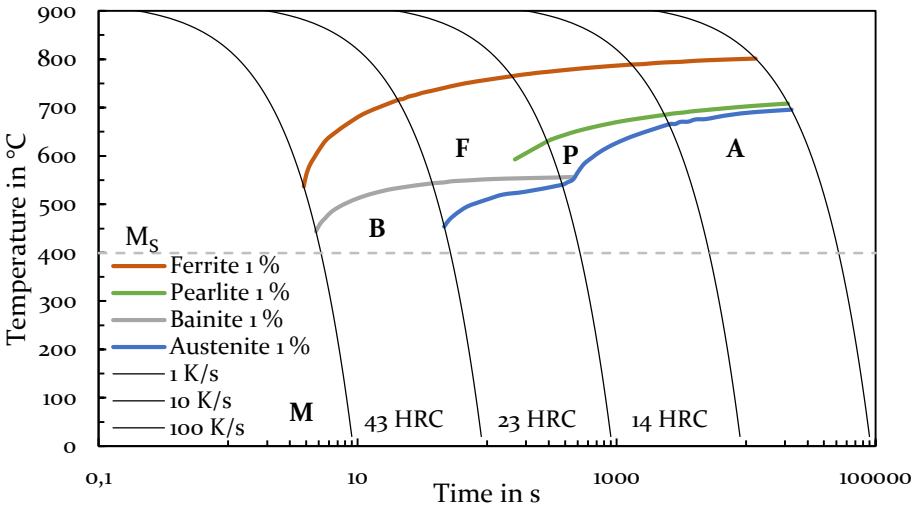

Figure 1: Continuous cooling transformation diagram of the case-hardening steel 16MnCr5. The CCT-diagram was calculated using the software JMatPro.

CCT diagrams provide an overview of the expected phase ratios and material hardness when cooling the material with a defined cooling rate. Continuous cooling operations are commonly applied for simple heat treatment operations like direct hardening of steels, which include the quenching of workpiece in an oil bath to room temperature. In this case, the resulting material is characterised by a mostly martensitic microstructure due to the high cooling rates (see left side of Figure 1) [29]. Consequently, laser-based processes are oriented in the left of CCT-diagrams since the high cooling rates support the formation of martensite through quenching-

like effects during laser-material processing. The high cooling rates also suppress carbon diffusion into neighboured grains, which is helpful for avoiding locally differing material compositions that are associated with different transformation behaviours [40]. Lowering the cooling rates supports the formation of microstructures with a lower strength that contain e.g., bainite, ferrite, or pearlite. These microstructures can be favourable since they possess a higher ductility compared to martensite [41].

Isothermal Transformation

The isothermal transformation is also known as time-temperature-transformation (TTT) [42]. Typically, the workpiece is quenched from austenitisation to a holding temperature in a salt bath to suppress undesired carbon diffusion from the austenite. Otherwise, carbon-saturated regions would remain within the workpiece that affect the transformation behaviour of the material [43]. During holding, the austenite is transformed into e.g., bainite, ferrite, or pearlite. Isothermal diagrams reveal the percentage of the different microstructural constituents that are formed after holding for a specific time. Figure 2 shows an exemplary TTT-diagram for the case-hardening steel 16MnCr5.

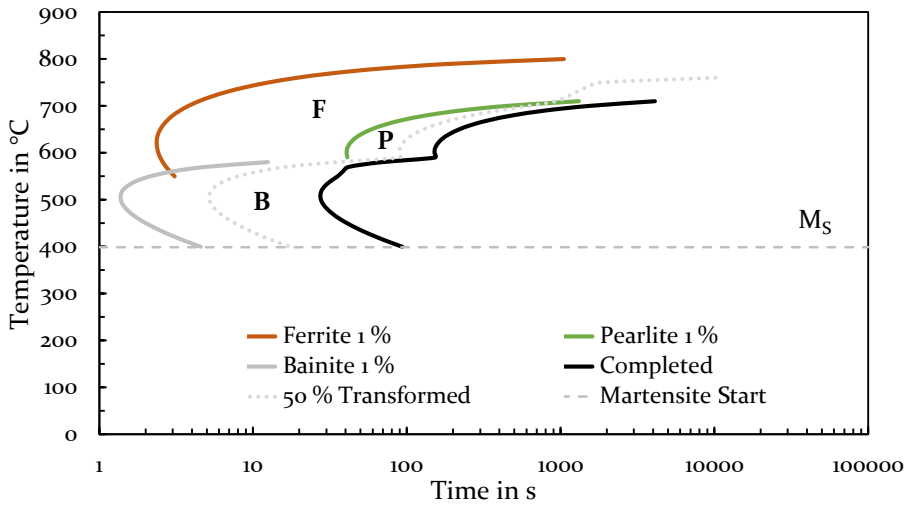

Figure 2: Isothermal transformation diagram of the case-hardening steel 16MnCr5. The TTT-diagram was calculated using the software JMatPro.

The transformation progresses for as long as the material is held at the respective temperature. After a specific amount of time, the transformation is fully completed (100 %). The workpiece is then cooled to room tempera-

ture. Isothermal transformations are often applied when homogeneous material properties are targeted throughout the workpiece. One major advantage compared to continuous cooling is that a more complete transformation of the austenite is achieved [44]. Bainitic and carbidic microstructures are typically generated through an isothermal transformation [45]. However, a combination of inappropriate holding times and temperatures can promote carbon diffusion from the austenite, which supports the formation of undesired martensitic-austenitic constituents [46].

2.1.2 Microstructure Constituents of High-strength Steels

Highly loaded products like tools for forming operations [47], gears [48], or bearings [49] demand wear-resistant surfaces whose hardness exceeds 56 HRC (≈ 615 HV) to avoid premature failure during operation. For low temperature applications, the surface hardness is primarily achieved through a martensitic-hardening of the specimen. The hardness of the martensite is defined by the carbon concentration of the material [50]. Increasing the carbon concentration results in a stronger distortion of the martensite and a higher hardness after quenching. In general, a higher hardness is associated with a poorer ductility of the material. Bainitic microstructures possess a trade-off between hardness and ductility [51]. However, the reduced hardness often hinders their applicability in highly loaded applications. Secondary phases like carbides provide a third lever for improving the strength due to their inherent high hardness [52]. Furthermore, these carbides help to improve the wear resistance of a material.

Properties of Martensite

Martensite is formed when the cooling rates are too high for the carbon to diffuse out of the crystalline structures. The martensitic reaction begins as soon as the martensite start temperature (M_s) is reached [53]. When exceeding the critical cooling rates for martensite formation, a transfer of the face-centered cubic austenite into a body-centered tetragonal structure takes place [54]. Martensite is characterised by a high number of dislocations in its phase as result of shear deformations. This number of dislocations depends on the overall carbon concentration. The higher the martensite concentration of the microstructure, the harder but more brittle is the material [16]. Martensite appears lath-like (< 0.5 wt.-% C), plate-like (> 0.8 wt.-% C) or as a mixture of both types (0.5 to 0.8 wt.-% C) [55].

The hardness of martensite can be as high as 900 HV1 [56]. Since martensite is not an equilibrium phase, the lattice distortion can be eliminated by

tempering the workpiece [57]. This heat treatment results in a tempered martensitic structure that is characterised by a reduced dislocation density. Consequently, the hardness of the workpiece is lowered and the ductility is improved [30]. Figure 3 presents an exemplary tempering curve for the bearing steel 100Cr6. The tempering curve shows the correlation between material hardness and tempering temperature.

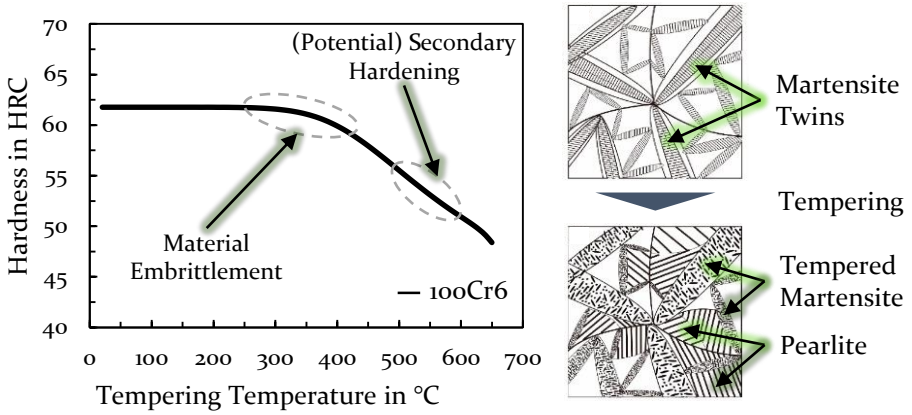

Figure 3: Tempering stability of martensitic-hardened steel 100Cr6 and a schematic presentation of martensite and tempered martensite according to [58]. The material properties were calculated using the software JMatPro.

Martensite is characterised by a poor tempering stability as the hardness decreases with higher temperatures. At temperatures between 150 °C and 200 °C, tempering will lead to a stress relief within the part, normally coupled with only a slight decrease in hardness [30]. The precipitation of Fe_xC carbides also begins at these temperatures [59] with cementite as the most known Fe-based carbide. Further increasing the tempering temperature results in a decomposition of retained austenite. The austenite is thereby transformed into a carbide-enriched ferritic structure. Temperatures between 250 °C and 400 °C lead to material embrittlement due to the formation of undesired constituents like Widmannstätten ferrite [60]. Therefore, these temperatures are typically avoided. Tempering the material between 500 and 550 °C promotes the formation of secondary carbides [19]. Thereby, Cr, Mo, V, or W carbides can precipitate. This is the key hardening mechanism applied in high-speed tool steels [61].

Properties of Bainite

Bainite is formed in the temperature range between martensite and pearlite and can be broken down into a primary and a secondary phase [45]. The main phase is a body-centred plate-like ferritic structure. This structure is also referred to as bainitic ferrite. The interspaces between these bainitic

ferrite structures are filled with either retained austenite, martensite, or cementite. The secondary phase depends strongly on the temperatures at which the transformation takes place. Due to the unique microstructure, diverse material properties are formed. In general, the part possesses a high hardness as well as a good ductility. The combination of these properties results in an excellent fatigue resistance and fracture toughness [62]. Looking at the appearance of the bainitic structure, the following two main types can be distinguished: lower bainite and upper bainite [19]. Generally, the main difference of these two structures is the temperature interval in which the bainitic microstructure was formed. This difference is then displayed in the morphology of the microstructure. Figure 4 shows the formation kinetics of lower and upper bainite, origining from an austenite grain boundary according to Takahashi and Bhadeshia [63], as well as their characteristic appearance.

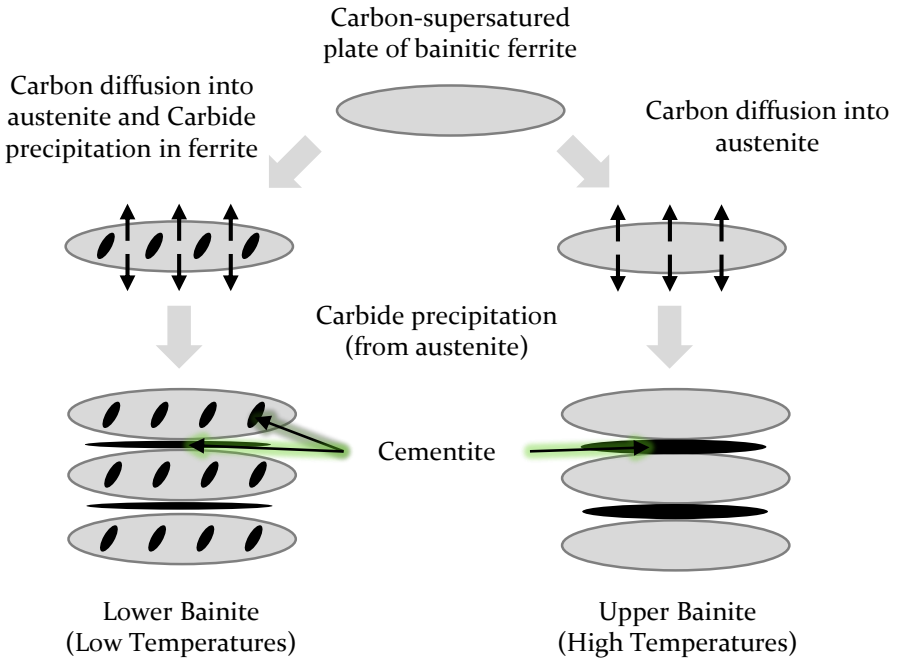

Figure 4: Formation of lower and upper bainite according to [63].

Lower bainite is formed at temperatures in the range of 250 to 400 °C and appears like a lath-like tempered martensite (see Fig. 4a) [64]. The $Fe_{2,4}C$-carbides are precipitated within the grains already during the transformation into ferrite. A clear differentiation between tempered martensite and lower bainite is often difficult to realise [65], especially for very fine microstructures [66]. However, in contrast to martensite, the carbides are

oriented in a preferential direction with a tilting angle of the cementide of 60 ° from the axis of the lath [67]. The low diffusivity of the carbon in the austenite coupled with the high transformation speeds at these low temperatures hinders the carbon diffusion from the ferrite lath into the neighbouring austenite. Correspondingly, the austenitic interspaces between the ferritic laths are not over-saturated with carbon. This causes the retained austenite to transform into a mostly martensitic structure during cooling to room temperature. Lower bainite is commonly characterised by a material hardness of up to 550 HV. Upper bainite is formed at higher temperatures that are typically between 400 and 550 °C [64]. These temperatures are closer to the ones required for the formation of pearlite. The bainitic ferrite consists of several lath-like structures that are oriented parallely to each other (see Fig. 4b). Unlike for lower bainite, the austenite that surrounds the ferrite is enriched with carbon [68]. Consequently, the carbides are preferably precipitated between the grain boundaries of the ferritic grains [69]. The typical hardness of upper bainite is in the range of 350 HV [70].

In contrast to martensite, bainitic microstructures are characterised by a better tempering stability due to the precipitated cementite within the ferritic microstructure [71]. The cementite takes longer to dissolve compared to supersatured martensite. Tempering bainite at elevated temperatures as high as 700 °C only slightly influences the morphology of the ferritic structure and the number of cementite particles [72]. Significant hardness reduction is mainly achieved when tempering the material at temperatures exceeding the austenitisation temperature [73]. Bush and Kelly also found that the carbide precipitation within the bainite is an important strengthening mechanism compared to carbide-free bainitic steels [74]. However, a reduced ductility can be identified since the carbides are primarily precipitated at the grain boundaries [75]. Furthermore, the alloying elements affect the tempering stability. Bainitic steels with molybdenum are characterised by a better thermal stability [76]. Correspondingly, a differentiation between a fine-grained martenisitic and lower-bainitic microstructures can be possible by comparing the tempering stability.

Carbide Precipitation

Carbides are M_xC_y phases that consist of a carbide forming element M and elemental carbon C. Typical carbide forming elements include Cr, Fe, Mn, Mo, Ti, V, and W [77]. These hard phases are precipitated at elevated temperatures and correspondingly possess a good thermal stability. The precipitated carbides can be distinguished into primary carbides (group-I) and

secondary carbides (group-II). Whereas primary carbides are formed upon solidification from the liquid state, secondary carbides are precipitated during heat treatment [78]. Group-I carbides possess an excellent thermal stability since they dissociate at temperatures that exceed the typical applications of steels [19]. These primary carbides can predominantly be found at the lath boundaries. The typical chemical composition of these carbides are M_3C, $M_{23}C_6$, M_7C_3, or M_6C. These carbides are however typically characterised by a lower strength due to the lower carbon concentration. Group-I carbides are larger compared to Group-II carbides [79]. For industrial applications, carbides of group-II are of higher interest since they can possess a hardness of up to 4,000 HV and are therefore often desirable for improving the surface hardness and wear resistance [80]. These carbides are either of type MC or M_2C. Tempering high-carbon steels that contain carbide-forming elements supports carbide precipitation, resulting in a secondary hardening of the workpiece [81]. The distribution of the carbides within the microstructure is depending on the heat treatment strategy. Cooling the heat-treated workpiece with low cooling rates results in a promoted carbide precipitation of larger carbides at the grain boundaries [82]. These larger carbides result in the formation of an extensive carbide network that reduces ductility and toughness of the workpiece [83]. Correspondingly, homogeneously and finely dispersed carbides are targeted for more ductile products, which can be achieved by a faster cooling of the specimen [82]. Figure 5 shows an exemplary illustration of primary and secondary carbides precipitated in a tempered martensitic steel.

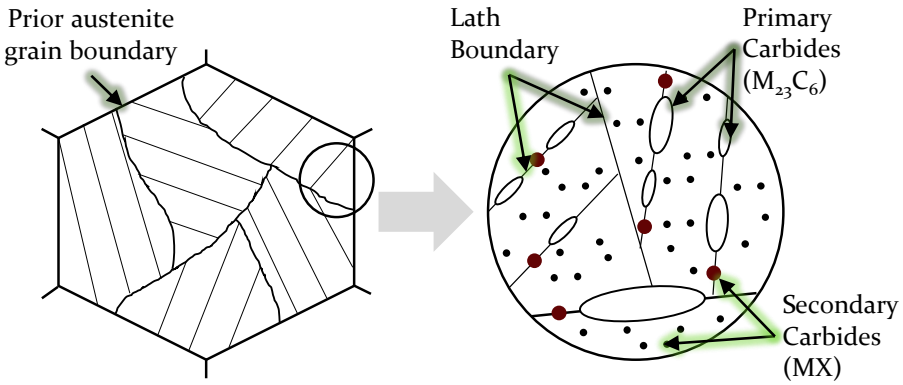

Figure 5: Schematic illustration of primary and secondary carbides precipitated in steels according to [79].

In general, the higher the hardness of the surface, the better its wear resistance [84]. However, a carbide-reinforced microstructure is favourable to meet dominant wear mechanisms like abrasive and adhesive wear [85].

A homogeneous distribution of these carbides within the matrix results in the best wear resistance [86]. Furthermore, ex-situ hard particles like titanium carbide (TiC) or tungsten carbide (WC) can be added to form a metal-matrix composite. These composites possess a better wear resistance than the unmodified base material [87].

Correspondingly, the selection of an appropriate heat treatment strategy is decisive for the properties of the final part. Figure 6 summarises established heat treatment strategies for the generation of different microstructures in high-strength parts. Furthermore, the benefits and disadvantages of the different microstructures are briefly presented.

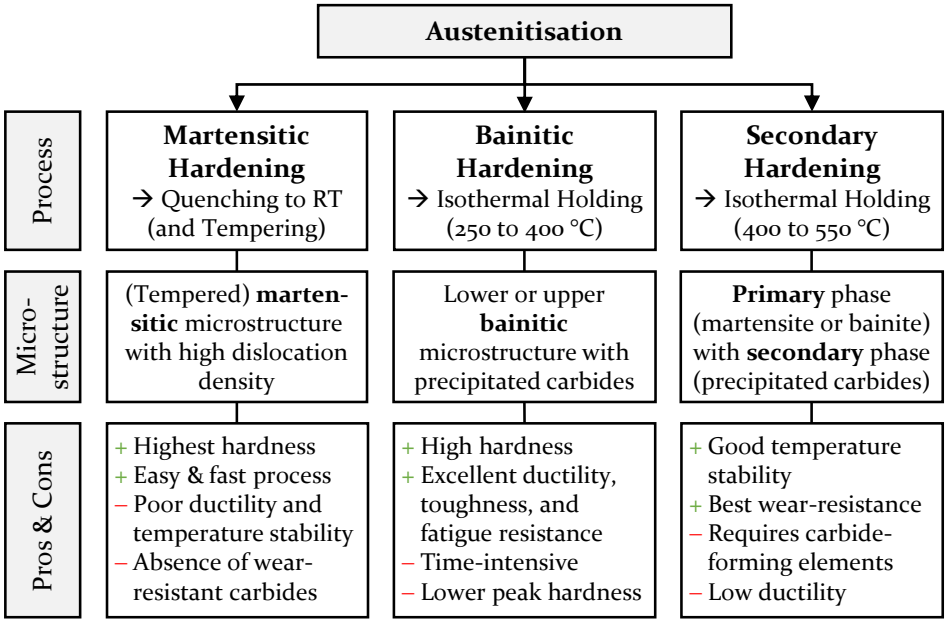

Figure 6: Heat treatment strategies of hardenable steels, the resulting predominant microstructure, and the associated material properties.

2.2 Case-hardening Steels in Mechanical Engineering

Case-hardening steels are normed according to DIN EN ISO 683-3 [88]. Their naming is derived from the subsequent case-hardening process, which is required for improving the hardenability since this class of steels is characterised by a low amount of carbon in the range of 0.1 to 0.3 wt.-%. Commonly used alloying elements include Cr, Mn, Mo, and Ni. These alloying elements follow different purposes and support e.g., carbon diffusion and hardenability [89]. These alloying elements are mainly present in

minor concentrations with a total of all alloying elements typically below 5 wt.-% [90]. Case-hardening steels are therefore colloquially also referred to as low-alloyed steels since they possess similar chemical compositions. Frequently used case-hardening steels include 16MnCr5, 20MnCr5, or 18CrNiMo [91]. The high ductility of the base material provides a good processability using different manufacturing processes like forming [92] and welding [93]. Conventional process chains start with the primary shaping of the raw material, are followed by a case-hardening process, and are concluded by a fine-machining of the hardened surface [94].

Case-hardening Process

The term case-hardening refers to a heat treatment process that improves the surface hardness of this class of steels. The case-hardening process is divided into three main steps: (1) carburisation/nitriding in a carbon/nitrogen atmosphere, (2) hardening, and (3) annealing [95]. Figure 7 presents the exemplary time-temperature diagram that describes the heat treatment of case-hardening steels as well as the resulting case-hardening depth (CHD) of a carburised specimen. In this example, the principle of carburising is explained. These fundamentals are also applicable for nitrided specimens.

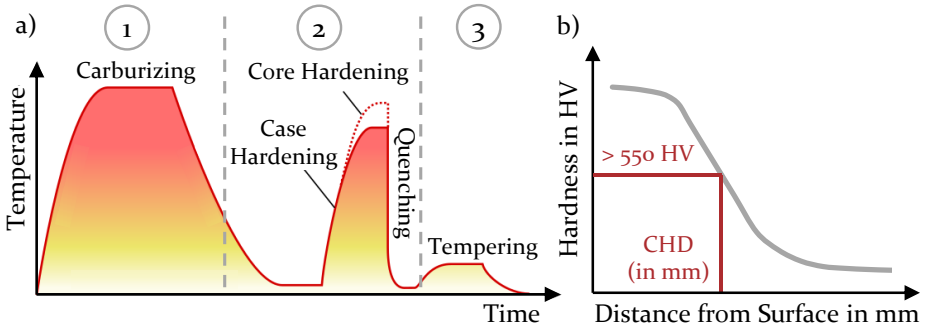

Figure 7: Fundamentals of (a) case-hardening with the three steps Carburising, Hardening and Tempering and (b) exemplary presentation of the case-hardening depth based on [95].

First, the workpiece is exposed to a carbon atmosphere at elevated temperatures that exceed the austenitisation temperature of the material. The carbon is present either in solid, liquid, or gaseous solution. When surpassing the austenitisation temperature of the material, the carbon diffuses into the austenitic phase and into the workpiece. The parameters holding temperature and holding time are decisive for the carbon diffusion into the workpiece [96]. Higher temperatures result in a faster carbon diffusion but also foster undesired effects like grain-coarsening. Longer holding times promote the diffusion of the carbon towards the core of the workpiece.

In the next step, the carbon-enriched workpiece is hardened [97]. This can be done either directly after carburisation or in a secondary hardening step after the workpiece was cooled down. In the latter case, the specimen is heated up above the austenitisation temperature before being quenched e.g., in an oil bath. This results in a martensitic microstructure. Correspondingly, the highest hardness is obtained in the surface region due to the highest carbon concentration after carburisation. The hardness progresses to decrease towards the center of the workpiece. Due to the lower distortion of the martensite, a more ductile core is formed. To improve the ductility of the hard-but-brittle surface, the workpiece is tempered in the third step. Typical tempering temperatures are in the range of 150 to 200 °C [94]. The chosen temperature value depends on the temperatures that arise during operation of the product to avoid a premature failure by e.g., temperature-induced softening of the surface.

The main parameter associated with the case-hardening process is the case-hardening depth (see Figure 7), which is defined in the corresponding international standard [98]. It describes the distance from the surface of the specimen at which the hardness of the workpiece still exceeds 550 HV. The case-hardening depth correlates with the carbon penetration into the case of the specimen. Common CHDs of gears or bearings in the automotive industry are in the range of 0.25 to 1.0 mm [99]. The surface of the specimen typically possesses a hardness between 56 and 64 HRC after low-temperature tempering [100].

Limitations of Case-hardening Steels

Despite the potentials, the use of case-hardening steels is coupled with several limitations when following the established process chain, as shown in Figure 8. First and foremost, the carburisation heat treatment is a time- and energy-consuming process [101]. The furnace that is used for carburisation needs to be heated and held at defined temperatures to achieve a homogeneous carburisation. Carburising the specimens can thereby become disadvantageous when only fabricating small batches. Another major drawback is the limited case-hardenability of complex products, since the process favours the distortion of e.g., thin-walled structures [102]. Furthermore, case-hardening steels are low-alloyed with only minor shares of carbide forming elements. Carburised specimens are primarily hardened and tempered to form a martensitic microstructure. The wear resistance is thereby limited compared to other high-strength steels due to the absence of wear-resistant carbides [103]. The quenching operation to harden the entire workpiece can

also be seen as disadvantageous. Complete hardening results in the formation of a predominantly martensitic structure throughout the entire specimen. This microstructure is associated with several drawbacks like a poorer tempering stability, which can be undesired especially when the microstructure that was formed during the previous manufacturing step would be characterised as advantageous for the final application. The latter is typically the case for hard but more ductile bainitic microstructures. Alternative measures like inductive surface hardening require geometry-specific tools, which are again counterproductive when aiming at the fabrication of smaller batches [104]. Key advantages of the established process route of case-hardening steels like the cost efficiency in mass production are presented in Figure 8. Furthermore, the associated limitations like the distortion in thin-walled parts when using this material group are also shown.

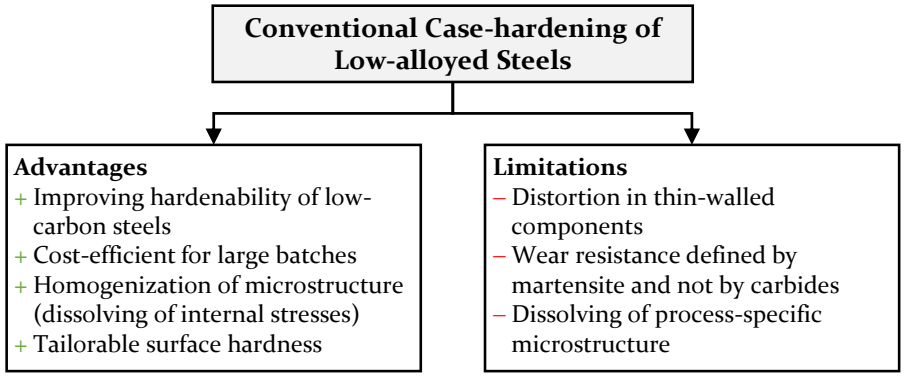

Figure 8: Advantages and limitations of the conventional case-hardening process comprising of carburisation and through-hardening.

2.3 Laser-based Additive Manufacturing of Metals

Additive manufacturing (AM) comprises manufacturing technologies that generate a defined geometry through the successive joining of material [105]. AM processes are also often referred to as rapid manufacturing, 3-D-printing, or generative manufacturing [106]. The workpiece is generated in a layer-by-layer manner. An external energy source provides the required energy for joining the newly applied material with the subjacent layers. Throughout the years, several different additive AM technologies have been developed for fabricating mainly metallic and polymeric products [107]. The material can be present either in a solid state e.g., as powder or

wire, or in a liquid state e.g., as resin [105]. Another distinguishing characteristic is the energy source used for bonding the layers, including lasers with different wavelengths for welding, melting, or photopolymerisation of different materials [108]. Further energy sources are electron beams for processing conductive materials and heating elements for the fabrication of parts from lower melting materials [109]. For processing polymers, technologies like stereolithography, laser sintering and fused deposition modelling are commonly used [110]. AM of metals is mainly performed using binder jetting, powder bed fusion, directed energy deposition, or wire-and-arc deposition processes [111].

2.3.1 Powder Bed Fusion and Directed Energy Deposition

Laser-based powder bed fusion of metals (PBF-LB/M) and laser-based directed energy deposition of metals (DED-LB/M) are the most established laser-based AM processes in industry. These two technologies can be distinguished regarding the supply of the powder material. In PBF-LB/M, the material is present inside a powder bed [112], whereas in DED-LB/M, the powder is supplied using a powder stream [113].

Laser-based Powder Bed Fusion of Metals (PBF-LB/M)

PBF-LB/M is used for generating highly complex products that are characterised by e.g., internal cooling channels or bionic lightweight structures [114]. In literature, different terms like selective laser melting and laser beam melting are also found that describe this process [107]. The fundamentals of the PBF-LB/M process can be found in [112]. Commercially available PBF-LB/M systems are normally equipped with laser systems with output powers of up to 1 kW [115]. The laser spot size is in the range of 80 µm [115] but can also go up to 500 µm [116]. The surface of the powder bed can be scanned by a laser beam with high velocities of up to several thousand mm/s [116]. These high scanning in combination with the small laser spot sizes result in highly detailed melt pools [7]. Consequently, the melt pool is maintained only for fractions of a second, which leads to extremely high cooling rates that can exceed 10^5 K/s [117]. The PBF-LB/M-specific cooling rates exceed the ones of conventional manufacturing technologies [118]. This fast cooling leads to a fine microstructure. However, the high cooling rates during PBF-LB/M result in a quenching-like-process on a microstructural level. The fast cooling induces residual stresses [119], which in combination with brittle microstructural constituents like martensite, support crack formation. To reduce the temperature gradient between the melt pool and the surrounding part, the substrate platform is often heated [120].

After the process is finished, the part is removed from the machine, optional support structures are removed, and additional post-processing steps like heat treatment are performed [121]. The latter is usually necessary to reduce the residual stresses that are formed inside the material during the laser-based process. By applying an appropriate heat treatment, these stresses are resolved, thus enhancing material properties like ductility or fatigue properties [122].

The material portfolio for PBF-LB/M provided by the machine suppliers includes aluminium alloys (e.g., AlSi10Mg), titanium alloys (e.g., Ti-6Al-4V), iron-based alloys (e.g., 1.4404, 1.2343, or 1.2709), and nickel-based superalloys (e.g., Inconel 718) [123]. The common feature of all these materials is the good to excellent weldability. Further iron-based systems like case-hardening steels [124], duplex steels [125], and high-speed steels [126], which might possess a poorer weldability due to different reasons, are currently investigated. Further materials that are of interest include refractory [127] or copper alloys [128] due to their potential application fields in aerospace and high-power applications.

Laser-based Directed Energy Deposition of Metals (DED-LB/M)

The origins of the DED-LB/M process can be found in conventional laser cladding using an auxiliary material [129]. Further names for this process are laser metal deposition and laser engineered net shaping. DED processes are used for the deposition of large volume structures or the processing of freeform surfaces due to its high flexibility [130]. A general introduction into DED-LB/M can be found in [131]. Since the average melt pool size in DED-LB/M is larger compared to PBF-LB/M, a reduced dimensional accuracy [132] as well as lower cooling rates in the range of 10^3 K/s [133] are obtained. The material spectrum for DED-LB/M covers similar materials as for PBF-LB/M. This includes stainless steels (e.g., 316L), tool steels (e.g., 1.2343, 1.2709), and nickel super alloys (e.g., In718) [134]. A good weldability of the material is again a basic prerequisite for this process. However, since only a local inert shielding gas atmosphere is generated, the processing of oxygen-sensitive materials like titanium-based alloys is challenging. The lower cooling rates in DED-LB/M [135] further support the processing of more crack-sensitive materials compared to PBF-LB/M [136]. Whereas the processability of high-speed steels like M2 is limited in PBF-LB/M and requires e.g. high heating temperatures to avoid cold cracking [137], these materials can be processed successfully by means of DED-LB/M [138]. The better processability is attributed to the lower cooling rates and the lower thermal gradients due to a promoted heat accumulation during build-up.

One main advantage in comparison to PBF-LB/M is the way of supplying the powder material [139]. The use of several independent powder hoppers allows to transport multiple different materials into the processing zone simultaneously. This flexibility allows to either generate new material compositions through in-situ alloying [140] or to form reinforced composites [141]. Applying this process also allows to generate graded structures that transit from e.g., a ductile to a high-strength material [142]. Furthermore, it is possible to generate functionally graded materials between e.g., stainless steels and nickel-based alloys [143] or stainless steels and titanium alloys [144]. One major point of interest is the graded zone between the different materials. This transition region can be susceptible to crack formation due to undesired secondary phases. It is therefore necessary to either select appropriate processing strategies that avoid the formation of these undesired constituents or select materials that are similar to each other when aiming at graded material properties. The main differences between the two presented laser-based AM processes PBF-LB/M and DED-LB/M are summarised in Figure 9.

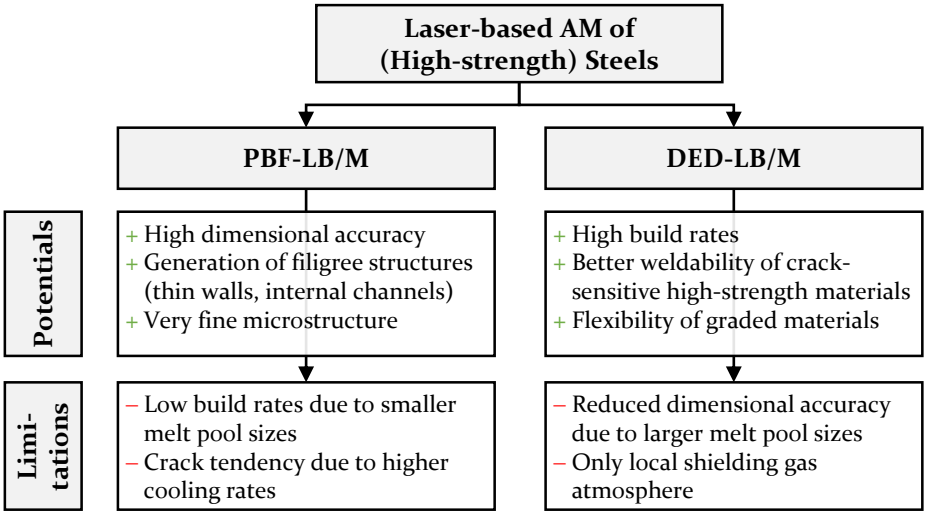

Figure 9: Comparison of the potentials and limitations of PBF-LB/M and DED-LB/M regarding the processing of high-strength steels.

It can be concluded that PBF-LB/M is better suited for the processing or materials with reduced strengths compared to DED-LB/M due to the higher cooling rates. However, the smaller melt pool sizes allow for the generation of high filigree products with internal structures, support key aspects like weight reduction and an efficient temperature control.

2.3.2 Heat Accumulation in Laser-based Additive Manufacturing

Laser-based AM processes are exposed to complex thermal boundary conditions. The layerwise part generation results in a continuous energy input into the workpiece. For PBF-LB/M, this is mainly determined by the laser power (P), spot size, scanning velocity (v), hatch distance (h), and the layer thickness (t). The majority of these parameters is summarised in the volumetric energy density (VED), a parameter that can be used for describing the energy input into the material [145].

$$VED = \frac{P}{v \cdot h \cdot t}$$

Associated with this energy input is a heat accumulation when the energy cannot dissipate completely between two consecutive layers. This heat accumulation acts as an in-situ heating system and affects the cooling conditions and consequently the transformation behaviour of the material [146]. In a first work, Mohr et al. [147] studied the interplay between the geometry of the part, build height, and the interlayer time when manufacturing stainless steel 316L parts by means of PBF-LB/M. The interlayer time (ILT) describes the time that passes between the illumination of the same surface of a part in two consecutive layers. Accordingly, the interlayer time depends on the recoating time as well as the time required for illuminating one layer of all parts within the build job. Mohr et al. [148] found that the temperature development is significantly affected by the applied VED and the interlayer time.

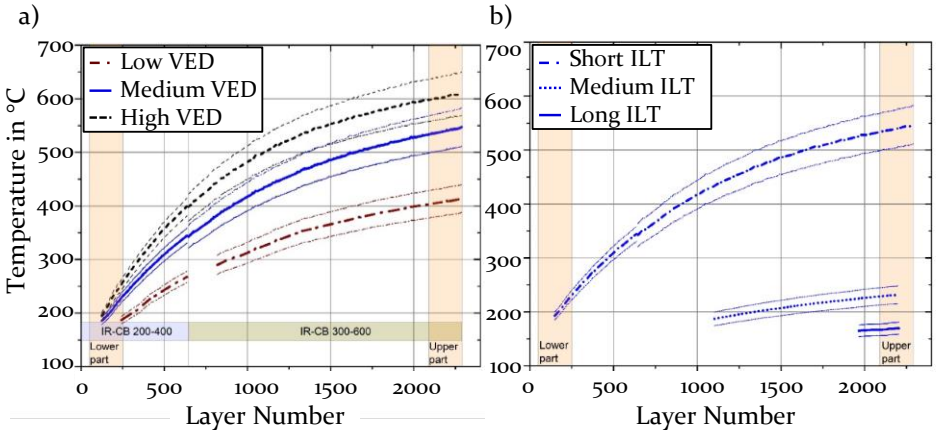

Figure 10: Development of the surface temperature for specimens manufactured with different VEDs and ILTs, extracted from Mohr et al. [149]. Permission is granted through the CC-BY license of this work.

Figure 10 shows an exemplary progression of the surface temperature for the two different process conditions according to Mohr et al. [149]. When manufacturing the same build job with different VEDs, the surface temperature can vary by several hundred degrees Celsius. Selecting an appropriate VED can minimise overheating effects. The interlayer time is a strong lever that influences process-specific overheating during PBF-LB/M. Increasing the interlayer time helps to reduce the maximum surface temperature per layer. However, this also affects the transformation behaviour and the resulting microstructure. Correspondingly, the in-situ temperature development due to heat accumulation is a critical factor that can affect the final material properties. In combination with the chemical composition of the material and the underlying transformation behaviour, the microstructure formation of the additively manufactured specimens can be altered significantly. Similar effects were observed for other materials like Inconel 718 [150]. Furthermore, the findings also apply for DED-LB/M, as shown by Denlinger et al. [151]. The main difference between DED-LB/M and PBF-LB/M is that during DED-LB/M commonly only one part is manufactured per build job while several parts are often fabricated in PBF-LB/M. Accordingly, the heat accumulates faster in DED-LB/M. The heat accumulation can result in part temperatures exceeding several hundred degrees Celsius (> 400 °C) after short times (≈ 2 min) [152]. As for PBF-LB/M, the integration of interlayer times helped to counteract overheating of the material and leads to an improved process result.

2.3.3 Laser-based Additive Manufacturing of Case-hardening and Low-alloyed Steels

Case-hardening steels have recently gained interest for laser-based AM. The good weldability in combination with the post-process carburisation allows to generate products with a hard surface like e.g., optimised lightweight gears [153]. In the following, the material properties of additively manufactured case-hardening and low-alloyed steels are distinguished between the as-built state and the case-hardened state for the processes PBF-LB/M and DED-LB/M.

As-built Material Properties

Early research on the processing of case-hardening steels by means of PBF-LB/M was performed by Kamps and Reinhart in 2014 [153]. These findings were complemented within the doctoral thesis of Kamps in 2018 [154]. Defect-free cubic specimens were fabricated by means of PBF-LB/M using a

layer thickness of 30 µm. The microstructure in the as-built state was described as fine-grained and the corresponding hardness in the as-built state was around 330 HV1. More thorough investigations on the processability of 16MnCr5 were performed by Schmitt et al. in 2018 [124]. The highest material hardness was obtained for the lowest applied laser powers. This high hardness was explained by the high cooling rates due to the small melt pool sizes. Additional studies on the microstructure formation were performed [155], where the PBF-LB/M-specific microstructure was specified as a mixture of martensite, bainite, and ferrite. Aumayr et al. [156] showed that another low-alloyed steel (Böhler E185 AMPO) could be processed successfully by means of PBF-LB/M. The resulting microstructure was also identified to be martensitic-bainitic. Associated with this was an ultimate tensile strength in the region of 900 to 1,100 MPa in the as-built state, as reported by the works of Aumayr et al. [156] and Schmitt et al. [155]. The elongation at break was as high as 17.5 %. Similar results were obtained by Wei et al. [157] when processing 24CrNiMo, a steel characterised by a slightly higher carbon content. The material possesses a bainitic microstructure with a high microhardness. Schmitt et al. [158] investigated the influence of different heating temperatures of up to 600 °C on the resulting material properties. The resulting microstructure depends on the underlying heating temperatures. For low temperatures, a mostly ferritic microstructure was obtained. With increasing heating temperature, a bainitic-ferritic or even pearlitic microstructure is formed. The microstructural changes also correlate with the material hardness, which decreases for higher heating temperatures. Later, Schmitt et al. [159] studied the influence of different part heights on the microstructure formation and hardness of 16MnCr5. Increasing the part height resulted in a slight decrease of material hardness due to the transition from a primarily martensitic microstructure towards one with increasing ferrite contents. Furthermore, grain coarsening effects were observed along the build direction. Yang and Sisson [160] investigated the processing of the case-hardening steel 20MnCr5. The as-built samples possess a higher hardness (up to 300HV) than conventionally manufactured specimens, which was attributed to the underlying tempered martensitic microstructure.

The research on DED-LB/M is mainly focused on the processability of low-alloyed and case-hardening steels rather than investigations on the case-hardenability. Mukherjee et al. [161] studied the DED-LB/M of a water-atomised low-alloyed steel powder. The manufactured specimens were permeated with pores and oxides, which are attributed to the poorer quality of

the water-atomised powder. Analysis of the microstructure revealed a polygonal ferritic matrix with the second phase being cementite aggregates and elongated carbides. Zhao et al. [162] analyzed the processability of the low-alloyed steel 12CrNi2 by means of DED-LB/M. The bainite, ferrite, and martensite ratios could be adjusted by adding interlayer times between consecutive layers. Another work on the same steel revealed a transition from a lath-like bainitic structure towards a granular bainitic microstructure [163]. The highest hardness was in the range of 330 HV, which is similar to the hardness of PBF-LB/M steels despite the lower carbon content. Cao et al. [164] and Ebrahimnia et al. [165] studied the processing of 24CrNiMo. Despite a high relative part density, crack formation could not be avoided completely. The underlying microstructure of this material is predominantly bainitic with lath-like martensite [166]. A hardness between 435 HV and 650 HV was identified and attributed to bainitc and martensitic microstructures [165]. However, the base material was characterised by a high carbon concentration of around 0.4 wt.-%. The higher carbon concentration therefore affects the peak hardness due to dilution effects. Kang et al. [167] have found a hardness between 430 and 490 HV1 with a hardness gradient forming along build direction. The ultimate tensile strength was determined to be around 1,200 MPa. In another work, Zhou et al. [168] studied the processability of the low-alloyed steel 24CrNiMo by means of DED-LB/M. Applying an ultrasonic field during processing helped to improve the relative part density up to 99.9 %. The resulting microstructure consisted of crystalline lower bainite, granular bainite, and shares of retained austenite. A maximum tensile strength of 1,060 MPa coupled with an elongation of break of 14 % was obtained for the optimum processing parameters. Wang et al. [169] investigated the DED of HSLA-100. The generated parts consisted of a ferritic microstructure with traces of martensite and secondary carbides. In general, it can be concluded that both low-alloyed and case-hardening steels can be processed successfully by means of DED-LB/M.

Figure 11 summarises the resulting material properties of case-hardening steels processed by means of PBF-LB/M and DED-LB/M. In PBF-LB/M, the investigations were focused on the case-hardening steel 16MnCr5. DED-LB/M experiments were mainly perfomed using the steels 12CrNi2 and 24CrNiMo. The different alloying compositions of these materials help to explain the different macroscopic material properties such as as-built hardness and tensile strength. Correspondingly, PBF-LB/M specimens are characterised by reduced mechanical properties compared to DED-LB/M sam-

ples. The microstructure of both processes appears similar since martensitic, bainitic, and ferritic structures can be identified within all materials. However, an in-depth qualification of the microstructure has barely been performed in PBF-LB/M.

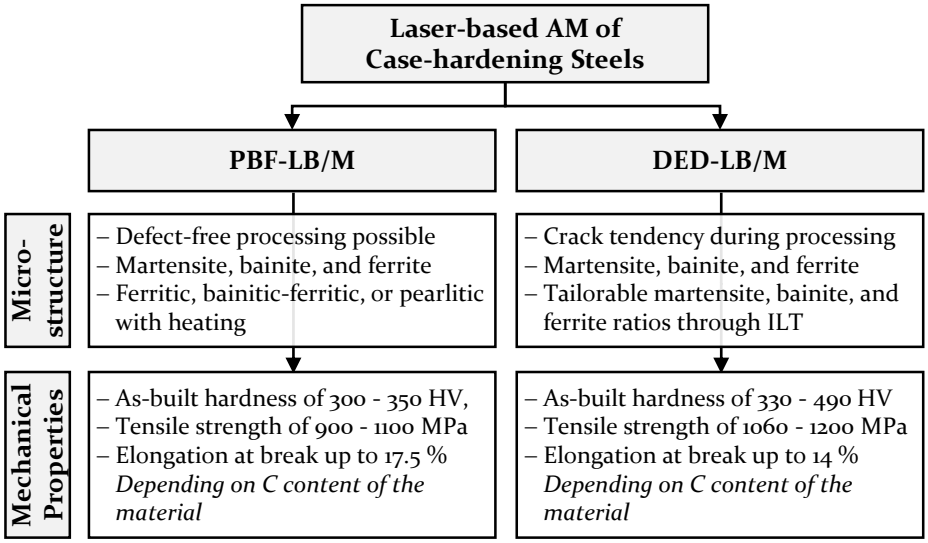

Figure 11: Comparision of the as-built properties of case-hardening steels processed by meands of PBF-LB/M and DED-LB/M.

Case-hardening of Additively Manufactured Specimens

Generally, a fine-grained microstructure is considered detrimental for the carburisation process as the carbon diffusion might be hindered [97]. Kamps [154] presents first results on the case-hardenability of additively manufactured 16MnCr5. The carburised PBF-LB/M samples possess a similar hardness as conventionally manufactured and carburised reference specimens after hardening. A similar case-hardenability for conventional and additively manufactured 16MnCr5 was determined by Schmitt et al. [155]. Their case-hardened PBF-LB/M samples possess a martensitic structure in the case and an upper bainitic microstructure within the core. Aumayr et al. [156] also identified a similar maximum hardness and hardness gradient for conventionally processed 16MnCr5 samples and additively manufactured E185 AMPO. Similar results were obtained for wrought and additively manufactured 20MnCr5 [160]. Both samples were normalised prior to carburisation. The AM parts are characterised by a slightly increased hardness at the surface while a similar case-hardening depth was determined. In another work, it was found that the microstructure formed

in PBF-LB/M affects the case-hardening properties [158]. The best properties regarding maximum surface hardness and case-hardening depth were obtained for martensite while the poorest ones were obtained for a bainitic-ferritic microstructure due to a hindered carbon diffusion. Additively manufactured low-alloyed steels typically possess a hardness between 300 and 350 HV1 in the as-built state. After case-hardening, a surface hardness of up to 800 HV1 can be achieved. This hardness is comparable to the one obtained for conventionally processed reference samples.

2.3.4 In-situ Modification for Tailored Material Properties

Powder materials can be modified easily since they are formed by many single particles. This opens potentials regarding the modification of the material properties by generating powder blends. For this purpose, additional alloying elements (in-situ alloying) like carbon or phase stabilising elements, or other constituents (in-situ particle reinforcement) such as hard particles or oxides can be added. A schematic illustration of the difference between the two approaches is presented in Figure 12.

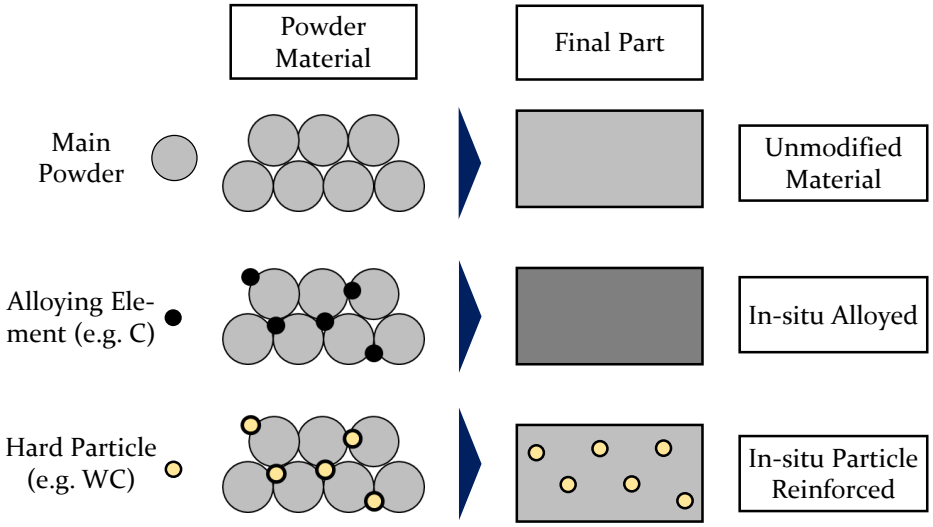

Figure 12: Approaches for the in-situ tailoring of the material properties through powder modification.

Processing these powder blends results in materials with properties e.g., a promoted ductility or hardness, that can be tailored by changing the type and concentration of the respective additives. Premixing the powder materials is preferred for PBF-LB/M since the powder supply from one main

feedstock material limits the spatially resolved deposition of different powder materials. However, recent developments of novel powder supply mechanisms aim at levering the potential of multi-material-generation in PBF-LB/M. Current investigations focus on the integration of dispensing systems [170] and novel electrostatic recoating systems [171]. Regarding the local tailoring of the material properties, DED-LB/M provides a higher flexibility. The chemical composition can be adjusted by changing between different powder materials when using multiple independent powder hoppers [172].

In-situ Alloying

In in-situ alloying, the base material as well as the additional alloying elements are molten to form a new alloy [173]. This approach can be used for generating materials from elemental powders, commonly used for e.g., high-entropy alloys [174], or by adding defined alloying elements to tailor the microstructural properties for e.g., steel products [175]. Hentschel et al. [135] studied the influence of the addition of different carbon concentrations on the material properties of tool steel H11 (1.2343). Carbon nanoparticles were used to modify the base powder. In total, carbon concentrations of up to roughly 0.8 wt.-% were investigated. The powders were premixed using a tumbling unit, which resulted in a homogeneous distribution of these particles at the surface of the base powder. Processing the material by means of DED-LB/M was possible without defect formation for carbon contents of up to 0.6 wt.-%. The material hardness increased for higher carbon concentrations. Furthermore, the hardness was constant within the layers, indicating that the carbon is distributed homogeneously within the matrix. This was validated by energy dispersive X-ray spectroscopy (EDS) images of the microstructure which reveal a promoted carbide formation at the grain boundaries for higher carbon concentrations. A similar approach was followed by Huber et al. [176]. Elemental powders were premixed using a tumbling unit to create a high entropy alloy powder blend. This powder mixture was processed by means of PBF-LB/M. The distribution of the single elements was shown by EDS analysis. An almost homogeneous distribution of the different alloying elements was obtained after processing by means of PBF-LB/M on a macroscopic level. The homogeneity was associated with the high cooling rates of the process. Furthermore, a preferential distribution of the different elements within the matrix was obtained on a microstructural level. Tantal and tungsten are predominantly orientated within the intradendritic regions while niob and molybdenum are found in both inter- and intradentritic regions. In another work, Schmitt et al. [175] modified the case of the case-hardening steel 16MnCr5

with carbon-reinforced powder material. The powder mixture was deposited using the approach presented by Anstätt et al. [177]. A homogeneous microstructure and material hardness were observed in the modified case of the specimen. However, the hardness in the as-built state did not surpass the one obtained after hardening since no complete martensite transformation was achieved. Huber et al. [178] have shown that it is possible to improve the ductility of rather brittle Ti-6Al-4V by adding elemental iron (Fe) and vanadium in their respective work. The addition of these elements allowed to tailor the alloy for the PBF-LB/M-specific process conditions. Similar findings were reported by Chen et al. [179] who present findings on the influence of elemental Fe powders on the material properties of Ti-6Al-4V. The Fe particles ($d_{50} \approx 6$ µm) were mixed with the larger titanium powder ($d_{50} \approx 33$ µm). By adding Fe, the material properties can be affected since phase stabilisation is performed. This helps to e.g., achieve higher ultimate tensile strengths. Furthermore, in-situ alloying can be used to improve properties like the thermal conductivity, as shown by Hassanin et al. [180]. Adding 40 wt.-% of copper (Cu) to the base material Inconel 718 helped to increase the thermal conductivity by 24 %, which can be favourable for an improved cooling. However, the compatibility of the alloying elements is decisive to avoid brittle interfaces between the materials and needs to be considered when selecting the different alloying elements [181].

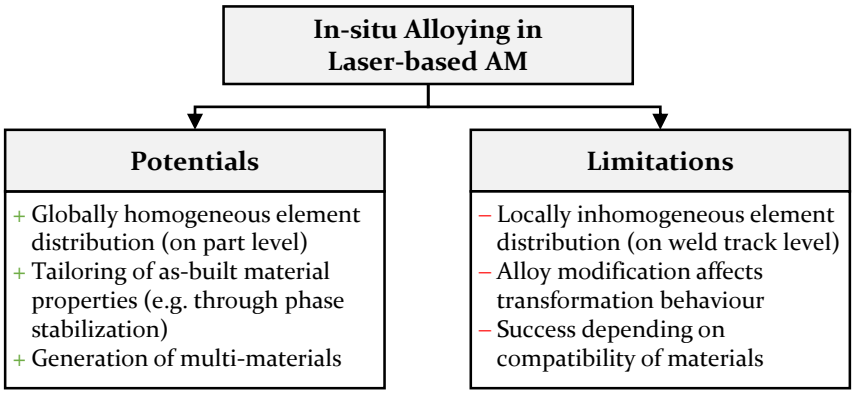

Figure 13: Potentials and limitations of in-situ alloying in laser-based additive manufacturing.

An extraction of the most relevant potentials and limitations of in-situ alloying in laser-based AM are illustrated in Figure 13. When selecting an additional alloying element, the compatibility with the base material as well as its influence on the transformation behaviour of the newly generated alloy should be considered [182].

In-situ Particle Reinforcement

The second approach for reinforcing metallic products is provided by the addition of secondary phases like carbides [183], nitrides [184], or oxides [185]. Depending on the applied processing strategy, these hard phases are either molten or remain finely dispersed within the matrix [186]. In the latter case, a metal-matrix-composite (MMC) is formed that strengthens the material through the embedding of foreign particles [187].

Over 40 years ago, Grünewald et al. [188] studied the laser surface alloying of a case-hardening steel with tungsten carbide and carbon. The reinforcement of the surface helped to improve the surface hardness and wear resistance. Tungsten carbide was beneficial compared to carbon when targeting a reduced wear. Adding hard phase particles is quite commonly used in PBF-LB/M [189] and DED-LB/M [190]. Liu et al. [191] investigated the influence of WC-Co particles on the material properties of the tempering steel C45E when processed by means of PBF-LB/M. The base material is characterised by a hardness of around 480 HV0.1 in the as-built state. Adding 10 wt.-% of WC-Co particles resulted in a maximum of hardness of around 820 HV0.1. Furthermore, it was found that the processing strategy, especially the energy input, affected the resulting material hardness. Higher line energy densities led to a higher hardness since a larger number of the WC-Co particles was dissolved. However, the addition of these high WC-Co concentrations promoted microcrack formation in the bonding region of these particles. Despite the crack tendency, the addition of these particles also improved the wear resistance by almost the factor of three compared to the base material.

The work by van Acker et al. [192] reports findings on the influence of different WC concentrations (10, 30, and 50 %) and particle sizes (32, 48, and 116 µm) on the material hardness and wear resistance. For the highest WC concentrations, a similar wear resistance was obtained for all particle sizes. Smaller particle sizes have been promising when using lower WC particle concentrations. When using lower WC concentrations in the range of 10 %, finer particles have proven more promising since larger particles tend to sink towards the bottom of the deposited cladding and agglomerate. Smaller particles sizes result in a more homogeneous distribution of these particles. Shi et al. [193] studied the influence of the particle size of WC particles (5, 10, and 21 µm) on the material properties of Inconel 718 processed by means of PBF-LB/M. They found that the average particle size affects the microstructure formation. Small particle sizes support the

growth of a fine dendritic microstructure originating from the WC particles, which promoted the bonding of the embedded particles to the metal matrix. Furthermore, the size of the embedded WC particles also affected the friction coefficient. Smaller WC particles also resulted in a reduced friction coefficient during wear testing. The reduced friction coefficient led to a homogenisation of the wear, which is indicated by a smoother surface without pits. Song et al. [194] added WC particles to stainless steel 316L and processed the material through DED-LB/M. A material hardness of around 550 HV0.5 was observed when adding up to 24 wt.-% of WC particles. Most of the particles were dissolved in the matrix. Hübner et al. [183] investigated the influence of WC particles on the material properties of Inconel 625. They found that the additive is distributed homogeneously within the matrix. Furthermore, the size should not fall below 5 µm to avoid dissolving of these particles during DED-LB/M. The addition of up to 10 wt.-% of WC-Co led to a maximum hardness of around 540 HV0.2. On the other hand, the unmodified material possessed a maximum hardness of around 425 HV0.2. The studies by Liu et al. [191] and Shi et al. [193] for PBF-LB/M as well as the work by Song et al. [194] and Hübner et al. [183] for DED-LB/M prove that the strengthening effects are not linear and depend both on the base material and the applied manufacturing process.

Furthermore, hard particles can act as nucleation agents and support grain-refinement [195]. Adding nucleation agents like TiC nanoparticles (< 200 nm) leads to a refined microstructure of the nickel-based superalloy Hastelloy X when processed through PBF-LB/M [196]. The presence of 3 wt.-% TiC was sufficient to counter crack formation within the material by promoting the total number of grain boundaries. However, the addition of hard phases can negatively affect the processability of the material [197]. Carbide particles possess poorer thermal properties like thermal expansion or shrinking compared to the surrounding steel matrix. The poorer thermal properties in combination with the fast cooling during laser-based processes can result in defects during solidification and cooling causing the formation of cracks or pores originating from the embedded particles [198].

The potentials and limitations of different particle sizes in PBF-LB/M and DED-LB/M are summarised in Figure 14. When reinforcing materials with hard particles, small microparticles with a particle size smaller than the average particle size of the matrix material should be selected due to the reduced tendency of bonding defects as well as their positive influence on the wear resistance.

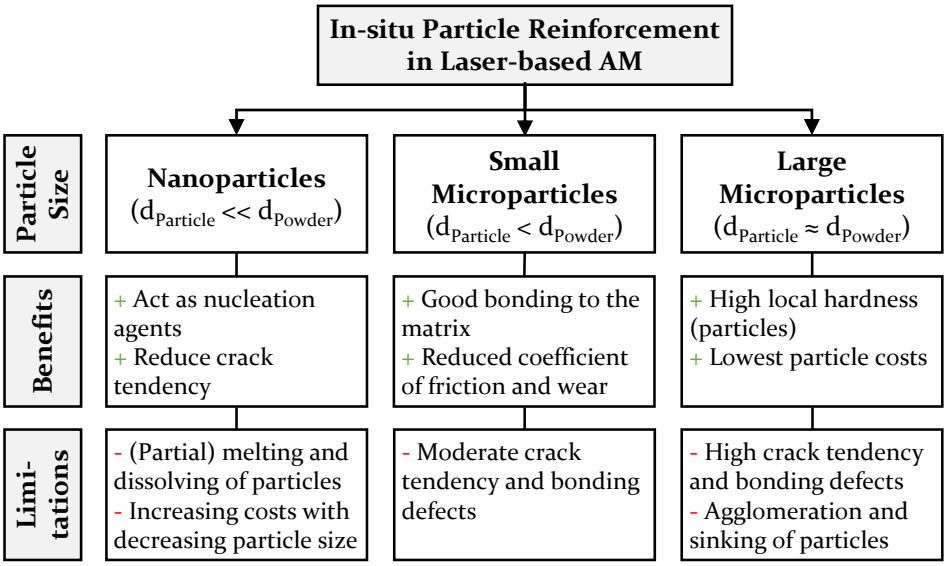

Figure 14: Summary of the limitations and benefits of different particle sizes in laser-based additive manufacturing.

2.4 Summarising Assessment of the State of the Art

Case-hardening steels fulfil one of the prerequisites for laser-based AM due to their good weldability. By exposing the workpiece to a post-process case-hardening heat treatment, wear-resistant products with a high surface hardness can be generated. The established processing route for the generation of products from case-hardening steels includes the three steps: (1) primary shaping, (2) case-hardening, and (3) final machining. Considering the respective potentials and application fields of PBF-LB/M and DED-LB/M, the first two process steps of the conventional process chain are of particular interest. Thereby, PBF-LB/M allows for the generation of highly complex structures, which can be beneficial when aiming at optimised products e.g., through a close-to-contour cooling. DED-LB/M supports the deposition of wear-resistant coatings through the in-situ modification of the material system, which cannot be realised at reasonable effort using PBF-LB/M due to the higher crack-tendency of the material.

The research on case-hardening steels in PBF-LB/M is mainly focused on generating defect-free specimens and analysing superficial material properties like hardness and **microstructure formation** using optical microscopy. Correspondingly, the underlying microstructure is typically described as martensitic or bainitic-martensitic due to the high cooling rates

and the in-situ heat treatment (see Section 2.3.3). However, the fine microstructure in combination with the limited resolution of optical light microscopy (OLM) impede a reliable assessment of the microstructure formation. In contrast to PBF-LB/M, little is known on the processing of case-hardening steels by means of DED-LB/M. Other low-alloyed steels like 24CrNiMo are characterised by a promoted crack tendency when processing the material using DED-LB/M. Correspondingly, the underlying microstructure is mostly unknown or not representative for potential applications. Therefore, the processing of case-hardening steels by means of DED-LB/M cannot be classified as state of the art. This deficit limits the application of this class of materials for repair or large volume production. Additional work is therefore required to identify the correlations between processing strategy and material properties to spread the use of these materials, especially for DED-LB/M.

The next important topic is the influence of the **thermal history** during laser-based AM. Until now, the influence of heat accumulation was only investigated superficially for case-hardening steels and part heights of up to 15 mm. However, literature shows (see Section 2.3.2) that the surface of steel parts can exceed temperatures of 500 °C during PBF-LB/M for large parts (height ≥ 60 mm). Linking these temperatures with the temperature-sensitive transformation behaviour of case-hardening steels (see Section 2.1.1), this should result in altered material properties compared to the commonly investigated smaller specimens. A transition from a tempered martensitic towards a bainitic microstructure could take place during PBF-LB/M for larger specimens. However, the influence of complex thermal cycle of laser-based AM processes on the resulting microstructural properties is vastly unknown for these materials. Additional research on the microstructure formation is therefore necessary when aiming at using additively manufactured specimens directly from the as-built state e.g., for construction parts. Furthermore, the influence of potential alternative heat treatment strategies on the final material properties is unclear. These heat treatments could again become necessary for achieving homogeneous material properties along build direction.

Furthermore, the **tailoring of the surface hardness** of case-hardening steels is a decisive factor. The case-hardenability of additively manufactured specimens was investigated in different reports. Goal of those studies was to compare the material properties of additively manufactured specimens with the ones of conventionally processed samples. The results indicate that the case-hardenability is comparable for additive and conven-

tional manufacturing. However, it remains unclear how different microstructures affect the case-hardenability after heat treatment. Potential heat treatments include stress-relief or grain-coarsening heat treatments, which become necessary to either avoid distortion after PBF-LB/M or to homogenise the microstructure so that material properties comparable to those of conventionally processed case-hardening steels are achieved. The later could become necessary to reduce certification issues for the use of additively manufactured specimens from certified case-hardening steels. Furthermore, the potentials of PBF-LB/M and DED-LB/M support the generation of hard and wear-resistant materials either through in-situ alloying or in-situ MMC formation (see Section 2.3.4). The in-situ modification possesses an alternative to case-hardening since the surface hardness and wear resistance of the final workpiece can be tailored. It was shown for other materials like stainless or tool steels that these approaches are feasible for improving these properties. However, the influence of these additional constituents on the material properties of case-hardening steels is almost completely unknown. First work was performed on the local addition of carbon to case-hardening steels in PBF-LB/M. However, this approach was linked to an increased defect formation in the transition zone. Further research needs to be conducted on the carbon reinforcement of these steels to understand the correlations between carbon concentration, processing strategy, and the resulting material properties like obtained hardness in the as-built and heat-treated state. Knowing these correlations, it could become possible to substitute the carburising heat treatment for the generation of the hard workpiece's surface. To further adopt the depicted potentials, the next logical step is to investigate the MMC formation in case-hardening steels. Due to the different thermal boundary conditions of PBF-LB/M and DED-LB/M, the in-situ modification of the base material needs to be investigated for both processes. PBF-LB/M is associated with higher cooling rates, which could be detrimental when generating MMCs due to e.g., crack formation. The lower cooling rates in DED-LB/M support the processing of high-strength materials at the absence of cracks. This needs to be investigated to identify which manufacturing technology is suitable to substitute the case-hardening process.

Correspondingly, three main research topics were identified, that still lack fundamental research to further establish case-hardening steels for laser-based AM: (1) **Microstructure Formation**, (2) **Thermal History**, and (3) **Tailoring of Surface Hardness**. Figure 15 presents an overview on the exisiting knowledge as well as the remaining deficits. These topics need to be

addressed to eliminate the deficits within the state of the art and to open new potentials for the application of case-hardening steels.

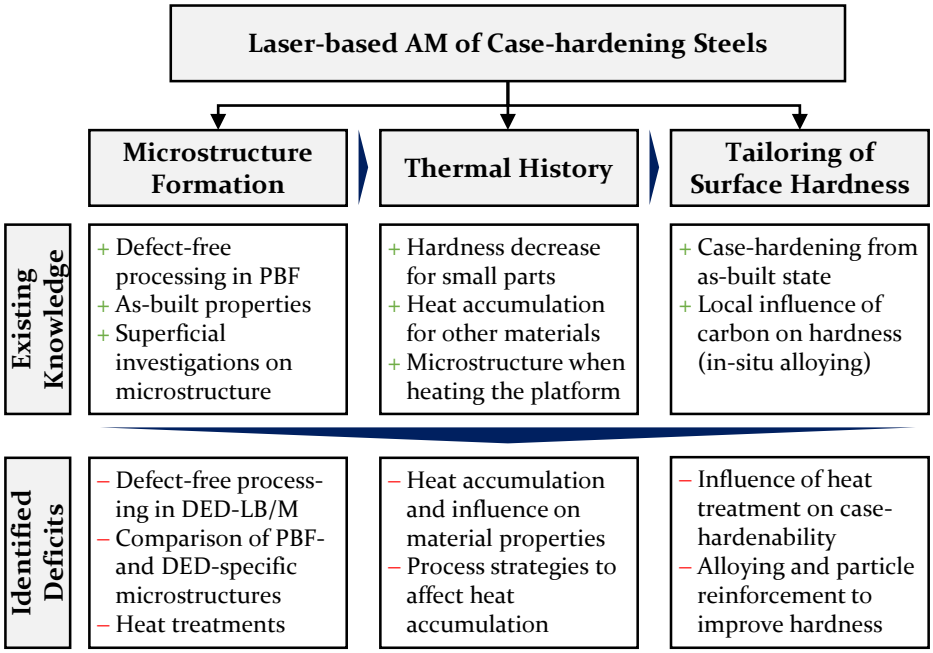

Figure 15: Existing knowledge on the laser-based AM of case-hardening steels and the associated deficits.

3 Goal and Methodological Approach

Up to now, the process chain for additively manufactured parts still proposes a conventional case-hardening heat treatment to improve the surface hardness of the final workpiece. The overarching goal of this work is to utilise the potentials of laser-based AM and substitute the post-process carburising heat treatment through the in-situ modification of the powder material. To achieve this, a fundamental understanding on the processing of case-hardening steels by means of laser-based AM needs to be generated.

In the first step, the correlations between processing strategy and the resulting **microstructure formation** are studied for small-scaled specimens. Key material properties are characterised and assessed based on a combination of different analysing methods to identify the similarities and differences of the microstructures and material properties resulting in PBF-LB/M and DED-LB/M. Knowing the microstructure of small-scaled specimens is decisive for understanding the second important factor, the **thermal history**. By scaling the geometry of the specimens, effects like heat accumulation and in-situ heat treatment during build-up are promoted. These effects are further forced by varying the energy input during additive manufacturing. The spatially-resolved analysis of key material properties allows to determine the influence of the thermal history on the resulting microstructural and associated macrostructural properties in different regions of the large-scaled parts. Correspondingly, the main mechanisms responsible for the microstructure formation in case-hardening steels are derived. In the final step, different approaches are studied for **tailoring the surface hardness**. Both ex-situ and in-situ approaches are investigated for improving the hardness. Ex-situ carburising is investigated to determine the influence of different pre-carburising heat treatments on the case-hardenability. To spare the carburising process, the case-hardening steels is also modified in-situ by adding different additives (C and WC) in varying concentrations. By analysing the interdependencies between material modifications, processing strategy, and resulting properties, the suitability of the different in-situ modification strategies can be assessed for both PBF-LB/M and DED-LB/M. The respective contribution to the main research goal (see Figure 16) will be provided by answering the following research questions (RQ):

RQ1: What are the microstructure and the associated material properties of case-hardening steels processed by means of PBF-LB/M and DED-LB/M?

RQ2: How does heat accumulation in PBF-LB/M affect the final material properties of case-hardening steels and which strategies are feasible for achieving homogeneous material properties?
RQ3: How do ex-situ heat treatments affect the case-hardenability of additively manufactured case-hardening steels?
RQ4: What are the potentials and limitations of the in-situ modification of case-hardening steels in laser-based additive manufacturing regarding key properties like processability, microstructure formation, and material hardness?

An in-detail methodological approach as well as the respective manuscripts for answering these questions are provided in Chapters 4 to 6. Throughout this work, the two case-hardening steels 16MnCr5 (1.7131) and Bainidur AM (1.7980) are investigated. 16MnCr5 is used for mirroring the conventional process chain (case-hardening) and in-situ modification in PBF-LB/M while Bainidur AM is used for analysing the underlying microstructure as well as the development of an alternative process chain via DED-LB/M.

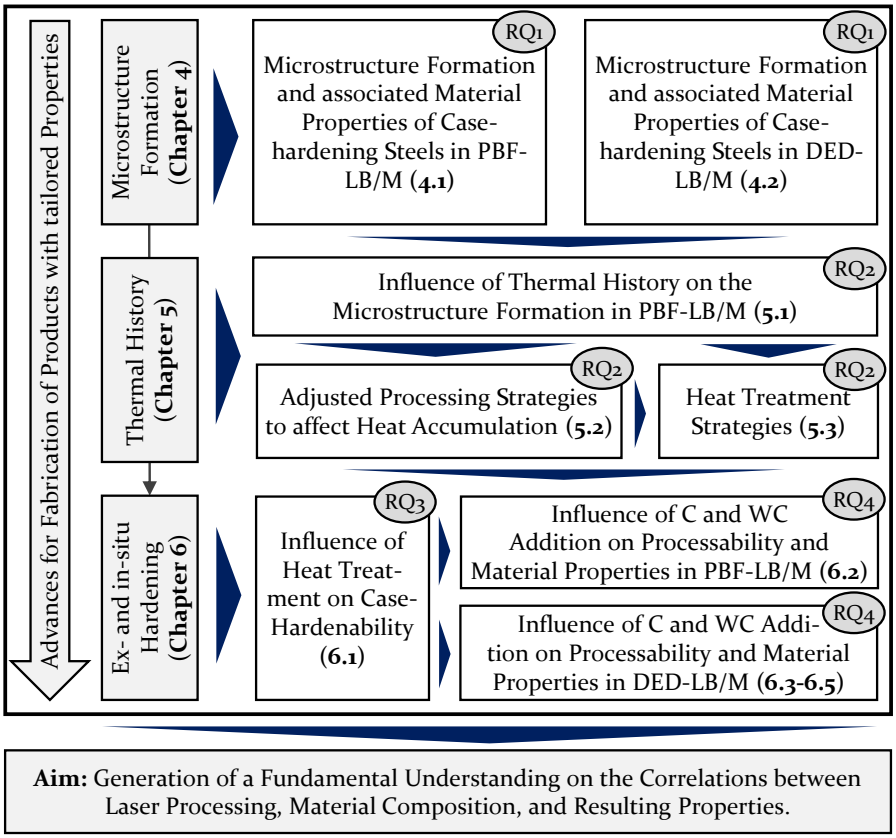

Figure 16: Structure of this work and the classification of the corresponding manuscripts.

4 Microstructure Formation of Case-hardening Steels

The microstructure of additively manufactured case-hardening steels is often described as martensitic-bainitic. This conclusion is performed based on a combination of material hardness, optical microscopy of etched cross-sections, and the underlying thermal cycle in AM. However, due to the fine-grained microstructure of laser-processed steels, a clear distinction between martensite, tempered martensite, and bainite is only barely reasonable using these proposed techniques.

Goal of Chapter 4 is to develop an understanding on the **microstructure formation (RQ1)** in small-scaled specimens manufactured from case-hardening steels. Therefore, the correlations between manufacturing process and material properties are studied. The investigations are carried out for PBF-LB/M and DED-LB/M to assess the resulting microstructure for both processes with the aim of generating a bainite-like microstructure in the respective processes. Since the differentiation between bainite and martensite is very difficult when generated through laser-based additive manufacturing, an analysis method that comprises of several sub-methods is followed for characterising the microstructure. In the first step, the as-built microstructure is analyzed by means of optical microscopy and scanning electron microscopy. This allows to assess the texture of the microstructure and to identify structures like e.g., carbides within the grain (martensite or lower bainite) or at the grain boundaries (upper bainite). In the next step, hardness measurements are performed in the as-built and quenched state. Different tempering temperatures of up to 600 °C are investigated in this context to differentiate between a thermally stable (bainite) and instable (martensite) microstructure. The influence of the heat treatment on the underlying microstructural properties is again determined by means of scanning electron microscopy. By combining the results obtained through microscopy and hardness measurements, it is possible to classify and specify the correlation between microstructure and material properties in small-scaled specimens.

At the end of Chapter 4, an understanding on the underlying microstructure of additively manufactured case-hardening steels will be present for the processes PBF-LB/M and DED-LB/M. This knowledge lays the foundation for the later design of advanced process chains that exploit the benefits of the as-built microstructure of the main body.

4.1 Microstructure Formation in PBF-LB/M

Title: PBF-LB/M of Low-Alloyed Steels: Bainite-like Microstructures despite High Cooling Rates [P6]

Journal: Materials, MDPI

DOI to Web-version: https://doi.org/10.3390/ma15176171

Authors: Dominic Bartels, Tobias Novotny, Andreas Mohr, Frank van Soest, Oliver Hentschel, Carsten Merklein, Michael Schmidt

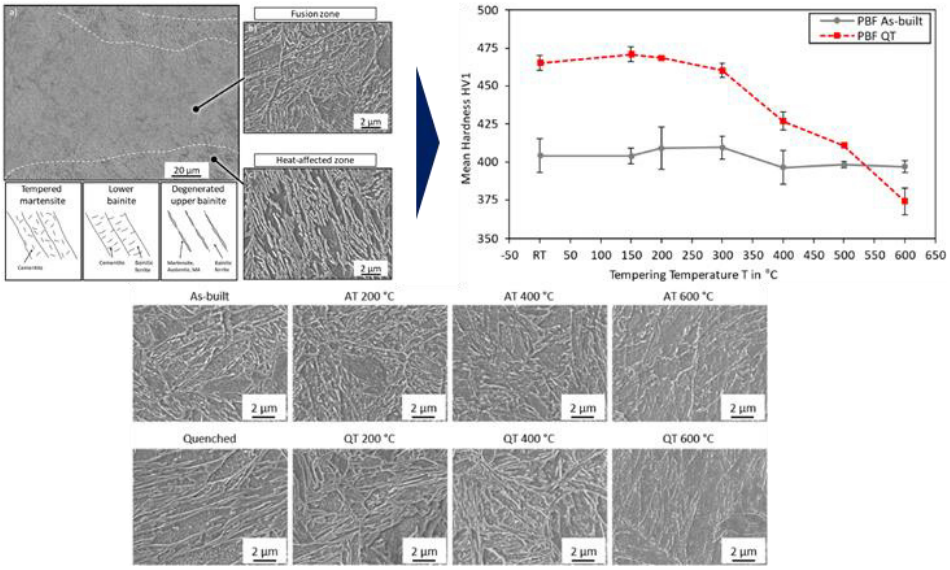

Motivation and Key Findings:

The use of case-hardening steels requires a fundamental understanding on the material properties depending on the applied processing strategy. Due to their good weldability, case-hardening steels can be processed successfully without meaningful defects over a large parameter window. However, up to now, the material properties have only been studied superficially. Indept analyses on the microstructure as well as the influence of different heat treatment strategies on the material properties are still missing. The **highlights** are:

- Excellent processability of case-hardening steel with carbon concentration of around 0.22 wt.-% by means of PBF-LB/M
- Bainitic microstructure with shares of lower and upper bainite
- Excellent tempering stability up to temperatures of 600 °C

materials

MDPI

Article

PBF-LB/M of Low-Alloyed Steels: Bainite-like Microstructures despite High Cooling Rates

Dominic Bartels [1,2,3,*], Tobias Novotny [1,4], Andreas Mohr [5], Frank van Soest [5], Oliver Hentschel [1,3], Carsten Merklein [4] and Michael Schmidt [1,2,3]

[1] Institute of Photonic Technologies (LPT), Friedrich-Alexander-Universität Erlangen-Nürnberg (FAU), Konrad-Zuse-Straße 3/5, 91052 Erlangen, Germany
[2] Collaborative Research Center CRC 814—Additive Manufacturing, 91052 Erlangen, Germany
[3] Erlangen Graduate School in Advanced Optical Technologies (SAOT), Friedrich-Alexander-Universität Erlangen-Nürnberg (FAU), Paul-Gordan-Straße 6, 91052 Erlangen, Germany
[4] Schaeffler Technologies AG & Co. KG, Industriestraße 1-3, 91074 Herzogenaurach, Germany
[5] Deutsche Edelstahlwerke Specialty Steel GmbH & Co. KG, Oberschlesienstraße 16, 47807 Krefeld, Germany
* Correspondence: dominic.bartels@lpt.uni-erlangen.de; Tel.: +49-09131-85-64101

Abstract: Laser-based powder bed fusion of metals (PBF-LB/M) is an emerging technology with enormous potential for the fabrication of highly complex products due to the layer-wise fabrication process. Low-alloyed steels have recently gained interest due to their wide potential range of applications. However, the correlation between the processing strategy and the material properties remains mostly unclear. The process-inherent high cooling rates support the assumption that a very fine martensitic microstructure is formed. Therefore, the microstructure formation was studied by means of scanning electron microscopy, hardness measurements, and an analysis of the tempering stability. It could be shown that additively manufactured Bainidur AM samples possess a bainitic microstructure despite the high process-specific cooling rates in PBF-LB/M. This bainitic microstructure is characterized by an excellent tempering stability up to temperatures as high as 600 °C. In contrast to this, additively manufactured and martensitic-hardened specimens are characterized by a higher initial hardness but a significantly reduced tempering stability. This shows the potential of manufacturing products from Bainidur AM for high-temperature applications without the necessity of a post-process heat treatment for achieving the desired bainitic microstructure.

Keywords: PBF-LB/M; selective laser melting; laser beam melting; low-alloyed steel; Bainidur AM; material properties; phase formation; tempering stability; bainitic steels; additive manufacturing

Citation: Bartels, D.; Novotny, T.; Mohr, A.; van Soest, F.; Hentschel, O.; Merklein, C.; Schmidt, M. PBF-LB/M of Low-Alloyed Steels: Bainite-like Microstructures despite High Cooling Rates. *Materials* **2022**, *15*, 6171. https://doi.org/10.3390/ma15176171

Academic Editors: Thomas Niendorf and Yuvaraj M. Hunge

Received: 1 August 2022
Accepted: 30 August 2022
Published: 5 September 2022

1. Introduction

Bearing and gear applications have an extremely high demand regarding the underlying material properties as a high-impact toughness is required while also providing a sufficient material hardness and wear resistance [1]. The material properties of parts are highly dependent on the underlying microstructure, especially the phase distribution [2]. In steels, for example, a high ductility is achieved through the austenitic or pearlitic phase, while the martensitic phase favors an elevated hardness at the cost of ductility [3]. A trade-off between these two phases is possessed by bainite, which is characterized by a material hardness comparable to tempered martensite [4]. The ductility of bainite is typically higher compared to that of martensite. When generating the bainite, however, a complex heat treatment with adjusted cooling conditions and prolonged holding times is typically necessary [5]. The heat treatment parameters are again dependent on the chemical composition of the material system [6]. Additive manufacturing technologies such as laser-based powder bed fusion (PBF-LB/M) and directed energy deposition (DED-LB/M) are known for their high cooling rates, which can exceed 10^3 K/s for both processes [7,8]. This would typically result in the formation of a martensitic phase in carbon steels [9]. In recent

years, the Deutsche Edelstahlwerke Specialty Steels GmbH (Krefeld, Germany) developed a low-alloyed case-hardening steel named Bainidur AM. The chemical composition of this alloying system was adjusted to favor the formation of a bainitic microstructure in the PBF-LB/M process [10]. Kelliger et al. [11] have used this material to manufacture nozzles with optimized cooling channels. However, no studies on the microstructural properties were performed within this work. Apart from that, Bartels et al. [12] showed the general processability of Bainidur AM by means of DED-LB/M. These early investigations indicate that at least a partial bainitic microstructure is formed during the DED-LB/M. However, extensive research on this material system and the corresponding phase formation in this material system is not available in the literature up to now.

Due to their low carbon content, case-hardening steels typically possess a good weldability, making them suitable for welding-based processes [13]. First studies on the processing of this group of steels by means of PBF-LB/M have already been performed. Independent researchers, e.g., Kamps [14], Schmitt et al. [15], and Bartels et al. [16], show that defect-free parts from 16MnCr5 can be manufactured additively. Schmitt et al. [17] also state in another work that a predominant bainitic microstructure with shares of martensite is formed when processing the low-alloyed steel 16MnCr5 by means of PBF-LB/M. However, thorough investigations on the microstructure are missing within this work as the focus was laid on studying the process chain for manufacturing gears using the PBF-LB/M process. Aumayr et al. [18] investigated the processing of the low-alloyed steel Böhler E185 AMPO, also using the PBF-LB/M process. The carbon content of this material is around 0.2 wt.%. Here, a defect-free processing was possible for different parameter combinations. This material was also characterized by an excellent impact toughness of around 140 J. Tensile strength and elongation at break were determined to be around 1150 N/mm^2 and 15%, respectively. This was attributed to the bainitic-martensitic microstructure formed during the PBF-LB/M process. After hardening, a higher tensile strength at the cost of a reduced ductility could be observed, which further underlines these findings that martensite is not the main phase within the microstructure. Zumhofen et al. [19] investigated the PBF-LB/M of 30CrNiMo8. This material is characterized by a higher carbon content compared to 16MnCr5, which could potentially favor defect formation during build-up. Their experiments show that defect-free specimen with a high relative part density can be fabricated using a platform preheating of 300 °C. The as-built material is characterized by an acicular microstructure compared to the same material in the quenched and tempered state. Damon et al. [20] studied the impact of the process intrinsic heat treatment on the mechanical properties of the quench and tempering (QT) steel 42CrMo4. Within their work, they found that a similar hardness of around 40 HRC could be observed when tempering the quenched material at 450 °C. Considering the high cooling rates of the PBF-LB/M process and the preheating temperature of around 200 °C, a significantly higher hardness of around 650 HV should be present after fabrication. Instead, the as-built microstructure possesses finely dispersed carbides, which are typical for tempered martensite. The authors assume that a reheating and tempering of lower layers takes place during the manufacturing process, which could explain the tempered martensitic structure. Another work by Beer et al. [21] investigated the processing of the case-hardening steel M50NiL by means of PBF-LB/M and compared the resulting material properties with the ones obtained for conventionally manufactured M50NiL. In both cases, similar microstructural and mechanical properties were obtained. Furthermore, additively manufactured samples mastered fatigue life testing without premature failure.

The literature review shows that parts from low-alloyed steels can be manufactured successfully using the PBF-LB/M process. However, fundamental investigations on the microstructure formation are still missing for this material class. These studies need to be performed to fully understand the phase formation and the resulting material properties after PBF-LB/M to fully exploit the benefits of the process-specific fine microstructure.

The goal of this work is to study the influence of different processing conditions and strategies on the phase formation in the low-alloyed steel Bainidur AM (1.7980;

18MnCrMoV4-8-7) in PBF-LB/M. As the name suggests, the material was designed to form bainite during additive manufacturing processes. It is assumed that a predominantly bainitic microstructure can be formed in PBF-LB/M despite the high cooling rates in the order of 10^3 to 10^5 K/s [7,8] of this process. Furthermore, the tempering stability will be analyzed as an indicator for a bainitic microstructure.

2. Materials and Methods

The powder material Bainidur AM (Deutsche Edelstahlwerke, Germany) was used for the underlying experiments. All experiments were performed on an AconityMINI (Aconity 3D, Germany) equipped with a 1 kW fiber laser. The average particle size distribution of the powder batch ranged from 15 to 45 µm ($d_{10\%}$ = 18.28 µm, $d_{50\%}$ = 32.72 µm, $d_{90\%}$ = 46.58 µm, measured using a Camsizer). Table 1 lists the chemical composition of the material system according to the supplier's certificate.

Table 1. Chemical composition of the Bainidur AM powder batch used within this work.

Batch	Element Content in wt.%								
	C	Si	Mn	P	S	Cr	Mo	Ni	V
Powder	0.22	0.7	1.2	<0.02	<0.02	1.0	0.9	<0.3	<0.15

The powder material is characterized by a low carbon content of 0.22 wt.%, which indicates that the material should be processed successfully without cracks using PBF-LB/M. An ELEMENTRAC CS-i (ELTRA GmbH, Haan, Germany) analyzer was used to validate the carbon content of the powder material. Furthermore, optical emission spectroscopy (OES) was used for determining the chemical composition of the material in the as-built state. A SPECTROMAXx (SPECTRO Analytical Instruments GmbH, Kleve, Germany) was used for these measurements. The composition was determined in the center of the specimen.

Figure 1a presents SEM images of the powder material used within this work, while Figure 1b shows an exemplary build job consisting of five cubic specimens.

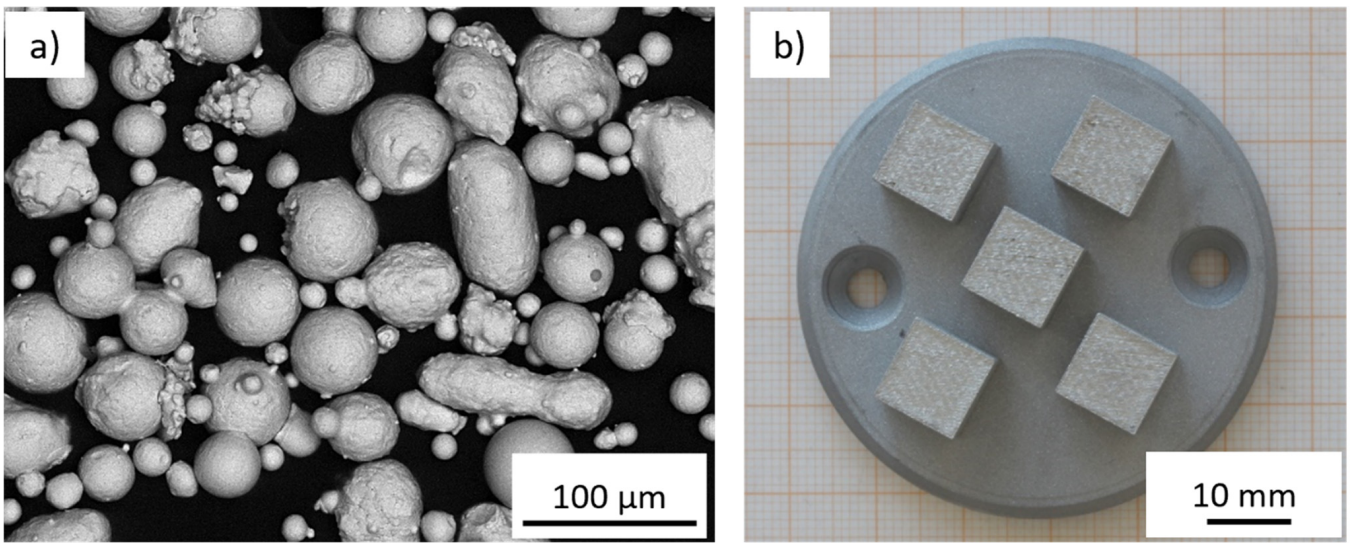

Figure 1. Morphology of the powder materials used (**a**) with a nominal size from 15 to 45 µm and (**b**) an exemplary design of the build job on the AconityMINI.

Primarily spherical particles can be observed with shares of sporadic, irregularly shaped particles with a longish form. A good flowability can be assumed, which is necessary for the supply of the powder layer during the PBF-LB/M process.

2.1. Identification of Process Window

For identifying the process window, the three dominant parameters of laser power, scanning speed, and hatch distance were varied in a wide range. Within these experiments, the contour parameters were maintained constant. The process parameter range was deduced using cubic specimens with dimensions of 10 × 10 × 10 mm. Laser spot size and layer thickness were maintained constant throughout all experiments. The investigated range of parameters is listed in Table 2.

Table 2. Investigated process parameter range.

Process Parameter	Parameter Range
Laser Power, P (W)	225–250–275
Scanning Speed, v (mm/s)	550–700–850
Hatch Distance, h (µm)	100–110–120
Layer Thickness, t (µm)	60
Laser Spot Diameter (µm)	105
Shielding Gas	Argon

The layer thickness was maintained constant at 60 µm per layer. The default scanning direction was turned by 67° after every layer on the AconityMINI, a commonly used scanning strategy in PBF-LB/M. All samples were manufactured without platform preheating.

2.2. Sample Preparation and Analysis

All specimens were embedded, ground, and polished to analyze the relative part density and material hardness on cross-sections. The approach for the sample preparation is presented in Figure 2.

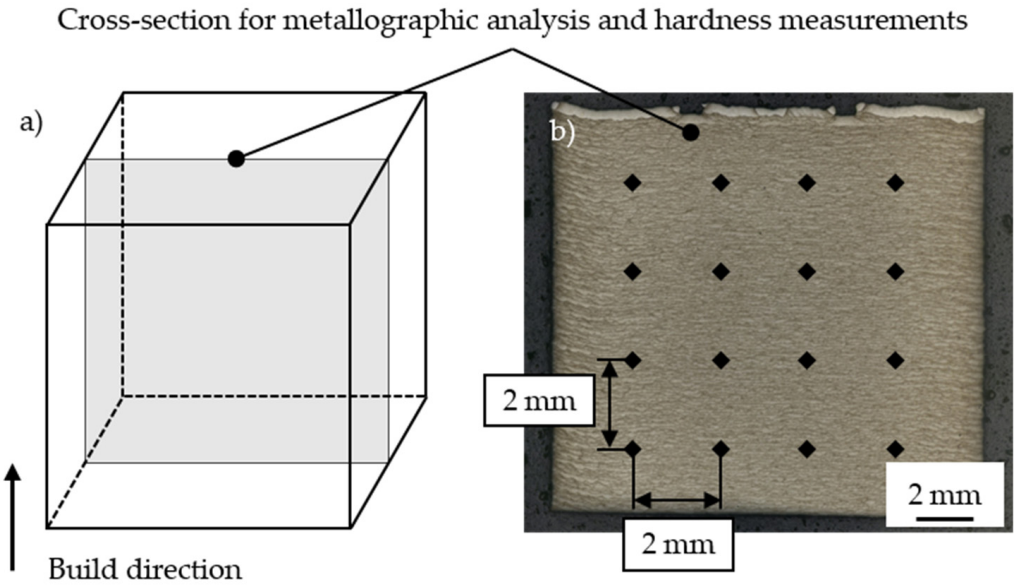

Figure 2. Experimental approach for (**a**) sample preparation for analysis of the relative part density and hardness measurements and (**b**) measurement pattern for determining the material hardness.

The relative part density was determined on cross-sections in x-z-direction within the center of the specimen. For this, the specimens were ground down to approximately 5 mm until the center was reached. The relative part density was determined based on the binarization method. An automatic threshold was set to distinguish pores or other defects (dark) from the solidified material (bright). The corresponding pixel ratio was

chosen as relative part density. Due to the high relative part density at low magnifications, the relative part density was also determined in the most porous-appearing region for larger magnifications.

The Vickers hardness (HV1) was determined in the central region of the specimens for the preliminary investigations using a Qness indentation tester (ATM Qness GmbH, Mammelzen, Germany). Therefore, a 4 × 4 pattern was placed in the center of the specimens. The distance between two measurement points was set to 2 mm. The average material hardness was calculated from the resulting 16 measuring points.

Microstructure analysis was performed by means of optical light microscopy using a Leica DM4 M. Therefore, the samples were etched for three seconds using a <5% Nital solution to reveal the microstructure.

A Tescan Vega and a Mira3 SEM were utilized for scanning electron microscopy (SEM) to generate images of the cross-sections with larger magnifications of up to 35,000 times. X-ray diffraction (XRD) was performed according to [22] using a D8 Discover (Bruker Corporation, Billerica, MA, USA) system equipped with a Lynxeye 1D-detector.

2.3. Post-Process Heat Treatment Strategy

Different post-process heat treatment strategies were examined to assess the formation of bainite. In the first steps, one reference series with a medium-volume energy density (VED, $VED = \frac{P}{v*h*t}$ in J/mm^3) was exposed to both a tempering and a quenching and tempering heat treatment. One half (approximately 5 × 10 × 10 mm) of the sample was annealed in the as-built state, while the other half (approximately 5 × 10 × 10 mm) was tempered from the quenched state. Table 3 presents the corresponding parameters for heat treatment.

Table 3. Heat treatment parameters.

Tempering Temperature	As-Built and Tempered	Quenched and Tempered
150 °C	AT150	QT150
200 °C	AT200	QT200
300 °C	AT300	QT300
400 °C	AT400	QT400
500 °C	AT500	QT500
600 °C	AT600	QT600

Austenitization was performed at 920 °C for 30 min, as stated in the supplier's data sheet for the conventional bainitic steel Bainidur 7980 CN [23]. An oil bath was used for quenching the specimens. The corresponding tempering temperatures varied between 150 and 600 °C as a high-temperature stability was expected for the as-built Bainidur AM samples. All samples were kept in the oven for 1 h. After heat treatment, the samples were air-quenched. The quenching experiments were performed in a furnace of type N 31/H (Nabertherm GmbH, Germany). Tempering was carried out in an N 30/85SHA (Nabertherm GmbH, Germany) oven. All experiments were performed under nitrogen gas atmosphere to avoid oxidation.

3. Results

This section is divided into three main parts. First, the results on the process window are presented, in which nearly defect-free specimens with a relative part density above 99.7% can be manufactured. These investigations are followed by a fundamental analysis on the microstructure formation and the material hardness. In the final step, the tempering stability of the additively manufactured material is assessed based on the material hardness and microstructural properties.

3.1. Process Window for the Defect-Free Fabrication of Bainidur AM

The AconityMINI system was used for identifying the potential process window. Due to the small build envelope, screening investigations can be performed already for low amounts of powder. Three different hatch distances (100, 110, and 120 µm) were studied for three different laser powers (225, 250, and 275 W) and three different scanning speeds (550, 700, and 850 mm/s). In each build job, five samples were manufactured. Figure 3 presents the results on the relative part density for the investigated parameter window. A larger representation of the different cross-sections can be found in Appendix A (Figures A1–A3).

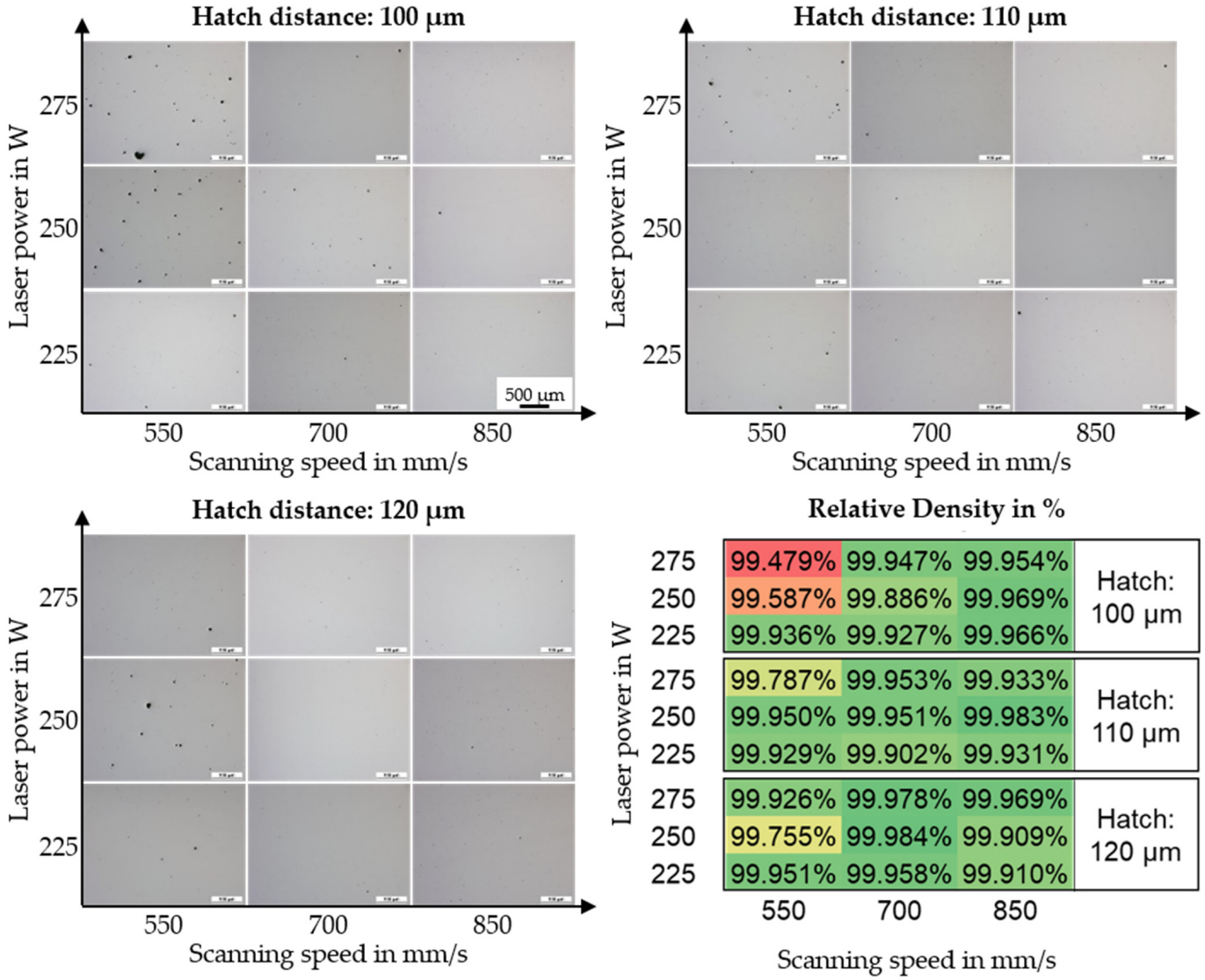

Figure 3. Results of the optical density analysis for the different processing parameters on the AconityMINI machine. The scale is magnified exemplary only once (225 W–850 mm/s–100 µm). Red indicates a lower relative part density, green indicates a higher relative part density.

The stated relative part density was determined within the areas of the cubic samples that appear to have the highest number of pores or defects (this approach can also be seen in Figure 4). Overall, Bainidur AM is characterized by a good processability by means of PBF-LB/M as part densities above 99.7% can be achieved for most parameter combinations. Figure 4 presents the relative part density for two different parameter combinations. One specimen (Figure 4a) was manufactured using a high VED. The other specimen (Figure 4c)

was manufactured using a lower volume energy density. Figure 4b,d show a magnified region of the specimen, which is characterized by a higher number of pores compared to the rest of the specimen.

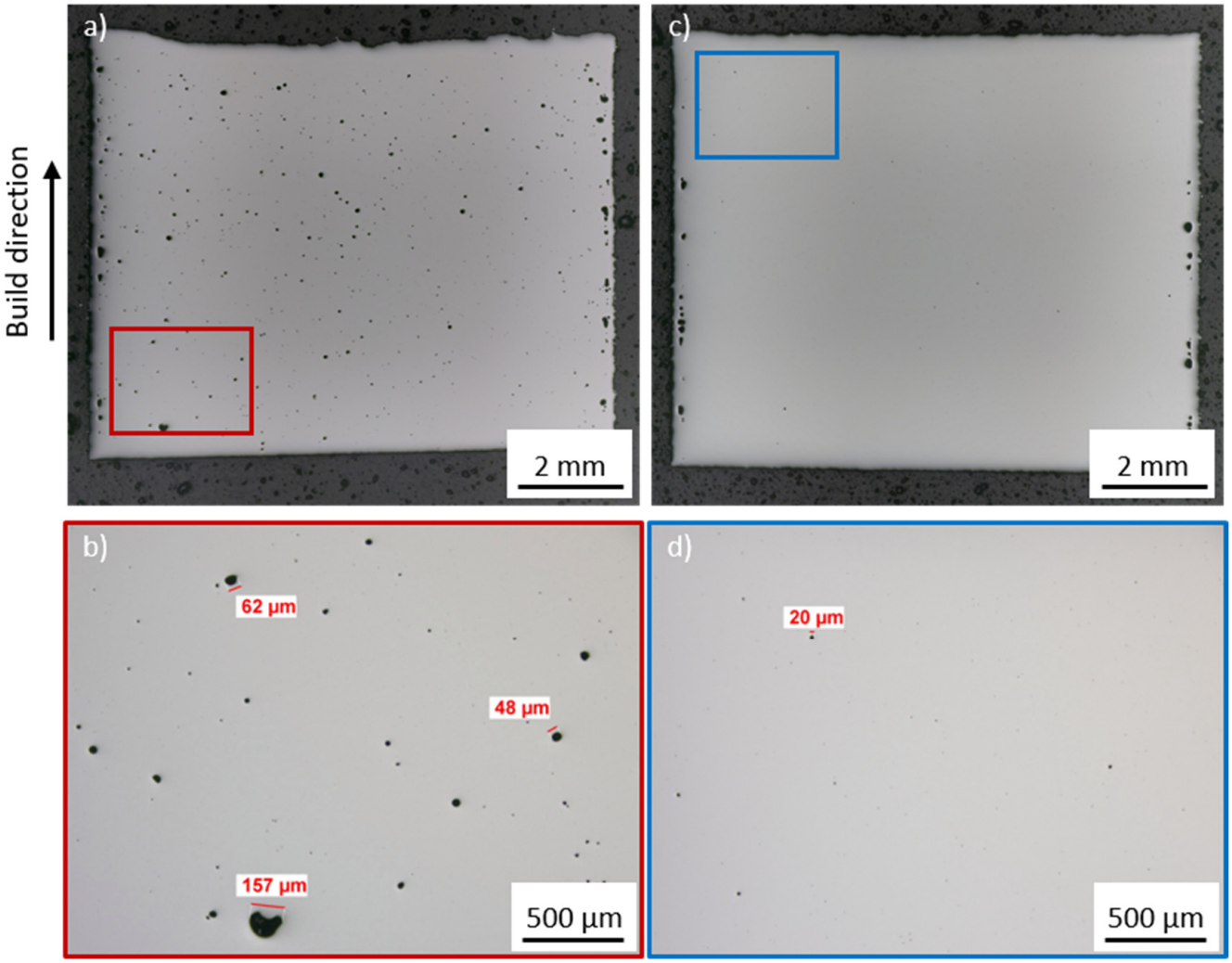

Figure 4. Exemplary (**a**,**c**) cross-sections and (**b**,**d**) magnified regions for determining the relative part density in the worst apparent regions of the specimen for (**a**,**b**) 275 W–550 mm/s–100 µm and (**c**,**d**) 275 W–700 mm/s–110 µm.

A high energy density tends to result in an increased defect formation within the specimen. Possible explanations for this are the increased keyhole tendency during the laser welding process [24]. This correlates well with the increased size of these pores, which regularly exceed 50 µm. A lowered energy density results in fewer pores, which, if evident, typically fall below a size of 20 µm. All in all, the porosity is distributed homogeneously within the specimen. The contour region is characterized by a high porosity, independent of the used parameter set. However, this can be attributed to the fact that the contour parameters have not been optimized within this work.

3.2. Microstructure and Material Hardness

Building on the previous investigations, the material hardness and microstructural properties of the additively manufactured specimens were investigated. Figure 5 shows results on the hardness for the material processed on the AconityMINI machine.

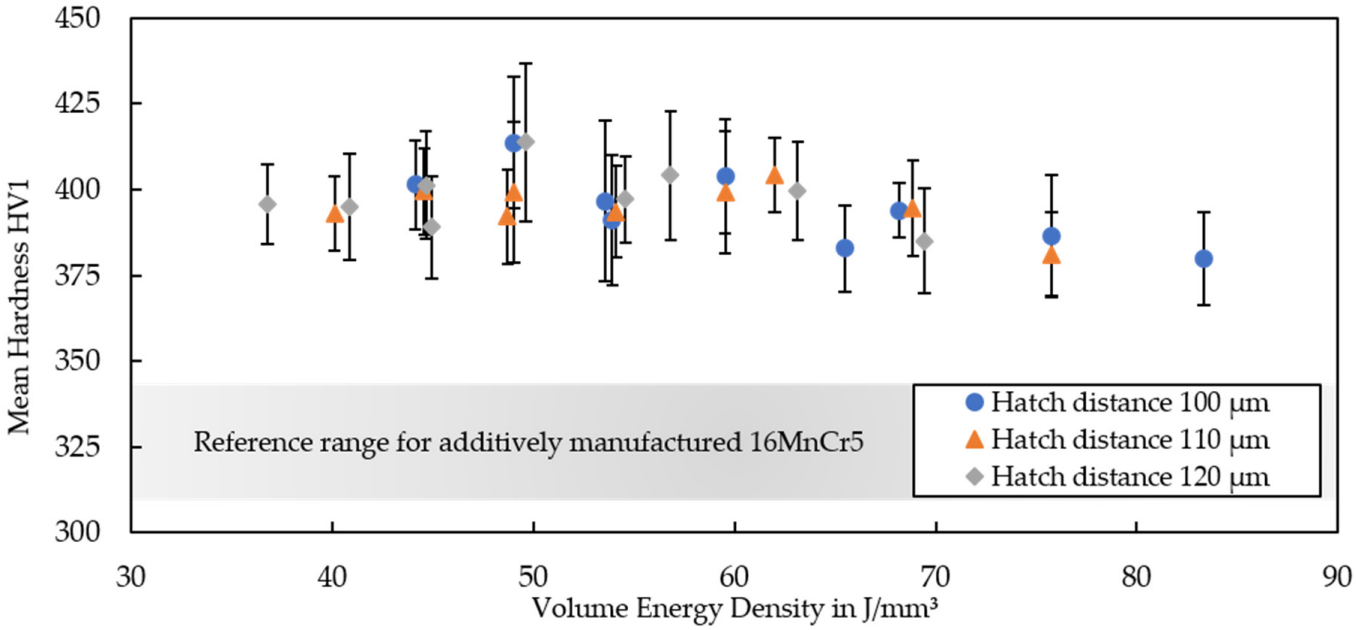

Figure 5. Mean hardness of test cubes manufactured on the AconityMINI systems using the different process parameters. The hardness of additively manufactured 16MnCr5 according to [15] is provided as a reference. Information on the respective standard deviations can be found in Appendix A.

Bainidur AM is characterized by a homogeneous material hardness over a wide range of parameters. The trend indicates that the material hardness decreases for increasing VEDs exceeding 70 J/mm^3. This appears logical, as higher VEDs—often due to lower scanning speeds or higher laser powers—typically result in a coarser microstructure compared to lower VEDs [25]. Furthermore, these samples possess a higher porosity, which was caused by overheating and keyhole formation during build-up. Apart from the highest VEDs, the material hardness remains constant for a wide parameter window, which can be helpful when manufacturing larger parts in the future to avoid a geometry-specific overheating. The hardness surpasses that of additively manufactured 16MnCr5 by up to 70 HV1 on average [15,16], showing the enormous potential of the low-alloyed steel Bainidur AM for the manufacturing of construction parts. This improved hardness can at least be partially explained by the higher carbon content of Bainidur AM. Apart from that, no significant differences between the specimens could be observed and all specimens were characterized by a continuous and homogeneous hardness in the build direction.

Next, optical analysis was performed on the etched cross-sections. The obtained results of the cross-sections for three different VEDs are presented in Figure 6.

Similar microstructural features were observed at all three VEDs. For low VEDs, the welding depth is reduced compared to the higher VEDs. The bright region of the top layers also increases for higher energy inputs, which underlines the correlation between energy input and weld depth. Apart from that, the lack of visible differences was also supported by the average hardness values, which only increased slightly for higher cooling rates. In all cases, however, different regions within the specimen can be observed. XRD measurements show no correlation between the applied VED and the retained austenite (RA) content, as the RA content remained constant at around 7% to 9%. This was studied for three different VEDs. Figure 7 shows two exemplary cross-sections in the center and in the top section of a specimen manufactured using a medium VED of 54.1 J/mm^3.

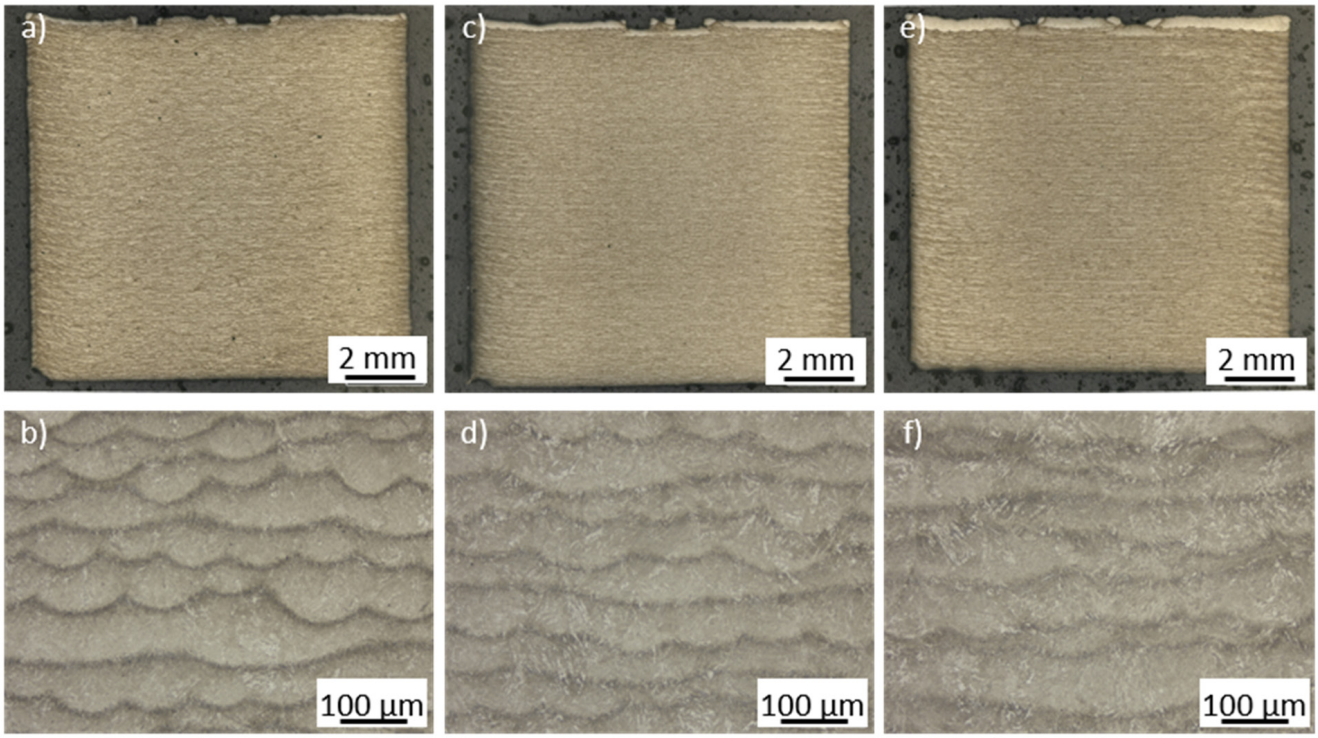

Figure 6. Etched cross-sections for samples manufactured using a (**a**,**b**) low (36.8 J/mm^3), (**c**,**d**) medium (54.1 J/mm^3), and (**e**,**f**) high VED (75.8 J/mm^3).

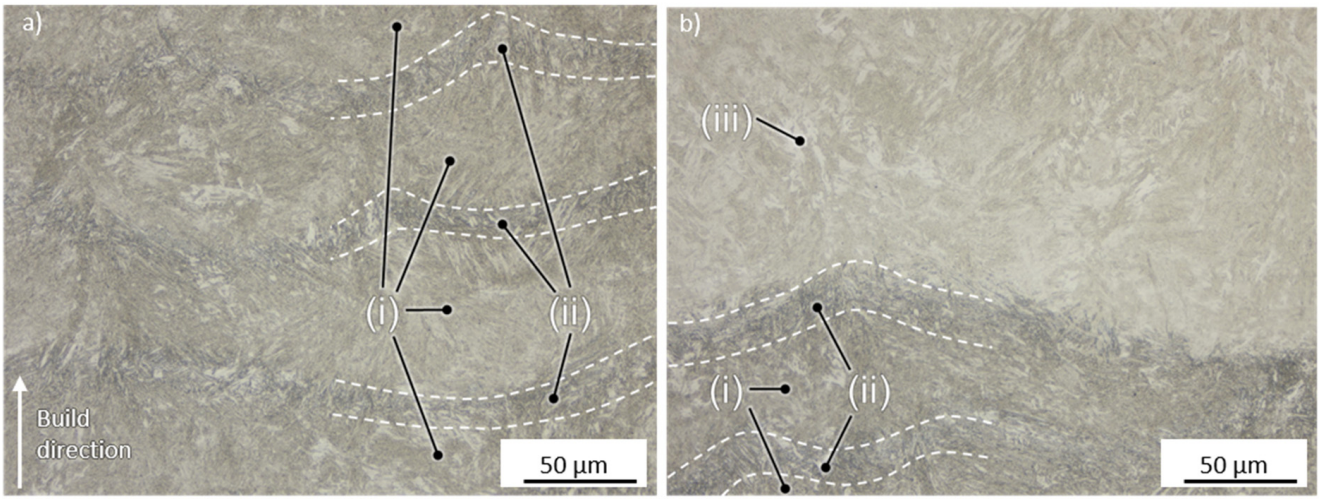

Figure 7. Different microstructural regions of PBF-LB/M specimens (**a**) in the core with the fusion zone (i) and heat-affected zone (ii) and (**b**) in case (iii), manufactured using a medium VED of 54.1 J/mm^3.

Three different regions can be identified within the specimen. The top layer (iii) appears brighter under the microscope as the heat input is lower due to the absence of the continuous reheating during the layer-wise manufacturing process. In contrast to this, the core region can be divided into the fusion zone (FZ, i) and the heat-affected zone (HAZ, ii), with the FZ being brighter than the HAZ. The FZ also appears to possess a finer grain than the surrounding HAZ. Correspondingly, SEM analysis was performed in these regions. Figure 8 presents the results for the FZ and HAZ.

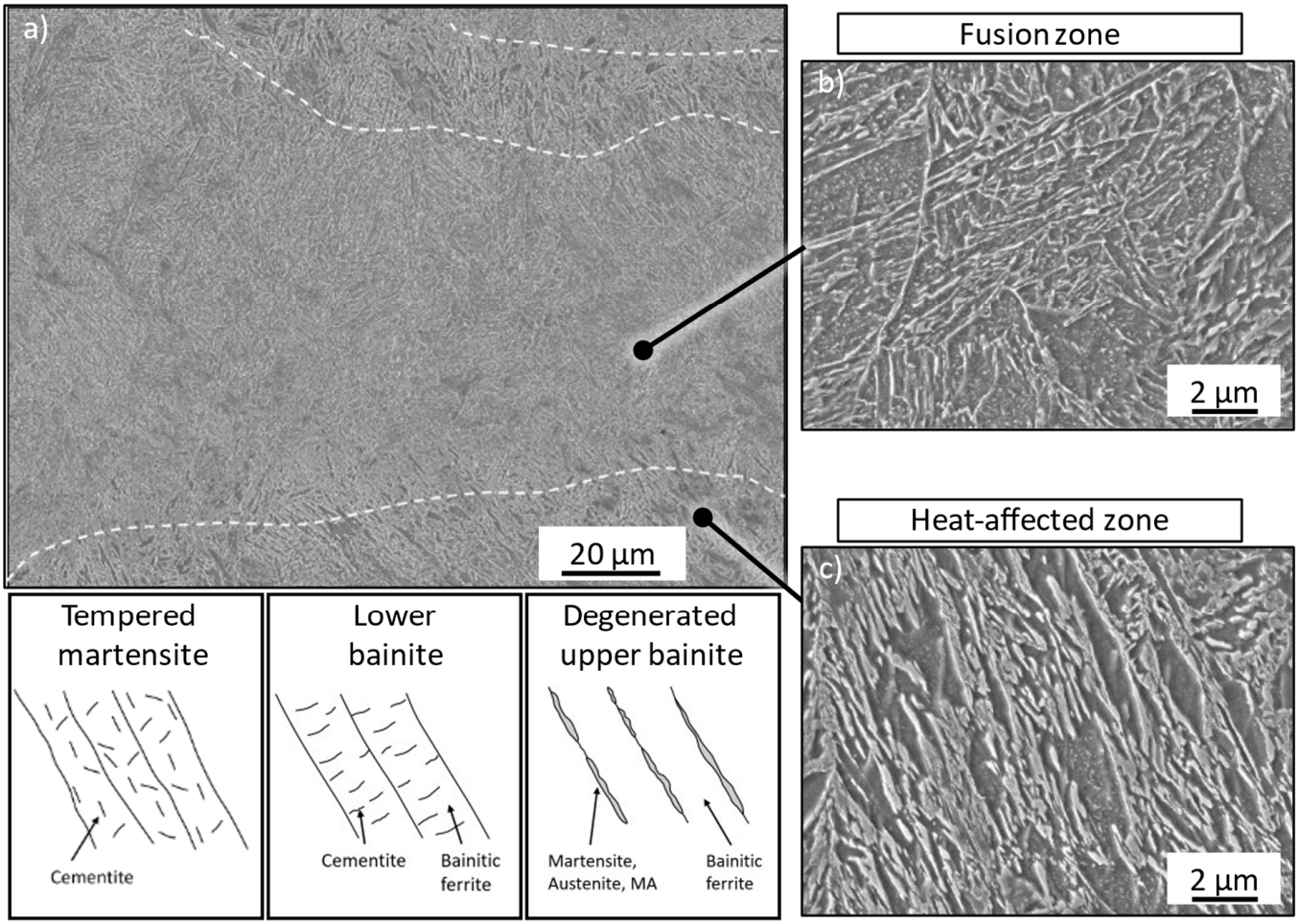

Figure 8. SEM images of the (**a**) fusion zone and the heat-affected zone within the core of the specimen as well as corresponding magnification of the (**b**) fusion zone and (**c**) the heat-affected zone. Exemplary illustrations of the apparent microstructure according to [26].

As expected, a different microstructure was formed within the HAZ and the FZ. The fusion zone is characterized by a more lath-like structure with carbides finely dispersed within the laths, which is similar to lower bainite or tempered martensite. Due to this fine carbide dispersion, a clear distinction between martensite (random orientation) and bainite (targeted orientation) is barely possible. In contrast, the heat-affected zone appears coarser, with areas appearing such as bainitic ferrite with coarse, partially segmented films between these laths. This seems like a degenerated upper bainitic structure. The less pronounced etching response and smooth surfaces of these films also suggest the presence of austenite or martensite in these areas. This region is further characterized by predominant carbide precipitations at the lath boundaries and less promoted carbide dispersion within the grain. The high process-specific cooling rates and the corresponding fine microstructure make it hard to assess what type of microstructure is underlying. Therefore, an additional analysis on the tempering stability was performed.

3.3. Tempering Stability as an Indicator for a Bainitic Microstructure

In theory, the bainite possesses a higher tempering stability than martensite [27]. To better assess the microstructure in the as-built state, a tempering series was started. Prior to this series, the chemical composition of the as-built specimens was determined by optical emission spectroscopy in the center of the specimen. The results are shown in Table 4.

Table 4. Chemical composition of the powder material according to the supplier's certificate and after PBF-LB/M determined by OES.

Batch	Element Content in wt.%						
	C	Si	Mn	Cr	Mo	Ni	V
Powder	0.22	0.7	1.2	1.0	0.9	<0.3	<0.15
As-built	0.20	0.67	1.35	1.01	0.86	0.09	0.02

Comparing the chemical composition of the sample with the powder, a slight decrease in carbon content from 0.22 wt.% (powder) to 0.20 wt.% (sample) could be observed. This decarburization can be attributed to the high temperatures during the manufacturing process, which was also reported for the martensitic steel AF9628 by Seede et al. [28]. Figure 9 presents the results on the tempering studies for as-built and tempered (AT) as well as quenched and tempered (QT) specimens.

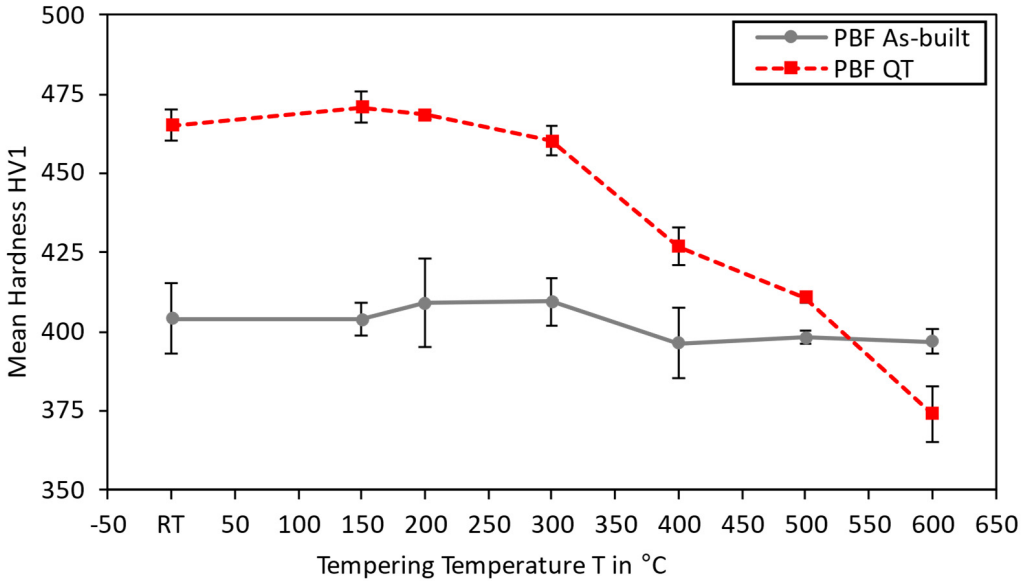

Figure 9. Material hardness for different tempering temperatures in the as-built as well as quenched and tempered states. The specimens were manufactured using a medium VED (54.1 J/mm^3).

The QT specimens possess the highest material hardness (470 HV1) at room temperature. Increasing the tempering temperature results in a hardness decrease, a common effect observed for tempered martensite in low-alloyed steels [29]. The corresponding material hardness falls as low as 370 HV for the highest tempering temperature of 600 °C. In contrast, as-built and tempered specimens possess a homogeneous material hardness of 405 HV1 at all temperatures. This indicates that a primarily bainitic microstructure is present after manufacturing. Santajuana et al. [30] and Peet et al. [31] have both found a similar high-temperature stability of bainite up to tempering temperatures of approximately 500 °C for steels with a higher carbon content. The work by Kafadar et al. [32] also indicates that the alloying elements, especially molybdenum, significantly affect the tempering stability. Sourmail et al. [33] report similar findings on the effect of vanadium. As both these alloying elements are present in the material Bainidur AM, it can be expected that these alloys result in carbide formation during cooling. Figure 10 presents images of the corresponding etched cross-sections after the respective tempering heat treatment.

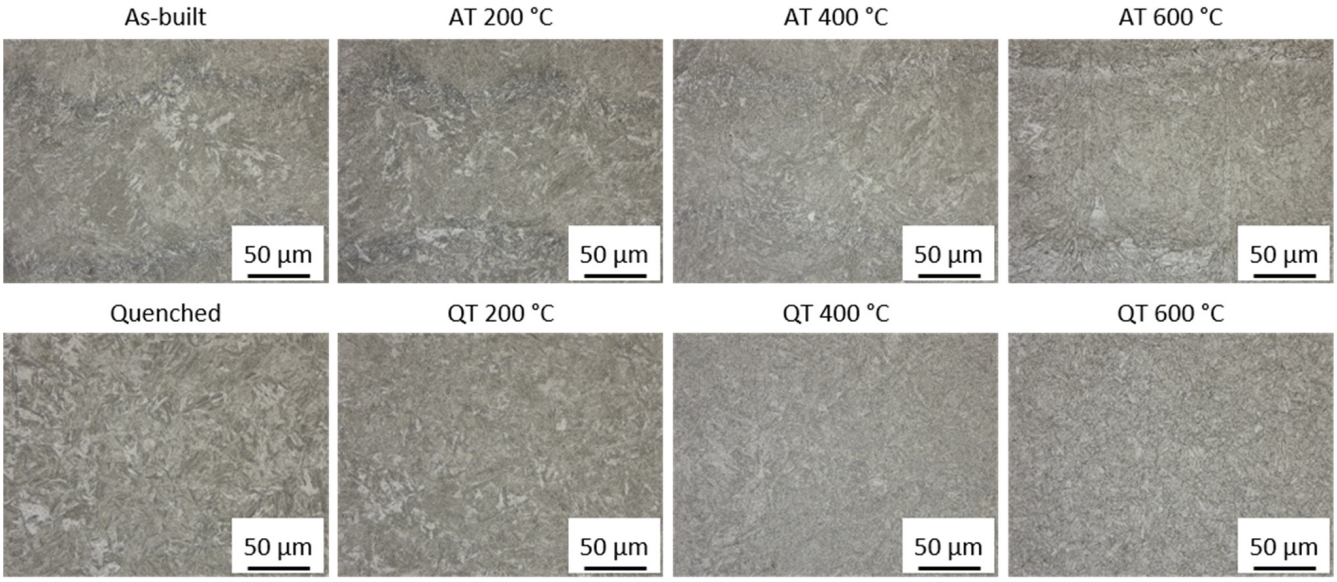

Figure 10. Etched cross-section of (**top**) as-built and tempered as well as (**bottom**) quenched and tempered specimens. The specimens were manufactured using a medium VED (54.1 J/mm^3).

In the as-built state, a clear distinction between the fusion zone and the heat-affected zone is present, even at tempering temperatures of 600 °C. Furthermore, a very fine microstructure can be observed throughout all temperatures. Increasing the tempering temperature results in a decomposition of the retained austenite (white clusters in Figure 10, as-built and AT 200 °C) within the specimen. For the QT specimens, an obvious change in microstructure is evident, which could explain the hardness drop. While the as-built specimens still possess the PBF-specific structure as the contour of the weld tracks can still be observed up to tempering temperatures of 600 °C, this structure can no longer be determined for the quenched specimens. Figure 11 shows additional SEM images of the microstructure of these specimens. A larger representation of these figures is shown in Appendix A (see Figure A4).

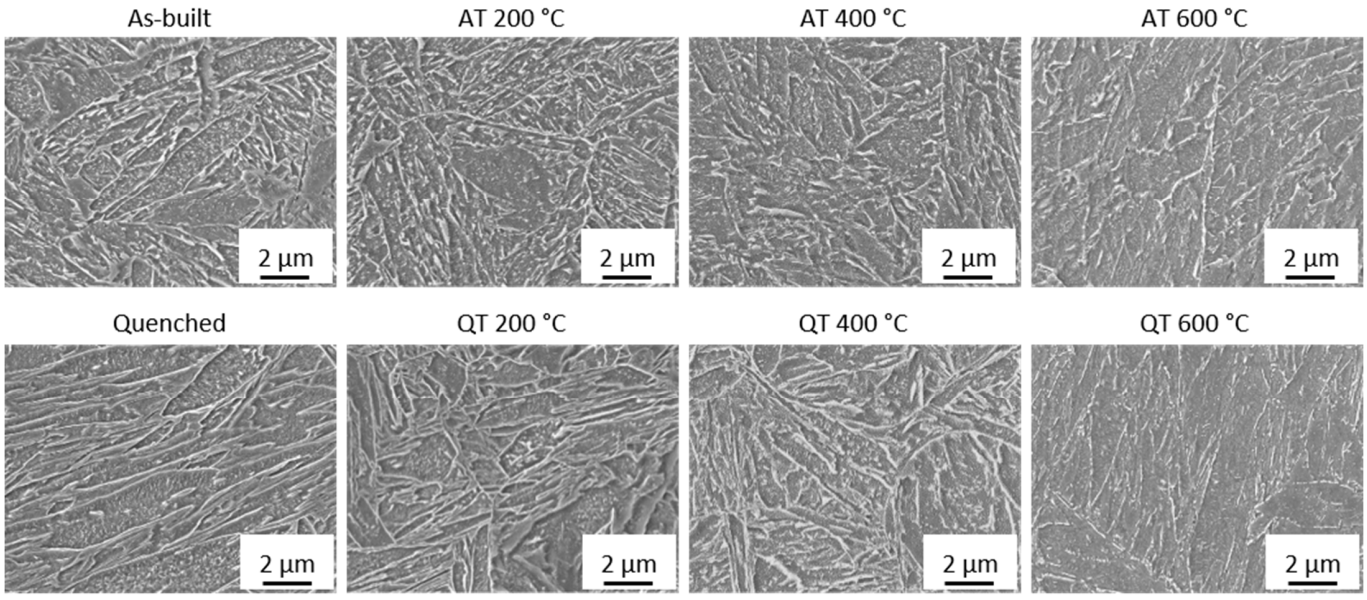

Figure 11. SEM images of the center region of the specimens in (**top**) as-built and tempered as well as (**bottom**) quenched and tempered states. The specimens were manufactured using a medium VED (54.1 J/mm^3).

The as-built and tempered samples possess finely dispersed carbides within the grains at all temperatures. These carbides can be the reason for the good thermal stability of the as-built specimens. At a tempering temperature of 600 °C, however, these carbide structures are harder to identify and barely present. Mohr et al. [34] have found the global temperatures at the surface of the specimen to fall below 250 °C for 10 mm specimens within their work (see Figure 4 in [34]). Thus, it is unlikely that the underlying microstructure is a tempered martensitic one, as a hardness drop-off would be expected when exceeding the process-specific temperature (in this case approximately 250 °C). Fine carbides can also be identified in the hardened (and tempered) specimens. However, these specimens were characterized by a hardness drop-off, which is typically observed when tempering martensite. It is therefore more likely that a bainitic microstructure is underlying in the as-built state, despite the optical similarities in the as-built and quenched states.

XRD analyses show that the retained austenite dropped from around 7.5% to around 1.1% after tempering the as-built specimens for 1 h at 600 °C. This falls below the detection limit of the XRD, which is around 2%, indicating that the retained austenite is almost fully transformed into bainite and possibly secondary carbides.

Overall, an extremely favorable, bainite-like microstructure is present after the PBF-LB/M process. Even though shares of retained austenite and even martensite cannot be ruled out, a consistent hardness even after being exposed to the highest tempering temperatures is observed. This indicates that a microstructure with bainite-like properties can be obtained after the PBF-LB/M process.

4. Conclusions

The low-alloyed steel Bainidur AM can be successfully processed using a wide range of parameters by means of PBF-LB/M. It was found that a predominantly bainitic or at least bainite-like microstructure could be generated in the as-built state despite the PBF-specific high cooling rates. This was validated by analyzing the material hardness, the tempering stability as an indicator for a bainitic microstructure, SEM analysis of the microstructure, and XRD measurements of the retained austenite content. The main findings of this work are:

- In the absence of elevated preheating temperatures, a fine bainitic microstructure was formed during PBF-LB/M.
- A structure similar to lower bainite was formed in the fusion zone, while the heat-affected zone appeared more like an upper bainitic structure.
- The as-built samples were characterized by a material hardness of around 400 HV1, surpassing that of other additively manufactured, low-alloyed steels.
- Samples manufactured from Bainidur AM possessed an excellent tempering stability, characterized by a homogeneous hardness up to tempering temperatures as high as 600 °C.
- Applying a post-process heat treatment helped in reducing the minor retained austenite content through the transformation into bainitic structures.

Overall, the material properties are very promising as Bainidur AM possesses an excellent hardness for a low-alloyed, case-hardening steel. Further in-depth analysis on the mechanical properties such as tensile strength and impact toughness will be within the scope of future studies to further validate this material system for PBF-LB/M.

Author Contributions: D.B.: conceptualization, methodology, validation, investigation, writing–original draft, visualization; T.N.: investigation, data curation, writing—review and editing, visualization; A.M.: conceptualization, resources, validation; F.v.S.: conceptualization, writing—review and editing, validation; O.H.: writing—review and editing, validation; C.M.: supervision, writing—review and editing, resources, project administration; M.S.: supervision, writing—review and editing, resources, project administration, funding acquisition, validation. All authors have read and agreed to the published version of the manuscript.

Funding: This research was funded by the German Research Foundation (DFG) for Project-ID 61375930, SFB 814—"Additive Manufacturing" TP A05.

Institutional Review Board Statement: Not applicable.

Informed Consent Statement: Not applicable.

Data Availability Statement: Raw data and material are available upon request.

Acknowledgments: The authors want to thank the German Research Foundation (DFG) for Project-ID 61375930–SFB 814—"Additive Manufacturing" TP A05. We acknowledge financial support by Deutsche Forschungsgemeinschaft and Friedrich-Alexander-Universität Erlangen-Nürnberg within the funding programme "Open Access Publication Funding". The authors gratefully acknowledge the support provided by the Erlangen Graduate School in Advanced Optical Technologies. We would also like to thank Schaeffler Technologies AG & Co. KG and Deutsche Edelstahlwerke Specialty Steel GmbH for their respective support within this work.

Conflicts of Interest: Both Schaeffler Technologies AG & Co. KG (products made from Bainidur AM) and Deutsche Edelstahlwerke Specialty Steel GmbH (powder material Bainidur AM) are interested in distributing their respective products in the future.

Appendix A

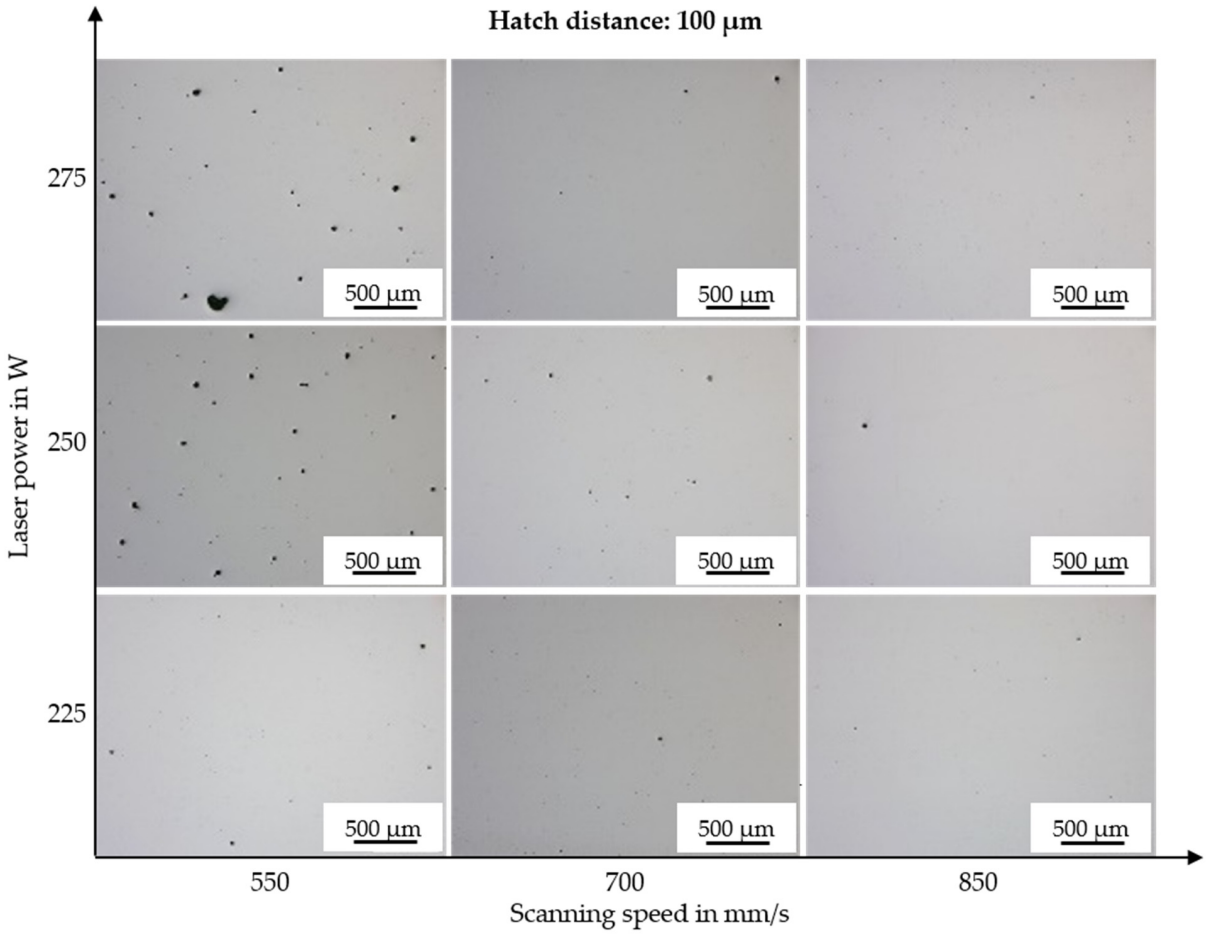

Figure A1. Cross-sections of the specimens manufactured with a hatch distance of 100 µm.

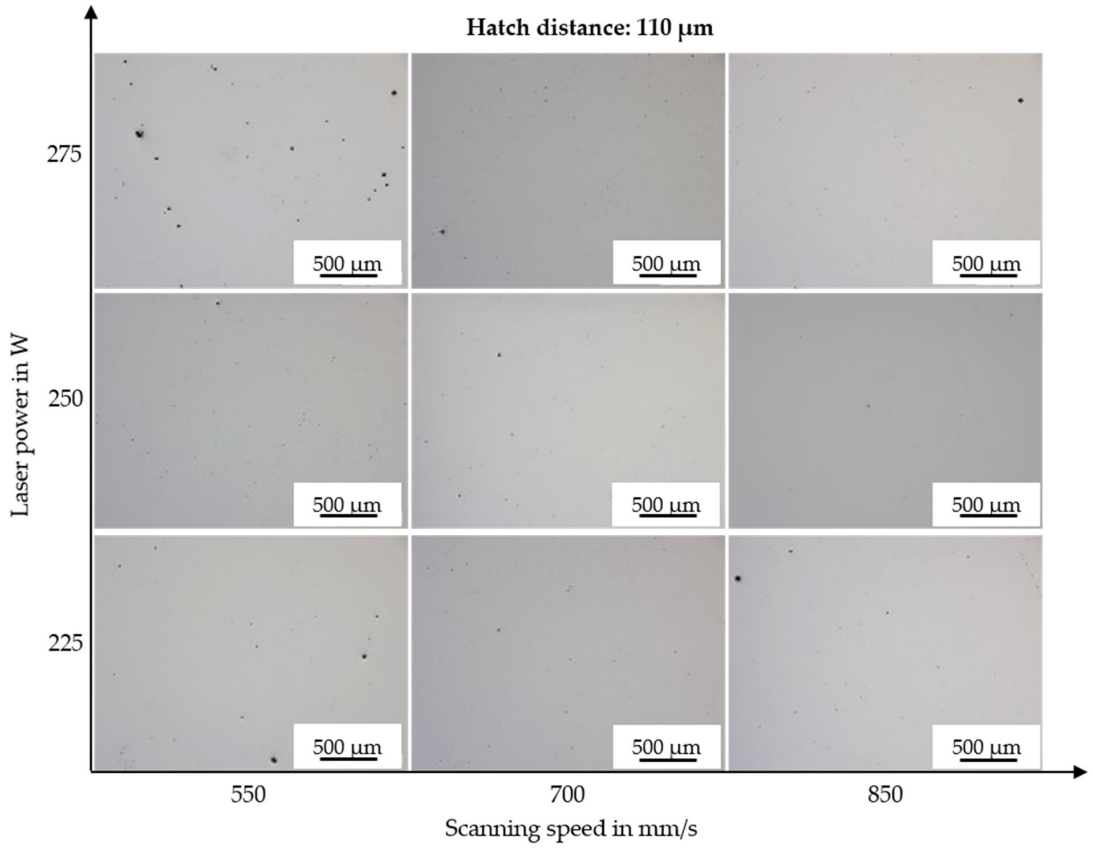

Figure A2. Cross-sections of the specimens manufactured with a hatch distance of 110 µm.

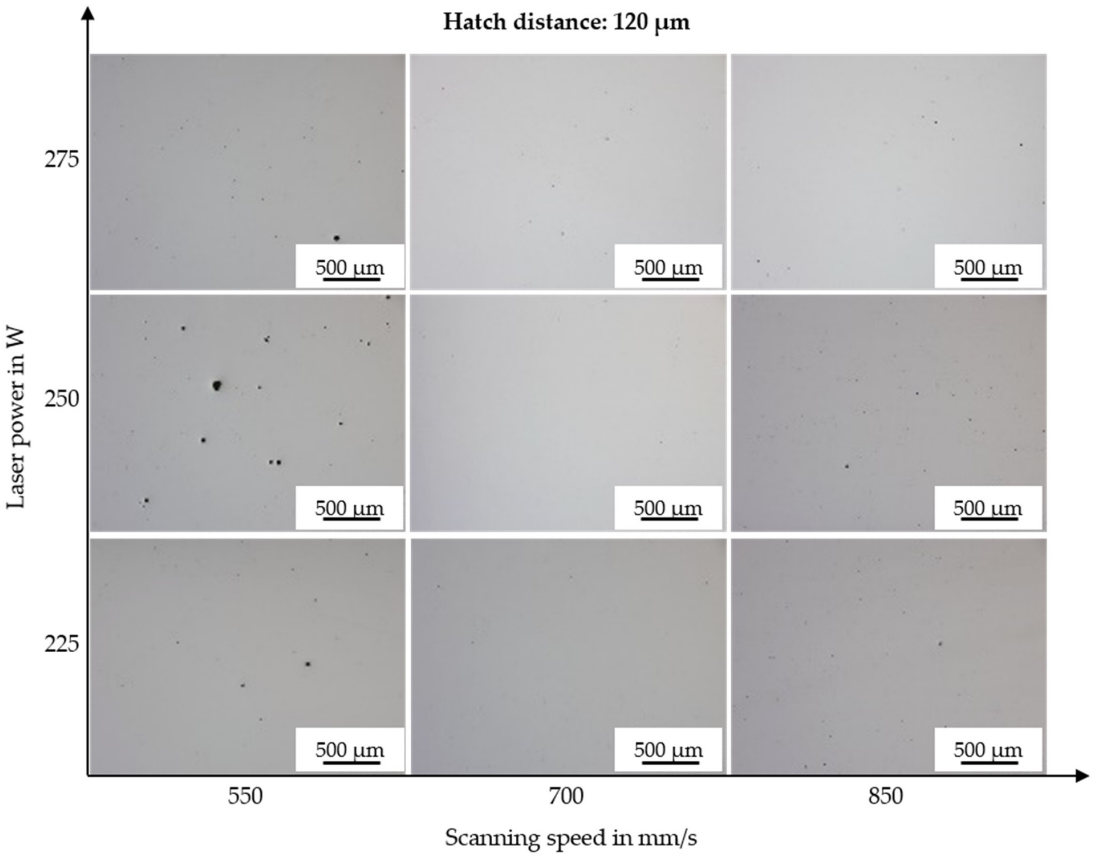

Figure A3. Cross-sections of the specimens manufactured with a hatch distance of 120 µm.

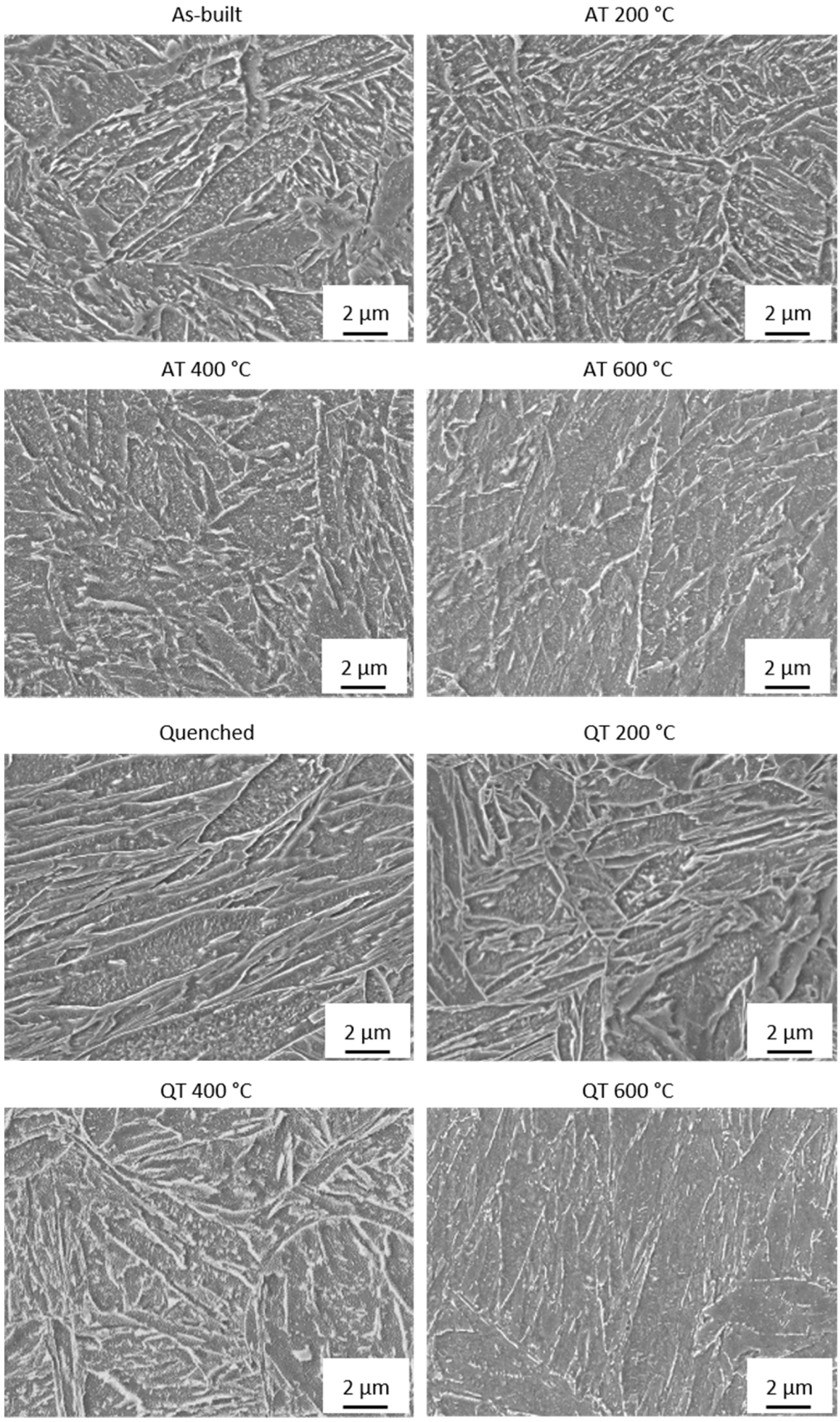

Figure A4. SEM images (from Figure 11) of the as-built and tempered as well as quenched and tempered specimens.

References

1. Eagan, J.R.; Shelton, C.H. Recent Test Data on Selection of Alloy Steels for Gears and Bearings. *SAE Trans.* **1972**, *81*, 1163–1171.
2. Honeycombe, R.W.K.; Bhadeshia, H.K.D.H. *Steels: Microstructure and Properties*, 2nd ed.; J. Wiley: New York, NY, USA, 1996; ISBN 9780470235683.
3. Rajput, R.K. *Engineering Materials & Metallurgy*; S. Chand: New Delhi, India, 2006; ISBN 9788121927093.
4. Tu, M.-Y.; Hsu, C.-A.; Wang, W.-H.; Hsu, Y.-F. Comparison of microstructure and mechanical behavior of lower bainite and tempered martensite in JIS SK5 steel. *Mater. Chem. Phys.* **2008**, *107*, 418–425. [CrossRef]
5. Bhadeshia, H.K.D.H.; Christian, J.W. Bainite in steels. *Metall. Trans. A* **1990**, *21*, 767–797. [CrossRef]
6. Prabhudev, K.H. *Handbook of Heat Treatment of Steels*; Tata McGraw-Hill: New Delhi, India, 1992; ISBN 0074518313.
7. Hooper, P.A. Melt pool temperature and cooling rates in laser powder bed fusion. *Addit. Manuf.* **2018**, *22*, 548–559. [CrossRef]
8. Amine, T.; Newkirk, J.W.; Liou, F. An investigation of the effect of direct metal deposition parameters on the characteristics of the deposited layers. *Case Stud. Therm. Eng.* **2014**, *3*, 21–34. [CrossRef]
9. Babasafari, Z.; Pan, A.V.; Pahlevani, F.; Hossain, R.; Sahajwalla, V.; Du Toit, M.; Dippenaar, R. Effects of austenizing temperature, cooling rate and isothermal temperature on overall phase transformation characteristics in high carbon steel. *J. Mater. Res. Technol.* **2020**, *9*, 15286–15297. [CrossRef]
10. Deutsche Edelstahlwerke Specialty Steel GmbH & Co. KG. Bainidur—From Additive Manufacturing to Serial Production. Available online: https://www.dew-powder.com/en/additive-manufacturing/bainidur-am (accessed on 3 March 2022).
11. Kelliger, T.; Liu, H.; Schraknepper, D.; Bergs, T. Investigations on the Impact of Additively Manufactured Coolant Channels and Outlet Nozzles on Free Jet and Jet Forces in High-Pressure Cutting Fluid Supply. *SSRN J.* **2021**, 041–049. [CrossRef]
12. Bartels, D.; Hentschel, O.; Dauer, J.; Burgmayr, W.; Schmidt, M. Processing of low-alloyed case-hardening steel Bainidur AM by means of DED-LB/M. In Proceedings of the Lasers in Manufacturing Conference (LiM) 2021, München, Germany, 21–24 June 2021.
13. Bailey, N. *Weldability of Ferritic Steels*; Elsevier Science: Cambridge, UK, 1994; ISBN 9781845698935.
14. Kamps, T. *Leichtbau von Stirnzahnrädern aus Einsatzstahl Mittels Laserstrahlschmelzen*; Universitätsbibliothek der TU München: München, Germany, 2018.
15. Schmitt, M.; Schlick, G.; Seidel, C.; Reinhart, G. Examination of the processability of 16MnCr5 by means of laser powder bed fusion. *Procedia CIRP* **2018**, *74*, 76–81. [CrossRef]
16. Bartels, D.; Klaffki, J.; Pitz, I.; Merklein, C.; Kostrewa, F.; Schmidt, M. Investigation on the Case-Hardening Behavior of Additively Manufactured 16MnCr5. *Metals* **2020**, *10*, 536. [CrossRef]
17. Schmitt, M.; Kamps, T.; Siglmüller, F.; Winkler, J.; Schlick, G.; Seidel, C.; Tobie, T.; Stahl, K.; Reinhart, G. Laser-based powder bed fusion of 16MnCr5 and resulting material properties. *Addit. Manuf.* **2020**, *35*, 101372. [CrossRef]
18. Aumayr, C.; Platl, J.; Zunko, H.; Turk, C. Additive Manufacturing of a Low-alloyed Engineering Steel. *Berg Huettenmaenn. Mon.* **2020**, *165*, 137–142. [CrossRef]
19. Zumofen, L.; Kirchheim, A.; Dennig, H.-J. Laser powder bed fusion of 30CrNiMo8 steel for quenching and tempering: Examination of the processability and mechanical properties. *Prog. Addit. Manuf.* **2020**, *5*, 75–81. [CrossRef]
20. Damon, J.; Koch, R.; Kaiser, D.; Graf, G.; Dietrich, S.; Schulze, V. Process development and impact of intrinsic heat treatment on the mechanical performance of selective laser melted AISI 4140. *Addit. Manuf.* **2019**, *28*, 275–284. [CrossRef]
21. Beer, O.; Merklein, C.; Gerhard, D.; Hentschel, O.; Rasch, M.; Schmidt, M. Processing of the Heat Resistant Bearing Steel M50NiL by Selective Laser Melting. *HTM J. Heat Treat. Mater.* **2018**, *73*, 187–201. [CrossRef]
22. E04 Committee. *Practice for X-ray Determination of Retained Austenite in Steel with Near Random Crystallographic Orientation*; ASTM International: West Conshohocken, PA, USA, 2013.
23. Deutsche Edelstahlwerke Specialty Steel GmbH & Co. KG. Bainidur®7980 CN: Bainitischer Stahl für die Serienproduktion 2020. Available online: https://www.dew-powder.com/fileadmin/files/metallpulver.de/documents/Publikationen/Deutsch/2020-05-07_Bainidur_7980_CN_DE.pdf (accessed on 25 July 2022).
24. Shrestha, S.; Starr, T.; Chou, K. A Study of Keyhole Porosity in Selective Laser Melting: Single-Track Scanning with Micro-CT Analysis. *J. Manuf. Sci. Eng.* **2019**, *141*, 071004. [CrossRef]
25. Zhang, S.; Lei, Y.; Chen, Z.; Wei, P.; Liu, W.; Yao, S.; Lu, B. Effect of Laser Energy Density on the Microstructure and Texture Evolution of Hastelloy-X Alloy Fabricated by Laser Powder Bed Fusion. *Materials* **2021**, *14*, 4305. [CrossRef]
26. Müller, M.; Britz, D.; Ulrich, L.; Staudt, T.; Mücklich, F. Classification of Bainitic Structures Using Textural Parameters and Machine Learning Techniques. *Metals* **2020**, *10*, 630. [CrossRef]
27. Garcia-Mateo, C.; Peet, M.; Caballero, F.G.; Bhadeshia, H. Tempering of hard mixture of bainitic ferrite and austenite. *Mater. Sci. Technol.* **2004**, *20*, 814–818. [CrossRef]
28. Seede, R.; Zhang, B.; Whitt, A.; Picak, S.; Gibbons, S.; Flater, P.; Elwany, A.; Arroyave, R.; Karaman, I. Effect of heat treatments on the microstructure and mechanical properties of an ultra-high strength martensitic steel fabricated via laser powder bed fusion additive manufacturing. *Addit. Manuf.* **2021**, *47*, 102255. [CrossRef]
29. Grange, R.A.; Hribal, C.R.; Porter, L.F. Hardness of tempered martensite in carbon and low-alloy steels. *Metall. Trans. A* **1977**, *8*, 1775–1785. [CrossRef]
30. Santajuana, M.A.; Rementeria, R.; Kuntz, M.; Jimenez, J.A.; Caballero, F.G.; Garcia-Mateo, C. Low-Temperature Bainite: A Thermal Stability Study. *Metall. Trans. A* **2018**, *49*, 2026–2036. [CrossRef]

31. Peet, M.J.; Babu, S.S.; Miller, M.K.; Bhadeshia, H.K.D.H. Tempering of Low-Temperature Bainite. *Metall. Trans. A* **2017**, *48*, 3410–3418. [CrossRef]
32. Kafadar, G.; Kalkanli, A.; Özdemir, A.T.; Ögel, B. Effect of Isothermal Transformation Treatment and Tempering on the Microstructure and Hardness of a Medium C and High Si Steels. *ISIJ Int.* **2021**, *61*, 1679–1687. [CrossRef]
33. Sourmail, T.; Otter, L.; Collin, S.; Billet, M.; Philippot, A.; Cristofari, F.; Secordel, P. Direct and indirect decomposition of retained austenite in continuously cooled bainitic steels: Influence of vanadium. *Mater. Charact.* **2021**, *173*, 110922. [CrossRef]
34. Mohr, G.; Sommer, K.; Knobloch, T.; Altenburg, S.J.; Recknagel, S.; Bettge, D.; Hilgenberg, K. Process Induced Preheating in Laser Powder Bed Fusion Monitored by Thermography and Its Influence on the Microstructure of 316L Stainless Steel Parts. *Metals* **2021**, *11*, 1063. [CrossRef]

Contribution to the Goal of this Work

This manuscript presents key findings on the material properties of case-hardening steels processed by means of PBF-LB/M. The as-built microstructure was characterised by a plethora of analysing methods. SEM investigations show that the microstructures in the fusion and heat-affected zones need to be distinguished. The fusion zone is characterised by fine precipitations within the grains, which is an indicator for either a martensitic or lower bainitc microstructure. In contrast to this, the carbides are rather precipitated at the lath boundaries in the heat-affected zone, resulting in a (degenerated) upper bainitic stucture. XRD measurements reveal a retained austenite content of around 7 to 8 % in the as-built state. The hardness difference between the as-built (405 HV1) and hardened state (460 HV1) further indicates that the as-built material cannot be fully martensitic due to its lower hardness. Correspondingly, the tempering stability of the specimens was analysed. These investigations reveal a homogeneous hardness for temperatures of up to 600 °C for the as-built specimens while the hardened specimens are characterised by a continuous decrease of the material hardness (down to 370 HV1). Tempering the as-built sampels led to a decrease of the retained austenite content down to 1.5 %, meaning that a transformation of the retained austenite took place. These findings support the conclusion that a predominantly bainitic microstructure with shares of austenite and martensite is formed in PBF-LB/M, addressing the first research question (RQ1). The bainitic microstructure can further be divided into lower (fusion zone) and upper bainite (heat-affected zone).

In the next step, this methodological approach will be applied to case-hardening steels processed by means of DED-LB/M. The average melt pool size is larger in DED-LB/M, resulting in lower cooling rates of the material. Furthermore, the heat accumulation during build-up is promoted since the part is typically fabricated in a continuous process compared to PBF-LB/M. Due to the different process conditions in DED-LB/M, an altered microstructure is expected. The lower cooling rates should support the formation of a bainitic microstructure. Furthermore, by performing the investigations with a similar material, it will be possible to compare the material properties of case-hardening steels manufactured by means of PBF-LB/M and DED-LB/M.

4.2 Microstructure Formation in DED-LB/M

Title: Directed Energy Deposition of Low-Alloyed Steels: An Insight on Microstructural and Mechanical Properties [P9]

Journal: Steel Research International, Wiley

DOI to Web-version: https://doi.org/10.1002/srin.202200925

Authors: Dominic Bartels, Andrea von Lattre-Hertel, Tobias Novotny, Andreas Mohr, Horst Hill, Carsten Merklein, Michael Schmidt

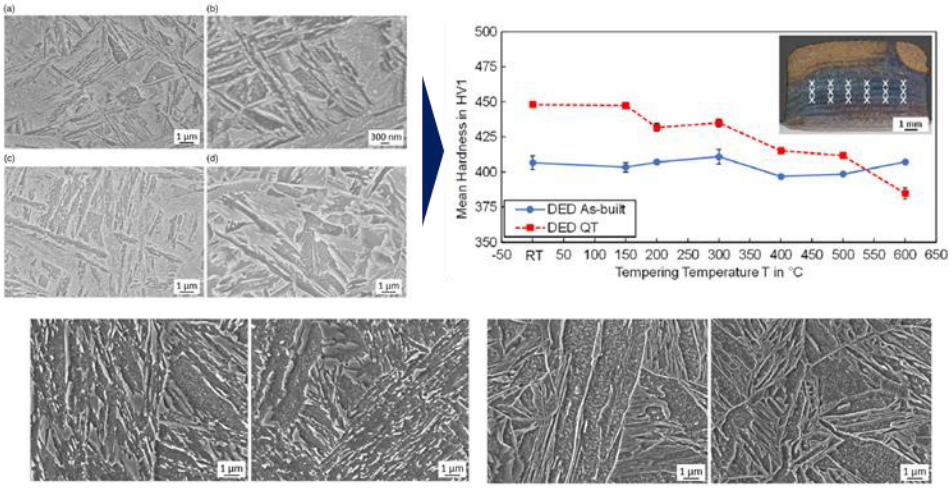

Motivation and Key Findings:

DED-LB/M processes can be used for different applications like cladding, repair, and additive manufacturing of large volume structures. The common prerequisite for all these processes is a good processability of the main material to avoid defects in the bonding zone. Up to now, the processing of case-hardening steels using the DED-LB/M technology cannot be classified as state of the art since crack formation is a major issue that hinders the use of this class of materials. This work presents investigations on the microstructure and the associated material properties that are formed in case-hardening steels processed by means of DED-LB/M. The **highlights** are:

- Excellent processability of case-hardening steel by means of DED-LB/M at the absence of cracks and larger pores
- Bainitic microstructure with larger shares of upper bainite and only minor shares of lower bainite
- Excellent tempering stability up to temperatures of 600 °C

steel research international
www.steel-research.de

Directed Energy Deposition of Low-Alloyed Steels: An Insight on Microstructural and Mechanical Properties

Dominic Bartels, Andrea von Lattre-Hertel, Tobias Novotny, Andreas Mohr, Horst Hill, Carsten Merklein, and Michael Schmidt*

Low-alloyed steels are used for a variety of different applications like bearings or gears. Additive manufacturing technologies like directed energy deposition (DED-LB/M) allow for a fast and close-to-contour fabrication of sophisticated products without excessive waste of material. However, the DED-LB/M process cannot be considered as state-of-the-art for this group of materials. This study presents findings on the material properties of the additively manufactured low-alloyed steel Bainidur AM by means of DED-LB/M. This includes studies on the mechanical properties (hardness, compression strength) as well as the microstructural properties (scanning electron microscopy [SEM]). The microstructure in the as-built state appears like a bainitic–martensitic one with shares of retained austenite which is not fully transformed during cooling. As a differentiation is barely possible from the SEM images, a plethora of investigations is further used to assess the microstructure. As-built samples possess a good combination of ductility and hardness. Furthermore, the specimens are characterized by a good tempering stability up to 600 °C. This tempering stability is characterized by a homogeneous hardness of around 400 HV1 for all temperatures. In contrast, the conventionally hardened specimens show a drop-off in material hardness, further indicating the excellent material properties of additively manufactured Bainidur AM.

1. Introduction

Bearing[1] and gear applications[2] have an extremely high demand regarding the underlying material properties. A sufficient surface hardness is required to avoid adhesive wear while a high impact toughness is required to absorb sudden shocks.[3] Low-alloyed steels like 16MnCr5 and 20MnCr5 were designed to meet these respective materials properties.[4] Due to their low-carbon content, products made from these case-hardening steels possess a good ductility after hardening due to the weaker martensite.[5] A corresponding heat treatment, also referred to as carburization, is typically performed to increase the carbon content in the case of the workpiece.[6] After hardening, the surface reaches a sufficiently high hardness while the core maintains its good ductility.[7]

Directed energy deposition (DED-LB/M) processes, often also referred to as laser metal deposition, allow for the selective generation of complex structures due to the layer-by-layer manufacturing process.[8] Additive manufacturing processes can be of particular interest for highly complex products that cannot be manufactured easily using conventional processing technologies.[9] DED processes can also be used for fabricating large volumes or for the repair of worn parts.[10] However, the complex thermal boundary conditions result in unique material properties.[11] This can be attributed to the high local cooling rates exceeding 10^3 K s-1[12] and the repetitive process-intrinsic heat treatment.[13] Furthermore, wear-resistant coatings can be generated using the DED-LB/M process.[14] The generation of these wear-resistant coatings provides the possibility of substituting the carburization heat treatment in the future. Fundamental investigations on the processability of the underlying material by means of DED-LB/M are typically required to assure a reproducible processing of the main material, which again is helpful in repairing worn products. Low-alloyed steels typically possess a good weldability due to their low-carbon content.[15] However, the DED-LB/M of steels like Bainidur AM or similar materials like 16MnCr5 or 20MnCr5 has barely been investigated yet. Bartels et al. have studied the general processing of Bainidur AM[16] as well as the development of a reinforced coating[17] based on this material by means of DED-LB/M. However, fundamental studies on the

D. Bartels, A. von Lattre-Hertel, T. Novotny, M. Schmidt
Institute of Photonic Technologies (LPT)
Friedrich-Alexander-Universität Erlangen-Nürnberg (FAU)
Konrad-Zuse-Str. 3/5, 91052 Erlangen, Germany
E-mail: dominic.bartels@lpt.uni-erlangen.de

D. Bartels, M. Schmidt
Erlangen Graduate School in Advanced Optical Technologies (SAOT)
Friedrich-Alexander-Universität Erlangen-Nürnberg (FAU)
Paul-Gordan-Straße 6, 91052 Erlangen, Germany

A. Mohr, H. Hill
Special Materials
Deutsche Edelstahlwerke Specialty Steel GmbH & Co. KG
Oberschlesienstraße 16, 47807 Krefeld, Germany

C. Merklein
Advanced Manufacturing Technologies
Schaeffler Technologies AG & Co. KG
Industriestraße 1-3, 91074 Herzogenaurach, Germany

The ORCID identification number(s) for the author(s) of this article can be found under https://doi.org/10.1002/srin.202200925.

DOI: 10.1002/srin.202200925

microstructure formation and the material properties are missing within these works.

Further experiments were performed on the processing of this class of steels by means of PBF-LB/M in recent years. Schmitt et al.,[18] Aumayr et al.,[19] and Zumofen et al.[20] have shown that defect-free parts from this group of steels can be manufactured successfully using AM technologies. These low-alloyed steels possess a mixture of a bainitic–martensitic microstructure. This is further indicated by the material properties like hardness and strength which fall below the one of hardened reference specimens.[19,20] These investigations support the assumption that low-alloyed steels can be processed reasonably using laser-based technologies. In contrast to PBF-LB/M, the fabrication of low-alloyed steel components by means of DED-LB/M is barely studied. Ebrahimnia et al.[21] focused their work on the processability of 24CrNiMo. Up to two layers were manufactured additively. Single-layer specimens could be fabricated without significant crack or pore formation. Multilayer specimens, however, supported the crack formation. Wang et al.[22] investigated the laser metal deposition of a low-alloyed steel HSLA with a carbon content of approximately 0.07%. They have shown that the material can be processes successfully by means of laser metal deposition without any larger defects. Liu et al.[23] studied the laser metal deposition of the high-strength steel M300 which is characterized by a carbon content of around 0.40 wt%. The material could be fabricated without significant defects and possessed a martensitic–bainitic microstructure in the as-built state.

Goal of this work is to study the microstructure formation of the low-alloyed steel Bainidur AM when processing this material by means of DED-LB/M. Due to the high cooling rates and continuous intrinsic heat treatment, a martensitic-to-bainitic microstructure is assumed.[24] The microstructure formation will therefore be characterized by analyzing the material properties in the as-built and heat-treated state. Special importance is devoted to the tempering stability as bainite is known for a better tempering stability compared to martensite as shown in refs. [25,26].

2. Experimental Section

DED-LB/M experiments were performed on a 5-axis ERLAS 50237 machine (ERLAS GmbH, Germany) equipped with a 4 kW diode laser of type Laserline LDF 4000-4 (Laserline GmbH, Germany) with a characteristic wavelength between 940 and 963 nm. The laser spot size can be varied between 1 and 3 mm by using a zoom optic. As powder material, the case-hardening steel Bainidur AM (Deutsche Edelstahlwerke Speciality Steel GmbH, Germany) was used with a nominal particle size distribution between 45 and 90 µm. **Figure 1** shows exemplary scanning electron microscopy (SEM) images of the Bainidur AM powder.

The powder material consists of mainly spherical and some nonspherical particles. Larger magnifications show that small satellites can be found on the surface of the particles, probably resulting from the atomizing process. The chemical composition of the powder material according to the supplier's certificate is listed in **Table 1**.

Experimentally determined d_{10}, d_{50}, and d_{90} values are 58.8, 80.8, and 100.4 µm, respectively. Argon was used as both shielding and carrier gas. Laser-cut 16MnCr5 circular blanks with a nominal diameter of Ø 60 mm and a thickness of 3.5 mm were used as substrates for the DED-LB/M experiments. The blanks were inserted into a mounting fixture made from aluminum and were not clamped mechanically. All substrates were used in the as-delivered, hot-rolled condition.

Within this work, 12-layer cubic samples with an edge length of 12 mm in x- and y-direction were manufactured additively. A meander-shape hatching strategy was used for generating the core of the specimens. This was followed by single contour weld tracks along the four edges of the specimen. After every layer, the fabrication sequence was shifted clockwise by 90° to homogenize the heat input into the specimen. The process parameters for both the hatching and the contour were maintained constant throughout the manufacturing process. **Table 2** shows the investigated parameter combinations for the following experiments. While the feed rate and the spot size were maintained constant,

Table 1. Chemical composition of Bainidur AM according to the supplier's certificate provided by the Deutsche Edelstahlwerke.

Batch	Element content in wt%								
	C	Si	Mn	P	S	Cr	Mo	Ni	V
DED	0.23	0.7	1.2	<0.02	<0.02	1.0	0.9	<0.3	<0.15

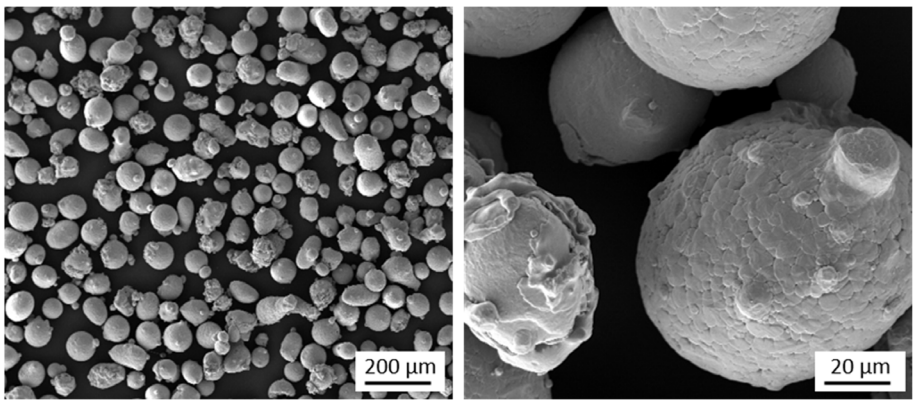

Figure 1. SEM image of the Bainidur AM powder material.

Table 2. Investigated process parameter set for the DED-LB/M experiments.

Set	Laser power [W]	Feed rate [mm min^{-1}]	Spot size [mm]	Avg. track width [mm]
A	600	400	1.5	1.50
B	700	400	1.5	1.70
C	800	400	1.5	1.85

the laser power was varied to investigate the influence of varying energy inputs on the material properties. Modifying the feed rate would result in different build rates, which is undesirable when comparing the material properties and the influence of the intrinsic heat treatment.

Powder mass flow, shielding gas, and carrier gas properties were kept constant at $2.60 \pm 0.02\,\mathrm{g\,min^{-1}}$, $20\,\mathrm{L\,min^{-1}}$, and $4\,\mathrm{L\,min^{-1}}$, respectively. The averaged weld track width was determined based on single weld tracks using the presented parameters. The overlap between adjacent weld tracks was set to 50% and maintained constant. Next, the additively manufactured samples were embedded in an epoxy resin, grinded, and polished for subsequent analysis of the material hardness. To analyze the microstructure formation, an additional etching step using a 3% Nital solution was performed.

2.1. Analysis of Microstructure Formation

In the first step, the relative density of the manufactured specimen was determined on nonetched cross sections. Therefore, images of the samples were made using an optical light microscope of type Olympus BX53M (EVIDENT Europe GmbH, Germany). The ratio of defect-free material and defects like pores or cracks was determined using binarization methods. This value resembles the relative density of the sample. Furthermore, magnified images of the etched cross sections were made to study the phase formation and orientation. SEM was used for analyzing the microstructure. A D8 Discover (Bruker 155 Corporation, Billerica, USA) system equipped with a Lynxeye 1D detector was used for X-ray diffraction (XRD) measurement of the retained austenite content.

2.2. Hardness Measurements

The hardness measurements are performed on nonetched cross sections. A KB30S (Hegewald & Peschke, Germany) was used for determining the hardness in the as-built state. The hardness of the heat-treated specimens was measured using a Qness indentation tester (ATM Qness GmbH, Germany). The hardness was determined in every layer, with a constant distance between two measurement points of the layer height t- in z-direction and 2 mm y-direction. Eight measurements are performed along the y-direction for every specimen. An exemplary depiction of the measurement grid is provided in **Figure 2**.

For each specimen, three independent samples were manufactured and analyzed. The layer height is determined based on the height of the part and the number of manufactured layers.

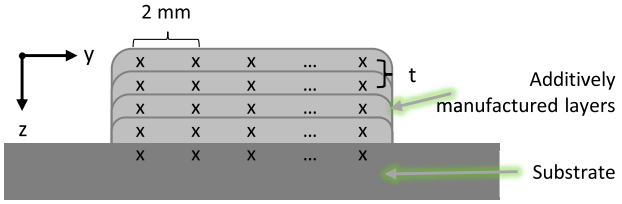

Figure 2. Measurement scheme for determining the hardness of the additively manufactured specimens.

2.3. Postprocess Heat Treatment

Additional postprocess heat treatment was performed on additively manufactured specimens to assess the tempering stability. Two different strategies were followed. On the one hand, the as-built specimens were exposed to a tempering heat treatment (AT) up to temperatures of 600 °C. On the other hand, the additively manufactured samples were quenched and tempered (QT) at the same temperatures. The tempering parameters are shown in **Table 3**.

All austenitization heat treatments were performed in a furnace of type N 31/H (Nabertherm GmbH, Germany). Austenitization was performed at 920 °C for 0.5 h. An N 30/85SHA (Nabertherm GmbH, Germany) oven was used for tempering the specimens. The specimens were tempered for 1 h. A nitrogen gas atmosphere was used for all heat treatment experiments.

2.4. Compression Testing

Furthermore, compression tests are performed on a universal testing machine of type QUASAR 100 kN (SCHÜTZ + LICHT Prüftechnik GmbH, Germany) according to DIN 50106 using cylindrical samples. As the ratio of height-to-diameter shall be between 1 and 2, a specimen geometry with a diameter of 4 mm and a height of 6 mm was chosen. The specimens were machined from 12-layered specimens to allow a comparability with the hardness measurements, which were performed along build direction. The specimens were extracted from the center of the additively manufactured structure. After machining, the samples were polished. Three samples were machined from independent specimens for compression analysis.

Table 3. Heat treatment parameters for the analysis of the tempering stability.

Tempering temperature [°C]	As-built and tempered	Quenched and tempered
150	AT150	QT150
200	AT200	QT200
300	AT300	QT300
400	AT400	QT400
500	AT500	QT500
600	AT600	QT600

3. Results and Discussion

The manufactured samples were analyzed regarding defect formation, phase formation, microstructural characteristics, and mechanical properties. **Figure 3** shows the 12-layered specimen fabricated by means of DED-LB/M using the three different parameter combinations.

All specimens could be manufactured without larger defects like cracks or pores, independent of the applied process parameter. The relative part density exceeds 99.9% in all cases. However, the specimens fabricated with a higher energy input are characterized both by a reduced dimensional accuracy and by a promoted etching indicated by the brown color in the top region. Both observations can be attributed to the heat agglomeration due to the layerwise process. For the lowest laser power, only the top three layers are characterized by a promoted brownish etching, whereas the lower layers are characterized by a bluish etching with darker regions at the bonding zone between two consecutive layers. The dark brown regions at the top indicate a fast cooling, which would correlate with a high material hardness. Increasing the laser power results in an enlarged size of the brownish etched zone, caused by the greater energy input during the manufacturing process. Furthermore, the brownish etched region appears brighter, appearing more like a ferritic structure. With an increasing size of this bright brown region, a reduced material hardness compared to the bluish parts of the specimens is assumed. Higher laser powers result in higher surface temperatures of the substrate. This effect can be linked very well with the etching response of the additively manufactured structure. The surface temperatures of the substrate indicate that the structure is continuously overheated. Correspondingly, the promoted heat accumulation of the substrate results in larger melt pools with increasing part height. This leads to an increased powder catchment within the enlarged melt pool, which explains the noticeable dimensional inaccuracies for higher energy inputs.

3.1. Hardness and Microstructure Formation

To further analyze and validate the material properties, the material hardness was measured for the additively manufactured Bainidur AM samples using the indentation tester. By determining the hardness in every layer, the influence of the build height and the corresponding intrinsic heat treatment on the mechanical properties is assessed. The corresponding hardness progressions are presented in **Figure 4**.

The maximum material hardness was measured in the top three layers of the specimens for laser powers of 600 W (455 HV1) and 700 W (440 HV1). For the highest laser power of 800 W, the highest hardness was determined close to the bonding zone of the substrate (third layer, 420 HV1). After that, a slight decrease in hardness was observed toward the top layer (390 HV1). This correlates well with the trends indicated by the etching colors in Figure 3. The differences in the maximum material hardness can be attributed to the different cooling rates and in situ preheating temperatures depending on the applied process parameters. Lower laser powers favor a faster cooling due to the smaller melt pool size, thus potentially resulting in a finer grain.[27] Furthermore, the decrease in material hardness along build direction for the highest laser power could be a cause of a sequential overheating. Due to the low thermal mass of the substrate, the excessive energy input will lead to higher in situ preheating temperatures. This assumption is supported by the finding that the specimens tended to bulge for higher energy inputs, without an increase in pore formation (see Figure 3). These promoted in situ temperatures will most likely result in a higher retained austenite content because the transformation to either martensite or bainite is not fully performed. This mechanism is temperature and time dependent and is therefore affected by the different processing times (due to the average weld track width) and the maximum temperatures (due to the energy input). Therefore, the obtained hardness values were correlated with the microstructure of the specimens. **Figure 5** presents the SEM images of the cross sections for three different

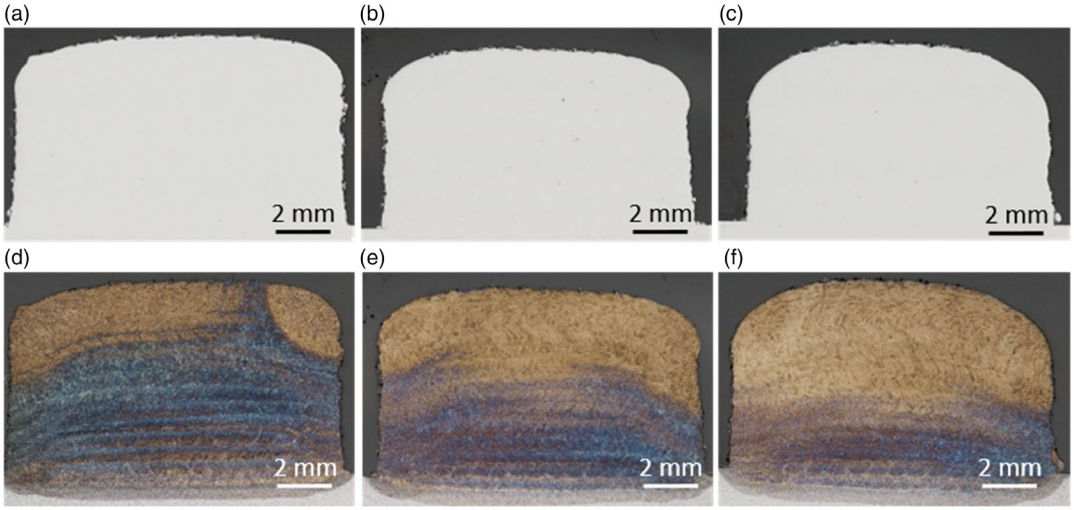

Figure 3. Cross section of 12-layered specimens manufactured using DED-LB/M for a,d) $P = 600$ W, b,e) $P = 700$ W, and c,f) $P = 800$ W. All specimens were manufactured with a feed rate of $v = 400$ mm min^{-1} and a spot size of $d_L = 1.5$ mm.

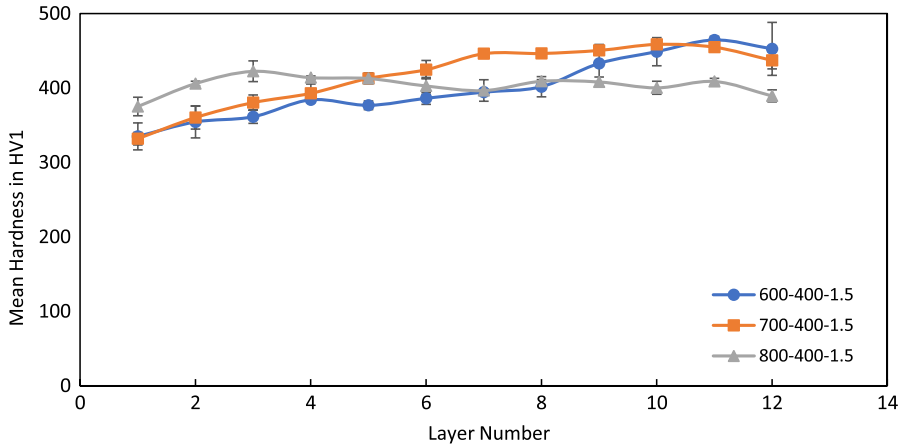

Figure 4. Material hardness for 12-layered specimens manufactured with three different laser powers ranging from 600 to 800 W.

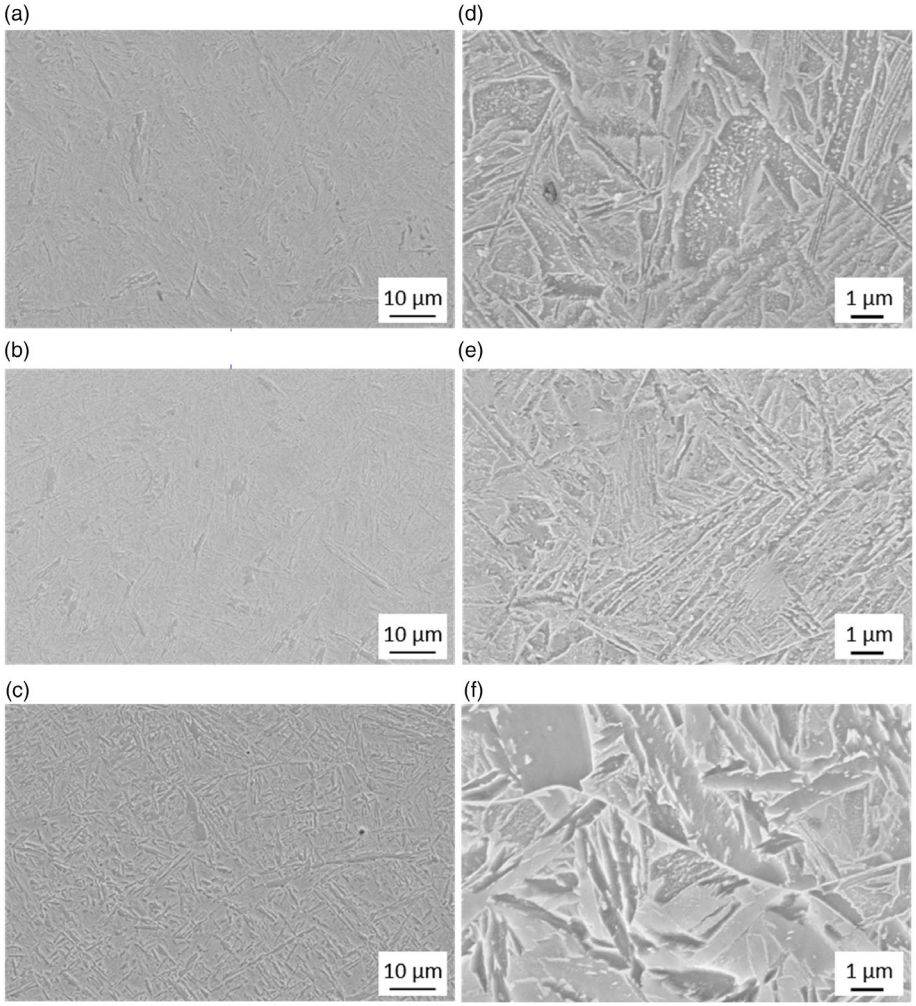

Figure 5. SEM images of the middle region of specimens manufactured by means of DED-LB/M using a laser power of a,d) 600 W, b,e) 700 W, and c,f) 800 W.

laser powers and two different magnifications within the center of the specimen.

The microstructures of the additively manufactured specimens appear similar at a low magnification of 3.0 K. Further zooming into the structures reveals differences for the different energy inputs. At the lowest energy input, a lath-like structure can be identified. The microstructure is characterized by precipitated carbides within the grain. Due to the fine dispersion of these carbides, probably cementite, the structure is either a martensitic or a lower bainitic one. Applying higher laser power (700 W) results in a minor change of the microstructure. The regions with the finely dispersed carbides within the lath are reduced. However, the mixture of the plate- and lath-like structure, which was also presented at a laser power of 600 W, is still evident. Contrary to these two lower laser powers, the highest applied laser power (800 W) results in an altered microstructure. The structure is characterized by an increased amount of the larger plates. These bright plates are separated by longish darker structures. This indicates that a partially (degenerated) upper bainitic structure might be present in the center of the specimen.[28]

Moving toward the surface of the substrate, the hardness typically reaches its peak. This can be attributed to the faster cooling due to air quenching when finishing the build job. **Figure 6** shows SEM images of the top region for the different laser powers.

Laser powers of 600 and 700 W result in a similar lath-like microstructure. The grains tend to precipitate very fine carbides. Furthermore, a globular-like structure can be identified within the grains for the lowest laser power. This might be some sort of globular bainite forming from inside these ferritic isles or a mixture of incomplete transformation products.[29] At a laser power of 700 W, a transformation toward a degenerated bainitic structure can be assumed. The granular structure can also be found within the ferritic cells and appears more pronounced compared to the lower laser power. Applying a laser power of 800 W results in a different microstructure compared to the two other energy inputs. At 800 W, a more isle-like structure could be identified. This structure appears like retained austenite which could not be transformed completely during cooling. One potential reason for this is the elevated temperature within the additively manufactured specimen. The higher preheating of the specimen most likely leads to an incomplete transformation of the austenite into bainite or martensite. The presumably increased retained austenite content helps in explaining the reduced material hardness in the top region of the specimen. Furthermore, the reduced hardness can be explained by the slightly coarser structure of the laths shown in Figure 6.

3.2. Analysis of Tempering Stability

Bainite is typically characterized by a higher tempering stability compared to a martensitic microstructure.[25] As the microstructure of the DED-LB/M specimens is difficult to assess due to its fine size, additional studies on the tempering stability of as-built (AT) and hardened (QT) samples were performed. This study was used as an additional analyzing method for differentiating the as-built microstructure from the hardened microstructure. **Figure 7** presents the results of the experimentally determined hardness values and the measurement scheme for the different tempering temperatures.

The results show that the hardness in the as-built state remains constant for all tempering temperatures as high as 600 °C. At room temperature, a hardness of around

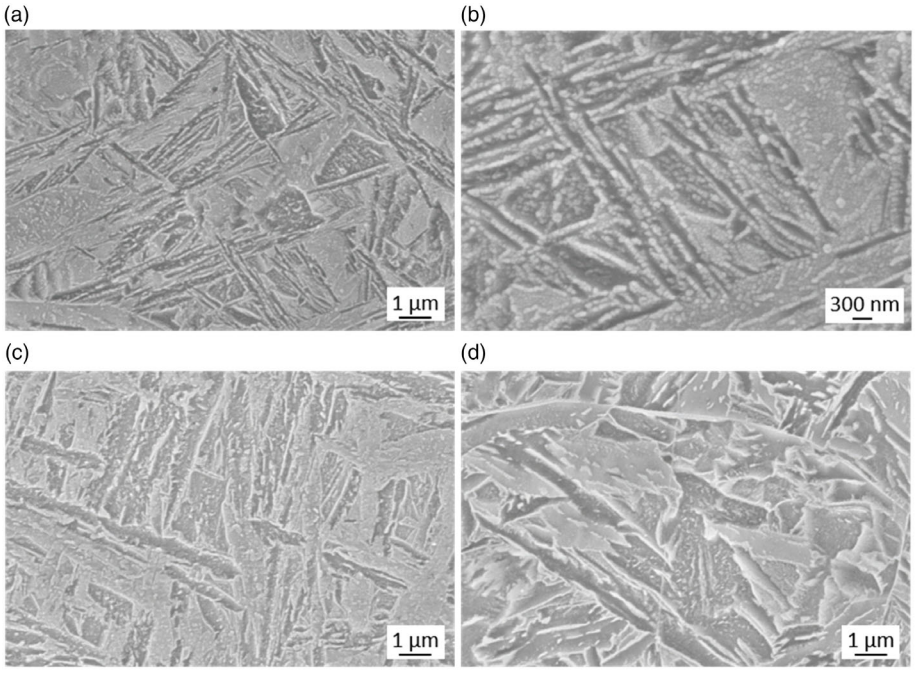

Figure 6. SEM images of the top region of specimens manufactured with a) 600 W, b) 600 W with a magnification of 50,000× showing the resolution limit, c) 700 W, and d) 800 W.

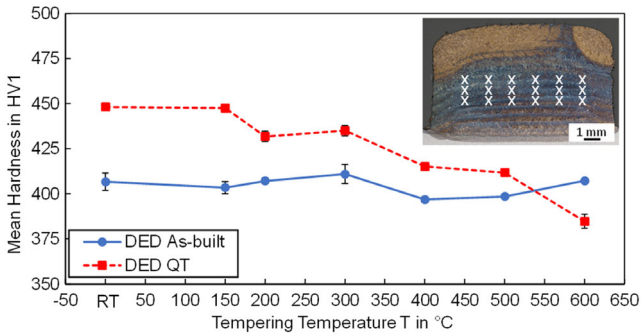

Figure 7. Tempering stability of as-built and quenched specimens. The samples were manufactured using a laser power of 600 W. Hardness measurements were performed in the center of the additively manufactured structure.

407 ± 5 HV1 was determined within the center of the sample. A minimum hardness of around 397 ± 2 HV1 was obtained after tempering the samples at 400 °C. Tempering at 600 °C resulted in a medium hardness of 407 ± 1 HV1. A small standard deviation could be obtained during all experiments, indicating a very homogeneous microstructure.

Quenching and tempering the samples results in an increased material hardness for low tempering temperatures. A maximum hardness of 448 ± 1 HV was obtained in the as-quenched state. However, a continuous decrease in hardness can be observed for temperatures exceeding 150 °C. The hardness (385 ± 4 HV1) falls below the one of the as-built specimens for the highest tempering temperature of 600 °C. This trend is characteristic for martensitic microstructures due to the poorer tempering stability of martensite compared to, e.g., bainite.[26]

The drop-off below the hardness of the as-built and tempered specimens makes it unlikely that the microstructure after DED-LB/M is a tempered martensitic one. In the next step, the microstructural characteristics were analyzed both for the as-built and tempered as well as the hardened and tempered state by means of SEM. **Figure 8** shows SEM images of the microstructure in the different heat-treated states. The microstructure is characterized by finely precipitated carbides within the lath and remains mostly similar up to a tempering temperature of 400 °C. These finely precipitated carbides could be an explanation for the excellent tempering stability of the material. Tempering at 600 °C results in slight changes as the previously promoted isles of retained austenite tend to decompose. The retained austenite content was in the range of 10 ± 2% within the center of the specimen prior to tempering. After tempering at 600 °C for 1 h, the retained austenite content fell below 3%. Additionally, the microstructural properties of the quenched and tempered specimens were analyzed by means of SEM. The microstructural characteristics are presented in **Figure 9**.

Quenching results in a destruction of the DED-specific microstructure. The quenched specimens possess a more promoted lath-like martensitic structure. Furthermore, the boundary of the lath-like martensitic structure is emphasized, which leads to a clear structure. Exposing the specimens to elevated temperatures results in a tempered martensitic microstructure. The lath boundaries are no longer as promoted as before as the carbon

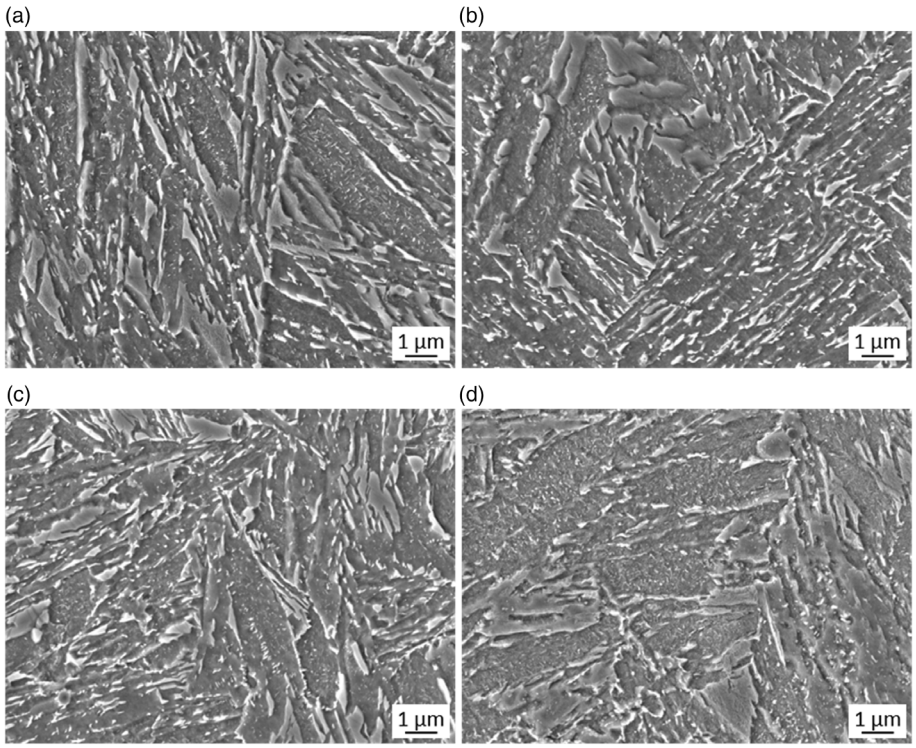

Figure 8. Microstructure of a) as-built specimens and after tempering from the as-built state at b) 200 °C, c) 400 °C, and d) 600 °C.

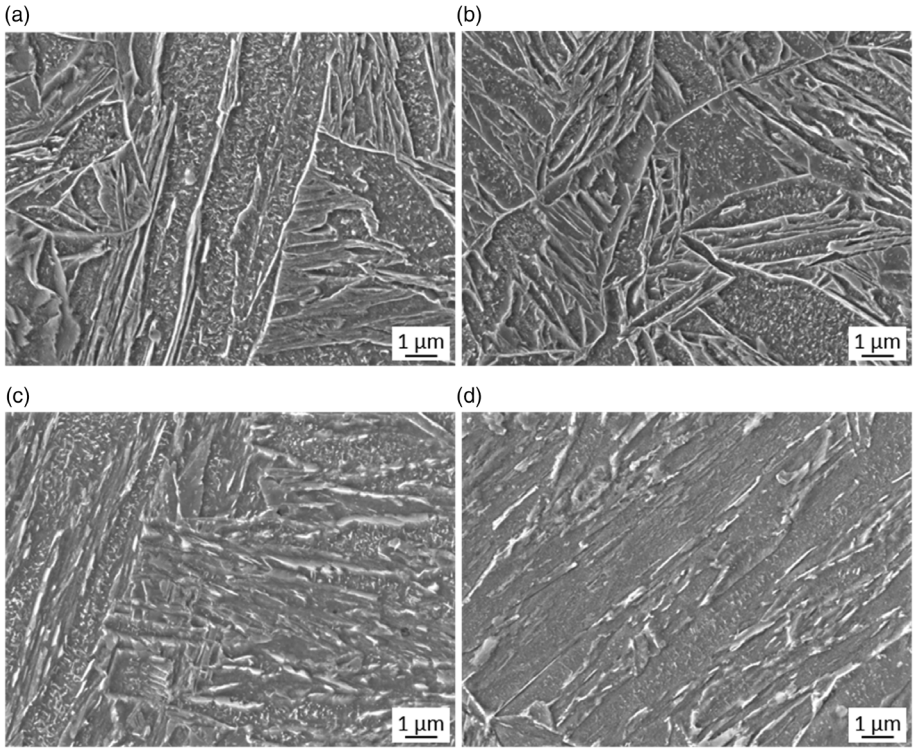

Figure 9. Microstructure of a) quenched and tempered specimens at temperatures of b) 200 °C, c) 400 °C, and d) 600 °C.

diffuses toward to grain boundaries. This helps to explain the reduced material hardness. Comparing the hardness after tempering (AT) and after hardening and tempering (QT) shows that the underlying microstructure in the as-built state is neither a fully martensitic nor a tempered martensitic one. This is supported by the better tempering stability up to 600 °C and the texture of the underlying microstructure. It is more probable that the marginal decomposition of the retained austenite and the beneficiary ferritic microstructure due to finely precipitated carbides[30] result in the homogeneous hardness along different tempering temperatures.

3.3. Compression Testing

Finally, the compression strength of the samples was analyzed. Compression testing can be seen as the inverse version of tensile testing and allows to assess the material properties for tooling applications. The maximum deformation rate for the abort criteria was set to 70%. All samples surpassed this deformation rate of 70% without breaking, which indicates the excellent ductility of additively manufactured Bainidur AM. The experimental results for the averaged values of the three different process parameters are presented in **Figure 10**.

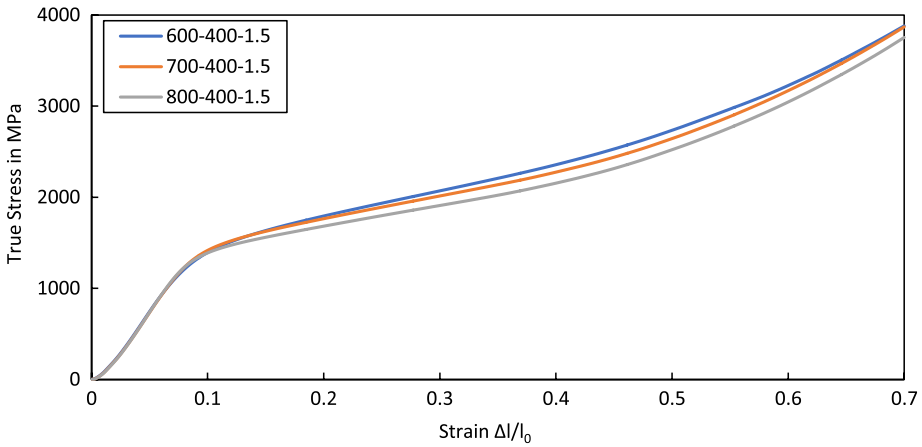

Figure 10. Compression strength of additively manufactured specimens using three different laser powers ranging from 600 to 800 W.

The highest compression strength ($3880 \pm 82\ N\ mm^{-2}$) was observed at the lowest laser power. Increasing the energy input resulted in a continuous decrease in compression strength, as the lowest strength ($3755 \pm 27\ N\ mm^{-2}$) was determined at the highest laser power. The corresponding yield strengths were 1402 ± 9 MPa (600 W), 1390 ± 11 MPa (700 W), and 1352 ± 11 MPa (800 W) for the three different laser powers. Overall, the determined compression and yield strength are very similar for the three different parameters. This correlates well with the comparable hardness values for the laser powers. The material properties are similar, even though a slight decrease in performance can be assumed for higher laser powers, both regarding the yield strength and the material hardness. The obtained yield strengths range between the ones of the additively manufactured steel M300 (approximately 1200 MPa)[31] and H11 tool steel (1770 MPa).[32] As both these materials are commonly used for tooling, a high potential for Bainidur AM as a base material for tooling applications can be assumed. A potential process route could include the deposition of a wear-resistant coating already during DED-LB/M.

4. Conclusion

This work presents thorough investigations on the material properties of additively manufactured Bainidur AM by means of DED-LB/M. It was shown that the selected process parameters and the corresponding process-intrinsic heat treatment affect the microstructure formation along build direction due to altered cooling conditions. A change from a lath-like toward a plate-like microstructure was observed for increased laser powers. This correlates with the hardness measurements, as the maximum hardness was observed both in the top layers and for the lowest laser powers. The as-built microstructure of the core region is further characterized by an excellent tempering stability up to 600 °C which indicates that the underlying microstructure should be at least partially bainitic. Bainidur AM also possesses an excellent yield strength for a low-alloyed steel around 1300–1400 MPa depending on the applied process parameters, linked with an excellent ductility. The high yield strength opens potentials in tooling, especially when additionally applying a wear-resistant coating during DED-LB/M. This shows the enormous potential of additively manufactured Bainidur AM as a base material due to its excellent properties, which are the consequence of the bainite-like microstructure. Future work will focus on the influence of different parameter combinations like higher or lower feed rates during DED-LB/M on the resulting microstructure. Furthermore, key properties like tensile strength will be determined to generate a database for the later use of this material.

Acknowledgements

The authors like to thank the BMWi for funding the project "HyConnect—Ressourcenminimale Fertigung durch hybride und hochvernetzte Prozesse" within the scope of the "Technologietransfer-Programm Leichtbau." Furthermore, the authors would like to thank the Deutsche Edelstahlwerke Speciality Steel GmbH for providing the powder material. The authors also like to thank Schaeffler Technologies AG & Co. Kg for their support within this work. The authors gratefully acknowledge the support provided by the Erlangen Graduate School in Advanced Optical Technologies.

Open Access funding enabled and organized by Projekt DEAL.

Conflict of Interest

The authors declare no conflict of interest.

Data Availability Statement

The data that support the findings of this study are available from the corresponding author upon reasonable request.

Keywords

Bainidur AM, bainitic microstructures, directed energy deposition (DED-LB/M), laser metal deposition, low-alloyed steels

Received: December 9, 2022
Revised: February 17, 2023
Published online:

[1] J. J. C. Hoo, *Effect of Steel Manufacturing Processes on the Quality of Bearing*, American Society for Testing and Materials, Philadelphia, PA **1988**.
[2] J. R. Davis, *Gear Materials, Properties, and Manufacture*, ASM International, Materials Park, OH **2010**.
[3] *Bearing Steel Technology: STP 1419* (Ed: J. M. Beswick), ASTM, West Conshohocken **2002**.
[4] F. Klocke, A. Kuchle, *Manufacturing Processes*, Springer, Berlin **2009**.
[5] R. K. Rajput, *Engineering Materials & Metallurgy*, S. Chand, New Delhi **2006**.
[6] J. R. Davis, *Surface Hardening of Steels: Understanding the Basics*, ASM International, Materials Park, OH **2002**.
[7] H. E. Boyer, *Case Hardening of Steel*, ASM International, Materials Park, OH **1987**.
[8] R. M. Mahamood, *Laser Metal Deposition Process of Metals, Alloys, and Composite Materials*, Springer International Publishing, Cham **2018**.
[9] A. Gebhardt, J.-S. Hötter, *Additive Manufacturing: 3D Printing for Prototyping and Manufacturing*, Hanser, Munich, Cincinnati op. **2016**.
[10] B. Graf, A. Gumenyuk, M. Rethmeier, *Physics Procedia* **2012**, *39*, 376.
[11] P. M. Sammons, D. A. Bristow, R. G. Landers, *J. Manuf. Sci. Eng.* **2013**, *135*, 054501.
[12] K. Zhang, W. Liu, in *Int. Conf. Measuring Technology and Mechatronics Automation*, IEEE, Piscataway, NJ **2009**, pp. 93–96.
[13] C. Barr, S. Da Sun, M. Easton, N. Orchowski, N. Matthews, M. Brandt, *Surf. Coat. Technol.* **2020**, *383*, 125279.
[14] a) M. N. Mokgalaka, S. L. Pityana, P. A. Popoola, T. Mathebula, *Adv. Mater. Sci. Eng.* **2014**, *2014*, 1; b) F. Shang, S. Chen, L. Zhou, W. Jia, T. Cui, J. Liang, C. Liu, M. Wang, *Surf. Coat. Technol.* **2021**, *421*, 127382.
[15] J. Dowden, W. Schulz, *Heat and Mass Transfer in Modern Technology*, Springer International Publishing; Imprint; Springer, Cham, Dordrecht **2017**.
[16] D. Bartels, O. Hentschel, J. Dauer, W. Burgmayr, M. Schmidt, in *Lasers in Manufacturing (LiM) 2021*, Munich **2021**.
[17] D. Bartels, J. Rohdenburg, A. Mohr, R. Rothfelder, M. Schmidt, *Procedia CIRP* **2022**, *111*, 237.
[18] M. Schmitt, T. Kamps, F. Siglmüller, J. Winkler, G. Schlick, C. Seidel, T. Tobie, K. Stahl, G. Reinhart, *Addit. Manuf.* **2020**, *35*, 101372.

[19] C. Aumayr, J. Platl, H. Zunko, C. Turk, *Berg Huettenmaenn. Monatsh.* **2020**, *165*, 137.
[20] L. Zumofen, A. Kirchheim, H.-J. Dennig, *Prog. Addit. Manuf.* **2020**, *5*, 75.
[21] M. Ebrahimnia, Y. Xie, C. Chi, *J. Laser Appl.* **2021**, *33*, 12007.
[22] Q. Wang, S. Zhang, C. Zhang, J. Wang, M. B. Shahzad, H. Chen, J. Chen, *Vacuum* **2019**, *161*, 225.
[23] F. Liu, X. Lin, M. Song, H. Yang, Y. Zhang, L. Wang, W. Huang, *J. Alloys Compd.* **2015**, *621*, 35.
[24] D. Bartels, T. Novotny, A. Mohr, F. van Soest, O. Hentschel, C. Merklein, M. Schmidt, *Materials* **2022**, *15*, 6171.
[25] M. J. Peet, S. S. Babu, M. K. Miller, H. K. D. H. Bhadeshia, *Metall. Mater. Trans. A* **2017**, *48*, 3410.
[26] M. A. Santajuana, R. Rementeria, M. Kuntz, J. A. Jimenez, F. G. Caballero, C. Garcia-Mateo, *Metall. Mater. Trans. A* **2018**, *49*, 2026.
[27] J. Shao, G. Yu, X. He, S. Li, R. Chen, Y. Zhao, *Opt. Laser Technol.* **2019**, *119*, 105662.
[28] S. Ragu Nathan, V. Balasubramanian, S. Malarvizhi, A. G. Rao, *Def. Technol.* **2015**, *11*, 308.
[29] S. Zajac, V. Schwinn, K. H. Tacke, *Mater. Sci. Forum* **2005**, *500–501*, 387.
[30] C. Garcia-Mateo, M. Peet, F. G. Caballero, H. Bhadeshia, *Mater. Sci. Technol.* **2004**, *20*, 814.
[31] C. Tan, D. Wang, W. Ma, Y. Chen, S. Chen, Y. Yang, K. Zhou, *Mater. Des.* **2020**, *196*, 109147.
[32] D. Junker, O. Hentschel, M. Schmidt, M. Merklein, *Metals* **2018**, *8*, 854.

Contribution to the Goal of this Work

This manuscript presents key findings on the material properties of case-hardening steels processed by means of DED-LB/M. The as-built microstructure was again analysed using various methods. SEM investigations show that a needle-like microstructure characterised by finely precipitated carbides is formed. However, in contrast to PBF-LB/M a larger share of the thin films can be observed. The microstructure in the as-built state thereby appears more like an upper bainitic one with lower shares of lower bainitic constituents. XRD measurements reveal a retained austenite content of around 10 % in the as-built state. The hardness difference between the as-built (405 HV1) and hardened state (450 HV1) indicates that the as-built material cannot be fully martensitic. Investigations on the tempering stability reveal a homogeneous hardness for temperatures of up to 600 °C for the as-built specimens while the hardened specimens are characterised by a continuous decrease of the material hardness (down to 385 HV1). Tempering the as-built sampels led to a decrease of the retained austenite content down to below 3 %, indicating that a transformation of the retained austenite took place. It can therefore be concluded that the DED-LB/M of case-hardening steels results in a predominantly bainitic microstructure with shares of austenite and martensite, again addressing the first research question (RQ1). In contrast to PBF-LB/M, the bainitic microstructure is predominantly upper bainitic. The reduced cooling rates of DED-LB/M as well as the faster heat accumulation result in smaller shares of lower bainite and in general a coarser microstructure.

Even though differences in the microstructures were observed, a similar hardness for both PBF-LB/M and DED-LB/M were obtained when using materials with similar chemical compositions. The key findings of Sections 4.1 and 4.2 with regard to the proposed research question are summarised in Figure 17.

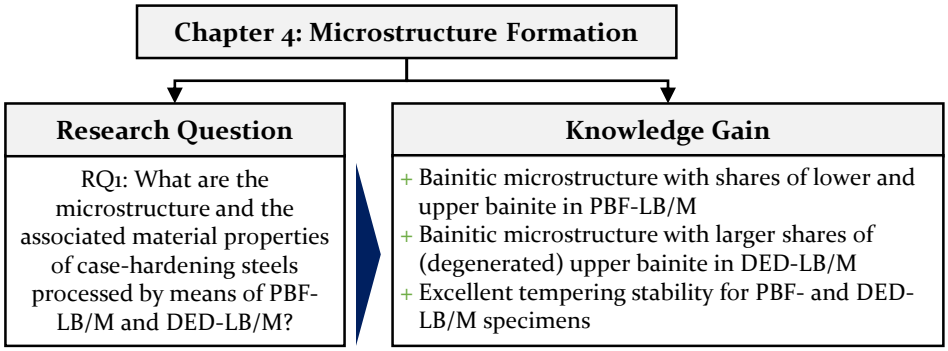

Figure 17: Summary of the key findings with regard to RQ1.

The excellent tempering stability of Bainidur AM manufactured using PBF-LB/M and DED-LB/M also opens the potential of using this material directly from the as-built state. Correspondingly, case-hardening steels with bainite-like properties could be of interest for the later local material modification through in-situ alloying. Introducing carbon and carbide-forming elements could promote the secondary hardening of the modified regions of the part, e.g. the case. Such multi- or graded-materials could then be tempered in a temperature interval at which carbide precipitation takes place. Due to the high tempering stability of the main body, the bainite-like properties are maintained while a reinforced case could be generated.

However, small-scaled specimens as studied within Chapter o are only conditionally representative for the final properties of more complex parts. The etching response of the specimens manufactured with different energy inputs in DED-LB/M reveal that the thermal history will have a non-negligible impact on the final material properties of larger specimens. Furthermore, first investigations indicate that the hardness of case-hardening steels decreases with increasing part heights. Correspondingly, the next chapter will focus on the influence of the thermal histoy on both microstructure formation and associated mechanical part properties.

5 Influence of Thermal History on Transformation Behaviour

The layer-by-layer AM process leads to a continuous energy input into the previously manufactured structure. When the supplied energy is larger than the energy that can be transferred away from the structure, either through heat flux or convection, this energy is accumulated. The degree of heat accumulation is affected by key process parameters like laser power, scanning speed, hatch distance, and layer thickness. Mohr et al. [149] have shown that surface temperatures exceeding 500 °C can arise during PBF-LB/M for high energy inputs. Since case-hardening steels are typically low-alloyed, the microstructure formation of these materials is very sensitive to the ambient temperature upon cooling. Correspondingly, a transition from continuous towards isothermal transformation is expected with increasing part height for excessive energy inputs.

Goal of this chapter is to investigate the influence of the **thermal history (RQ2)** on the microstructure formation of case-hardening steels in laser-based AM. The part height is varied from 10 mm to 60 mm to stimulate heat accumulation during PBF-LB/M. By adjusting the selected processing parameters, an excessive overheating is either forced (High VEDs) or avoided (Low VEDs). The aim is to identify the mechanisms responsible for microstructure formation in large-scale specimens. Thereby, the microstructure could either form in a continuous way or through an isothermal holding at elevated temperatures during build-up. The resulting material properties are analysed by means of SEM, XRD, and hardness measurements. These results are then correlated with the expectable surface temperatures, which are approximated based on literature findings. The surface temperature, material hardness, and retained austenite content are then again linked with the isothermal transformation diagram to derive the transition point at which the isothermal transformation sets in. To round these investigations, additional countering strategies are studied that supress heat accumulation during build-up. Therefore, promising strategies like additional interlayer times or even further reduced energy inputs are investigated with the goal of homogenising the material properties along build direction.

At the end of Chapter 5, knowledge on the mechanisms that are responsible for the microstructure formation in case-hardening steels will be available. This will help for the design of build jobs to avoid overheating during build-up with the aim of achieving homogeneous material properties.

5.1 Influence of Part Height on Microstructure Formation in Case-hardening Steels

Title: Effect of Volumetric Energy Density and Part Height on the Material Properties of Low-Alloyed Steels Manufactured by Laser-Based Powder Bed Fusion of Metals [P13]

Journal: Advanced Engineering Materials, Wiley

DOI to Web-version: https://doi.org/10.1002/adem.202300009

Authors: Dominic Bartels, Tobias Novotny, Moritz Albert, Andreas Mohr, Frank van Soest, Horst Hill, Carsten Merklein, Michael Schmidt

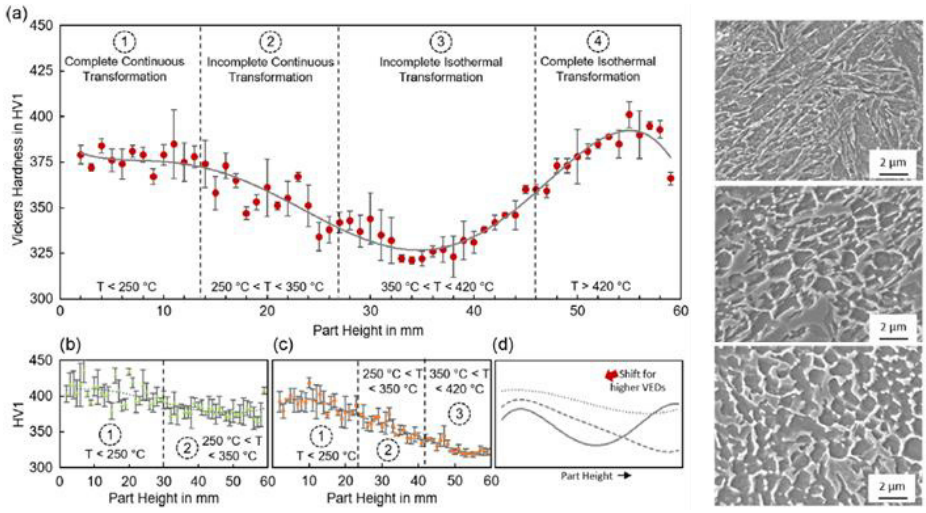

Motivation and Key Findings:

Additively manufactured case-hardening steels are characterised by bainite-like material properties in small-scaled specimen. However, when considering the temperature-sensitive transformation behaviour of these steels as well as the expectable heat accumulation during PBF-LB/M, microstructural changes need to be expected. This work presents investigations on the influence of the thermal history on the resulting material properties of large-scaled specimens. The **highlights** are:

- Heat accumulation during build-up of large parts in PBF-LB/M results in an altered transformation behaviour
- The retained austenite content and the associated hardness is affected by the part height and the energy input
- Incomplete transformations can be countered partially by an ex-situ heat treatment

ADVANCED ENGINEERING MATERIALS
www.aem-journal.com

Effect of Volumetric Energy Density and Part Height on the Material Properties of Low-Alloyed Steels Manufactured by Laser-Based Powder Bed Fusion of Metals

Dominic Bartels, Tobias Novotny, Moritz Albert, Andreas Mohr, Frank van Soest, Horst Hill, Carsten Merklein, and Michael Schmidt*

The layer-by-layer manufacturing approach in laser powder bed fusion of metals (PBF-LB/M) leads to heat accumulation in the workpiece with increasing part heights. The effect of this heat accumulation on the resulting material properties has, however, only barely been studied for low-alloyed steels. The goal of this work is to analyze the influence of different PBF-LB/M-specific boundary conditions like varying part heights and volumetric energy densities (VED) on the resulting material properties. It isfound that lower part regions possess similar hardness (380–410 HV1) and retained austenite values (7%–8%), independent of the applied VED. Higher energy inputs lead to higher retained austenite contents of up to 20% due to an incomplete transformation upon cooling. This rise in retained austenite content is also linked to a decreased material hardness down to 320 HV1. In higher part regions, this effect is reversed as the retained austenite content starts to decrease for the highest investigated VED. This is caused by the in situ preheating temperatures caused by heat accumulation, which favor a bainitic transformation. The part height-specific properties indicate that the microstructure formation forms through a continuous transformation in lower part regions and through an isothermal transformation in higher regions.

1. Introduction

Low-alloyed steels have recently been the subject of investigations in laser-based powder bed fusion of metals (PBF-LB/M). Due to their good weldability, case-hardening steels are suited very well for the PBF-LB/M process. In combination with the extraordinary design freedom, highly sophisticated products can be generated by additive manufacturing. The general processability of these materials has been studied throughout different works.[1–3] In the first work, Kamps[4] investigated the processing of 16MnCr5 by means of PBF-LB/M. The microstructure was described as fine-grained and resulted in an average hardness of around 330 HV1. More thorough investigations by Schmitt et al.[5] found a martensitic-bainitic microstructure with shares of ferrite. This conclusion on the underlying microstructure was performed based on the high process-specific cooling rates, which can be in the order of 10^3 to 10^5 K s^{-1}[6,7] in PBF-LB/M. Aumayr et al.[1] investigated the material properties of the low-alloyed steel Böhler E185 AMPO when processed by means of PBF-LB/M. This material could be processed successfully without larger defects. The resulting microstructure was described as bainitic-martensitic. It was also possible to process the tempering steel 30CrNiMo8 by means of PBF-LB/M.[3] Due to the higher carbon concentration (≈0.3 wt%) of this material, the substrate was preheated to 300 °C. The as-built tensile strength was almost as high as the one of the quenched and tempered reference specimens. In their work, Schmitt et al.[8] investigated the influence of different platform preheating temperatures on the material properties of 16MnCr5. For the lowest temperatures, a mostly ferritic structure was observed. Increasing the platform temperatures leads to a transition toward

D. Bartels, T. Novotny, M. Albert, M. Schmidt
Institute of Photonic Technologies (LPT)
Friedrich-Alexander-Universität Erlangen-Nürnberg (FAU)
Konrad-Zuse-Straße 3/5, 91052 Erlangen, Germany
E-mail: dominic.bartels@lpt.uni-erlangen.de

The ORCID identification number(s) for the author(s) of this article can be found under https://doi.org/10.1002/adem.202300009.

DOI: 10.1002/adem.202300009

D. Bartels, M. Schmidt
Erlangen Graduate School in Advanced Optical Technologies (SAOT)
Friedrich-Alexander-Universität Erlangen-Nürnberg (FAU)
Paul-Gordan-Straße 6, 91052 Erlangen, Germany

A. Mohr, F. van Soest, H. Hill
Deutsche Edelstahlwerke Specialty Steel GmbH & Co. KG
Oberschlesienstraße 16, 47807 Krefeld, Germany

C. Merklein
Schaeffler Technologies AG & Co. KG
Industriestraße 1-3, 91074 Herzogenaurach, Germany

a bainitic-ferritic and even pearlitic microstructure of the PBF-LB/M specimens. Wang et al.[9] processed the low-alloyed steel 24CrNiMo by means of PBF-LB/M. The resulting microstructure was found to be bainitic and the material possesses a high microhardness in the as-built state. Wei et al.[10] found that 24CrNiMo steels transform into bainite for high energy inputs due to heat accumulation during PBF-LB/M. The work of Bartels et al.[11] indicates that a bainite-like microstructure is formed when processing Bainidur AM by means of PBF-LB/M. In contrast to the hardened specimens, the additively manufactured material is characterized by a good tempering stability. This thermal stability indicated that the underlying microstructure is more thermally stable than martensite, which is typically associated with a hardness drop-off on tempering. Similar results were observed when processing Bainidur AM by means of DED-LB/M.[12]

The microstructure formation of steels upon cooling from the austenitization temperature can be distinguished into continuous cooling and isothermal transformation.[13,14] A continuous cooling is typically defined by specific cooling rates.[15] Martensite (fast), bainite (intermediate), and pearlite/ferrite (slow cooling) forms depend on the underlying cooling rates.[16] The isothermal transformation is characterized by a cooling to a defined temperature followed by an isothermal holding at this temperature for a defined time.[17] Thereby, the austenite is transformed in different microstructural constituents depending on the holding time at these temperatures. Martensite is typically formed through continuous cooling while bainite is formed through an isothermal transformation.[18] Transferring the fundamentals regarding the microstructure formation to PBF-LB/M, the ambient temperature of the workpiece gains importance. This temperature can be affected through either a (high-temperature) preheating[19,20] or heat accumulation[21,22] caused by the continuous energy input during build-up.

In their work, Mertens et al.[23] studied different preheating temperatures from 100 to 400 °C for the PBF-LB/M process. When preheating the substrate to a temperature of 400 °C, the martensite transformation is suppressed. This results in a homogeneously distributed bainitic microstructure. Saewe et al.[24] also applied a high-temperature preheating to improve the processability of the high-speed steel M50. The increased substrate temperatures affected the microstructure formation and resulted in a transition from an epitaxial (200 °C) toward a columnar dendritic microstructure (500 °C). The findings by Paravicini Bagliani[25] et al. also indicate that the degree of the retained austenite of low-alloyed steels is strongly affected by the temperature to which is the material is quenched. Already minor differences in temperature can significantly affect the retained austenite content of the final workpiece. Kunar et al.[26] further found that the partitioning time plays a major role regarding the formation of retained austenite. Regarding heat accumulation, Mohr et al.[27] found that the part height is highly influential on the phase formation. High volume energy densities (VEDs) and short interlayer times (ILT) favor an overheating of the to-be-produced parts with increased part heights. The high energy inputs further result in deeper melt pool depths, thus favoring keyhole porosity. This effect could be at least partially countered by reducing the energy input either by adjusting the VED or by increasing the interlayer times. An approach to counter this overheating by modulating the laser power was performed by Ettaieb et al.[28] for the titanium alloy Ti-6Al-4V. Consequently, the fluctuations of the melt pool size due to self-reinforcing overheating could be countered when using adjusted laser powers. Furthermore, a significant difference in subgrain size up to a factor of six depending on the applied parameter combinations was obtained within the investigations of Mohr et al.[27]. The corresponding effect on temperature development was proven in an additional work by Mohr et al. using thermography.[29] It is shown that the temperature within the workpiece can vary between approximately 150 and 600 °C depending on the parameter combination, chosen interlayer times, and part height. Williams et al.[30] developed an in situ thermography approach for determining the temperature development during the PBF-LB/M process. They found that the interlayer time significantly affects the surface temperature of the workpiece. Low ILTs can result in a drastic temperature increase for the same applied process parameters. From these studies, it can be assumed that the microstructure formation of low-alloyed steels could be altered extremely during the PBF-LB/M process as the different transformation intervals of the steels will be passed. Schmitt et al.[31] studied the influence of different part heights of up to 15 mm on the hardness of 16MnCr5 in their respective work. They found that the hardness decreased with increasing part heights and attributed this to grain coarsening effects. Furthermore, they stated that the microstructure transitioned from a martensitic toward a ferritic one.

The goal of this work is to study the influence of varying part heights and VEDs on the microstructure formation and the corresponding material properties of the low-alloyed steel Bainidur AM in PBF-LB/M. It is assumed that the transformation behavior is significantly altered by the energy input and transitions from a continuous cooling for small parts and low VEDs toward an isothermal transformation for larger parts and high VEDs. The investigations will be performed using the low-alloyed case-hardening steel Bainidur AM (1.7980; 18MnCrMoV4-8-7). By analyzing the geometry-specific as-built properties, we aim at expanding the application field of additively manufactured case-hardening steels to the use for construction parts due to their good combination of ductility and strength.

2. Experimental Section

All experiments were performed on an AconityMINI machine (Aconity 3D, Germany). Bainidur AM (Deutsche Edelstahlwerke Speciality Steel GmbH, Germany) was used as powder material with a nominal particle size from 15 to 45 µm. The particle size distribution ($d_{10\%} = 18.28$ µm, $d_{50\%} = 32.72$ µm, $d_{90\%} = 46.58$ µm) was determined using a CamsizerX2 (Microtrac Retsch GmbH, Germany). **Table 1** lists the chemical composition of the Bainidur AM powder material according to the supplier's certificate.

Table 1. Chemical composition of the Bainidur AM powder batch according to the supplier's certificate.

Batch	Element content in wt%								
	C	Si	Mn	P	S	Cr	Mo	Ni	V
Aconity	0.22	0.7	1.2	<0.02	<0.02	1.0	0.9	<0.3	<0.15

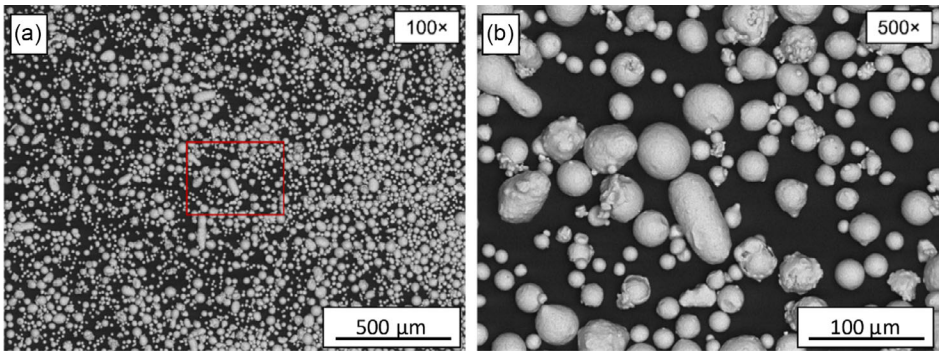

Figure 1. Morphology of the powder material Bainidur AM with a nominal size from 15 to 45 µm for a) 100× magnification and b) 500× magnification.

The moderate carbon content of 0.22 wt% indicates a good weldability of the material. Apart from that, the powder is characterized by minor concentrations of Si, Mn, Cr, and Mo, all in the range of around 1 wt%. **Figure 1** presents the morphology of the Bainidur AM powder determined by means of scanning electron microscopy. The powder is mainly spherical with shares of potato-shaped particles.

The carbon content of the powder material was also validated using an elemental CS-Analyzer (ELTRA GmbH, Germany). A carbon content of 0.219 wt% was determined, meaning that no statistically relevant fluctuations of the carbon content could be observed. Furthermore, the powder was dried in a vacuum furnace at 110 °C for 12 h prior to the experiments to get rid of undesirable powder moisture, which might hinder the flowability and thus the coating operation.

2.1. Process Parameters

The parameter window was deduced using cubic specimens with a dimension of $10 \times 10 \times 10\,mm^3$ in previous studies.[11] From these results, three different volumetric energy densities (VEDs) were selected for the investigations on the influence of the part height on the corresponding material properties. The studied parameter combinations are listed in **Table 2**.

Laser spot size was maintained constant at around 105 µm. A constant layer thickness of 60 µm was used. The scanning direction was rotated by 67 ° after every layer. All experiments were performed under argon gas atmosphere.

2.2. Sample Preparation and Analysis

The additively manufactured specimens were cut in half, embedded in an epoxy resin, grinded toward the center, and polished for analyzing the relative part density. Relative part density was determined using the same approach as presented in the study of Bartels et al.[11] Etching was performed with a nital solution (<5%) for the preliminary investigations. A Qness indentation tester Q10 A+ (ATM Qness GmbH, Germany) was used for determining the Vickers Hardness (HV1). The microstructure was analyzed using optical light microscopy (Leica DM4 M) and scanning electron microscopy (Tescan Vega and Mira3 SEM). Retained austenite (RA) content was determined by means of X-Ray diffraction (XRD) using a D8 discover system (Bruker Corporation, Billerica, USA).

Tensile testing was performed using specimens according to DIN 50125:2009-07 using shape C with an inner diameter of 4 mm. Specimens with and edge length of 10 mm in *x*- and *y*-direction and a total height of 60 mm were manufactured additively. Afterward, the parts were machined to the final geometry of the tensile sample. The experiments were performed on a QUASAR 100 (SCHÜTZ + LICHT Prüftechnik GmbH, Germany). Elongation at break was determined using an extensometer.

Table 2. Investigated process parameter range for the fabrication of the specimens.

Process parameter	Low VED	Medium VED	High VED
Laser power P [W]	225 W	250 W	275 W
Scanning speed v [mm s^{-1}]	850 mm s^{-1}	700 mm s^{-1}	550 mm s^{-1}
Hatch distance h [µm]	120 µm	110 µm	110 µm
Volumetric energy density [J mm^{-3}]	36.8 J mm^{-3}	54.1 J mm^{-3}	75.8 J mm^{-3}

2.3. Part-Height-Specific Microstructure

Specimens with different part heights were manufactured to assess the influence of the number of layers on the microstructure formation. Five different heights (10, 15, 25, 35, and 60 mm) were studied. The edge length in *x*- and *y*-direction was maintained constant at 10 mm each. No additional minimum layer times were defined. **Figure 2** displays the exemplary build jobs fabricated on the AconityMINI machine with different VEDs and part heights.

For these experiments, the hardness was measured along build direction. The distance between two measurement points in *z*-direction was set to 1 mm. At least three hardness measurements were performed at each *z*-position. Microstructural characteristics were obtained through optical light microscopy and SEM. Klemm-I etching was applied to reveal the microstructure. Additional XRD analyses were performed in five regions to obtain the corresponding retained austenite content, which is then correlated with the material hardness. To assess the tempering stability of the additively manufactured specimens, samples were heat-treated in a furnace of type N 30/85SHA (Nabertherm GmbH, Germany). The heat treatment parameters were chosen

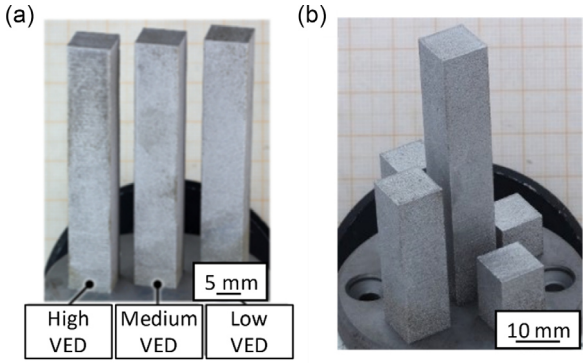

Figure 2. Exemplary build job with cuboid specimens for analyzing the build-height-specific microstructure for a) solid cuboids processed with the three different VEDs and b) cubes with different part heights from 10 to 60 mm. Tensile specimens were manufactured from the same build job as in (b) with all specimens possessing a part height of 60 mm.

based on a previous study.[11] Tempering was performed at 600 °C since the as-built material was known to withstand this temperature without significant hardness losses. Oxidation of the samples was avoided by preventing the experiments in a nitrogen gas atmosphere.

3. Results and Discussion

The applied process parameters were extracted from a previous study on the processability and the microstructure formation on Bainidur AM. Based on these findings, three different parameter combinations resulting a low, medium, and high VED were selected. In the first step (Section 3.1), the influence of different part heights on the microstructure formation will be analyzed. These investigations are followed by a study on the role of the volume energy density (Section 3.2) regarding the microstructure formation for specimens with a part height of 60 mm.

3.1. Influence of Different Part Heights on Material Properties

The part-height-specific microstructural properties are assessed for specimens with five different part heights up to 60 mm for a medium VED. All specimens were manufactured on the same build plate within one build job. The samples could be manufactured without larger noticeable defects, as indicated in **Figure 3**. It is noticeable that the intensity of the etching increases along the build direction. This correlates with the increased weld depth which was observed for the 60 mm specimen. The corresponding energy input is higher than the energy output from the specimens due to heat flux or surface cooling. Furthermore, this overheating will also act as an in situ preheating during the fabrication process, as shown by Mohr et al. in their respective work.[29] As known from isothermal transformation diagrams for steels, elevated temperatures and holding times affect the resulting microstructure significantly.

The average penetration depth of the single layers into the lower layer increases, as can be seen in Figure 3 (green, orange, and red boxes). This is the consequence of an increased preheating temperature of the previously manufactured layers, which results in a higher melt pool temperature and thus melt pool size during PBF-LB/M. It is therefore assumed, that the material properties, in this case the hardness, will also be affected by the altered transformation behavior. **Figure 4** shows the results on the hardness gradient and the corresponding retained austenite content for the different part heights.

The material hardness decreased continuously for a higher number of manufactured layers. All specimens possess the highest hardness in the bottom region of the specimen (bottom 10 mm), typically in the range between 390 and 410 HV1. At a part height of around 30–35 mm, a hardness of around 360–370 HV1 was determined both for the samples with a part height of 35 mm and 60 mm. As the trend is similar for all specimens and independent of the part height, a thermally-induced effect is assumed. Scanning electron microscopy (SEM) was used in the next step to analyze the microstructure within the bottom and top regions of the Bainidur AM samples. **Figure 5** shows the respective microstructure in the different regions of the specimens.

The bottom area of the specimen is characterized by two distinct regions, the fusion zone and the heat-affected zone. Whereas the fusion zone is characterized by finely dispersed carbides within the laths similar to lower bainite or (tempered) martensite, the heat-affected zone is more similar to a degenerated upper bainitic-like structure due to the cementite between the ferritic structures. A more detailed characterization of the bainitic phase can be found in the study of Bartels et al.[11] However, the top regions are no longer characterized by this distinction between the fusion and heat-affected zone. Larger shares of austenitic isles can be identified (Figure 5a) that appear like granular bainite without precipitated carbides within the grains. This could be explained by the slower cooling rates in the top regions and the higher expected temperatures, which would favor the transformation into a globular bainitic or at least bainite-like structure.[32] Further regions can also be identified that seem like a degenerated upper bainitic structure (Figure 5b). However, this structure possesses larger areas of austenitic isles compared to the bottom region of the specimen (Figure 5c). The top region is further characterized by a most likely complete absence of carbides. However, a validation of the absence of these (if present) nanoscaled carbides in the different regions of the specimens (top and bottom) would require the use of a transmission electron microscope.

Due to the low amount of carbon and other austenite-stabilizing alloying elements, a ferritic transformation can be expected. The microstructure in low-alloyed steels was already proven to be mostly bainitic-martensitic for small specimens.[11] Correspondingly, the isothermal time-temperature-transformation (TTT) diagram was calculated for the low-alloyed steel Bainidur AM using JMatPro. The diagram is shown in **Figure 6**. A quenching temperature of 920 °C was chosen. Since PBF-LB/M is known to produce a very fine microstructure, an average grain size of 9 µm was chosen for the calculation.

The TTT diagram reveals that an isothermal transformation during PBF-LB/M requires a global temperature of at least 350 °C. Furthermore, the beginning of the bainitic transformation can start for extremely low holding times at around 4 s. At a temperature of around 450 °C, a complete isothermal

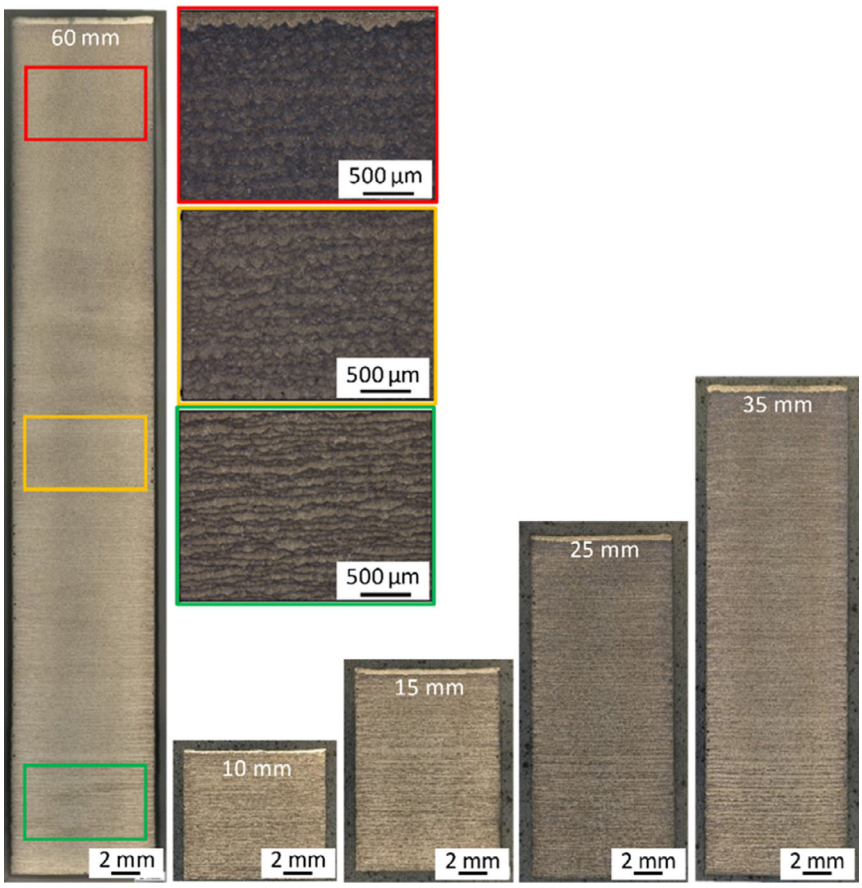

Figure 3. Cross-sections for specimens with different part heights manufactured using a medium VED.

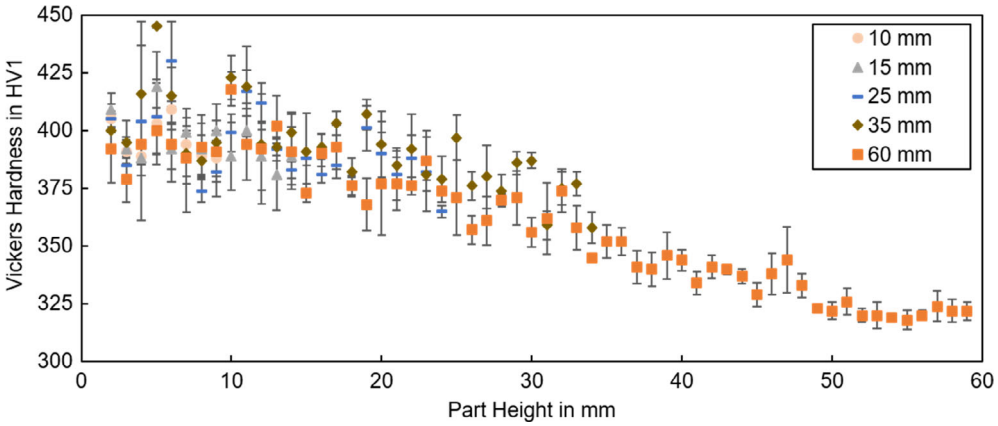

Figure 4. Development of the material hardness depending on the respective part height for VED Medium.

transformation can take place within approximately 100 s. Both lower and higher temperatures will again require longer holding times to support a complete transformation of the austenite into bainite during cooling. A literature review shows that the part height significantly affects the surface temperature of the specimen. The findings of Mohr et al.[29] indicated that surface temperatures between 300 and 400 °C can be obtained during the PBF-LB/M process when applying a comparable medium VED (see **Figure A1**). Correlating this information with the obtained RA content, the resulting material hardness, and the microstructural characteristics obtained through SEM, an incomplete bainitic transformation is concluded. The incomplete transformation correlates well with the obtained microstructural characteristics (see Figure 5) even though

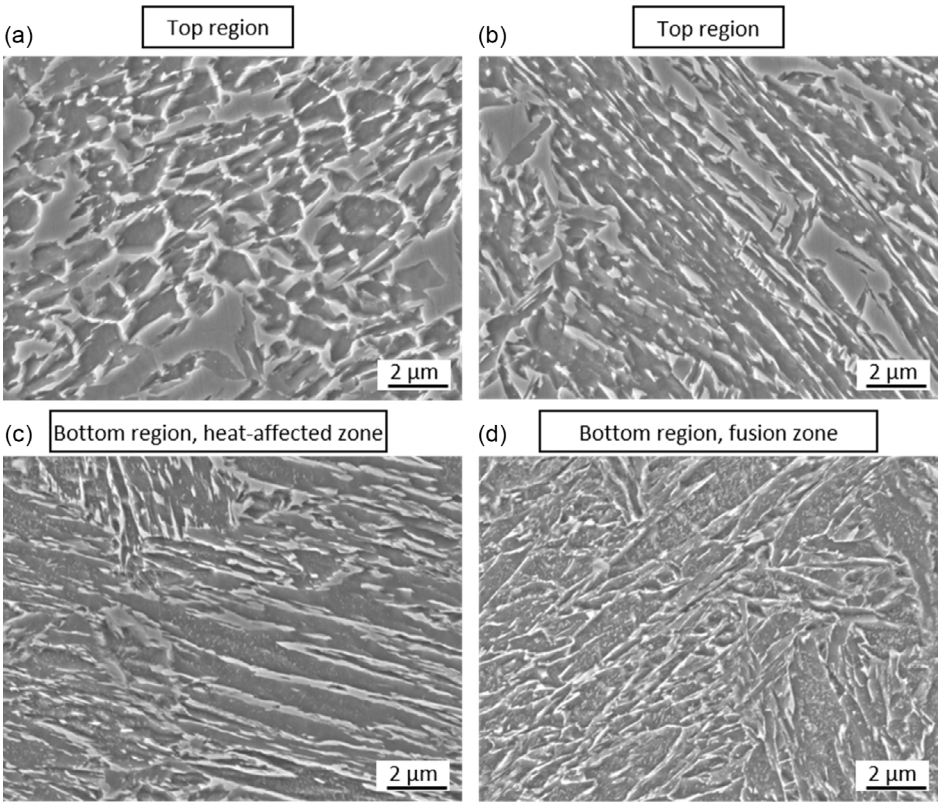

Figure 5. Microstructure in the (a,b) top region of the specimen showing a) a globular structure with austenite isles and b) a degenerated upper bainitic-like structure as well as the region in (c,d) the bottom of the specimen characterized by c) a degenerated upper bainitic-like structure in the HAZ and d) a fine lower bainitic- or martensite-like structure in the fusion zone for specimens with a part height of 60 mm and a medium VED.

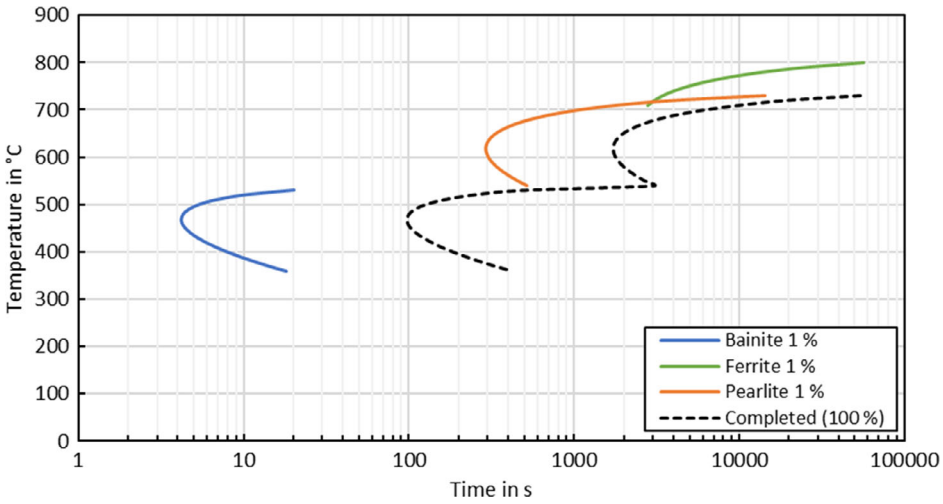

Figure 6. Isothermal time-temperature-transformation diagram for the low-alloyed steel Bainidur AM calculated using JMatPro. An average grain size of 9 µm and a quenching temperature of 920 °C were selected for calculation.

shares of (tempered) martensite and other phases cannot be concluded completely at this state. This assumption is based on two main points: on the one hand, the preheating temperature is too high to support the formation of martensite or bainite through continuous cooling. On the other hand, the holding times are too short to form 100% bainite by an isothermal transformation.

To validate this assumption, additional tempering investigations were performed. The hardness was measured on one-half of the specimen in the as-built state, while the other half was

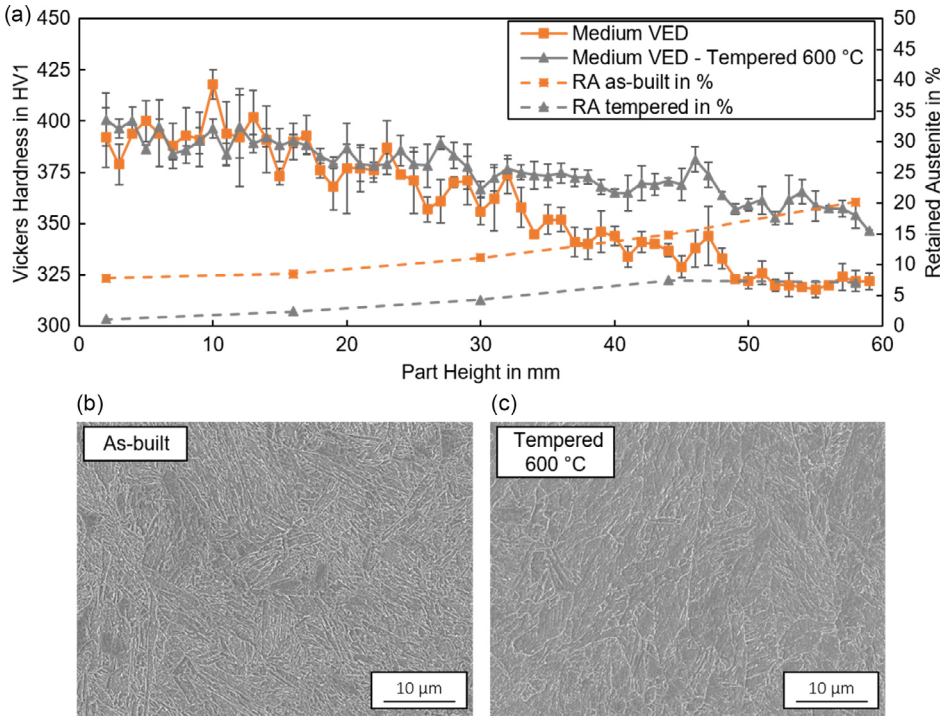

Figure 7. Experimentally determined a) material hardness and corresponding retained austenite content along build direction after tempering at 600 °C. b,c) Shows the microstructure in the bottom region in the as-built and tempered state. The specimens were manufactured on the AconityMINI machine using the medium (54.1 J mm^{-3}) VED.

exposed to a tempering step at 600 °C for 1 h before determining the hardness. Furthermore, the retained austenite content was determined both in the as-built state and in the tempered state. **Figure 7** presents the propagation of the obtained hardness and the corresponding retained austenite content. The hardness in the lower half of the specimens is barely affected by the tempering heat treatment and falls between 375 HV1 and 400 HV1 until a part height of around 20 mm is reached. XRD measurements reveal an RA content of around 7% in the as-built state, which falls to below 2% after tempering. Here, a transformation of the retained austenite into bainitic structures is most likely taking place. After passing a part height of 25 mm, a difference between the material hardness in the as-built and tempered state can be identified. While the hardness of the as-built specimens drops to around 360 HV1, the hardness of the tempered samples remains constant around 375 HV1. This effect is also reflected in the retained austenite content, which increases to around 11% in the as-built state. Tempering led to a transformation of the austenite, resulting in an increased hardness. Moving to the upper half of the specimens, an even more significant difference could be identified. While the hardness decreases continuously in the as-built state and reaches a minimum of 320 HV1, a complementary increase of the retained austenite (up to 15% and 20%) content was determined. After tempering, the retained austenite content dropped to around 7% in both cases. Furthermore, the material hardness exceeded a minimum hardness of 350 HV1 in the tempered state. Through-hardening of the additively manufactured specimens leads to an average hardness of around 470 HV1.[11]

It can further be seen that the bottom region possesses a fine-grained structure that appears like lower bainite. After tempering, this microstructure is coarsened and slightly resolved due to the high temperatures. These results support the assumption that the microstructure during PBF-LB/M is initially formed based on a continuous transformation at the absence of a platform preheating. This is supported by the fact that the material hardness in the lower regions is only barely affected by the cyclic energy input during the manufacturing process (see Figure 4). When building larger parts, an incomplete transformation of the austenite during cooling is present in the upper regions of the parts (see Figure 7). One reason for this is that the increased preheating temperatures during PBF-LB/M affect the transformation behavior, which is highly depending on the holding temperatures and times. Here, it is most likely that an isothermal transformation of the material takes place within the specimen. The increased retained austenite content in the top regions can then be explained by either too short holding times or too low holding temperatures during PBF-LB/M to assure a complete transformation into e.g., bainite. This is assisted by the finding on the tempering behavior, as the hardness increases by around 30 HV1 in the top regions when tempering the material at 600 °C for 1 h. This is contrary to the hardness in the bottom region, which was not affected by the tempering process. Correspondingly, the bottom region can either be tempered martensitic structure, a bainite-like structure, or a combination of both. The elevated temperatures of the specimen in the higher part regions might then result in locally altered chemical compositions, which would then affect

the stability of the retained austenite by element saturation and diffusion. A longer holding time might help to further reduce the RA content, as shown in the study of Saha Podder and Bhadeshia.[33]

3.2. Influence of Different VEDs on Material Properties

Based on the previous findings, two different approaches will be followed. On the one hand, the energy input will be decreased by applying a lower VED. The goal of this parameter set is to investigate whether the continuous transformation and the associated increase of the retained austenite content can be prolonged with lower energy inputs. On the other hand, the energy input will be increased. The aim is to find out whether the higher VED results in an earlier overheating of the structure. Correspondingly, this overheating should result in higher holding temperatures and longer holding times during build-up, thus resulting in a more complete transformation of the retained austenite. All specimens were built with a part height of 60 mm. **Figure 8** presents the cross-sections of the additively manufactured specimens along build direction for a low, medium, and high VED.

A high VED results in a reduced relative part density along build direction even though the bottom segments were characterized by a high relative part density. The specimens manufactured using the medium VED possess a mostly homogeneous density along build direction. A slight decrease could be identified along build direction. In contrast, the lowest VED is characterized by a homogenous relative part density for all regions within the specimens. The decrease in relative part density for increasing VEDs can therefore be attributed to a continuous overheating which must take place during build-up. This overheating can favor keyhole formation during PBF-LB/M, thus resulting in keyhole porosity, which is known for its spherical pores.[34]

Additionally, the specimens manufactured with a low VED and high VED were etched for analyzing the microstructure. The obtained results are presented in Figure 8. Again, three different sections were studied per specimen. A clear difference in the etching behavior can be observed for the specimens manufactured with the two different VEDs. Whereas the weld track boundaries can be easily identified for the parameter set with a low VED in all regions of the sample, the geometry of the weld tracks cannot be determined any longer for elevated part heights when applying a high VED. It can be seen for the low VED that the average weld penetration depth increases in higher regions within the part. This is attributed to the elevated preheating temperatures of the underlying structure, which results in the larger weld track depths since the overall thermal energy is higher.

The different regions of the specimens are further characterized by a different etching behavior. For the lowest VED, a brownish etching can be identified within all regions of the sample. The darker regions at the edges of the weld tracks most likely resemble a martensitic or bainitic-ferritic microstructure.[35] This correlates well with the findings presented in a previous work for this class of low-alloyed steels.[11] Throughout all three images in Figure 8a, only minor whitish areas, which would resemble retained austenite,[36] can be identified within the cross-sections. A slight transition toward a bluish color is however visible in the top regions. The change in etching color can be explained by two factors. First, the lower regions are continuously tempered throughout the manufacturing process.[37] Second, the heat agglomeration during build-up affects the initial microstructure formation in the top regions.[29] This effect can be especially identified when considering the development of the etching colors for parameter VED High in Figure 8b. Here, a promoted bluish etching can already be observed within the center region

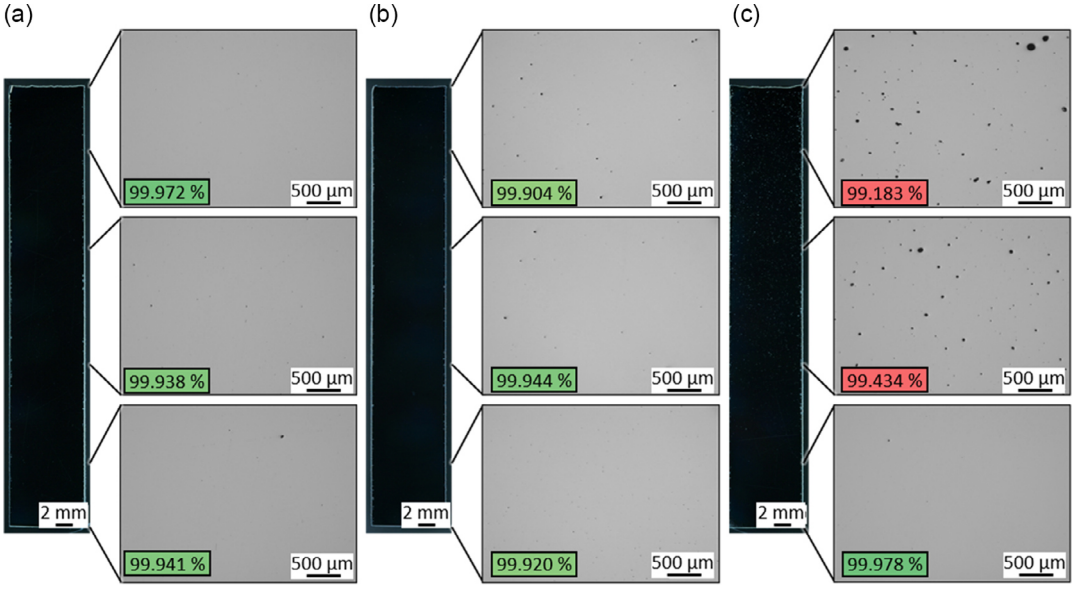

Figure 8. Build-height-specific porosity formation for a a) low (36.8 J mm^{-3}), b) medium (54.1 J mm^{-3}), and c) high VED (75.8 J mm^{-3}). The specimens possess a part height of 60 mm.

of the specimen even though the bottom regions are similar independent of the applied VEDs. Furthermore, the amount of the brighter white regions presenting retained austenite tends to increase.[36] Moving further toward the top, the single weld tracks that form the final geometry can no longer be distinguished from one another. Here, a switch toward a blue-grayish microstructure is evident. This supports the assumption, that an excessive in situ preheating temperature is present during the build-up of larger components in PBF-LB/M. To better evaluate the effect of this in situ heat agglomeration on the material properties, the hardness was determined along build direction for the different VEDs. Figure 10 presents the findings on the material hardness as well as the corresponding retained austenite content. The material hardness in the bottom region is the highest for the lowest VED and decreases with increasing VED. Possible reasons for this a fine-grain-hardening effects. Lower VEDs are typically characterized by a faster scanning or lower laser power, both favoring higher cooling rates. The faster cooling again results in a finer grain, an effect commonly observed in PBF-LB/M. As for the medium VED, the lowest VED results in a continuous decrease in material hardness. The lowest VED is however characterized by a very slow decrease in material hardness. Even after manufacturing a part with a height of 60 mm, a hardness of around 380 HV1 was obtained in the top region. This correlates well with the measured RA contents of these specimens, which continuously increased from 7% in the bottom region to around 10% in the top region. The slower increase backs the assumption that the initial transformation of the austenite is performed through continuous cooling. The highest VED results in the fastest decrease of the material hardness. A minimal hardness of 320 HV1 was already reached after a part height of approximately 35 to 40 mm in the center region of the sample. However, the top region of the specimen is characterized by a higher hardness of up to 400 HV1, which is similar to the original hardness in the bottom region.

The evaluation of the material hardness also correlates with the retained austenite content. XRD measurements reveal the highest RA contents of around 17% in the center region of the specimen. The top region, however, is characterized by a lower RA content of 6%, similar to the bottom region, which also correlates well with the high material hardness. This supports the assumption that the higher holding temperatures for the highest VED positively affect the transformation of the austenite to a bainitic or bainite-like microstructure. Overall, the material hardness develops differently for the three investigated VEDs for an exemplary part height of 60 mm. This further manifests the theory that the phase formation needs to be distinguished into a continuous and an isothermal transformation. The retained austenite content is sensitive to the underlying quenching temperature.[25] Increasing temperatures due to heat accumulation could then affect the transformation of the retained austenite upon cooling. Considering the propagation of the retained austenite content along with increasing part height, a differentiation into the two mechanisms isothermal and continuous transformation is possible. A potential differentiation into these two mechanisms is shown in Figure 11. The different regions were defined based on the corresponding hardness and retained austenite

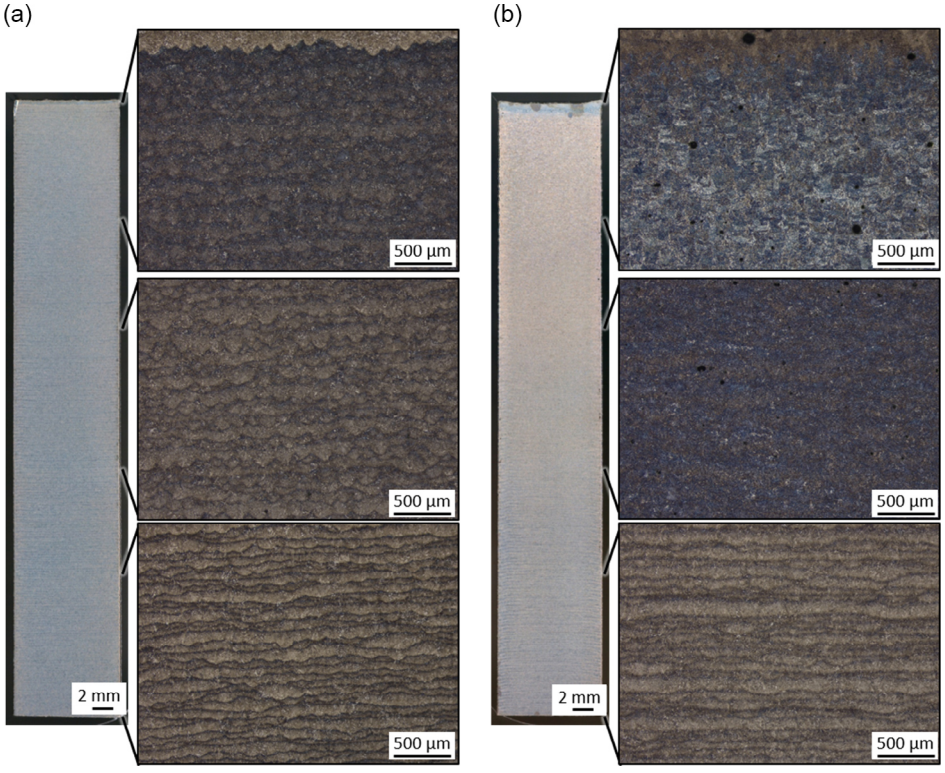

Figure 9. Cross-sections of different regions within the part manufactured with a) low VED and b) high VED. The specimens were etched using a Klemm-I reagent.

contents (see Figure 10) as well as the underlying microstructure (see **Figure 9**). Since the AconityMINI machine does not provide a port for an infrared camera, the temperature values were approximated based on the work by Mohr et al.[29]

In lower regions of the specimens, a continuous transformation of the austenite takes place. With increased part heights, the process intrinsic preheating temperatures of the specimens rise. This temperature rise is independent of the applied VED. These increased temperatures result in an isothermal holding of the workpiece. Since the transformation from austenite to, e.g., bainite is a time and temperature-dependent process, both the holding time as well as the holding temperature are decisive. Four different transformation mechanisms could be observed within the specimens: 1) Complete continuous transformation, 2) incomplete continuous transformation, 3) incomplete isothermal transformation, and 4) complete isothermal transformation. At this point, it needs to be mentioned that a clear differentiation between the mechanism (2) and (3), which describe an incomplete continuous and an incomplete isothermal transformation, is hardly possible. Applying the highest VED results in the fastest decrease of the material hardness, as previously shown in **Figure 10**. Based on the isothermal transformation diagram of Bainidur AM (see Figure 6) and the work of Mohr et al.,[29] the underlying temperatures can be assigned to the different transformation regions. The highest hardness in the early stages (1) can be associated with an almost complete transformation of the austenite during cooling. This is mirrored in the microstructure (see **Figure 11**e), which appears lower-bainitic or tempered-martensitic. Results on the bainitic-martensitic microstructure in this region can be found in previous work.[11] After that, the second stage (2) is characterized by an increasingly incomplete transformation. The findings from the literature indicate that temperatures below 350 °C should be obtained in these regions. This temperature is below the bainite finish temperature (≈360 °C) and above the martensite finish temperature of the material (≈240 °C). Correspondingly, larger shares of retained austenite are present. The third region (3) is characterized by elevated temperatures that reach the ones required for the formation of lower bainite. However, the short holding times and the late onset of the transformation of the austenite into bainite (see Figure 2) might not be sufficient to completely transform the austenite into bainite during holding.[38,39] Thereby, the heat flux toward the substrate, especially between consecutive layers, will hinder the austenite from an almost complete bainitic transformation. The resulting microstructure (see Figure 11f) is correspondingly characterized by high ratios of retained austenite, which are responsible for the reduced material hardness in this region. With increasing part height, a close to complete isothermal transformation is achieved (4). This is due to the expectable elevated temperatures that exceed 420 °C. According to the isothermal TTT of Bainidur AM, the required holding time falls in the range of approximately 100 s to undergo a complete transformation of the austenite. This helps in explaining the reduced austenite content and increased material hardness for higher part heights of the specimens manufactured with VED high. SEM images of this microstructure reveal a pronounced globular structure (see Figure 11g). This structure is characterized by a reduced share of the blocky austenite compared to the previous region. The globular structure might therefore be granular bainite, which forms at these elevated temperatures for comparable materials.[40] However, due to the high process-specific cooling rates, other constituents like a softer martensite that is formed upon the final cooling of the entire part cannot be ruled out. Reducing the VED shifts the underlying transformation mechanisms toward higher part heights and delays the onset of the isothermal transformation. For a medium VED (see Figure 11b), the fourth region, which is characterized by a close-to-complete isothermal transformation, is no longer evident. It can, however, be expected that this mechanism would occur when further increasing the part height. This is underlined by the fact that only regions (1) and (2) are present for the lowest VED. Here, the in situ preheating temperature is too low to even transition toward

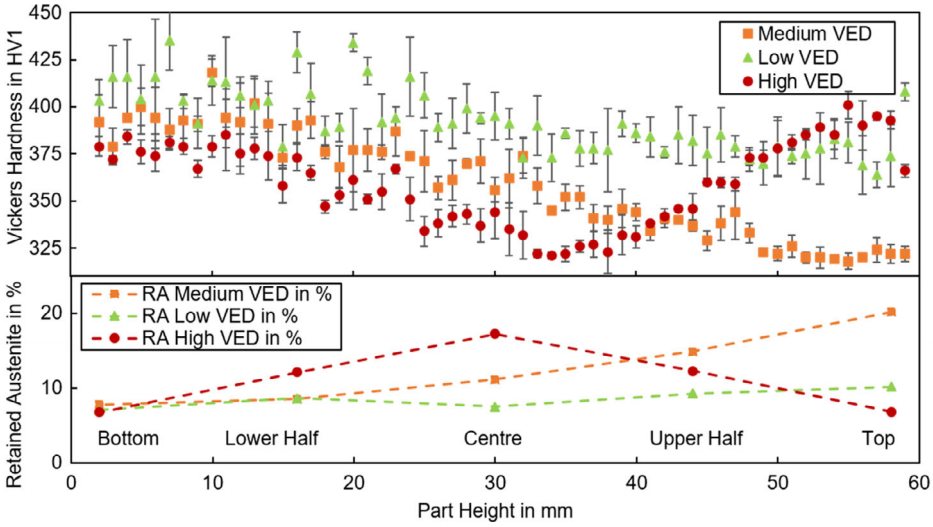

Figure 10. Experimentally determined values of material hardness (top) and retained austenite (bottom) content along build direction for different VEDs. The specimens were manufactured on the AconityMINI machine. The standard deviation is not shown for better perceptibility.

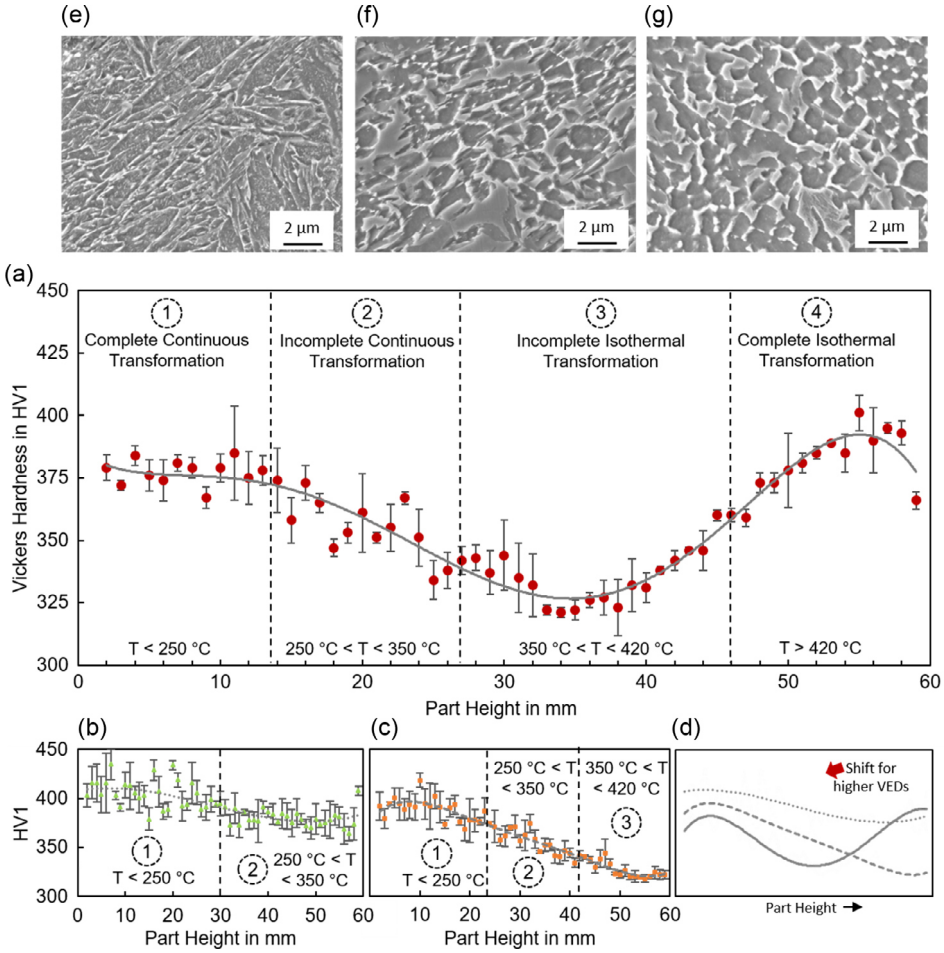

Figure 11. Differentiation into the four different transformation mechanisms during PBF-LB/M which are affected by the part height and the applied energy input, which can be distinguished for a a) high VED, b) low VED, and c) medium VED. d) Shows the arising shift of the transformation toward lower part heights when applying a higher VED. e,f,g) show the microstructure that is formed in the regions 1 (e), 2 + 3 (f), and 4 (f). The underlying temperatures were estimated based on the finding by Mohr et al.[29]

an isothermal holding. This is manifested by the comparably low retained austenite contents and the associated slow hardness drop-off. The findings by Mohr et al. further back this assumption since different maximum surface temperatures were obtained for comparable VEDs.[29] Processing the material with VED High leads to maximum surface temperatures of almost 500 °C after 1000 layers (= 60 mm). Applying a parameter comparable to VED medium lowers the maximum surface temperature to around 400 °C while VED Low would result in a temperature in the range of 300 °C. These temperature correlate with the expectable intervals for the austenite-to-bainite transformation within this work. An exemplary scheme of the propagation of the expectable surface temperatures is presented in Appendix A (see Figure A1). These findings support the assumption that the microstructure is initially formed through continuous transformation processes since only a minor heat accumulation is observed. With an increasing energy input and corresponding heat accumulation during build-up, the main transformation mechanism progresses toward isothermal holding. However, the transformation cannot be completed fully in lower part regions since the underlying holding temperature is not sufficient. This is associated with the lowest hardness values and the highest retained austenite contents. Moving toward larger parts, an almost complete isothermal transformation is observed. To manifest these findings, future research should focus on the application of a high-temperature preheating system to already start the build job within a temperature range at which an isothermal transformation takes place.

4. Tensile Properties of Additively Manufactured Bainidur AM

Furthermore, the tensile properties of the additively manufactured samples were analyzed. Vertically fabricated cubes were machined into tensile specimens. Five parts were manufactured within one build job for each parameter set. The obtained properties are listed in **Table 3**.

All specimens possess a similar ultimate tensile strength of 1200 ± 22 MPa (Low VED), 1222 ± 14 MPa (Medium VED),

Table 3. Tensile properties of the additively manufactured specimens for three different VEDs (low, medium, and high). *Ductility of the specimens processed with the highest VED could not be obtained from the tensile test as the breaking occurred outside of the region observable with the extensometer.

Material property	Low VED	Medium VED	High VED
Yield strength [MPa]	997 ± 62 MPa	900 ± 55 MPa	1097 ± 61.6 MPa
Tensile strength [MPa]	1200 ± 22 MPa	1222 ± 14 MPa	1203 ± 21 MPa
Elongation at break [%]	15.2 ± 1.7%	13.7 ± 0.6%	5.4 ± 2.4% *

and 1203 ± 21 MPa (High VED), respectively. However, the yield strengths and elongation at breaks varied significantly throughout the different parameter combinations. All samples broke in the top third of the specimen, which could be expected due to the reduced material hardness in this region. The specimens manufactured with the lowest VED possess an excellent ductility of around 15.2 ± 1.7% and a yield strength of 997 ± 62 MPa. A medium VED resulted in an average ductility of 13.7 ± 0.6% and a yield strength of 900 ± 55 MPa. The highest VED also resulted the highest yield strength of 1097 ± 61.6 MPa. However, no precise information about the ductility can be provided at this point as the specimens tore outside of the region of the extensometer. The obtained ductility falls in the range of 5.4 ± 2.4%, which falls below the ductility of hardened steels. One potential reason for the reduced ductility with increasing VEDs can be found in the gradual overheating of the structures and the corresponding pore formation in higher regions of the part (see Figure 8). This explains the ductile breaking of the samples for the low and medium VED which developed toward a brittle fracture for the high VED due to the increased porosity in the top regions. Furthermore, the different tensile behaviors could be explained by mechanisms like work hardening.[41] This effect could be promoted differently depending on the underlying microstructure. During load, the retained austenite might transform into other microstructural constituents that possess a higher strength. This work hardening could explain the difference between yield strength and tensile strength for the different VEDs. Materials with a higher retained austenite content might favor the deformation-induced transformation of the retained austenite into fresh martensite, which is characterized by a higher strength.[42] Furthermore, the fine distribution of the retained austenite in different shares might have beneficiary effects on the material properties like ductility. Higher austenite contents could help to explain the differences in ductility,[26] as observed in this work. However, additional work on this is required for better understanding the tensile properties. Future work will address important issues like dimple formation, which can tremendously affect the fracture behavior.[43] These investigations will focus on the most promising process parameters to analyze the influence of parameters like varying grain size and austenite contents, which can be achieved by a tailored heat treatment. By comparing quenched and tempered specimens with bainitized and as-built ones, the goal is to identify the influence of the microstructure on the underlying fracture mechanisms. Overall, the tensile properties of Bainidur AM exceed the ones of additively manufactured 16MnCr5[5] and are in the range of the quench and tempering steel 30CrNiMo8.[3] Even though all VEDs result in an inferior ultimate tensile strength compared to the results for 42CrMo4 shown by Damon et al.[44] and Shi et al.,[45] a significantly higher elongation at break can be observed when using either a low or medium VED.

5. Conclusion

This work presents investigations on the influence of the part height and the energy input on the material properties of additively manufactured Bainidur AM. Increasing the part height results in a continuous overheating of the specimen. This overheating again affects the transformation behavior of low-alloyed steels during PBF-LB/M. The main findings of our work are:

Increased part heights negatively affect porosity during build-up due to overheating, which is indicated by the increased weld penetration depth in higher part regions.

The process-intrinsic preheating results in a hardness decrease due to an incomplete transformation of the austenite during cooling for all VEDs. Higher retained austenite contents result in hardness drop-off by up to 25%.

Low VEDs result in a slow rise of the preheating temperatures of the additively manufactured specimens during build-up, leading to a mostly consistent hardness along the build direction with only a minor decrease in the average hardness.

High VEDs lead to a fast rise of the intrinsic preheating temperatures and thereby result in an altered microstructure associated with an increased retained austenite content and hardness drop-off.

Ultimate tensile strength is similar for all parameter combination. The main differences can be identified in the respective yield strength and ductility, which are affected by the applied VED and most likely the underlying fracture mechanisms.

Therefore, it is concluded that large specimens form their respective microstructure initially through a continuous transformation in the lower regions close to the substrate. In higher regions, the heat accumulation results in an elevated preheating. Consequently, the transformation behavior is affected, indicating that an isothermal transformation occurs in the upper regions of the specimens. Controlling the energy input during PBF-LB/M allows to manipulate this transformation behavior to generate parts with almost homogeneous material properties in the as-built state.

Appendix A

Figure A1 presents the expected surface temperatures. The VEDs used within this work were corrected since Mohr et al.[29] applied a layer thickness of 50 μm within their experiments. After correction, similar VEDs were obtained for the different parameters.

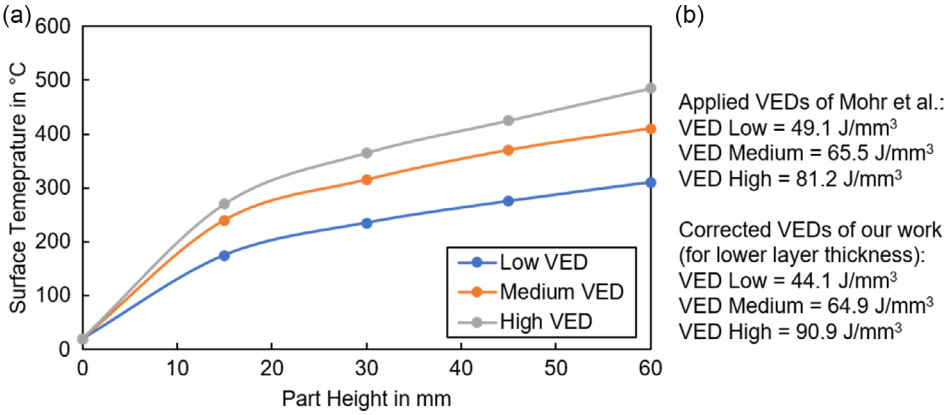

Figure A1. Estimated surface temperatures based on the findings by Mohr et al.[29] The VEDs applied within this work were corrected to a lower layer thickness (from 60 µm down to 50 µm) to match the formula.

Since a different material was used (316L), minor changes in the peak surface temperatures should be expected (e.g., due to altered heat conduction and energy absorption).

Received: January 2, 2023
Revised: September 7, 2023
Published online:

Acknowledgements

The authors want to thank the German Research Foundation (DFG) for Project-ID 61375930–SFB 814 – "Additive Manufacturing" TP A05. The authors gratefully acknowledge the support provided by the Erlangen Graduate School in Advanced Optical Technologies. The authors would also like to thank Schaeffler Technologies AG & Co. KG and Deutsche Edelstahlwerke Specialty Steel GmbH for their respective support within this work.

Open Access funding enabled and organized by Projekt DEAL.

Conflict of Interest

The authors declare no conflict of interest.

Author Contributions

D.B.: Conceptualization, methodology, validation, investigation, writing – original draft, visualization; T.N.: Investigation, data curation, writing – review and editing; M.A.: Investigation; A.M.: Conceptualization, resources, validation; H.H.: Validation, writing – review and editing; F.V.S.: Methodology, writing – review and editing, validation; C.M.: Supervision, writing – review and editing, resources, project administration; M.S.: Supervision, writing – review and editing, resources, project administration, fFunding acquisition.

Data Availability Statement

The data that support the findings of this study are available from the corresponding author upon reasonable request.

Keywords

additive manufacturing, Bainidur AM, laser-based powder bed fusion of metals, low-alloyed steel, material properties, microstructure formation

[1] C. Aumayr, J. Platl, H. Zunko, C. Turk, *Berg Huettenmaenn Monatsh* **2020**, *165*, 137.
[2] M. Schmitt, G. Schlick, C. Seidel, G. Reinhart, *Procedia CIRP* **2018**, *74*, 76.
[3] L. Zumofen, A. Kirchheim, H.-J. Dennig, *Prog. Addit. Manuf.* **2020**, *5*, 75.
[4] T. Kamps, *Leichtbau von Stirnzahnrädern aus Einsatzstahl mittels Laserstrahlschmelzen*, Universitätsbibliothek der TU München, München **2018**.
[5] M. Schmitt, T. Kamps, F. Siglmüller, J. Winkler, G. Schlick, C. Seidel, T. Tobie, K. Stahl, G. Reinhart, *Addit. Manuf.* **2020**, *35*, 101372.
[6] P. A. Hooper, *Addit. Manuf.* **2018**, *22*, 548.
[7] T. Amine, J. W. Newkirk, F. Liou, *Case Stud. Thermal Eng.* **2014**, *3*, 21.
[8] M. Schmitt, B. Kempter, S. Inayathulla, A. Gottwalt, M. Horn, M. Binder, J. Winkler, G. Schlick, T. Tobie, K. Stahl, G. Reinhart, *Procedia CIRP* **2020**, *93*, 581.
[9] Q. Wang, Z. Zhang, X. Tong, S. Dong, Z. Cui, X. Wang, L. Ren, *Opt. Laser Technol.* **2020**, *128*, 106262.
[10] M. Wei, S. Chen, L. Xi, J. Liang, C. Liu, *Opt. Laser Technol.* **2018**, *107*, 99.
[11] D. Bartels, T. Novotny, A. Mohr, F. van Soest, O. Hentschel, C. Merklein, M. Schmidt, *Materials* **2022**, *15*, 6171.
[12] D. Bartels, A. von Lattre-Hertel, T. Novotny, A. Mohr, H. Hill, C. Merklein, M. Schmidt, *Steel Res. Int.* **2023**, *94*, 2200925.
[13] H. Bhadeshia, R. Honeycombe, *Steels: Microstructure and Properties*, 4th ed., Elsevier Science and Technology Books, Inc, Oxford, UK **2017**.
[14] R. W. K. Honeycombe, R. F. Mehl, *Metall. Trans. A* **1976**, *7*, 915.
[15] M. Atkins, *Atlas of Continuous Cooling Transformation Diagrams for Vanadium Steels: A Collect. of 200 CCT Diagr. from 12 Countr. in Europe, North America and Asia*, Vanitec is the Vanadium International Technical Committee, Westerham, Kent **1985**.
[16] E. Pereloma, D. V. Edmonds (Eds.), *Phase Transformations in Steels*, Elsevier, Sawston, UK **2012**.
[17] American Society for Metals, *Atlas of Isothermal Transformation and Cooling Transformation Diagrams*, American Society for Metals, Detroit, MI **1977**.
[18] E. Pereloma, D. V. Edmonds, *Diffusionless Transformations, High Strength Steels, Modelling and Advanced Analytical Techniques*, Woodhead Pub Ltd, Sawston, UK **2012**.

[19] F. Huber, C. Bischof, O. Hentschel, J. Heberle, J. Zettl, K. Y. Nagulin, M. Schmidt, *Mater. Sci. Eng. A* **2019**, *742*, 109.
[20] S. Moritz, U. Ziesing, J. Boes, J. Lentz, S. Weber, M. Reuber, *Procedia CIRP* **2022**, *111*, 171.
[21] J. Jhabvala, E. Boillat, T. Antignac, R. Glardon, *Virtual Phys. Prototyp.* **2010**, *5*, 99.
[22] T. Craeghs, S. Clijsters, J.-P. Kruth, F. Bechmann, M.-C. Ebert, *Phys. Procedia* **2012**, *39*, 753.
[23] R. Mertens, B. Vrancken, N. Holmstock, Y. Kinds, J.-P. Kruth, J. van Humbeeck, *Phys. Procedia* **2016**, *83*, 882.
[24] J. Saewe, C. Gayer, A. Vogelpoth, J. H. Schleifenbaum, *Berg Huettenmaenn Monatsh* **2019**, *164*, 101.
[25] E. Paravicini Bagliani, M. J. Santofimia, L. Zhao, J. Sietsma, E. Anelli, *Mater. Sci. Eng. A* **2013**, *559*, 486.
[26] A. Kumar, V. K. Sharma, A. K. Sharma, S. K. Biswas, S. Kumar, K. Muraleedharan, *Mater. Res. Express* **2018**, *5*, 116503.
[27] G. Mohr, S. J. Altenburg, K. Hilgenberg, *Addit. Manuf.* **2020**, *32*, 101080.
[28] K. Ettaieb, K. Godineau, S. Lavernhe, C. Tournier, *Rapid Prototyp. J.* **2022**, *29*, 80.
[29] G. Mohr, K. Sommer, T. Knobloch, S. J. Altenburg, S. Recknagel, D. Bettge, K. Hilgenberg, *Metals* **2021**, *11*, 1063.
[30] R. J. Williams, A. Piglione, T. Rønneberg, C. Jones, M.-S. Pham, C. M. Davies, P. A. Hooper, *Addit. Manuf.* **2019**, *30*, 100880.
[31] M. Schmitt, F. Gerstl, M. Boesele, M. Horn, G. Schlick, J. Schilp, G. Reinhart, *Procedia CIRP* **2021**, *104*, 726.
[32] D. De-Castro, A. Eres-Castellanos, J. Vivas, F. G. Caballero, D. San-Martín, C. Capdevila, *Mater. Charact.* **2022**, *184*, 111703.
[33] A. Saha Podder, H. Bhadeshia, *Mater. Sci. Eng. A* **2010**, *527*, 2121.
[34] S. Shrestha, T. Starr, K. Chou, *J. Manuf. Sci. Eng.* **2019**, *141*, 071004.
[35] E. Weck, E. Leistner, *Farbätzmittel nach Beraha und ihre Abwandlungen*, Dt. Verl. für Schweißtechnik, Düsseldorf **1983**.
[36] S. Reisinger, G. Ressel, S. Eck, S. Marsoner, *Micron* **2017**, *99*, 67.
[37] W. Hearn, K. Lindgren, J. Persson, E. Hryha, *Materialia* **2022**, *23*, 101459.
[38] Y. Xia, G. Miyamoto, Z. G. Yang, C. Zhang, T. Furuhara, *Acta Mater.* **2015**, *91*, 10.
[39] V. Kotěšovec, I. Vorel, Š. Jeníček, J. Káňa, K. Ibrahim, *IOP Conf. Ser.: Mater. Sci. Eng.* **2017**, *179*, 12041.
[40] A. Graux, S. Cazottes, D. de Castro, D. San-Martín, C. Capdevila, J. M. Cabrera, S. Molas, S. Schreiber, D. Mirković, F. Danoix, D. Fabrègue, M. Perez, *Metals* **2020**, *10*, 824.
[41] P. Agrawal, S. Shukla, S. Thapliyal, P. Agrawal, S. S. Nene, R. S. Mishra, B. A. McWilliams, K. C. Cho, *Adv. Eng. Mater.* **2021**, *23*, 2000845.
[42] T. P. Zhou, C. Y. Wang, C. Wang, W. Q. Cao, Z. J. Chen, *Mater. Sci. Eng. A* **2020**, *798*, 140147.
[43] J. H. Kim, T. S. Byun, D. T. Hoelzer, *J. Nucl. Mater.* **2010**, *407*, 143.
[44] J. Damon, R. Koch, D. Kaiser, G. Graf, S. Dietrich, V. Schulze, *Addit. Manuf.* **2019**, *28*, 275.
[45] C. Shi, S. Dietrich, V. Schulze, *Int. J. Adv. Manuf. Technol.* **2022**, *121*, 1899.

Contribution to the Goal of this Work:

The influence of varying part heights and different energy inputs were analysed in this manuscript. For increasing part heights, a reduced material hardness is observed. The hardness reduction can be attributed to in-situ heat accumulation effects, which affect the underlying microstructure of the specimens. By adjusting the energy input, the degree of this heat accumulation can be tailored. Even though no temperature measurements were performed, this can be concluded based on the determined material hardness and temperature information obtained from literature [149]. Lower VEDs result in only minor hardness reductions along build direction while higher VEDs promote this hardness decrease. The material hardness further correlates with the retained austenite content, indicating that an incomplete transformation of the austenite upon cooling takes place. SEM images reveal altered microstructures in the different part regions along build direction. Lower regions are characterised by a lower bainitic microstructure in the fusion zone, as previously shown in 4.1. In higher regions, an increased share of degenerated and even granular bainite was determined. These microstructural constituents usually form in isothermal heat treatments and require high part temperatures that exceed 400 °C. This work reveals that the thermal history plays an important role in the microstructure formation in case-hardening steels, thus contributing to RQ2. Manufacturing a part with a high VED leads to areas that are characterised by low (7 %), high (20 %), and again low (7 %) retained austenite contents. The retained austenite contents mirrors the regions in which the microstructure is formed predominantly through (1) continuous cooling, (2) incomplete isothermal holding, and (3) isothermal transformation. Reducing the VED shows that the onset points for these regions can be moved towards higher part regions, thus postponing the onset of the isothermal transformation.

This transition from a continuous towards an isothermal transformation in continuous build-up processes complicates the generation of parts with homogeneous material properties. Correspondingly, the next step will focus on adequate countering strategies to avoid these varying material properties. Two potential approaches could be followed: On the one hand, a heating unit could be used that allows to surpass the bainite finish temperature. This platform heating would allow to achieve a homogeneous isothermal transformation. Since a high-temperature heating unit was not available, strategies for avoiding the undesired heat accumulation are followed. These strategies include even lower VEDs and the introduction of additional inter-layer times.

5.2 Approaches for Homogenising the Material Properties of Case-hardening Steels in PBF-LB/M

Title: On the Influence of Volumetric Energy Density and Inter-Layer Time on the Material Properties of Case-Hardening Steels [P12]

Journal: Alloys, MDPI

DOI to Web-version: https://doi.org/10.3390/alloys2030013

Authors: Dominic Bartels, Moritz Elias Albert, Florian Nahr, Michael Schmidt

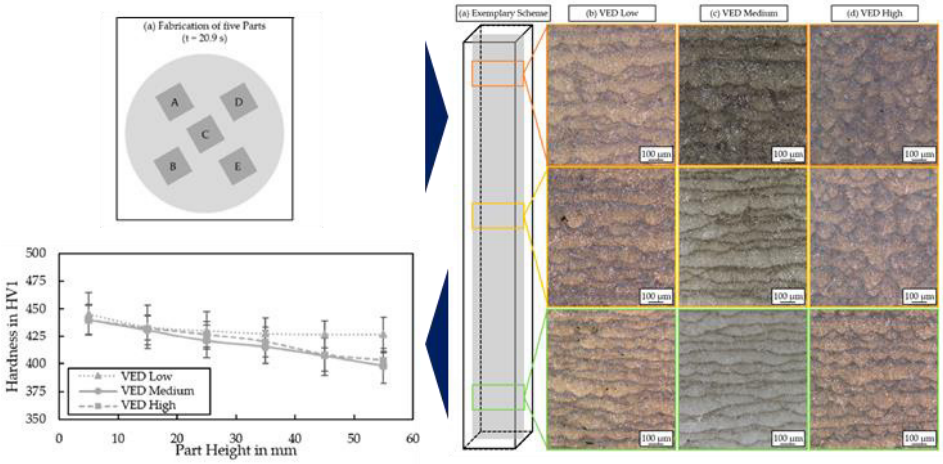

Motivation and Key Findings:

It was shown in the previous study that the microstructure formation for larger parts is significantly affected by the applied energy input. The resulting part properties are therefore inhomogeneous along build direction, which hinders the direct use of these parts from the as-built state. This work presents different countering strategies to meet this process-induced overheating with the goal of achieving homogeneous properties along build direction. The **highlights** are:

- Further reducing the energy input promotes less heat accumulation and almost homogeneous hardness
- The introduction of inter-layer times is a feasible approach for higher energy inputs to achieve a homogeneous hardness
- Homogeneous part properties can be achieved by reducing the energy input during build-up, promoting a continuous microstructure formation

alloys

MDPI

Article

On the Influence of Volumetric Energy Density and Inter-Layer Time on the Material Properties of Case-Hardening Steels

Dominic Bartels [1,2,*], Moritz Elias Albert [1], Florian Nahr [1,2] and Michael Schmidt [1,2]

[1] Institute of Photonic Technologies (LPT), Friedrich-Alexander-Universität Erlangen-Nürnberg (FAU), Konrad-Zuse-Straße 3/5, 91052 Erlangen, Germany
[2] Erlangen Graduate School in Advanced Optical Technologies (SAOT), Friedrich-Alexander-Universität Erlangen-Nürnberg (FAU), Paul-Gordan-Straße 6, 91052 Erlangen, Germany
* Correspondence: dominic.bartels@lpt.uni-erlangen.de; Tel.: +49-09131-85-64101

Abstract: Case-hardening steels are gaining increasing interest in the field of laser powder bed fusion (PBF-LB/M) due to their excellent weldability. In combination with post-process carburization heat treatment, the surface properties can be improved to generate high-strength products. When manufacturing larger products by means of PBF-LB/M, the in situ heat accumulation and the altered cooling rates affect the resulting material properties. Therefore, the fabrication of larger products requires an understanding on the influencing factors that affect the material properties. This work investigates the effect of different volumetric energy densities (VED) on the resulting microstructural and mechanical properties. It is found that the hardness decreases continuously along the build direction. The gradient depends on the applied energy and is stronger for higher energy inputs due to heat accumulation and lowered cooling rates. Furthermore, countering strategies are investigated to avoid process-specific hardness reduction along the build direction. This includes a reduced number of parts within the build job as well as a modified inter-layer time (ILT) between consecutive layers of the specimen. Applying a moderate inter-layer time helps to counter process-specific overheating, which is indicated by an almost homogeneous material hardness and melt pool size along the build direction.

Keywords: PBF-LB/M; additive manufacturing; case-hardening steels; Bainidur AM; inter-layer time; microstructure formation; hardness; part height

Citation: Bartels, D.; Albert, M.E.; Nahr, F.; Schmidt, M. On the Influence of Volumetric Energy Density and Inter-Layer Time on the Material Properties of Case-Hardening Steels. *Alloys* **2023**, *2*, 168–183. https://doi.org/10.3390/alloys2030013

Academic Editor: Giovanni Meneghetti

Received: 19 June 2023
Revised: 11 August 2023
Accepted: 23 August 2023
Published: 25 August 2023

1. Introduction

Case-hardening steels like 16MnCr5 and 20MnCr5 are used for a variety of different applications due to their beneficiary material properties. Their good ductility facilitates the processing using shaping technologies, while their excellent carbon diffusivity supports the local hardening of the material for later use [1]. Typical products are shafts, gearings, or bearing applications. By exposing these specimens to a carbon- or nitrogen-rich atmosphere at elevated temperatures, these elements diffuse into the case of the material and improve the hardenability of the material [2]. The resulting microstructure (e.g., martensite or iron nitrides) leads to a high surface hardness, which is required for the aforementioned applications [3]. When aiming at optimizing these products or at expanding the application portfolio of this class of materials even further, conventionally established processes like forming reach their limitations [4]. Additive manufacturing processes like laser powder bed fusion of metals (PBF-LB/M), however, enable the generation of highly complex structures with bionic [5] or load-adapted geometries [6]. This high freedom of design facilitates the integration of, e.g., complex cooling/tempering and lightweight structures to improve performance and longevity of the final product [7].

Reviewing the literature reveals that these low-alloyed steels like 16MnCr5 [8] and 20MnCr5 [9] have recently been processed with great success. The works by Schmitt

et al. [10,11] show that this class of material can be processed without larger defects. Further investigations focused on the case-hardenability of additively manufactured case-hardening steels [12,13]. Comparable hardness values could be obtained after hardening even though the process-specific fine microstructure might negatively affect the carbon diffusion. Furthermore, the first approaches in the field of in situ alloying were carried out for the low-alloyed steel 16MnCr5 with the goal of substituting these energy-intensive carburizing processes [14,15]. When aiming at avoiding these processes, e.g., via the application of in situ alloying approaches, a profound understanding on the microstructure formation in the as-built state is necessary. The first investigations by Schmitt et al. [11] and Aumayr et al. [13] state that a bainitic–martensitic microstructure is achieved when processing low-alloyed steels by means of PBF-LB/M. The material properties were thereby concluded based on the underlying hardness, which is typically lower than the one of martensite but higher than the one of lower-strength microstructure constituents like ferrite. In-depth investigations by Bartels et al. [16] using a different case-hardening steel show that a predominantly bainite-like microstructure is achieved when processing low-alloyed steels by means of PBF-LB/M.

However, for completely exploiting the potential of the PBF-LB/M process, manufacturing strategies are required that facilitate the defect-free fabrication of structures that are larger than that of the typically investigated small cubic specimens with an edge length of 10 mm [16] or even only 6 mm [17]. One major issue is the formation of defects along the build direction. PBF-LB/M parts are typically characterized by several defects like (micro-)crack formation, lack-of-fusion, and gas porosity defects [18]. Whereas cracks typically do not occur for low-carbon materials like case-hardening steels, lack-of-fusion defects can be avoided by selecting a sufficiently high energy for melting the powder [19,20]. In doing so, the formation of pores, which is typically the consequence of an excessive energy input during PBF-LB/M [21,22], needs to be avoided.

Mohr et al. [23,24] have found that the layer-by-layer approach in PBF-LB/M can result in an excessive heat accumulation along the build direction. This heat accumulation acts as in situ platform preheating and lowers the required energy input for melting the material. Due to the consequently reduced energy delta required for melting the material in higher layers, an increased porosity can be observed along the build height in PBF-LB/M. High volumetric energy densities (VEDs) result in high penetration depths of the melt pool into the underlying material. In contrast, lower VEDs reduce the penetration depth since the overall energy input is reduced. Similar observations were made by Keshavarzkermani et al. [25]. These altered melt pool geometries again affect the thermal gradients during PBF-LB/M. Smaller melt pools are characterized by a faster cooling [26]. Larger melt pools, in contrast, result in a slower cooling of the structure. Thus, the corresponding hardness will be lower for higher VEDs since hardness-beneficiary effects like fine-grain hardening are not as pronounced as for lower VEDs [27]. The first investigations by Schmitt et al. [11] have shown that when fabricating larger specimens, the altered cooling gradients and in situ heat treatments during PBF-LB/M result in a reduced hardness along the build direction. Similar effects can be observed for other materials like AlSi10Mg [28] and 316L [23].

Another decisive factor for influencing this overheating is the time that lies between the manufacturing of two consecutive layers. This time is often referred to as idle time [29] or inter-layer time [30]. Keeping this time at minimum results in the largest penetration depths of the single weld tracks [23]. When increasing the inter-layer time, the penetration depth of the weld track is reduced since the specimen gains more time to dissipate the excessive heat through heat flux. Furthermore, Mohr et al. [23] found that the ratio of area exploitation (which will here be referred to as the number of parts) plays a significant role when designing a build job. This is mainly caused by the fact that the number of parts affects the inter-layer time since less parts require a shorter illumination. Thus, the inter-layer time and the corresponding cooling time is reduced between two layers.

In this work, the influence of different process conditions on the material properties of case-hardening steels are investigated to facilitate the fabrication of larger parts with

specific material properties. Since the resulting material properties depend strongly on the design of the build job, two main influencing factors were manipulated. On the one hand, the applied energy for manufacturing the specimens was altered. The aim is to study how different VEDs affect the resulting material properties. On the other hand, the process-specific boundary conditions like the number of parts and the inter-layer time are varied to investigate how adjusted inter-layer times affect the microstructure and hardness. The overarching goal of this work is to derive processing strategies that help to avoid an overheating of the specimens and that support homogeneous material properties. This goal is divided into the following two sub-goals:

1. How does the VED affect the properties, primarily the hardness, of the material for large part heights?
2. Which countering strategies are promising to counter inhomogeneous material properties, primarily the hardness, along the build direction?

2. Materials and Methods

The nitrogen-gas-atomized low-alloyed steel Bainidur AM (Deutsche Edelstahlwerke Speciality Steel GmbH, Krefeld, Germany) was used for performing the experiments. A particle size distribution of 15 to 45 µm was selected for the PBF-LB/M process. The used powder material was mainly spherical. Figure 1 shows the particle shape and the experimentally determined particle size distribution using a CamSizer (Microtrac Retsch GmbH, Haan, Germany).

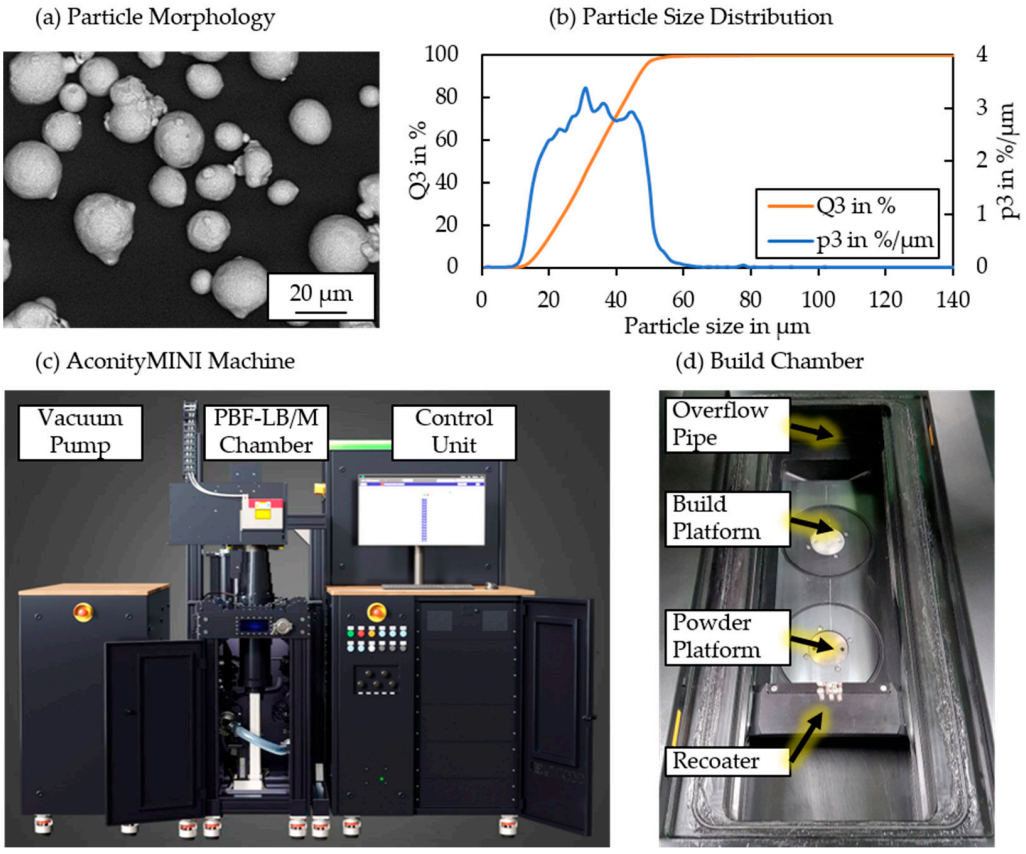

Figure 1. (**a**) Morphology of the Bainidur AM particles, (**b**) its particle size distribution, (**c**) the AconityMINI machine used for the experiments, and (**d**) the build chamber with the reduced build envelope.

The powder was dried in a vacuum furnace at 120 °C for twelve hours prior to processing. All experiments were performed on a commercially available PBF-LB/M

machine of type AconityMINI (Aconity 3D, Herzogenrath, Germany). The machine was operated with a reduced build envelope that allows smaller amounts of powder to be processed (see Figure 1d). A 1 kW SPI redPower QUBE single-mode fiber laser emitting at a wavelength of 1080 nm was used for the investigations (Southampton, UK). The scanner used was an AxialScan-30 from Raylase GmbH (Wessling, Germany). As substrate, the low-alloyed steel 16MnCr5 (Abrams Stahl, Osnabrück, Germany) was used. Circular blanks with a diameter of 55 mm were laser-cut using a CO_2 laser. The thickness of these plates was 6.3 mm. Table 1 shows the chemical composition of the Bainidur AM powder material.

Table 1. Elemental composition of the Bainidur AM powder material according to the supplier's certificate.

Element Concentration in wt.-%									
C	Si	Mn	P	S	Cr	Mo	Ni	V	Fe
0.22	0.7	1.2	<0.02	<0.02	1.0	0.9	<0.3	<0.15	Bal.

2.1. Sample Fabrication

Different build jobs were designed to investigate the influence of different PBF-LB/M-specific conditions. Thereby, reference investigations were performed using three different VEDs. Five parts were manufactured per build job for these initial investigations. Building on these findings, the number of parts as well as the average time per layer were modified. The methodological approach is presented in Figure 2. The fundamental design of the build job and the part geometry were maintained constant throughout all experiments. Edge length in x- and y-direction was set to 10 mm each, while the part height (z-direction) was set to 60 mm. Layer thickness and laser spot size were kept constant at 60 µm and 105 µm, respectively.

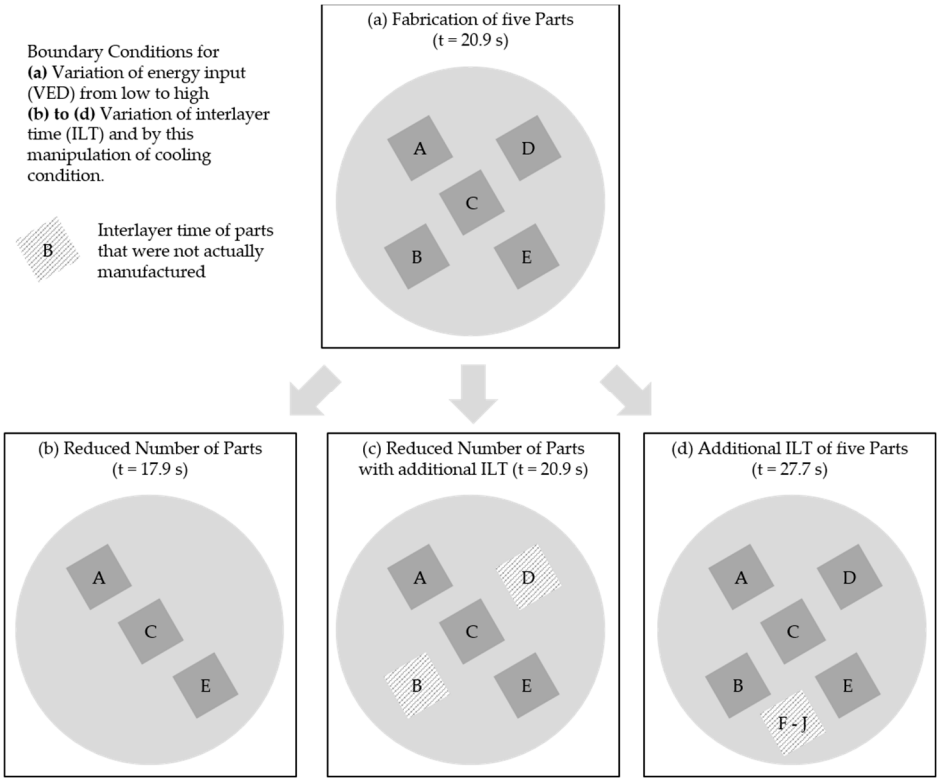

Figure 2. Methodological approach for the investigations within this work.

The scanning orientation was rotated by 67° after every layer. Laser power and scanning speed for manufacturing the contour were set to 325 W and 450 mm/s, respectively.

No preheating was applied throughout the experiments. In the first step (see Figure 2a), three different volumetric energy densities (VEDs) were studied. Laser spot size was set to 105 µm. The applied process parameters are presented in Table 2. These parameters are oriented at a previous study for the material Bainidur AM [16].

Table 2. Process parameters selected for the fabrication of the specimens.

Parameter	VED Low	VED Medium	VED High
Laser Power [W]	175 W	200 W	250 W
Scanning Speed [mm/s]	950 mm/s	850 mm/s	700 mm/s
Hatch Distance [µm]	120 µm	120 µm	110 µm
Avg. Time per Layer [s]	19.6 s	20.2 s	20.9 s
VED [J/mm^3]	25.6 J/mm^3	32.7 J/mm^3	54.1 J/mm^3

The aim of a decreased VED is to avoid the process-specific overheating, which was already described by Mohr et al. [24]. Correlated with modified VEDs, especially when adjusting hatch spacing or scanning speed, the average time required for manufacturing one layer decreased (see Table 2). This time per layer was averaged over several consecutive layers (>20 layers).

The following investigations regarding the influence of different boundary conditions (Figure 2b–d) were performed using the parameter set VED High. This process parameter was chosen since VED High resulted in the most noticeable hardness gradient along the build direction while still possessing a good relative part density.

In the next step, the number of parts per build job was reduced from five to three specimens (RNP, see Figure 2b). Reducing the number of parts results in a decreased average layer time (from 20.9 s to 17.9 s). Correspondingly, the time for cooling the additively manufactured structures is reduced compared to when five samples are fabricated within one build job. Furthermore, the overall energy input into the substrate during PBF-LB/M is reduced, which could affect overheating effects in the early stages of the process.

Further investigations were performed by building the reduced number of parts (three specimens) with an additional inter-layer time (RNP + ILT, 1.4 s per specimen; in total, 2.8 s). The aim was to add this inter-layer time to make up for the time that is missing when two specimens are removed (see Figure 2c). In combination with the studies using the reference parameter set (Figure 2a) and the reduced number of parts (Figure 2b), this allows the assessment of whether the time per layer or the number of parts is more decisive regarding overheating.

In the final step, a build job with five specimens and an additional inter-layer time, which was equal to five more parts, was designed (see Figure 2d). The average time per layer correspondingly increased from 20.9 s to 27.7 s. After fabrication, all specimens were analyzed regarding their micro- and macroscopic materials. This includes investigations on the relative part density, microstructure formation, and the associated material hardness.

2.2. Sample Preparation

Figure 3 presents the approach for sample preparation. The as-built samples were cold-embedded using an epoxy resin. After solidification of the resin, the specimens were grinded until the center region was reached before polishing the surface down to one µm (exemplary shown in Figure 3b). Next, optical light microscopy was used to analyze the specimens regarding internal defects like pores, lack of fusion, or cracks. A Zeiss microscope was used for generating the images. These images were binarized for determining the residual porosity. After that, the specimen was grinded and polished again to reveal porosity and internal defects in a different position within the specimen. This procedure was repeated three times per sample. Furthermore, the hardness was determined on the polished cross-sections using an indentation tester of type KB30S (Hegewald & Peschke, Nossen, Germany). Since the part height can significantly affect the material properties, the

relative part density and hardness were measured in different regions of the specimen. The relative part density was determined in different regions of the specimen (Figure 3c).

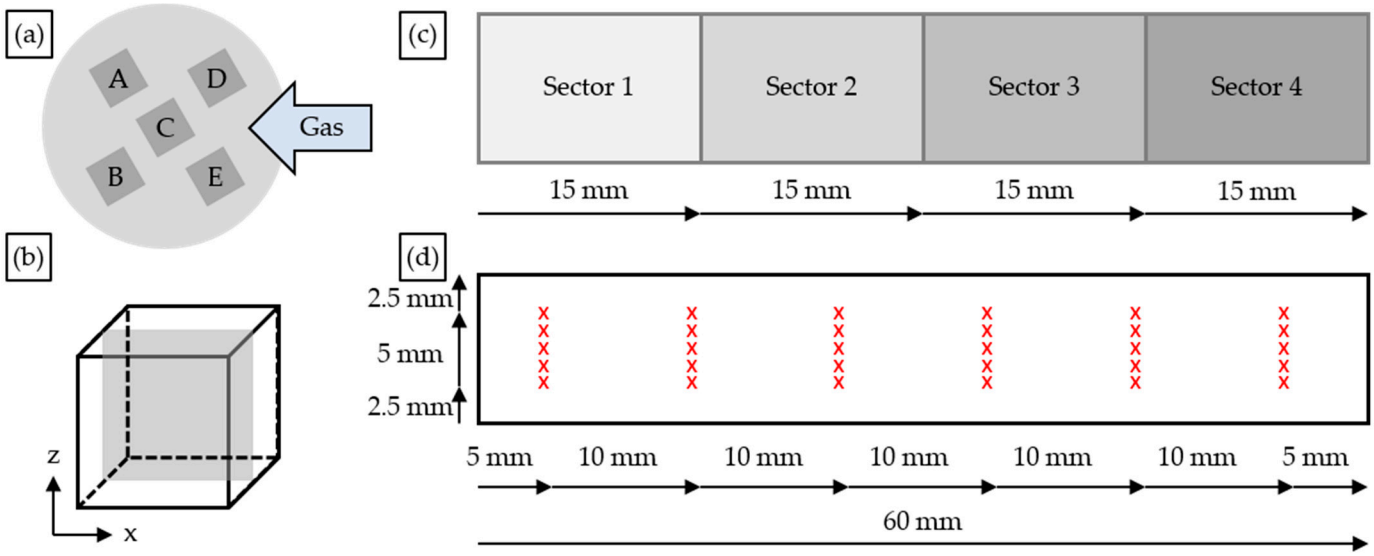

Figure 3. (**a**) Build job design, (**b**) sample preparation, (**c**) regions for determining the relative part density, and (**d**) scheme for hardness measurements.

The material hardness was determined at specific positions within the specimens (see Figure 3d). Six measurement rows were defined: one in the bottom (after 5 mm), lower half (after 15 mm), middle (after 25 and 35 mm), upper half (after 45 mm) and top (after 55 mm). Six indentations were made per measurement row to determine the hardness. Since specimen D always possessed a high porosity (possibly due to the inert gas flow, indicated in Figure 3a), this sample was spared from the investigations.

After the hardness measurements were performed, the specimens were etched using a 3% Nital etching solution. The microstructure was again analyzed using optical light microscopy. Since the specimens were not polished prior to this etching procedure, the microstructure could be investigated specifically in the regions where the hardness measurements were performed earlier.

3. Results

This section is divided into three sub-sections. In the first step, the relative part density for the different processing strategies is analyzed. The second subsection focusses on the influence on the resulting mechanical material properties. In the third subsection, the underlying microstructure is studied and correlated with the applied processing strategies.

3.1. Relative Part Density

In the first step, the relative part density was assessed for the different VEDs. The part density was determined on longitudinal cross-sections along the build direction. Four specimens were analyzed per build job since one specimen was highly affected by the part positioning on the substrate (specimen D). Figure 4 presents the results on the cross-sections for the different VEDs. Three different regions were thereby selected according to the scheme in Figure 4a. All parameter combinations facilitate the fabrication of almost fully dense specimens. The relative part density exceeds 99.7% in all investigated regions of the specimens. For the parameter combination VED Low, a fine porosity can be identified in the bottom region of the specimen. This potentially could be lack-of-fusion porosity due to an insufficient energy input. With an increasing part height, these defects reduce, which manifests this assumption.

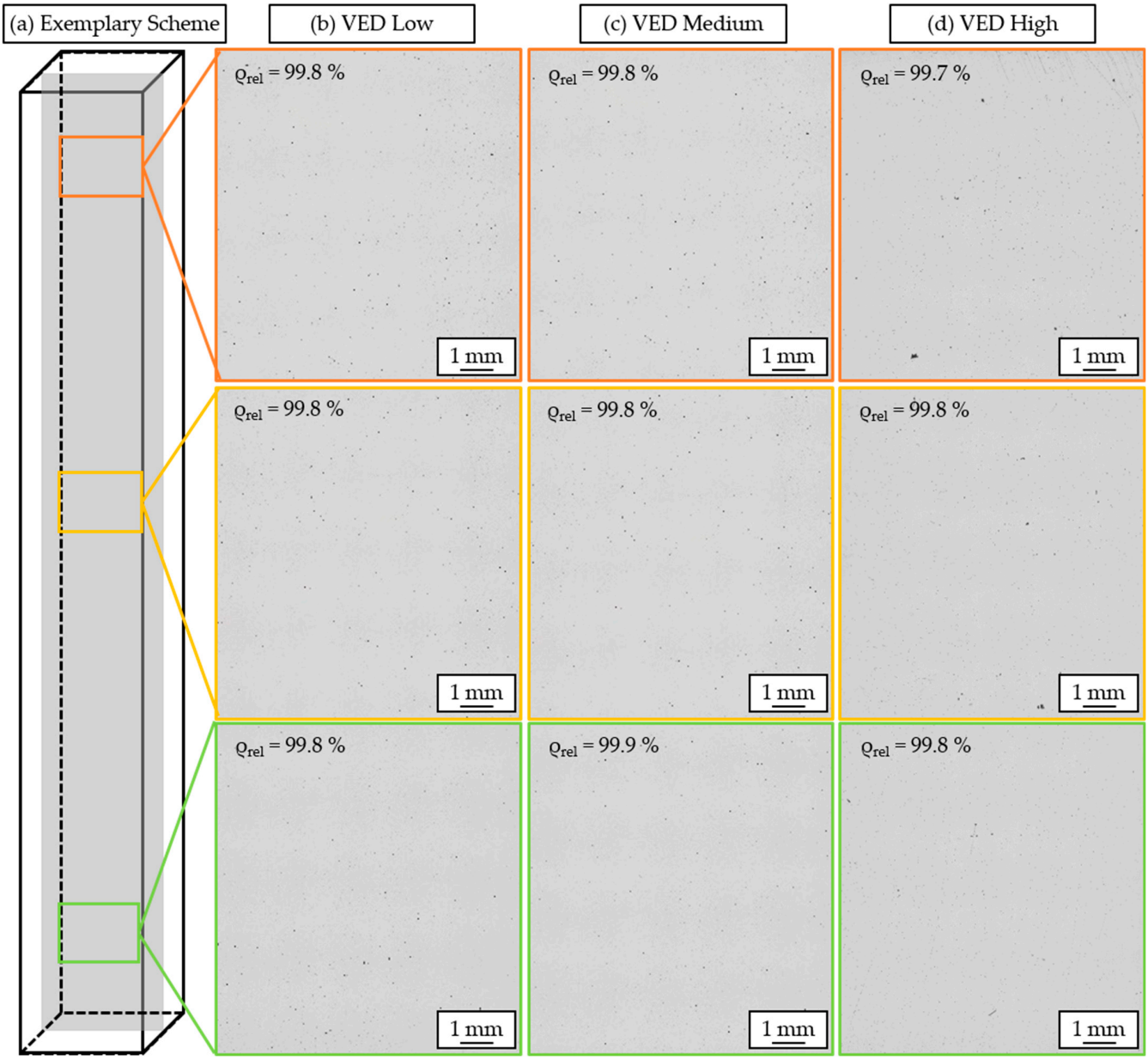

Figure 4. Cross-sections of the specimens manufactured with the different VEDs. The images were extracted from three different regions along build direction.

Both VED Medium and VED High also result in a homogeneous relative part density along the build direction. For VED High, a slightly lower relative part density can be observed, which could again be attributed to a partial overheating of the specimen, especially in the higher regions of the sample. Overall, all parameter combinations are characterized by a good part density that exceeds 99.7% in all regions.

Next, the influence of different countering strategies like inter-layer times, and number of parts on the relative part density was studied. The parameter set VED High was chosen for these investigations. Figure 5 shows the cross-sections of the specimens manufactured using the different countering strategies. Reducing the overall number of parts in one build job without adjusting the inter-layer time (RNP, Figure 5a) promotes porosity formation along the build direction. Thereby, mainly spherical pores can be observed. The shape indicated that the pores might be the consequence of keyholing mechanisms during PBF-LB/M, which can result in gas entrapment when the keyhole collapses [21]. However,

additional investigations on this topic are required to exclude other mechanisms for the formation of these defects.

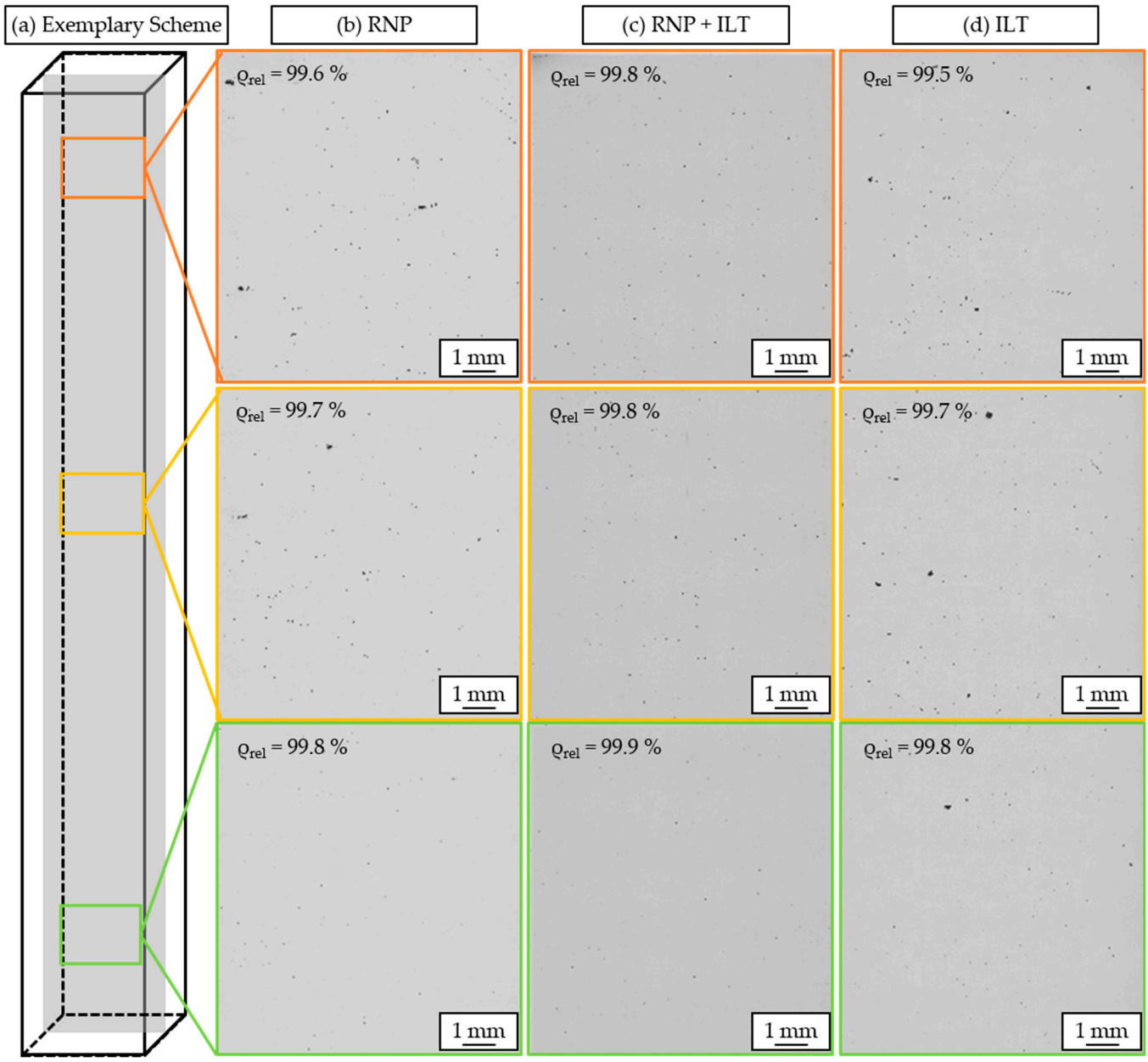

Figure 5. Cross-sections of the specimens manufactured with different countering strategies to avoid the intrinsic overheating. The specimens were extracted from three different regions along the build direction.

When adding an additional inter-layer time equivalent to the time required for manufacturing two specimens (RNP + ILT, Figure 5c), an almost homogeneous porosity along the build direction can be achieved. The porosity is lower compared to both the specimens manufactured with VED High (Figure 5d) as well as the ones with fewer samples (Figure 5a). However, further increasing the inter-layer time to the equivalent of five specimens (Figure 5d, ILT) reduces the relative part density significantly. The defects are shaped asymmetrically, indicating lack-of-fusion defects. Thereby, the inter-layer time was too long to facilitate defect-free fabrication. Comparing the different processing strategies, it is recommended to use as little energy as possible when aiming at fabricating nearly fully dense specimens. To avoid undesired gas porosity defects, the applied VED should be kept

as low as possible. Otherwise, overheating effects might negatively affect the porosity with increasing part size. The inter-layer time should further be selected to avoid an excessive cooling of the structure. Increasing the average time per layer by approximately 20% has proven suitable to avoid negative effects on the relative part density.

3.2. Microhardness along Build Direction

Since all specimens possess a sufficient relative part density exceeding 99.5%, no negative influence of minor defects like pores or cracks on the resulting hardness is assumed. The hardness was determined in different regions within the samples to assess the impact of the part height on the material properties. Figure 6 shows the hardness propagation for different (a) VEDs and (b) boundary conditions.

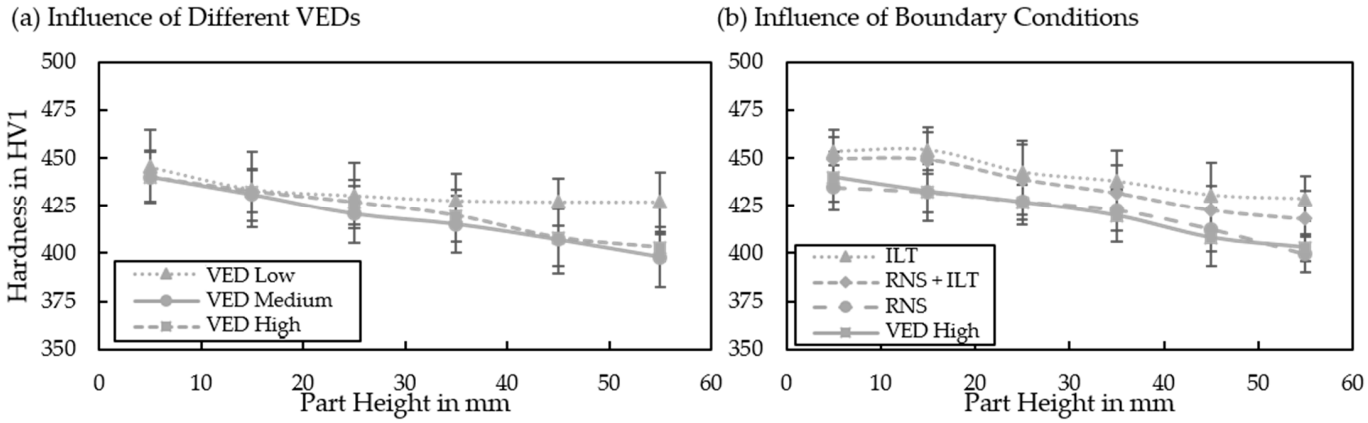

Figure 6. Material hardness of the specimens manufactured with (**a**) different VEDs and (**b**) different countering strategies.

For all parameter combinations, the highest hardness was observed in the bottom region of the layer. VED Low, VED Medium, and VED High (see Figure 6a) all possess a similar hardness after a build height of approximately 5 mm. After that, the hardness decreased for all specimens, independently of the applied volumetric energy density. For VED Low, only a minor decrease in the material hardness was detected. The initial hardness of 446 ± 19 HV1 falls to 427 ± 16 HV1 in the top region after manufacturing approximately 55 mm. Applying VED Medium and VED High, a stronger drop-off in hardness is detectable. While the hardness in the bottom region is comparable (440 ± 14 HV1 for VED Medium, 440 ± 13 HV1 for VED High), a similar trend for the hardness fall-off is evident. The hardness in the highest regions of the specimens falls to 398 ± 16 HV1 (VED Medium) and 403 ± 7 HV1 (VED High). This hardness exceeds the one of additively manufactured specimens from Bainidur AM obtained in a previous work by Bartels et al. [16]. The hardness in the bottom regions is somewhere in the middle between the hardness of the as-built (around 405 HV1) and hardened (around 460 HV1) specimens. However, since lower VEDs were applied in this work, a promoted fine-grain hardening can be assumed as one reason for the increased hardness [31]. Another potential explanation might be that powder-aging effects favored oxidation of the material. The oxidized particles would then reinforce the matrix, which could help in explaining the slightly higher hardness in the as-built state [32]. They could also affect the weldability since higher energies are required for a sufficient melting of the material. This could explain the partially increased porosity. Furthermore, the thermal cycle during PBF-LB/M associated with heat accumulation could promote secondary hardening mechanisms like carbide precipitation during the manufacturing process [33].

Figure 6b shows the material hardness for the different countering strategies to reduce the process-intrinsic overheating. The lowest hardness is observed for the specimens manufactured with the reduced number of samples (RNS). Here, the shorter inter-layer time (17.9 s) favors an overheating of the structure. The increased preheating temperatures of

the specimens during cooling then result in a reduced cooling rate. Thus, the maximum material hardness decreases since beneficiary effects like fine-grain-hardening are attenuated. The second lowest hardness is observed when fabricating five specimens (VED High). Even though more specimens were manufactured, a similar trend can be identified. Adding an inter-layer time that is equivalent to two specimens (RNS + ILT) results in a higher average hardness along the build direction. The slightly promoted cooling of the entire build job due to heat flux is thereby almost sufficient to counter the process-intrinsic overheating. When manufacturing five specimens with an additional inter-layer time equivalent to five specimens (ILT), a further increase in the hardness is observed. Apart from the bottom region, a homogeneous hardness can be observed along the z-direction. This shows the power of both processing strategies when aiming at optimizing the material properties for larger parts.

The decreasing material hardness with increasing part height can be explained by the heat accumulation during the layer-by-layer manufacturing process. Consequently, the energy delta required for melting the powder material is reduced. Since the applied VED remains the same throughout the manufacturing process, the average melt pool depth and size will most likely increase along the build direction. This increase in the melt pool size is strongly correlated with the material hardness and can be attributed to at least two effects. First, larger melt pools result in lower cooling rates since the molten volume is larger [34,35]. Thus, the beneficiary effect of fine-grain hardening is mitigated in the top regions for larger parts. Secondly, the process-induced overheating affects the transformation of the phases during cooling. High-strength phases like martensite are formed at high cooling rates. These cooling rates are typically present in laser-based processes. However, elevated temperatures might suppress a complete transformation into the martensite or result in a tempering of the martensitic structure. Correspondingly, the strength of the final part reduces. To validate whether the heat accumulation is mirrored in the weld tracks that form the final specimen, the cross-sections were etched and analyzed using optical light microscopy.

3.3. Microstructure Formation

Similarly to the relative part density, the development of the microstructure was analyzed for the different process conditions. Thereby, a distinction into overview images of several weld tracks and magnifications of a region that only consists of few single tracks was made. Figure 7 shows optical overview images of the etched cross-sections for the three different VEDs. These cross-sections were analyzed in three different regions of the specimen, as indicated in Figure 7a. For the lowest VED, lack-of-fusion pores can be identified within the bottom region of the specimen. These defects are characterized by their aspheric shape and can be predominantly found at the lower boundaries of the weld tracks within the additively manufactured structure. Their presence reduces with an increasing part height. Here, an influence of the heat accumulation along the build direction is assumed. This correlates with the weld track geometry, which is also affected by the applied VEDs. In the bottom region, the entire weld tracks appears like a longish block. Moving towards higher regions, the typical lenticular shape of the weld tracks starts to form. The increased penetration depth is associated with a reduced material hardness, as shown in Figure 6a. This supports the assumption that the reduced hardness is caused by the heat accumulation and the lower cooling rates along the build direction during PBF-LB/M. Furthermore, the weld track boundaries possess a blueish color. This can be an indicator for ferrite, which correlates with previous findings that were obtained for the case-hardening steel Bainidur AM [16].

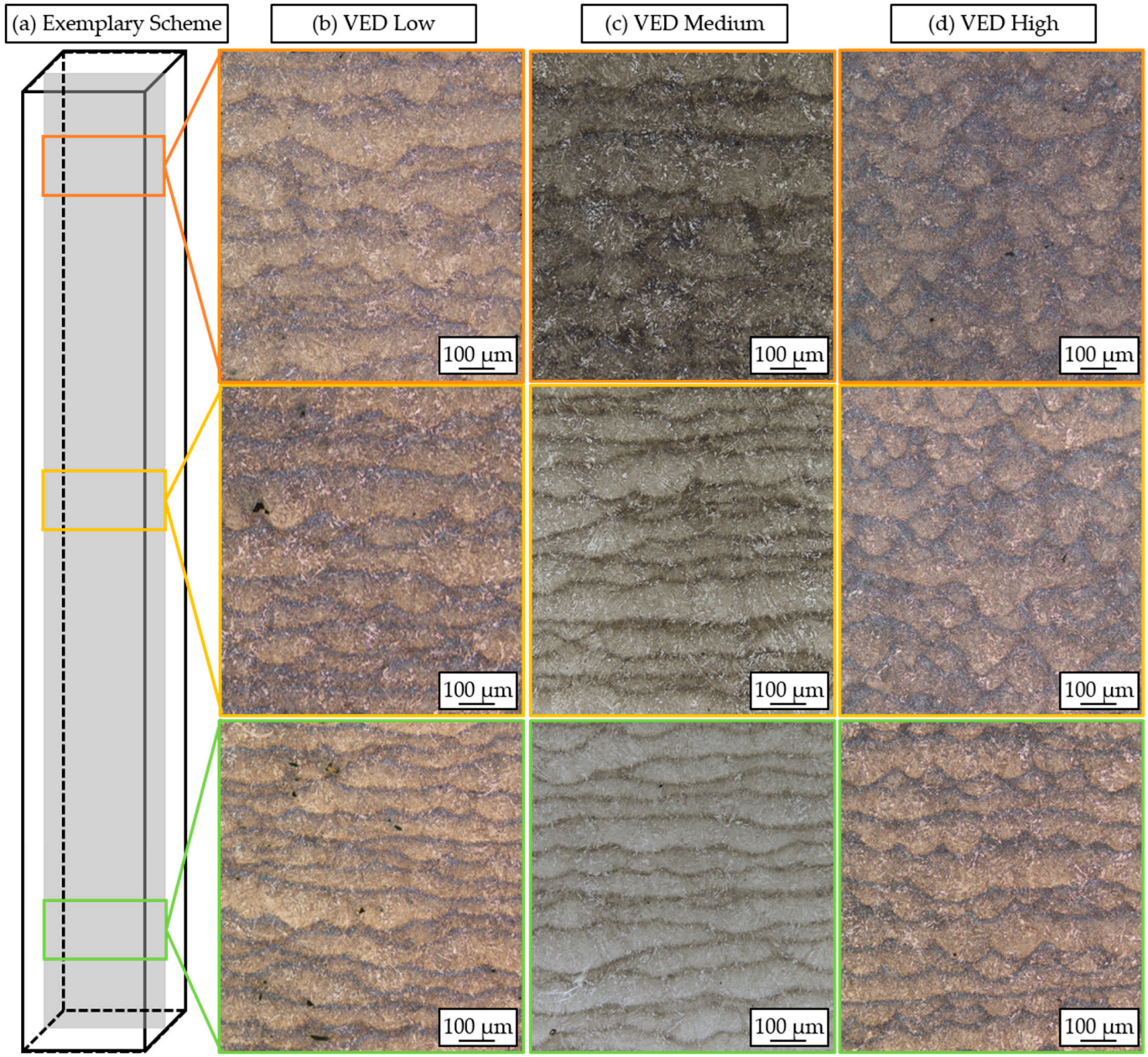

Figure 7. Etched cross-sections of the specimens manufactured with different VEDs.

Increasing the VED results in a larger penetration depth into the lower layers of the weld track already in the bottom regions. As for VED Low, this effect is further promoted when moving towards higher regions within the specimen. Here, the weld track depth increases with increasing part height. The heat accumulation during PBF results in an in situ preheating. These elevated temperatures result in larger melt pools, as can be seen for the different VEDs. Since this effect is thermally driven, the influence of the different PBF-LB/M-specific boundary conditions on the formation of the weld tracks was studied. Figure 8 presents the cross-section of the specimens RNP, RNP + ILT, and ILT.

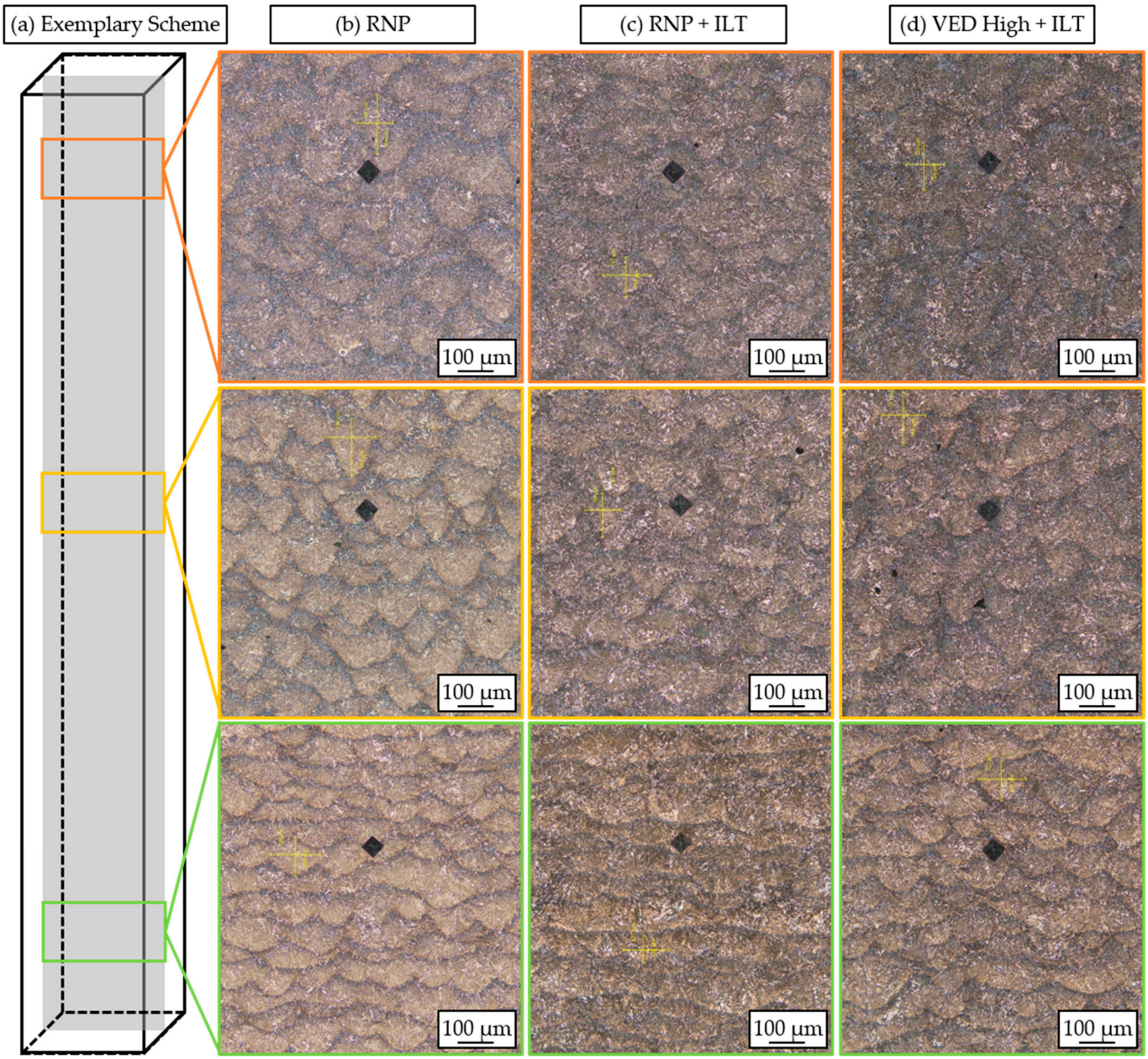

Figure 8. Etched cross-sections of the specimens manufactured with different countering strategies.

Reducing the number of parts (Figure 8b) results in a larger penetration depth in the bottom region compared to the specimens that were manufactured in a build job with more parts (Figure 7d). As for the different VEDs, it can be seen that the weld track geometry is altered when moving towards higher regions within the specimen. This effect is observed independent of the applied countering strategy.

This effect is damped when adding an additional inter-layer time while still manufacturing the same amount of parts (Figure 8c). The added time (2.8 s) provides more time for the heat to dissipate. Even though this time is very short, a difference in the penetration depth of the weld tracks can be observed. Consequently, the average size of the weld tracks reduces. This effect is also seen when manufacturing five samples with an additional inter-layer time that is equal to five specimens. However, this inter-layer time appears too high, as increased defect formation can be determined for this parameter set. It is therefore recommended to avoid excessive inter-layer times when lower energy inputs, which might only be just sufficient for melting the powder material, are chosen. To better

assess the microstructure, even larger magnifications of the underlying weld tracks and their corresponding microstructures were generated. Figure 9 shows the microstructure of the specimens manufactured with VED High and the three different countering strategies.

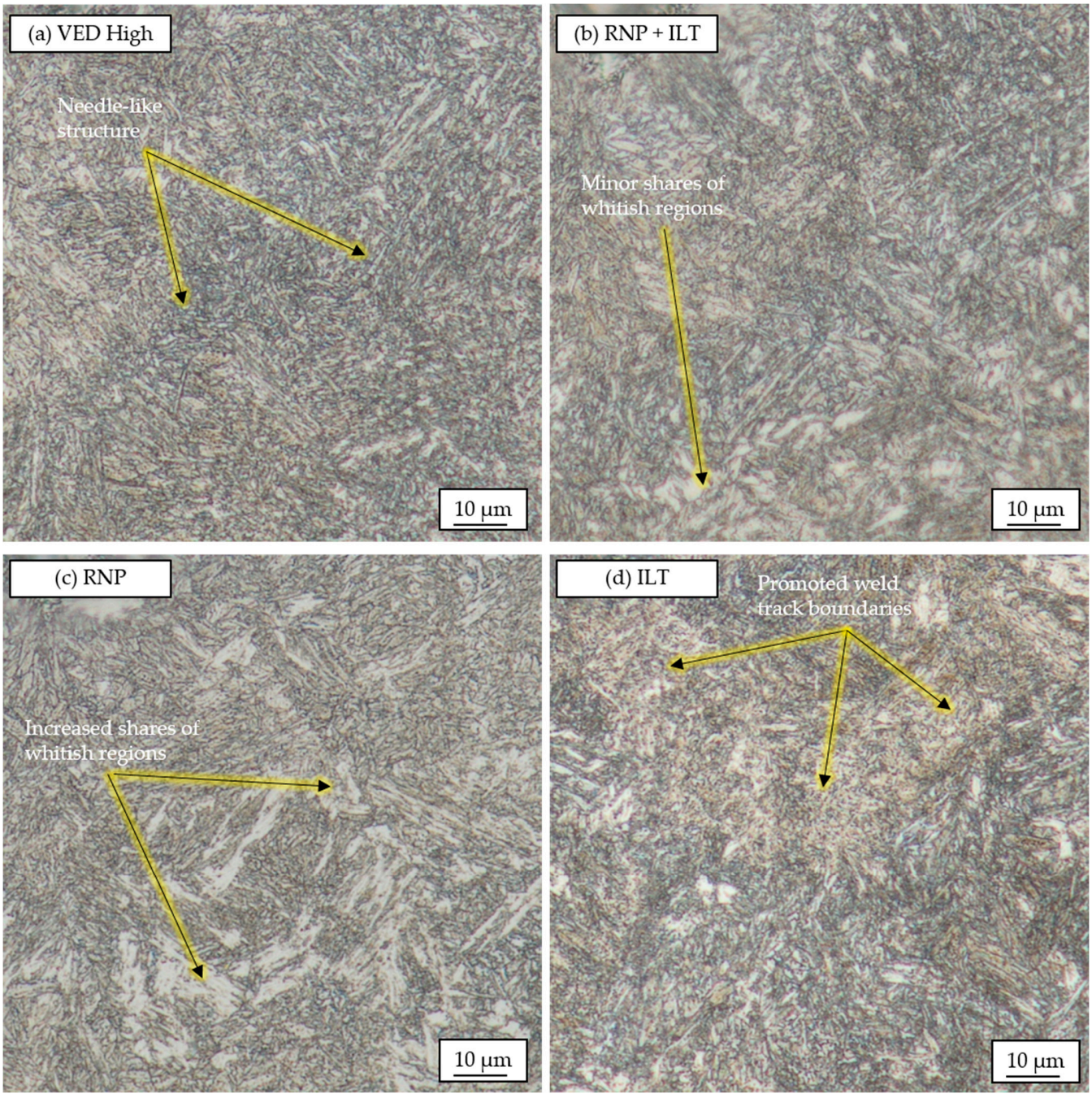

Figure 9. Magnified cross-sections of the specimens manufactured using different countering strategies.

Parameter combination VED High is characterized by a fine and needle-like structure (Figure 9a). This structure appears to be like a martensitic one. When reducing the number of specimens within the build job, an increased amount of whitish blocks can be observed within the samples (Figure 9c). This is an indicator for retained austenite, which correlates well with the reduced material hardness for these specimens. When increasing the dwell time between two layers (Figure 9b), the amount of these whitish

blocks decreases. Increasing the inter-layer time even further leads to an almost complete absence of these whitish regions within the geometry. The longer dwell times support a better heat dissipation, which again leads to lower average layer temperatures. This helps to achieve a more homogeneous transformation of the martensite upon cooling. Furthermore, the weld track boundaries are more pronounced for longer inter-layer times. A similar effect was also shown in Figure 8.

Overall, the appearance of the microstructure is affected by the different processing strategies. Slight changes can be identified when modifying the processing strategy through the addition of, e.g., inter-layer times or by reducing the number of parts within one build job. This shows the sensitivity of the final material properties of low-alloyed steels when processed by means of laser-based additive manufacturing.

4. Conclusions

This work shows the influence of different volumetric energy densities (VEDs) on key material properties like microstructure, weld track geometry, and material hardness. Since a correlation between the applied VED and the resulting properties that can be associated with a process-intrinsic overheating could be observed, additional countering strategies were investigated. These include prolonged inter-layer time and a modified number of parts per build job. The main findings of this work are as follows:

- The applied VED strongly affects the material properties as higher energy inputs result in overheating. Associated with this overheating are increased weld penetration depths and hardness drop-offs.
- By modifying the applied VED, the severity of this effect can be reduced, even though it cannot be avoided completely.
- While low VEDs almost completely avoid the hardness drop-off, lack-of-fusion defects make this parameter combination unsuited for the fabrication of loaded products.
- The inter-layer time between two consecutive layers was identified to be the most critical influencing factor to avoid or force an overheating of the specimens.
- Increasing the inter-layer time can help in reducing overheating effects. This, however, might be associated with undesired material properties (e.g., brittle martensitic phases due to higher cooling gradients) and prolonged manufacturing times. The characterization of these properties will be scope of future work using experimental techniques like X-ray diffraction.
- The minimal VED should not fall below 25 J/mm^3 to avoid lack-of-fusion defects during build-up.
- Adding moderate inter-layer times that are equivalent to a few specimens (≈20% of the build job time) helps in homogenizing the material properties by suppressing or at least postponing overheating effects.

It is recommended to use low VEDs for the fabrication of larger structures. However, the VEDs should be sufficiently high to avoid lack-of-fusion porosity. Future work could focus on the influence of different processing strategies on the material properties within specific part regions. This could include the continuous lowering of the VED or the spatial adjustment of the material properties to generate discontinuous material properties.

Author Contributions: D.B.: Conceptualization, Methodology, Validation, Investigation, Writing—original draft preparation, Visualization; M.E.A.: Investigation, Validation; F.N.: Writing—review and editing, Methodology; M.S.: Writing—review and editing, Supervision, Project administration, Funding acquisition, Resources. All authors have read and agreed to the published version of the manuscript.

Funding: This research was funded by the German Research Foundation (DFG) for Project-ID 61375930, SFB 814—"Additive Manufacturing" TP A05.

Data Availability Statement: Raw data and material are available upon reasonable request.

Acknowledgments: The authors want to thank the German Research Foundation (DFG) for Project-ID 61375930–SFB 814—"Additive Manufacturing" TP A05. We acknowledge financial support provided by Deutsche Forschungsgemeinschaft and Friedrich-Alexander-Universität Erlangen-Nürnberg within the funding program "Open Access Publication Funding". The authors gratefully acknowledge the support provided by the Erlangen Graduate School in Advanced Optical Technologies. We would also like to thank Deutsche Edelstahlwerke Specialty Steel GmbH for their respective support within this work.

Conflicts of Interest: The authors declare no conflict of interest.

References

1. Grosch, J.; Bartz, W.J. *Einsatzhärten: Grundlagen–Verfahren–Anwendung–Eigenschaften einsatzgehärteter Gefüge und Bauteile*; Kontakt & Studiumv. 356; Expert: Tübingen, Germany, 2019.
2. Sharma, R.C. *Principles of Heat Treatment of Steels*; New Age International: New Delhi, India, 1996.
3. Rakhit, A.K. *Heat Treatment of Gears—A Practical Guide for Engineers*; ASM International: Materials Park, OH, USA, 2010.
4. Kamps, T. Leichtbau von Stirnzahnrädern aus Einsatzstahl mittels Laserstrahlschmelzen. Ph.D. Thesis, Technische Universität München, München, Germany, 2018.
5. Emmelmann, C.; Sander, P.; Kranz, J.; Wycisk, E. Laser Additive Manufacturing and Bionics: Redefining Lightweight Design. *Phys. Procedia* **2011**, *12*, 364–368. [CrossRef]
6. Elliott, A.M.; Waters, C. *Additive Manufacturing for Designers—A Primer*; SAE International: Warrendale, PA, USA, 2019. [CrossRef]
7. Todd, M.K. High Value Manufacturing: Advanced Research in Virtual and Rapid Prototyping. In Proceedings of the 6th International Conference on Advanced Research in Virtual and Rapid Prototyping, Leiria, Portugal, 1–5 October 2013; CRC Press: Boca Raton, FL, USA, 2013.
8. Bartels, D.; Klaffki, J.; Pitz, I.; Merklein, C.; Kostrewa, F.; Schmidt, M. Investigation on the Case-Hardening Behavior of Additively Manufactured 16MnCr5. *Metals* **2020**, *10*, 536. [CrossRef]
9. Yang, M.; Sisson, R.D. Carburizing Heat Treatment of Selective-Laser-Melted 20MnCr5 Steel. *J. Mater. Eng. Perform.* **2020**, *29*, 3476–3485. [CrossRef]
10. Schmitt, M.; Schlick, G.; Seidel, C.; Reinhart, G. Examination of the processability of 16MnCr5 by means of laser powder bed fusion. *Procedia CIRP* **2018**, *74*, 76–81. [CrossRef]
11. Schmitt, M.; Gerstl, F.; Boesele, M.; Horn, M.; Schlick, G.; Schilp, J.; Reinhart, G. Influence of Part Geometry and Feature Size on the Resulting Microstructure and Mechanical Properties of the Case Hardening Steel 16MnCr5 processed by Laser Powder Bed Fusion. *Procedia CIRP* **2021**, *104*, 726–731. [CrossRef]
12. Schmitt, M.; Kempter, B.; Inayathulla, S.; Gottwalt, A.; Horn, M.; Binder, M.; Winkler, J.; Schlick, G.; Tobie, T.; Stahl, K.; et al. Influence of Baseplate Heating and Shielding Gas on Distortion, Mechanical and Case hardening Properties of 16MnCr5 fabricated by Laser Powder Bed Fusion. *Procedia CIRP* **2020**, *93*, 581–586. [CrossRef]
13. Aumayr, C.; Platl, J.; Zunko, H.; Turk, C. Additive Manufacturing of a Low-alloyed Engineering Steel. *BHM* **2020**, *165*, 137–142. [CrossRef]
14. Schmitt, M.; Gottwalt, A.; Winkler, J.; Tobie, T.; Schlick, G.; Stahl, K.; Tetzlaff, U.; Schilp, J.; Reinhart, G. Carbon Particle In-Situ Alloying of the Case-Hardening Steel 16MnCr5 in Laser Powder Bed Fusion. *Metals* **2021**, *11*, 896. [CrossRef]
15. Bartels, D.; Novotny, T.; Hentschel, O.; Huber, F.; Mys, R.; Merklein, C.; Schmidt, M. In situ modification of case-hardening steel 16MnCr5 by C and WC addition by means of powder bed fusion with laser beam of metals (PBF-LB/M). *Int. J. Adv. Manuf. Technol.* **2022**, *120*, 1729–1745. [CrossRef]
16. Bartels, D.; Novotny, T.; Mohr, A.; van Soest, F.; Hentschel, O.; Merklein, C.; Schmidt, M. PBF-LB/M of Low-Alloyed Steels: Bainite-like Microstructures despite High Cooling Rates. *Materials* **2022**, *15*, 6171. [CrossRef]
17. Huber, F.; Rasch, M.; Schmidt, M. Laser Powder Bed Fusion (PBF-LB/M) Process Strategies for In-Situ Alloy Formation with High-Melting Elements. *Metals* **2021**, *11*, 336. [CrossRef]
18. Zhang, B.; Li, Y.; Bai, Q. Defect Formation Mechanisms in Selective Laser Melting: A Review. *Chin. J. Mech. Eng.* **2017**, *30*, 515–527. [CrossRef]
19. Kumar, P.; Farah, J.; Akram, J.; Teng, C.; Ginn, J.; Misra, M. Influence of laser processing parameters on porosity in Inconel 718 during additive manufacturing. *Int. J. Adv. Manuf. Technol.* **2019**, *103*, 1497–1507. [CrossRef]
20. Cacace, S.; Semeraro, Q. On the Lack of fusion porosity in L-PBF processes. *Procedia CIRP* **2022**, *112*, 352–357. [CrossRef]
21. Moussaoui, K.; Rubio, W.; Mousseigne, M.; Sultan, T.; Rezai, F. Effects of Selective Laser Melting additive manufacturing parameters of Inconel 718 on porosity, microstructure and mechanical properties. *Mater. Sci. Eng. A* **2018**, *735*, 182–190. [CrossRef]
22. de Terris, T.; Andreau, O.; Peyre, P.; Adamski, F.; Koutiri, I.; Gorny, C.; Dupuy, C. Optimization and comparison of porosity rate measurement methods of Selective Laser Melted metallic parts. *Addit. Manuf.* **2019**, *28*, 802–813. [CrossRef]
23. Mohr, G.; Altenburg, S.J.; Hilgenberg, K. Effects of inter layer time and build height on resulting properties of 316L stainless steel processed by laser powder bed fusion. *Addit. Manuf.* **2020**, *32*, 101080. [CrossRef]

24. Mohr, G.; Sommer, K.; Knobloch, T.; Altenburg, S.J.; Recknagel, S.; Bettge, D.; Hilgenberg, K. Process Induced Preheating in Laser Powder Bed Fusion Monitored by Thermography and Its Influence on the Microstructure of 316L Stainless Steel Parts. *Metals* **2021**, *11*, 1063. [CrossRef]
25. Keshavarzkermani, A.; Marzbanrad, E.; Esmaeilizadeh, R.; Mahmoodkhani, Y.; Ali, U.; Enrique, P.D.; Zhou, N.Y.; Bonakdar, A.; Toyserkani, E. An investigation into the effect of process parameters on melt pool geometry, cell spacing, and grain refinement during laser powder bed fusion. *Opt. Laser Technol.* **2019**, *116*, 83–91. [CrossRef]
26. Tang, M.; Pistorius, P.C.; Narra, S.P.; Beuth, J.L. Rapid Solidification: Selective Laser Melting of $AlSi_{10}Mg$. *JOM* **2016**, *68*, 960–966. [CrossRef]
27. Song, B.; Dong, S.; Deng, S.; Liao, H.; Coddet, C. Microstructure and tensile properties of iron parts fabricated by selective laser melting. *Opt. Laser Technol.* **2014**, *56*, 451–460. [CrossRef]
28. Rasch, M.; Bartels, D.; Sun, S.; Schmidt, M. AlSi10Mg in Powder Bed Fusion with Laser Beam: An Old and Boring Material? *Materials* **2022**, *15*, 5651. [CrossRef] [PubMed]
29. Montevecchi, F.; Venturini, G.; Grossi, N.; Scippa, A.; Campatelli, G. Idle time selection for wire-arc additive manufacturing: A finite element-based technique. *Addit. Manuf.* **2018**, *21*, 479–486. [CrossRef]
30. Denlinger, E.R.; Heigel, J.C.; Michaleris, P.; Palmer, T. Effect of inter-layer dwell time on distortion and residual stress in additive manufacturing of titanium and nickel alloys. *J. Mater. Process. Technol.* **2015**, *215*, 123–131. [CrossRef]
31. Spierings, A.B.; Dawson, K.; Uggowitzer, P.J.; Wegener, K. Influence of SLM scan-speed on microstructure, precipitation of Al3Sc particles and mechanical properties in Sc- and Zr-modified Al-Mg alloys. *Mater. Des.* **2018**, *140*, 134–143. [CrossRef]
32. Lee, H.; Jung, J.E.; Kang, D.-S.; Jeong, H.W.; Yun, D.W.; Choe, J.; Yoo, Y.S.; Seo, S.-M. Oxide dispersion strengthened IN718 owing to powder reuse in selective laser melting. *Mater. Sci. Eng. A* **2022**, *832*, 142369. [CrossRef]
33. Wang, M.; Li, W.; Wu, Y.; Li, S.; Cai, C.; Wen, S.; Wei, Q.; Shi, Y.; Ye, F.; Chen, Z. High-Temperature Properties and Microstructural Stability of the AISI H13 Hot-Work Tool Steel Processed by Selective Laser Melting. *Met. Mater. Trans. B* **2019**, *50*, 531–542. [CrossRef]
34. Hooper, P.A. Melt pool temperature and cooling rates in laser powder bed fusion. *Addit. Manuf.* **2018**, *22*, 548–559. [CrossRef]
35. Pauly, S.; Wang, P.; Kühn, U.; Kosiba, K. Experimental determination of cooling rates in selectively laser-melted eutectic Al-33Cu. *Addit. Manuf.* **2018**, *22*, 753–757. [CrossRef]

Contribution to the Goal of this Work:

This work presents investigations on different processing strategies that can be used for achieving homogeneous material properties along build direction. By reducing the energy input even further, the hardness decrease can be countered almost completely. The hardness difference between the bottom and top region can be reduced down to 5 % when selecting the lowest VED. The success of this strategy is also mirrored in the average weld track size, which is only slightly increasing along build direction for the lowest energy input. A similar result was achieved when manufacturing the specimens with a higher VED but by modifying the build-up strategy through either a decreased number of parts or the introduction of additional inter-layer times. The hardness difference between bottom and top regions of the specimens could be reduced down to below 5 % by prolonging the average time per layer. In both cases, it is likely that a martensite-dominated microstructure with only smaller shares of bainite is formed. This assumption is backed by the peak hardness of the specimens, which is similar to the one of quenched samples from the same material. Overall, the findings of this work show that the build job design plays an important role. The final part properties can be homogenised by avoiding heat accumulation during build-up. However, this is associated with a transition towards a more martensite-dominated microstructure, as indicated by the material properties. The main contribution to RQ2 is, that at the absence of a high-temperature platform heating, adjusted processing strategies that aim at a reduced energy input over time will support a continuous transformation of the austenite upon cooling. Associated with this is a martensite-dominated and no longer a bainite-like microstructure, which is mirrored in the hardness of the material.

The next step examines the tensile properties of additively manufactured case-hardening steels in different heat treatment states. These properties are important characteristics of a material and are decisive for the design of products. Factors like internal stresses might still affect the long-term part behaviour. A feasible approach to influence these properties is provided via heat treatments. By analysing these properties for as-built and heat-treated parts, the influence of the different microstructures determined in Section 4.1 and Section 5.1 on the tensile properties can be quantified. Establishing a fundamental database on these characteristics is decisive for the selection of appropriate heat treatment strategies.

5.3 Tensile Properties of Additively Manufactured Case-hardening Steel Bainidur AM

This section provides additional unpublished work on the tensile properties of additively manufactured Bainidur AM. The powder material Bainidur AM possessed a similar chemical composition as the one used within Chapters 5.1 and 5.2. The only difference was a slightly higher Cr content of 1.3 wt.-% compared to 1.0 wt.-% of the powder batch used in the previous chapters. The cubic samples (10 x 10 x 60 mm³) for tensile testing were manufactured on an EOS M290 (EOS GmbH, Germany). Tensile testing was performed according to DIN EN 50125 using the test geometry of type E. All specimens were fabricated using the same parameter combination (P = 275 W, v = 700 mm/s, h = 110 µm). An average layer thickness of 60 µm was chosen for the investigations. The laser spot diameter was set to 100 µm. Five samples were investigated per parameter combination. During PBF-LB/M, the substrate plate was heated to 80 °C. All specimens were tested in the as-built and heat-treated state using a ZwickRoell Z250 (ZwickRoell GmbH & Co. KG, Germany). Heat treatments include hardening as well as tempering up to 600 °C. Tempering was performed both for specimens in the as-built and hardened state. Furthermore, the specimens were also quenched to and hold at elevated temperatures. This process was described as bainitizing (BZ) in this context, even though the holding temperatures are too low to support an isothermal transformation into bainite.

In the first step, the stress-strain-curve and fracture region was analysed. Figure 18a presents an exemplary illustration of the stress-strain-curves for the as-built material.

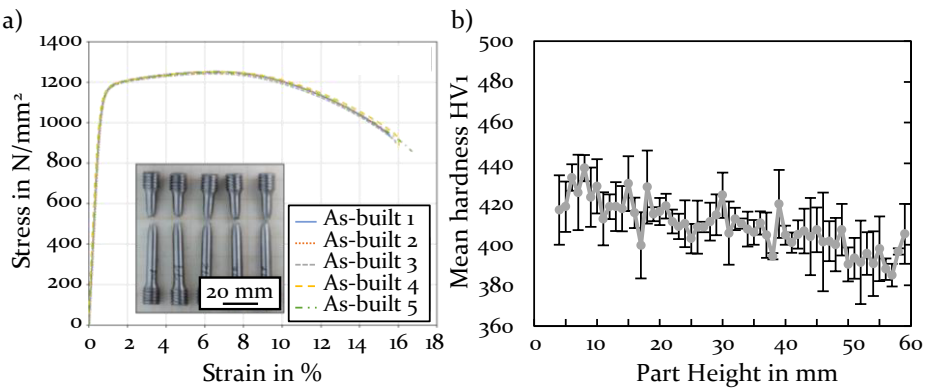

Figure 18: (a) Stress-strain-curve of additively manufactured Bainidur AM in the as-built state and (b) hardness gradient of Bainidur AM along build direction.

The material breaks preferably in the top region of the tensile specimen. A potential explanation for the defect formation in this region is that the samples possess a natural hardness gradient, as indicated in Sections 5.1 and 5.2. This gradient results in a reduced material strength but higher ductility in the higher regions. To assure this assumption, additional hardness measurements were performed (see Figure 18b). Here, a decrease of the hardness along build direction is found. The bottom regions of the specimens are characterised by a hardness of approximately 420 HV1. A linear decrease of the material hardness can be observed with increasing part height. Higher regions of the specimens possess a lower hardness (390 HV1), most likely due to in-situ tempering effects and an incomplete bainitic transformation. The underlying mechanisms responsible for the hardness decrease were already described in Section 5.1. Throughout these experiments, a similar trend was observed for all specimens, since all tensile samples broke preferably in the top third. The lower hardness gradient compared to Section 5.1 can be explained by a larger number of parts within one build job. The larger number of parts helps to reduce overheating effects by increased dwell times between consecutive layers. Figure 19 presents the tensile strength and elongation at break of Bainidur AM in the as-built and in different heat treatment states.

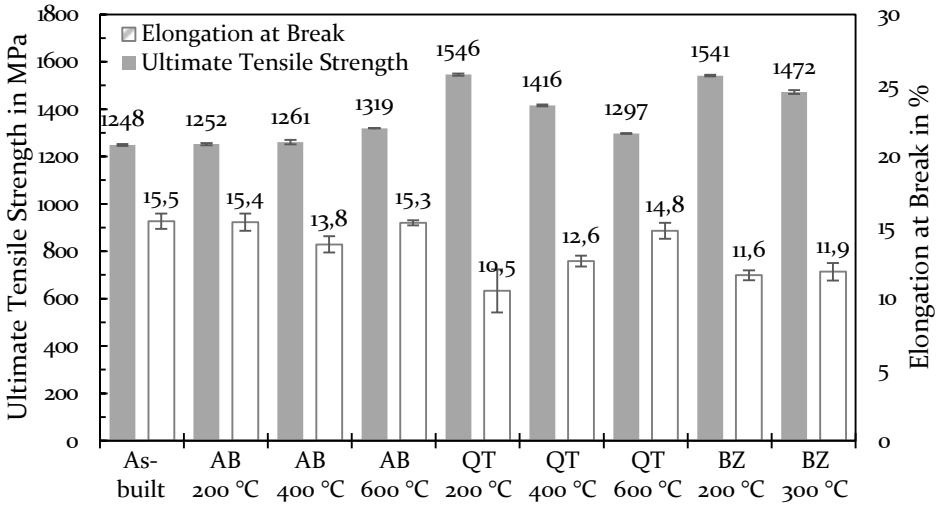

Figure 19: Ultimate tensile strength and elongation at break of additively manufactured and heat-treated Bainidur AM specimens.

Bainidur AM possesses an ultimate tensile strength of approximately 1,250 MPa in the as-built state. The associated elongation at break was measured at 15.5 %. Tempering increases the tensile strength to 1,320 MPa

and decreases the elongation at break to 15.3 % for a tempering temperature of 600 °C. Overall, the tensile strength is very homogeneous for all tempering temperatures and only rises marginally from room temperature to the highest investigated temperature. The influence on the elongation at break is more obvious. For a tempering temperature of 400 °C, a minimal elongation at break of 13.8 % was determined. The poor ductility can be explained by material embrittlement which occurs in this temperature range. Correspondingly, this temperature should be spared for post-process heat treatments for as-built specimens.

Hardening and tempering the specimens at 200 °C results in the highest tensile strength of around 1,550 MPa. The highest tensile strength comes at the cost of ductility, which is demonstrated by the lowest elongation at break of 10.5 % for these samples. Increasing the tempering temperature leads to a reduction of the tensile strength and a simultaneous increase of the elongation at break. The lowest tensile strength of around 1,300 MPa and highest elongation at break of 14.8 % was observed after tempering at 600 °C. These properties are similar to the ones of the as-built Bainidur AM with a slightly higher tensile strength but poorer elongation at break. Quenching the specimens directly to a temperature of 200 °C results in similar material properties as the quenched and tempered samples. It is therefore not decisive whether a part is quenched to room temperature or directly in an oil bath at elevated temperatures. Bainitizing at 300 °C results in a tensile strength and an elongation at break that lie between the ones of quenched and tempered specimens at 200 °C and 400 °C. Overall, Bainidur AM possesses excellent mechanical properties in different heat treatment states. The as-built properties are characterised by a tensile strength of 1,250 MPa and a ductility of approximately 15 %. These values exceed the ones of the comparable case-hardening steel E185 AMPO from Böhler regarding both the tensile strength and elongation at break in the as-built state [156]. Furthermore, the tensile strength in the as-built state exceeds the one of additively manufactured 16MnCr5 by a wide margin (up to 200 MPa) [155]. This proves the suitability of additively manufactured Bainidur AM parts, independent of the heat treatment strategy the specimen was exposed to previously.

Consequently, the key findings of Chapter 5 with regard to RQ2 are summarised in Figure 20. These findings reveal the importance of the thermal history of additively manufactured parts. While small-scaled specimens are characterised by microstructure formation predominantly through continuous cooling, the microstructure in larger parts is formed through isothermal transformation when excessive heat during build-up is accumulated to

act as a part heating. However, the correlation between holding temperature and holding time during isothermal transformation affects the final material properties. These interdependencies result in the formation of an inhomogeneous microstructure along build direction, which is mirrored in the retained austenite content and the hardness of the material. Consequently, inhomogeneous material properties result along build-direction, which could hinder the direct use of additively manufactured parts. It is possible to avoid the transition towards an isothermal transformation by either applying additional inter-layer times or reducing the energy input during manufacturing. Applying a post-process heat treatment also allows to homogenise the material properties prior to the later use, which might be helpful for countering internal stresses.

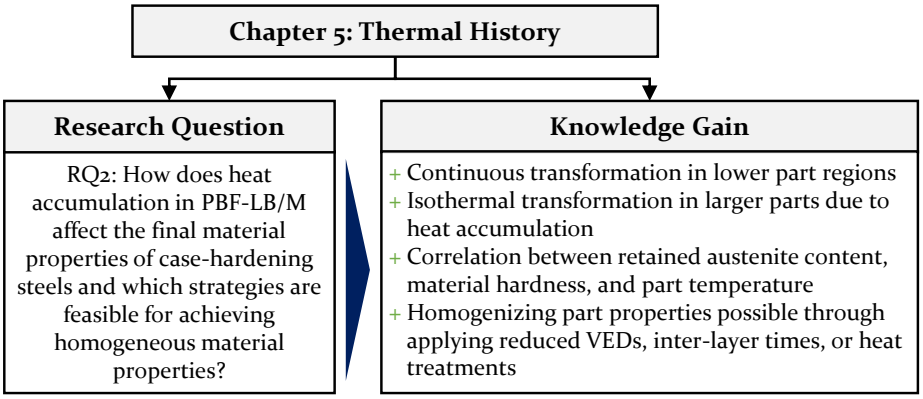

Figure 20: Summary of the key findings with regard to RQ2.

The next step will consequently focus on the modification of the hardness of additively manufactured case-hardening steels. Since the as-built and even heat-treated properties of additively manufactured case-hardening steels, especially the ones of Bainidur AM, are excellent regarding tensile strength and ductility due to the underlying predominantly bainitic microstructure, alternative approaches to the established ex-situ hardening will be followed. These methods include the in-situ reinforcement with additives such as carbon or tungsten carbide that result in an improved hardness.

6 Tailoring of Material Hardness

Case-hardening steels are normally exposed to a carburising heat treatment (see Section 2.2) to improve the hardenability. During these heat treatments, the austenitisation temperature is surpassed, dissolving the underlying bainite-like microstructure, as shown in Chapter 4. However, since case-hardening steels are typically selected to maintain a good ductility of the workpiece's core, a conventional heat treatment might be inconvenient.

Goal of Chapter 6 is therefore to generate an understanding on different approaches for **tailoring the material hardness** of case-hardening steels. Both ex-situ **(RQ3)** and in-situ strategies **(RQ4)** will be followed for improving the hardenability of the material. The requested properties like surface hardness (> 615 HV1) and, if applicable, case-hardening depth are thereby inspired by the conventional process route. In the first approach (Section 6.1), ex-situ hardening of additively manufactured case-hardening steels is investigated. Therefore, conventionally and additively manufactured specimens are carburised. The holding times are varied to analyse different case-hardening depths. Furthermore, additively manufactured specimens are exposed to heat treatments (stress relief and grain-coarsening heat treatment) prior to carburising to investigate the influence of different microstructures on the case-hardenability. The resulting material properties are determined through hardness measurements and optical microscopy. The second concept (Section 6.2 to Section 6.5) focuses on different in-situ hardening approaches. In-situ alloying by adding elemental carbon as well as in-situ particle reinforcement by the addition of tungsten carbide are studied. Different concentrations of the respective additives are studied until the requested surface hardness is reached. However, the risk of this in-situ modification is that the high cooling rates might result in a promoted defect formation like e.g., cracks or an insufficient bonding of the secondary phases to the metal matrix. These investigations are performed both for PBF-LB/M and DED-LB/M to further determine the influence of the respective process on key characteristics like e.g., crack or pore formation, and hardness. Furthermore, the wear-resistance of the materials is analysed through pin-on-dic and scratch testing.

Chapter 6 will provide knowledge on the potentials and limitations of different concepts that can be used for improving the hardness and wear resistance of case-hardening steels in laser-based AM. Considering these limitations, recommendations for the specific design of parts are derived to render a post-process hardening no longer necessary.

6.1 Ex-situ Case-hardening of Additively Manufactured Specimens

Title: Investigation on the Case-Hardening Behavior of Additively Manufactured 16MnCr5 [P1]

Journal: Metals, MDPI

DOI to Web-version: https://doi.org/10.3390/met10040536

Authors: Dominic Bartels, Julian Klaffki, Indra Pitz, Carsten Merklein, Florian Kostrewa, Michael Schmidt

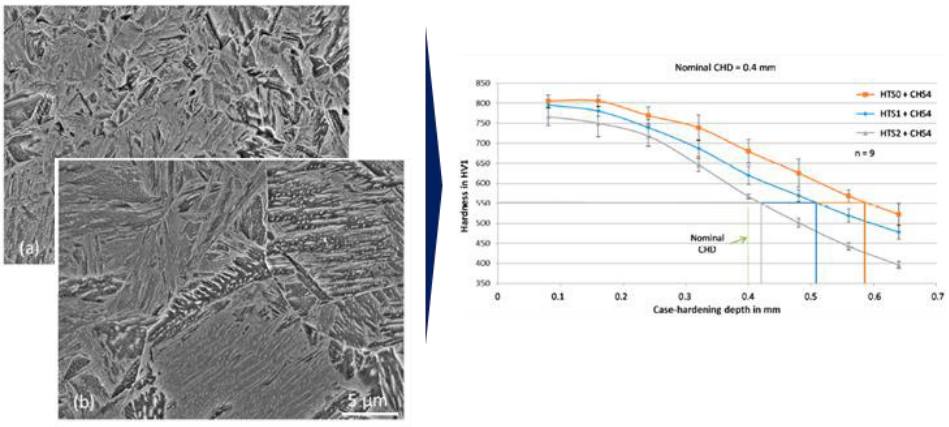

Motivation and Key Findings:

Additively manufactured specimens typically possess a fine-grained microstructure in the as-built state. These fine grains, however, are assumed to be detrimental regarding the carbon diffusivity during carburising. Therefore, this work investigated both the carburising of as-built materials as well as heat-treated specimens to investigate the influence of the microstructure on the case-hardenability. The **highlights** are:

- The influence of different pre-carburising heat treatments on the case-hardenability
- Improved case-hardenability of PBF-LB/M specimens compared to conventional reference samples due to fine-grain hardening
- Better case-hardenability can be used either for reduced carburising times or as an additional safety factor during product design

metals

MDPI

Article

Investigation on the Case-Hardening Behavior of Additively Manufactured 16MnCr5

Dominic Bartels [1,2,*], Julian Klaffki [1], Indra Pitz [3], Carsten Merklein [3], Florian Kostrewa [4] and Michael Schmidt [1,2]

1 Institute of Photonic Technologies (LPT), Friedrich-Alexander-Universität Erlangen-Nürnberg (FAU), Konrad-Zuse-Straße 3/5, 91052 Erlangen, Germany
2 Erlangen Graduate School in Advanced Optical Technologies (SAOT), Friedrich-Alexander-Universität Erlangen-Nürnberg (FAU), Paul-Gordan-Straße 6, 91052 Erlangen, Germany
3 Schaeffler Technologies AG & Co. KG, Industriestraße 1-3, 91074 Herzogenaurach, Germany
4 H-O-T Härte- und Oberflächentechnik GmbH & Co. KG, Kleinreuther Weg 118, 90425 Nürnberg, Germany
* Correspondence: Dominic.bartels@lpt.uni-erlangen.de; Tel.: +49-09131-85-64101

Received: 2 April 2020; Accepted: 14 April 2020; Published: 21 April 2020

Abstract: Additive manufacturing (AM) technologies, such as laser-based powder bed fusion of metals (PBF-LB/M), allow for the fabrication of complex parts due to their high freedom of design. PBF-LB/M is already used in several different industrial application fields, especially the automotive and aerospace industries. Nevertheless, the amount of materials being processed using AM technologies is relatively small compared to conventional manufacturing. Due to this, an extension of the material portfolio is necessary for fulfilling the demands of these industries. In this work, the AM of case-hardening steel 16MnCr5 using PBF-LB/M is investigated. In this context, the influences of different processing strategies on the final hardness of the material are studied. This includes, e.g., stress relief heat treatment and microstructure modification to increase the resulting grain size, thus ideally simplifying the carbon diffusion during case hardening. Furthermore, different heat treatment strategies (stress relief heat treatment and grain coarsening annealing) were applied to the as-built samples for modifying the microstructure and the effect on the final hardness of case-hardened specimens. The additively manufactured specimens are compared to conventionally fabricated samples after case hardening. Thus, an increase in both case-hardening depth and maximum hardness is observed for additively manufactured specimens, leading to superior mechanical properties.

Keywords: additive manufacturing; case-hardening steel; 16MnCr5; laser-based powder bed fusion of metals; hardness measurements; laser beam melting; selective laser melting; case hardening

1. Introduction

Sustainability, resource efficiency and energy efficiency are just some challenges modern industries need to face in the future [1]. These aspects can be satisfied at least partially by, e.g., improving the performance of products due to reduced weights, thus leading to lower energy consumption during usage. Additive Manufacturing (AM) technologies support the previously mentioned demands, as topology-optimized high-performance products can be produced using this manufacturing approach.

1.1. PBF-LB/M

Laser-based powder bed fusion of metals (PBF-LB/M) is an additive manufacturing technology characterized by the layer-wise generation of the final geometry by selectively melting and solidifying powdery materials [2]. This provides a unique possibility for industrial applications, as the high freedom of design supports the fabrication of highly complex components containing, e.g., lightweight

support structures or inner cooling channels [3]. PBF-LB/M, often also referred to as selective laser melting (SLM) or laser beam melting (LBM), shows a high level of detail as small contours around 100 µm can be generated. An exemplary illustration of the iterative PBF-LB/M process is shown in Figure 1.

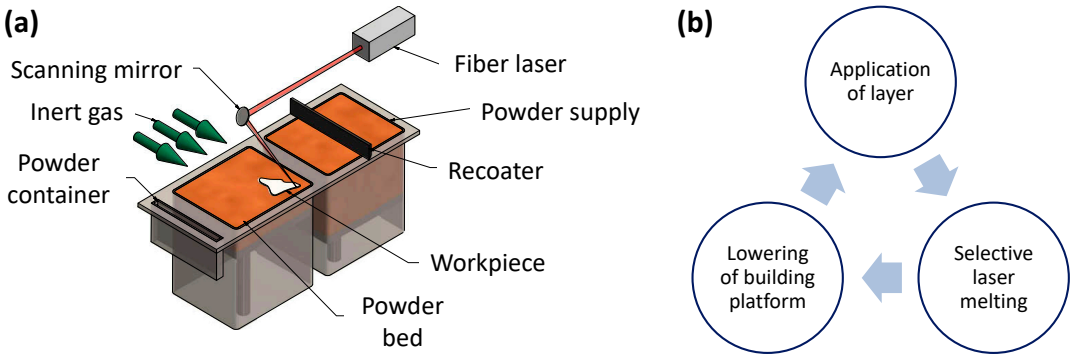

Figure 1. Machine set-up for powder bed fusion of metals (PBF-LB/M) (**a**); iteratively repeated processing steps (**b**).

First, a layer of powder is applied on the substrate using a recoating mechanism. In the next step, this layer is selectively exposed to laser radiation, thus melting the material wherever required. Thirdly, the building platform is lowered, and the mentioned steps are repeated iteratively. After finishing the AM process, the final part is cut off the substrate and subsequent processing steps, such as removing support structures and surface polishing, are carried out.

In AM technologies, the melting process is highly dynamic due to the use of a laser beam as an energy source. Thus, high intensities and cooling rates in the order of 10^6 K/s can be observed during the production of parts [4]. These high cooling rates support the formation of a very fine microstructure compared to conventional manufacturing technologies such as, e.g., casting or forging [5,6]. In general, a finer microstructure is preferred to a coarser one, as small grains improve key material properties such as hardness, tensile strength and ductility by suppressing, or at least delaying, crack growth propagation [7]. The fast cooling of carbon-containing steels supports the formation of a fine martensitic structure [8] instead of an austenitic, bainitic or ferritic one when compared to conventional primary shaping processes [9]. This is desirable for the fabrication of ready-to-use components, as a subsequent heat treatment for the hardening of the final product is not necessarily required.

However, due to the close linkage of AM to laser welding, the processing of high carbon-containing steels is difficult, as hot cracks susceptibility increase with larger amounts of carbon. Thus, the available steel alloys for powder bed-based processes are not ideally suited for applications requiring high surface hardness and wear resistance, while also providing sufficient ductility.

1.2. Case-Hardening Steel 16MnCr5-1.7131

Case-hardening steels such as 16MnCr5 are typically characterized by a ductile material core and a hardened surface - the so-called case. By applying a subsequent heat treatment, also referred to as carburizing, an increase in carbon content is realized, leading to a corresponding growth in hardness and wear resistance [10]. Due to this, case-hardening steels, as defined in DIN 10084 [11], are very well suited for highly demanding applications in the field of gear, shaft and bearing technologies. For material hardness, values in the range of 250–400 HV1 can be achieved without carburizing [12]. However, case-hardened samples show a surface hardness of up to 800 HV1 and are characterized by a ductile core with a hardness of around 300 HV1 [10]. One critical parameter for surface hardening is the so-called case-hardening depth (CHD) describing the distance from the surface to an inboard point, for which the corresponding hardness does not fall below 550 HV1 [13]. For products made from 16MnCr5, the CHD value is typically in the range of 0.2–1.00 mm, depending on the holding time and temperature during carburizing. The present microstructure is also an influencing factor on

case-hardening behavior, as a finer microstructure tends to reduce carbon diffusion into the material [10]. In contrast to conventional fabrication technologies, AM processes support the formation of a finer grain structure [14], thus requiring further investigation into the case-hardening behavior of additively manufactured specimens.

Subsequently, a tempering heat treatment is conducted to adjust the desired material properties. This step is typically carried out at around 180 °C for 2 h and is dependent upon the targeted hardness of the case [10]. Conventionally manufactured specimens are characterized by a tensile strength in the range of 880–1180 MPa and a yield strength of 635 MPa. The elongation at break can be found at values of 9% to 11%, depending on the diameter of the sample, according to Deutsche Edelstahlwerke [15].

1.3. Additive Manufacturing of 16MnCr5

The up-to-date additive manufacturing of 16MnCr5 has barely been investigated. Schmitt et al. [16] presented the first results on the processing of this steel using PBF-LB/M, showing high relative densities above 99.5% for a laser power of 200 W and a layer thickness of 30 µm. The volumetric energy density was set to 100 J/mm^3, with a constant hatch distance and varying scanning speeds, though exact values are not stated. Subsequent hardness testing showed values in the range of 320–335 HV10, depending on the applied laser power and scan strategy. In his dissertation, Kamps [17] investigated the additive manufacturing of gear components made of 16MnCr5. For processing, the same layer thickness (H = 30 µm) was used. The laser power varied between 150 and 200 W, while scanning speed varied in the range of 600–1400 mm/s. For a scanning speed of 900 mm/s, a hatch distance of 70 µm and a laser power of 200 W, with relative densities above 99.5%, were observed for additively manufactured 16MnCr5 samples by means of optical analysis. Furthermore, Kamps investigated the effect of case hardening on the resulting hardness and CHD. As-built specimens were exposed to a stress relief heat treatment at 650 °C for 6 h prior to case hardening. Additionally, the effect of varying holding times during case hardening on CHD and the maximum hardness was studied. For the as-built components, a hardness of 330 HV10 was observed without additional hardening. By case hardening, values of up to 800 HV10 were detected. Stress relief heat treatment led to a finer grain and a reduction in hardness to about 235 HV10. Kamps also showed that there was no noticeable difference in the maximum hardness values for samples manufactured by additive or conventional manufacturing. Furthermore, additively fabricated samples showed a decrease in CHD by approximately 10%. According to Kamps, the finer microstructure, which is typically generated using AM technologies, might act adversely during case hardening, as the diffusion and propagation of carbon into the boundary layers is impeded. The aim of this work is to study the effect of different processing strategies on the resulting hardness and CHD of case-hardened specimens made from 16MnCr5 using PBF-LB/M. This includes a comparison between as-built as well as stress relief heat-treated and grain coarsening heat-treated specimens. Grain coarsening heat treatment is conducted based on the assumption that a coarser microstructure supports carbon diffusion. Finally, case hardening is conducted to increase the carbon content and, based on the resulting material hardness, the effect of the different strategies is evaluated.

2. Materials and Methods

Up to now, barely any experiments have been published on the processing of 16MnCr5 by means of PBF-LB/M and applying case-hardening strategies for increasing the material hardness. It can be assumed that the process-specific fine grain leads to improved material properties for additively manufactured specimens compared to conventional processing routes. In the present work, the effect of varying subsequent heat treatment strategies and case hardening on the resulting material hardness are examined. The obtained values for material hardness and CHD are finally compared to conventionally manufactured specimens that were case-hardened in the same batch. A schematic illustration of the experiments conducted in this work is presented in Figure 2.

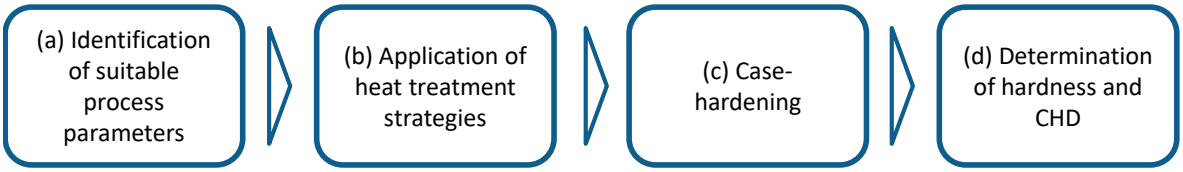

Figure 2. Experimental approach for the investigation of case-hardening behavior of additively manufactured 16MnCr5.

In the first step (a), the process parameters for the defect-free fabrication of 16MnCr5 specimens were developed. As the base material, a gas-atomized 16MnCr5 powder produced by Nanoval GmbH & Co. KG in Berlin, Germany, with an average grain size (d_{50}) of 29.2 µm, was used. The raw material for the atomization process was provided by Schaeffler AG. Particle size and distribution were analyzed using a Camsizer X2 (Microtrac Retsch GmbH, Haan, Germany). Additionally, optical microscopy was carried out to determine the size and shape of the particles. The experimental results of the powder characterization show the particle mass distribution Q3 (share of total mass is 10 %, 50 % and 90 %) for the analyzed powder to be 17.12 µm, 27.65 µm and 40.46 µm, respectively. An optical analysis of the powder indicates the primarily spherical shape of the base material, as illustrated in Figure 3 even though some irregularly shaped particles, as well as locally adhered particulates, can be found at the surface.

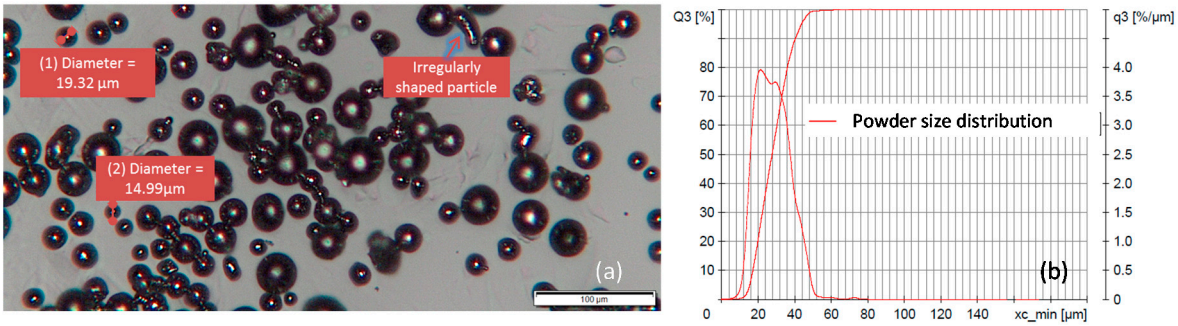

Figure 3. Experimentally determined shape of 16MnCr5 powder (**a**) via optical imaging and particle size distribution (**b**) via Camsizer, provided by FIT AG, Lupburg, Germany.

The nominal chemical composition of conventional 16MnCr5, according to DIN EN 10084, is listed in Table 1 [11]. Energy-dispersive X-ray spectroscopy (EDX) measurements show a slight increase in Mn compared to the standard. This might be due to the powder atomization process.

Table 1. Chemical composition of 16MnCr5 according to DIN EN 10084 [11] and measured by means of energy-dispersive X-ray spectroscopy (EDX).

Elemental Range	Elemental Composition					
	C	**Si**	**Mn**	**Cr**	**S**	**P**
Min.	0.14	-	1.0	0.8	-	-
Max.	0.19	0.14	1.3	1.1	0.04	0.025
EDX	Not detectable	0.17 ± 0.02	1.33 ± 0.03	1.03 ± 0.01	0	0

Furthermore, the carbon content of the base powder material was determined using a carbon analyzer ELEMENTEAC CS-I (ELTRA GmbH, Haan, Germany). The results show the carbon content to be around 0.164% ± 0.002%.

Specimens (10 × 10 × 10 mm^3) were manufactured on a commercially available SLM 280 2.0 (SLM Solutions AG, Lübeck, Germany) machine equipped with a 400 W fiber laser and a nominal spot diameter of 78 µm in the focal plane. For the fabrication of the specimens, the layer thickness H was set constant at 40 µm. Using this layer thickness, the increase in build time compared to lower

layer thicknesses is targeted, as time-consuming recoating steps are reduced. Substrate steel plates, which were previously sandblasted to increase the surface roughness, were used. The preheating temperature of the build platform was set to a constant value of 150 °C for all investigations. Laser power (P_L), scanning speed (v_s) and hatch distance (h) were altered. The analyzed range for the different factors is presented in Table 2.

Table 2. Investigated processing parameters for the fabrication of 16MnCr5 specimens using PBF-LB/M.

Parameter	Parameter Range
Laser power (P_L) [W]	250–300
Scanning speed (v_s) [mm/s]	600–1000
Hatch distance (h) [µm]	120–160

Relative density was determined by means of optical microscopy on polished microsections. For this, several different planes in build direction, as well as different samples built with the same processing parameters, were analyzed. Then, the presented samples were cut into two halves in the middle region. The generated specimens were embedded in resin before being grinded (P240–P1200) and polished using a polishing agent with a grain size of 1 µm. Subsequently, microscope images, which are commonly used in validating additively manufactured cross-sections, were made to analyze the relative density. These pictures were converted into binary images and the bright (solid material) and dark (defects) pixels were related to each other, thus representing the relative density of the sample. This was done for numerous single images with a large magnification, which were then merged into one large image. Samples for further investigations were produced based on the most promising results regarding relative density. The additional etching of the samples using 1-% Nital was done for subsequent microstructural analysis.

In the second step (b), two different approaches for heat treating were followed. First, specimens were exposed to stress relief heat treatment (HTS1) at 680 °C for 2 h. Second, coarse grain annealing (HTS2) was conducted to support grain growth. The aim was to investigate whether a grain coarsening approach supports carbon diffusion during case hardening. All experiments were carried out in an argon atmosphere using a constant inert gas stream of 12 L/min. The processing chamber was flooded prior to heating.

In addition, as-built samples (HTS0) were fabricated and were used as a reference if no heat treatment was applied. The heating rate was kept constant at 5 K/min, while the cooling was carried out in the oven for all specimens. The investigated parameters are listed in Table 3.

Table 3. Heat treatment strategies and corresponding parameters for tempering (HTS1) and coarse grain annealing (HTS2).

Heat Treatment Strategy	Temperature [°C]	Holding Time [h]	Heating Rate [K/min]	Cooling
HTS0	Resembles the as-built state			
HTS1	680	2	5	Oven cooling
HTS2	1050	6	5	Oven cooling

The next step (c) covers several different approaches for case hardening. In this case, three different strategies were investigated. As a reference, a commonly used heat treatment strategy for achieving a CHD of 0.4 mm (CHS4) for 16MnCr5 was used. Additionally, the effect of shorter and longer holding periods, aimed at CHDs of 0.3 mm (CHS3) and 1.0 mm (CHS10), were studied. For the sake of comparison, conventional specimens were also placed in the carburizing oven to allow for the comparison of additively and conventionally manufactured specimens of the same batch. The case hardening was done by H-O-T Härte- und Oberflächentechnik GmbH & Co. KG (Nuremberg, Germany) in a carbon atmosphere. The different parameters for the applied heat treatment strategies are presented in Table 4. The holding time for different case-hardening strategies depended on

the targeted case-hardening depth. All samples were annealed for 2 h at 180 °C after carburizing. For every set of parameters, three specimens were built. This led to a total of 27 samples for each CHD, divided into the nine analyzed approaches for improving CHD and material hardness.

Table 4. Detailed listing of the applied case-hardening strategies, which were carried out at H-O-T in Nuremberg.

Case-Hardening Strategy	Temperature [°C]	Austenitizing Temperature [°C]	Nominal CHD [mm]	Annealing
CHS3	900–950	820–860	0.3	180 °C, 2 h
CHS4	900–950	820–860	0.4	180 °C, 2 h
CHS10	900–950	820–860	1.0	180 °C, 2 h

In the end (d), hardness measurements were carried out for the determination of material hardness and CHD. The case-hardened samples produced in step (c) were, again, metallographically prepared for hardness testing. Hardness measurements were carried out using a semi-automatic hardness testing device, KB 30S, produced by KB Prüftechnik GmbH, Hochdorf-Assenheim, Germany. For the sake of comparability to the literature, HV1 was used as the testing load. To determine CHD, seven measurement points per sample were set at distances of 0.2, 0.4, 0.6, 0.8, 1.0, 1.2 and 1.4 times the nominal CHD each in z-direction. The offset in the x-direction was set to values larger than 300 µm, avoiding interfering effects between measurement points due to the overlapping of the diamond tip spots. The measurement of CHD was carried out three times per specimen. Additionally, three measurement points were placed in the center of the sample to determine the corresponding core hardness. A total of 24 measurement points is summarized and illustrated in Figure 4 for better understanding.

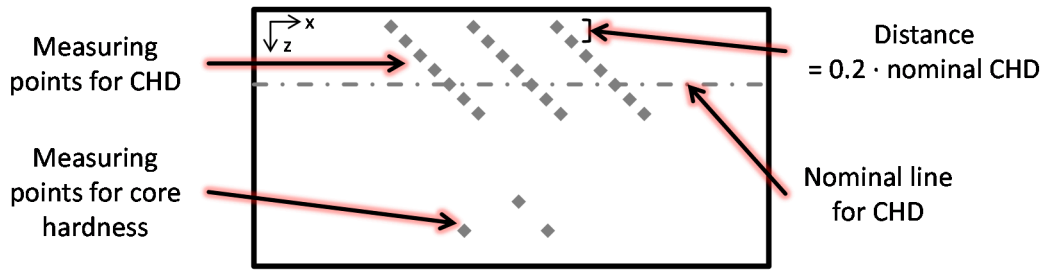

Figure 4. Selection of measurement points for determination of case-hardening depth (CHD) and core hardness.

Furthermore, the hardness of conventionally fabricated reference samples was measured by H-O-T, assuring the suitability of the selected case-hardening parameters. The reference sample was purchased as a bar stock from Günther + Schramm GmbH, Oberkochen, Germany.

3. Results and Discussion

3.1. Identification of Suitable Parameter Range

Appropriate parameters are characterized by a relative density > 99.7%, ideally only showing small internal defects, like cracks (if existent). For the investigated parameter sets, relative densities between 99.3% (e.g., P_L = 300 W; H = 40 µm, h = 160 µm, v_s = 650 mm/s), with comparably large pores, and 99.9% (P_L = 300 W; H = 40 µm, h = 120 µm, v_s = 850 mm/s) could be observed. The latter parameter combination appears to be the most suitable one for the fabrication of specimens, as the highest relative density was observed. Microscope images of the rectangular specimen are shown in Figure 5. The size of the largest defects detected by means of optical analysis was in the order of 50 µm. On the outer edge of the specimens, some minor defects, such as small pores, could be observed in the

manufactured samples. However, this is not considered critical, as the application of a subsequent case-hardening strategy requires the machining of the part surface before parts made of 16MnCr5 can be used for, e.g., gear applications.

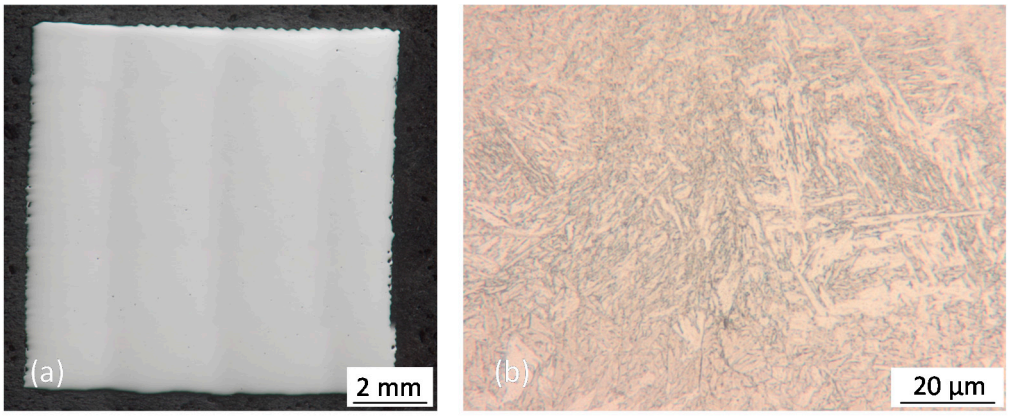

Figure 5. Cross-section of test sample used for density measurements (**a**) and a magnified etched cross-section of the same sample (**b**). Used additive manufacturing parameters: P_L = 300 W; H = 40 µm, h = 120 µm, v_s = 850 mm/s.

Etching of the cross-section shows a primary martensitic microstructure with areas characterized by small amounts of retained austenite. Forthcoming experiments were conducted based on this parameter set, as it appears to be promising for the fabrication of nearly defect-free specimens made of case-hardening steel 16MnCr5. This is important, as internal defects can act as crack initiators, as it was already shown for different metallic materials in [18,19].

3.2. Determination of Mechanical Hardness and Case-Hardening Depth

In this step, the results for various CHDs are provided for both conventionally and additively manufactured specimens. The corresponding figures illuminate the most promising approaches for as-built samples without additional microstructure modification, as well as the different heat treatment strategies. Hardness measurements for untreated, additively manufactured specimens show a typical hardness of around 357 ± 19 HV1. This increase, compared to conventional samples which show typical hardness values of around 300 HV1, is the result of a finer grain structure due to the ultra-high cooling rates of AM processes of up to 10^6 K/s [4]. For case hardening (Figure 6), an increase in maximum hardness for the first measurement points compared to conventional specimens can be identified for all investigated specimens.

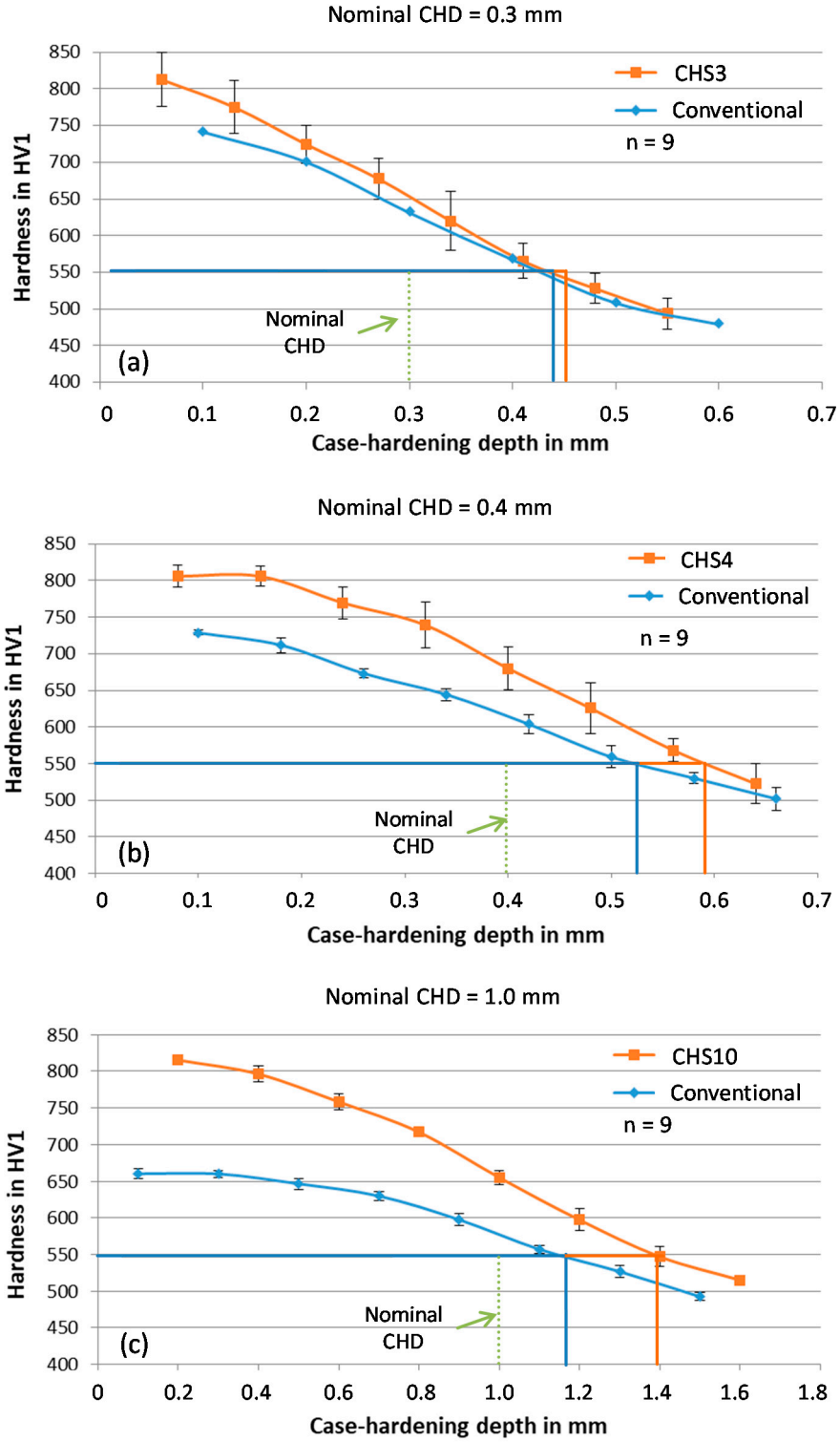

Figure 6. Comparison of CHD over hardness for conventionally and additively manufactured specimens ((**a**) CHD = 0.3 mm; (**b**) CHD = 0.4 mm; (**c**) CHD = 1.0 mm), no heat treatment strategy.

For low CHDs (CHS3 and CHS4), the difference is approximately 70–80 HV1 for the tested samples (805 ± 14 HV1 for Additive and 728 ± 4 HV1 for Conventional, CHS4). This trend increases for larger CHDs, as the difference in hardness rises to approximately 150 HV1 in boundary layers for a CHS10. Furthermore, an increase in CHD for additively manufactured specimens can be identified for larger nominal CHDs. For a targeted CHD of 0.4 mm (CHS4), a CHD of 0.59 mm was measured for additively

manufactured samples; meanwhile, the CHD for conventionally fabricated samples was determined to be around 0.52 mm. This accounts for an increase of approximately 13.5 % in CHD.

This difference is hardly noticeable for lower CHDs (0.3 mm), as no clear trend towards the nominal line can be observed. Hardness values in the core of the different samples were identified to be around 376 ± 8 HV1 (CHS3), 375 ± 8 HV1 (CHS4) and 428 ± 22 HV1 (CHS10), respectively. Here, a rise in core hardness between 25% and 35% per sample could be observed compared to conventional test pieces. This increase might be attributable to the fine microstructure formed, as shown in Figure 7. Furthermore, it can be assumed that smaller amounts of carbon diffused into the core, thus leading to a slight increase in hardness. However, for the validation of this hypothesis, the tracking of the carbon content is elementary.

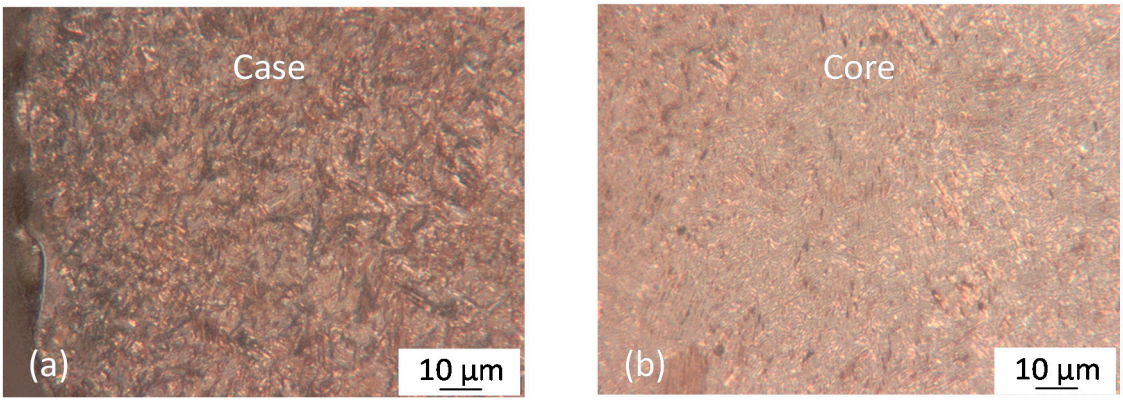

Figure 7. Chemically etched microstructure of as-built and case-hardened specimen (**a**) and grain-coarsened and case-hardened specimen in the core region (**b**). Used additive manufacturing parameters: P_L = 300 W; H = 40 µm, h = 120 µm, v_s = 850 mm/s.

Here, a fine morphology for both cross-sections can be assumed. As expected, the as-built state and case-hardened state leads to a fine microstructure both in the case (a) and in the core (b), even though the samples were exposed to excessive temperatures during carburization.

In summary, in contrast to Kamps, an increase in hardness and CHD for additively manufactured samples compared to conventional ones was observed. Potential reasons for this could be the fact that the temperatures increased to 930 °C during carburization in the presented experiments, compared to 900 °C seen in the studies by Kamps. Furthermore, a reduction in grain size might be another reasonable explanation. These beneficiary hardness values could also occur due to carbide formation, the presence of internal stresses or the lower content of retained austenite. Further studies to determine these influences are necessary and will be carried out in future works.

3.3. Evaluation of the Influence of Different Heat Treatment Strategies

In this step, the influences of the varying strategies on microstructure modification are illustrated. The results of an exemplary nominal CHD of 0.4 mm are presented in Figure 8.

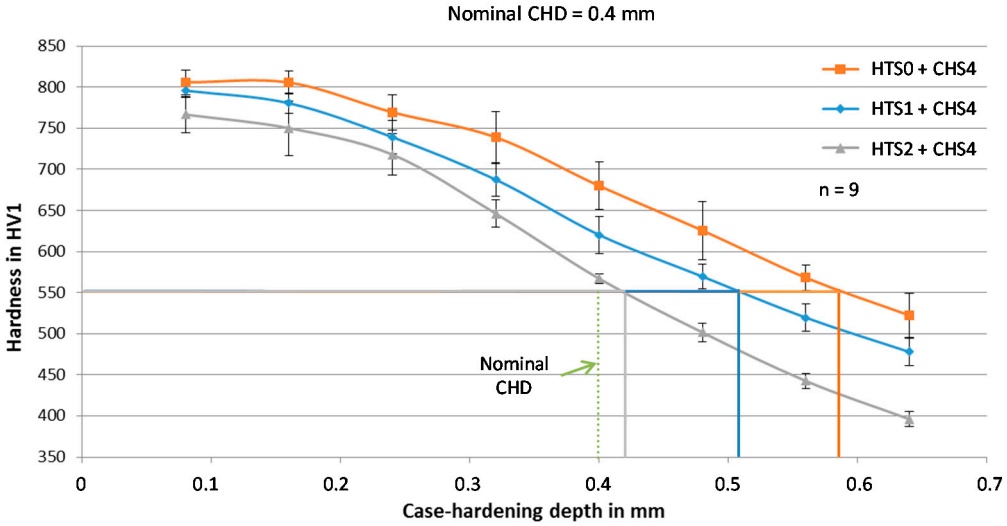

Figure 8. Effect of different heat treatment strategies on CHD and the corresponding material hardness. HTS0 + CHS4 represents the as-built state without heat treatment, HTS1 + CHS4 is stress relief treated (680 °C, 2 h) before case hardening and HTS2 + CHS4 is the material exposed to coarse grain annealing (1050 °C, 6 h) prior to case hardening. Used additive manufacturing parameters: P_L = 300 W; H = 40 µm, h = 120 µm, v_s = 850 mm/s.

Here, a decrease in nominal hardness and case-hardening depth can be observed for approaches aiming to develop a coarser microstructure. Furthermore, stress relief heat treatment led to a reduction in hardness and CHD, as a decrease in CHD by approximately 12 % is detectable. This effect can be attributed to the removal of internal stresses via the application of this heat treatment strategy. However, a more homogeneous hardness distribution is detectable as the average standard deviation decreased from ± 23.7 HV1 to ± 16.4 HV1. According to Figure 9a finer microstructure is formed for the as-built state (Figure 9a) compared to the longer martensitic needles for specimens exposed to grain-coarsening heat treatment (Figure 9b).

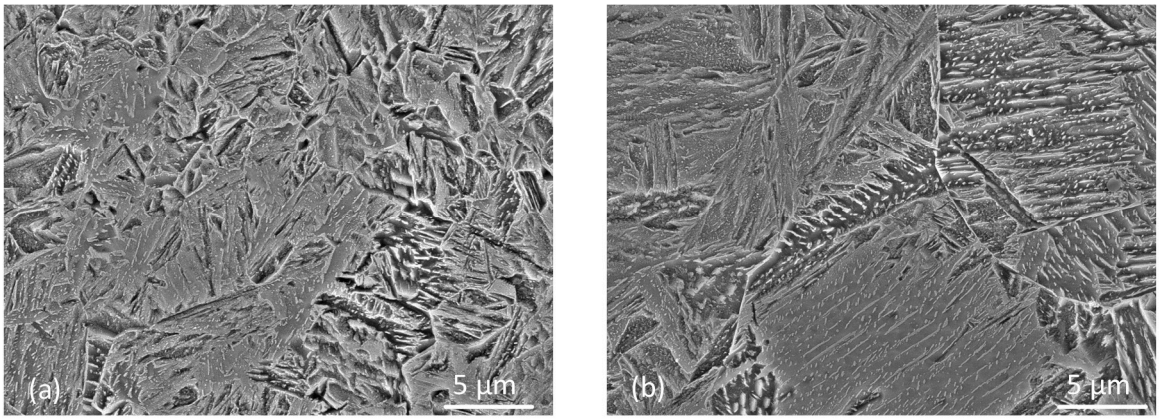

Figure 9. Chemically etched microstructure at the inner boundary of nominal CHD (= 0.4 mm) for (a) as-built state (**a**) and grain-coarsening heat treatment before case hardening (**b**), magnification x10.000. Used additive manufacturing parameters: P_L = 300 W; H = 40 µm, h = 120 µm, v_s = 850 mm/s.

However, even though an increase in carbon content can be assumed due to better diffusion effects [10], no correlated increase in hardness is detectable. In contrast, decreased values for hardness were measured. Apparently, microstructure formation, especially grain growth, is more critical for the resulting material hardness than a slight increase in carbon content due to better diffusion processes. This appears to be similar to results presented by Muszka et al. [20], as they observed an increase by up

to almost 25 % in tensile strength in micro-alloyed steel by simply reducing the grain size. This effect is also recognizable for the other investigated CHDs (CHS3 and CHS10), as the nominal hardness and CHDs are larger compared to conventional samples, even though the grain coarsening heat treatment was conducted. However, further microstructure analyses to determine grain size and the content of retained austenite using, e.g., X-ray diffraction (XRD) measurements, or determining the carbon distribution in different areas, are required in order to fully understand the underlying mechanisms.

4. Conclusions and Outlook

In this study, the effects of different case-hardening and microstructure modification strategies on the resulting material hardness and case-hardening depth of additively manufactured 16MnCr5 were investigated. Parameters for defect-free processing of the mentioned case-hardening steel were developed, characterized by a high relative density above 99.9%. Finally, samples were fabricated to determine the effects of case hardening on additively produced components.

The increase in material hardness for additively manufactured specimens (805 ± 14 HV1) compared to conventionally manufactured ones (728 ± 4 HV1) can be attributed to the fine grain in the material, also leading to an increase in case-hardening depth by approximately 13.5 % for CHS4. Thus, additively produced parts of 16MnCr5 can possess superior material properties after carburizing. It is evident that the process-specific fine grain size was barely affected by stress relief heat treatment. Grain coarsening heat treatment negatively impacts material hardness. Here, it is assumed that the positive effects of fine grain formation due to AM-specific high cooling rates during solidification were negated by subsequent grain coarsening strategies and could not be counteracted by an improved carbon diffusion. Furthermore, additively manufactured specimens show a higher material hardness, as well as a larger CHD, due to fine grain formation hindering displacements in the solid material. Based on these results, two different conclusions can be drawn. On the one hand, a potential reduction in case-hardening time can be targeted, as the threshold values for CHD in additively manufactured specimens are generally reached faster compared to conventionally fabricated ones. On the other hand, the increased hardness and CHD can be seen as an additional safety factor during product and process development, as a higher hardness is achieved.

In another study, carbide formation, grain size development and formation, as well as the influence of internal stresses on material hardness, will be investigated. Furthermore, an analysis of the carbon diffusion and distribution throughout the case will be done in order to determine the carbon propagation into the material.

Author Contributions: Conceptualization, D.B., I.P., C.M. and M.S.; investigation, D.B., J.K. and F.K., methodology, D.B.; resources, C.M., F.K. and M.S.; supervision, M.S.; writing-original draft, D.B.; writing-review & editing, I.P., C.M. and M.S. All authors have read and agreed to the published version of the manuscript.

Funding: Funded by Schaeffler Technologies AG & Co. KG.

Acknowledgments: This work was supported by the Schaeffler Hub for Advanced Research at Friedrich–Alexander University Erlangen–Nürnberg (SHARE at FAU). The authors gratefully acknowledge the support provided by the Erlangen Graduate School in Advanced Optical Technologies.

Conflicts of Interest: The authors declare no conflict of interest.

References

1. Riecke, M.; Teipel, F. *Econsense Resource Efficiency Challenge*; Econsense–Forum for Sustainable Development of German Business: Berlin, Germany, 2012.
2. Gibson, I.; Rosen, D.W.; Stucker, B. *Additive Manufacturing Technologies*; Springer: Boston, MA, USA, 2010; ISBN 978-1-4419-1119-3.
3. Emmelmann, C.; Sander, P.; Kranz, J.; Wycisk, E. Laser additive manufacturing and bionics: Redefining lightweight design. *Phys. Procedia* **2011**, *12*, 364–368. [CrossRef]
4. Hooper, P.A. Melt pool temperature and cooling rates in laser powder bed fusion. *Addit. Manuf.* **2018**, *22*, 548–559. [CrossRef]

5. Tian, L.; Guo, Y.; Li, J.; Xia, F.; Liang, M.; Bai, Y. Effects of solidification cooling rate on the microstructure and mechanical properties of a cast Al-Si-Cu-Mg-Ni piston alloy. *Materials* **2018**, *11*, 1230. [CrossRef] [PubMed]
6. Gorsse, S.; Hutchinson, C.; Gouné, M.; Banerjee, R. Additive manufacturing of metals: A brief review of the characteristic microstructures and properties of steels, Ti-6Al-4V and high-entropy alloys. *Sci. Technol. Adv. Mater.* **2017**, *18*, 584–610. [CrossRef] [PubMed]
7. Morris, J.W. *The Influence of Grain Size on the Mechanical Properties of Steel*; Lawrence Berkeley National Laboratory: Berkeley, CA, USA, 2001.
8. Qiao, Z.X.; Liu, Y.C.; Yu, L.M.; Gao, Z.M. Effect of cooling rate on microstructural formation and hardness of 30CrNi3Mo steel. *Appl. Phys. A Mater. Sci. Process.* **2009**, *95*, 917–922. [CrossRef]
9. Van Bohemen, S.M.C.; Sietsma, J. The kinetics of bainite and martensite formation in steels during cooling. *Mater. Sci. Eng. A* **2010**, *527*, 6672–6676. [CrossRef]
10. Liedtke, D. *Merkblatt 452"Einsatzhärten"*; Wirtschaftsvereinigung Stahl: Düsseldorf, Germany, 2008.
11. Deutsches Institut für Normung. *Einsatzstähle—Technische Lieferbedingungen*; Deutsches Institut für Normung : Berlin, Germany, 2008; DIN EN 10084:2008-06.
12. Sobottka, G. *Case-Hardening Steels*; Edelstahl Witten-Krefeld GmbH: Krefeld, Germany, 1999.
13. International Organization for Standardization. *Steel—Determination of the Thickness of Surface-Hardened Layers*; ISO 18203:2016(en); International Organization for Standardization: Geneva, Switzerland, 2016.
14. Song, B.; Zhao, X.; Li, S.; Han, C.; Wei, Q.; Wen, S.; Liu, J.; Shi, Y. Differences in microstructure and properties between selective laser melting and traditional manufacturing for fabrication of metal parts: A review. *Front. Mech. Eng.* **2015**, *10*, 111–125. [CrossRef]
15. Deutsche Edelstahlwerke GmbH. *Lieferzustand, Technische Bezeichnungen, Normen-1.7131 Datasheet*; Deutsche Edelstahlwerke GmbH: Krefeld, Germany, 2016.
16. Schmitt, M.; Schlick, G.; Seidel, C.; Reinhart, G. Examination of the processability of 16MnCr5 by means of laser powder bed fusion. *Procedia CIRP* **2018**, *74*, 76–81. [CrossRef]
17. Kamps, T. Leichtbau von Stirnzahnrädern aus Edelstahl Mittels Laserstrahlschmelzen. Ph.D. Thesis, Technische Universität München, München, Germay, 2018.
18. Liverani, E.; Toschi, S.; Ceschini, L.; Fortunato, A. Effect of selective laser melting (SLM) process parameters on microstructure and mechanical properties of 316L austenitic stainless steel. *J. Mater. Process. Technol.* **2017**, *249*, 255–263. [CrossRef]
19. Koutiri, I.; Pessard, E.; Peyre, P.; Amlou, O.; De Terris, T. Influence of SLM process parameters on the surface finish, porosity rate and fatigue behavior of as-built Inconel 625 parts. *J. Mater. Process. Technol.* **2018**, *255*, 536–546. [CrossRef]
20. Muszka, K.; Majta, J.; Bienias, Ł. Effect of grain refinement on mechanical properties of microalloyed steels. *Metall. Foundry Eng.* **2006**, *32*, 87. [CrossRef]

Contribution to the Goal of this Work:

Within this work, the influence of different heat treatment strategies on the case-hardenability of additively manufactured 16MnCr5 were investigated. It was found that additively generated specimens possess a better case-hardenability than conventionally processed steels. The hardness of conventional specimens is approximately 10 % lower than the one of additively manufactured parts near the surface after case-hardening. Furthermore, the average case-hardening depth of additively generated parts is larger than for conventional referece specimens. The improved hardenability can be attributed to fine-grain hardening caused by the fine microstructure obtained in PBF-LB/M. This was validated by also exposing additively manufactured specimens to a grain-coarsening heat treatment at 1,050 °C. The coarser microstructure is correlated with a reduced hardness after case-hardening, even though larger grains are in theory better suited for the carbon diffusion during carburisation. Since AM parts are typically prone to distortion due to the formation of residual stresses, a stress-relief heat treatment was also applied prior to case-hardening. The stress-relief treatment negatively affected the case-hardenability of the additively generated parts. However, the case-hardenability is still better compared to the conventional reference samples. These investigations contribute to RQ3 as the benchmark for the hardening of additively manufactured case-hardening steels. The key finding is that the improved hardenability opens the potential for reducing the average holding time during carburisation of AM parts, as shown in Figure 21. To profit from the improved case-hardenability, peak heat treatment temperatures should be selected as low as possible. Choosing low carburising temperatures reduces negative effects such as grain coarsening, which would then again affect the peak hardness of the final material.

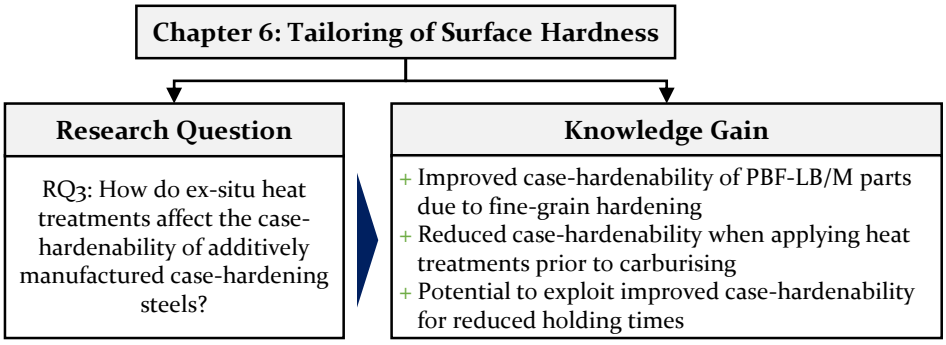

Figure 21: Summary of the key findings with regard to RQ3.

In the next step, different in-situ approaches are followed for improving the hardness of additively manufactured parts with the goal of sparing the carburisation process. Therefore, the powder material will be modified with additives that are known to improve the hardenability of the final workpiece. Elemental carbon is the main lever for improving the hardenability of steels. Correspondingly, the possibility of already providing the carbon in-situ during laser-based additive manufacturing and not ex-situ during carburisation will be studied. The low amount of carbide-forming elements in case-hardening steels is adverse for the wear resistance of the final product. Consequently, hard particles like WC are added to improve the wear resistance of the final part through the formation of an MMC. The goal is to identify suitable carbon and tungsten carbide concentrations in PBF-LB/M so that a sufficiently high material hardness can be achieved without the need for applying an ex-situ carburisation step.

6.2 In-situ Modification of Case-hardening Steels in PBF-LB/M

Title: In situ modification of case-hardening steel 16MnCr5 by C and WC addition by means of powder bed fusion with laser beam of metals (PBF-LB/M) [P5]

Journal: The International Journal of Advanced Manufacturing Technology, Springer

DOI to Web-version: https://doi.org/10.1007/s00170-022-08848-3

Authors: Dominic Bartels, Tobias Novotny, Oliver Hentschel, Florian Huber, Ruslana Mys, Carsten Merklein, Michael Schmidt

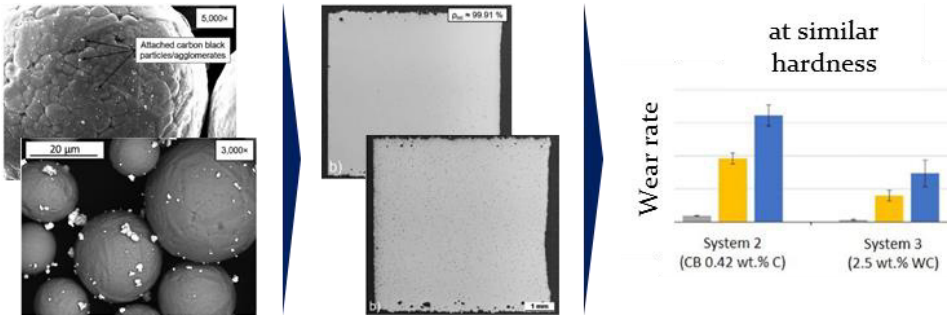

Motivation and Key Findings:

The carburisation of parts is associated with long holding times, which is counterintuitive to the fast supply of spare parts or thin-walled parts that can be targeted when using the PBF-LB/M process. An alternative for substituting this carburisation is the modification of the powder materials to adjust the chemical composition already in-situ. Therefore, the two different approaches in-situ alloying and in-situ particle reinforcement can be followed. This work presents findings on the processability and the associated material properties of case-hardening steels modified with elemental carbon and tungsten carbide particles. The **highlights** are:

- Influence of different carbon concentrations on the processability and material properties of case-hardening steels
- Effect of varying WC concentrations on the processability and material properties of case-hardening steels
- Influence of C and WC on wear resistance of additive manufactured case-hardenng steels at a similar material hardness

The International Journal of Advanced Manufacturing Technology (2022) 120:1729–1745
https://doi.org/10.1007/s00170-022-08848-3

ORIGINAL ARTICLE

In situ modification of case-hardening steel 16MnCr5 by C and WC addition by means of powder bed fusion with laser beam of metals (PBF-LB/M)

Dominic Bartels[1,2] · Tobias Novotny[1,3] · Oliver Hentschel[1,2] · Florian Huber[1,2] · Ruslana Mys[3] · Carsten Merklein[3] · Michael Schmidt[1,2]

Received: 1 November 2021 / Accepted: 27 January 2022 / Published online: 14 February 2022

Abstract
Typical high-strength products are made from carbon-rich steels possessing relatively high carbon content, thus reducing weldability. In this work, preliminary studies on designing and tailoring a low-alloyed steel for the laser-based powder bed fusion (PBF-LB/M) process by adding carbon black (C) nanoparticles and tungsten carbide (WC) particles for enhancing the material properties are provided. First, the base material 16MnCr5 is modified with different concentrations of C and WC. It was found that an increased C and WC content resulted in an elevated material hardness in the as-built state. However, this comes at the cost of a poorer processability as pore formation increased for C-modified and crack tendency increased for WC-modified 16MnCr5. When applying a post-process quenching and optional tempering heat treatment, material hardness in the range of 615 HV can be achieved for C-enriched 16MnCr5 in the tempered state, which would be suitable for bearing and gearing applications. The addition of WC particles favored an improved wear resistance which is twice as high as the one of C-modified material for similar material hardness, showing the enormous potential of WC addition for reducing the wear rate. Complementary SEM and EDX analyses show that both the dilution and bonding zone of the WC particles are affected by the processing conditions and the WC concentration. Furthermore, it was found that a nearly defect-free fabrication of WC-enriched 16MnCr5 was possible for up to 2.5 wt.-% of WC, proving that the occurring defects are highly sensitive to the WC concentration.

Keywords Additive manufacturing · PBF-LB/M · Selective laser melting · Case-hardening steel · In situ alloying · Hardness · Wear resistance · WC

1 Introduction

Case-hardening steels such as 16MnCr5, 20MnCr5, and 17CrNiMo6 are commonly used in various fields including bearing and gear applications [1]. These low-alloyed materials typically provide excellent ductility. However, as high contact forces demand elevated material hardness, subsequent chemical carburizing or nitrating are necessary before quenching and tempering steps are performed for increasing the strength and hardness of the workpiece. Resulting products are characterized by a highly ductile core and wear-resistant case due to the increased C or N content. This leads to energy-intensive process chains on the one hand. On the other hand, carburizing effects can support warping of the workpiece or lead to irregularities on the surfaces of the workpiece, which is especially crucial for highly complex parts. According to Palaniradja et al. [2], about 10% of all case-hardened products are characterized by unwanted defects. Such sophisticated products, which could be characterized by, e.g., internal cooling or lightweight structures, can be produced by means of additive manufacturing (AM). One commonly used technology is laser-based powder bed fusion of metals (PBF-LB/M). This AM

✉ Dominic Bartels
dominic.bartels@lpt.uni-erlangen.de

[1] Institute of Photonic Technologies (LPT), Friedrich-Alexander-Universität Erlangen-Nürnberg (FAU), Konrad-Zuse-Straße 3/5, 91052 Erlangen, Germany

[2] Erlangen Graduate School in Advanced Optical Technologies (SAOT), Friedrich-Alexander-Universität Erlangen-Nürnberg (FAU), Paul-Gordan-Straße 6, 91052 Erlangen, Germany

[3] Schaeffler Technologies AG & Co. KG, Industriestraße 1-3, 91074 Herzogenaurach, Germany

process is characterized by several iterative steps including the application of powder material, selective illumination, and solidification using an energy source, and lowering of the build platform by a defined height. Due to the small size of the powder used, typically in the range of 20 to 63 µm, and potentially small laser spot sizes varying between 50 and 250 µm, fine structures can be produced. Furthermore, laser-based AM processes possess extremely high cooling rates in the range of 10^3 to 10^5 K/s, thus supporting ultrafine grain formation [3]. This can lead to superior part properties compared to conventional manufacturing processes [4].

In the field of powder bed-based AM processes, low-alloyed case-hardening steels such as 16MnCr5 have only been investigated recently. Kamps [5] focused his work on generating lightweight gears using the PBF-LB/M process. By applying a post-process carburizing step, similar hardness values for additively and conventionally manufactured specimens were observed. Conventionally manufactured specimens were generated through continuous casting and forging. Schmitt et al. [6] also studied the general processability of 16MnCr5 by means of PBF-LB/M. Furthermore, the researchers presented results on the overhanging angles and the influence of contour scans on the corresponding roughness values. Within their work, Bartels et al. [7] studied the carburizing and hardening of additively manufactured 16MnCr5 specimens. They found that an increased hardness and case-hardening depth can be observed for additively manufactured specimens from case-hardening steels. Schmitt et al. [8] have also shown the processability of these steels using PBF-LB/M, building on their previous publication from 2018, while also investigating case-hardening behavior and tensile properties of additively manufactured samples. Aumayr et al. studied the processing of a newly developed low-alloy steel E185 AMPO. Relative part density was determined to be above 99.5% [9]. Material hardness in the as-built state was in the range of 38 HRC, which is approximately 370 to 380 HV. After case-hardening, peak hardness of 720 HV0.5 was found, similar to case-hardened 16MnCr5 specimens from bulk material. Yang and Sisson investigated the processing and case-hardening behavior of 20MnCr5 [10]. In the as-built state, an average material hardness of 287 HV0.5 was determined. Measured hardness for case-hardened samples increased up to 857 HV0.5 near the surface.

Zumofen et al. [11] investigated AM of tempering steel 30CrNiMo8 using PBF-LB/M. This steel is characterized by higher carbon content between 0.26 and 0.34 wt.-% compared to case-hardening steels. They found out that a nearly defect-free processing was possible for a defined processing window for varying laser power and exposure time. Mechanical testing in quenched and tempered state showed properties similar to conventionally fabricated specimens from bulk material.

Another possibility for improving the material strength is provided by in situ alloying. This term describes the generation of a material within the manufacturing or solidification process itself. In PBF-LB/M, this can be achieved by premixing a base powder with additional elements, leading to a modified material after solidification with adjusted part properties.

One adjusting lever in steel modification is increasing the carbon content as material strength significantly rises with higher carbon content. The theoretically achievable martensitic hardness can be approximated knowing the carbon content of a material [12]. Typical carbon contents for case-hardening steels are in the range from 0.4 to 0.8 wt.-% leading to material hardness between 600 and 800 HV after hardening and annealing.

This has already been investigated by Bischof et al. for FE4800 which has been modified with varying carbon concentrations of up to 0.3 wt.-% [13]. However, additively manufactured carbon-rich steels (> 0.4 wt.-% C) typically require a post-process heat treatment for hardening and achieving the theoretically possible material hardness [14]. Process-intrinsic heat treatment in PBF-LB/M leads to tempering effects in underlying layers, thus resulting in reduced hardness values. Schmitt et al. also studied the in situ alloying of 16MnCr5 by adding different carbon concentrations. They claim that a defect-free processing with high relative densities above 99.8% is possible. When scaling the experiments towards gear parts, an increase in porosity was observed, which is attributed to the unsuited contour illumination strategy. When analyzing the material properties, a rise in hardness was observed for increased carbon contents. Furthermore, the ductility of the specimens decreased with higher carbon contents [15].

In laser metal deposition, Hentschel et al. studied the influence of carbon black (CB) nanoparticle addition on material hardness for tool steel 1.2343 [16]. With the addition of 0.1 wt.-% carbon black nanoparticles, hardness increased by approximately 50 HV1 up to 700 HV1. Further enhancing the carbon content to 0.2 wt.-% also resulted in higher hardness even though the rise was not as significant as before. Here, determined hardness was in the range of 725 and 750 HV1.

WC addition provides a second opportunity for improving mechanical hardness and wear resistance of material systems. For PBF-LB/M, different investigations on the reinforcing effects of different WC-concentrations have been performed by Yan et al. [17]. They found that a WC content of approximately 2% led to a rise in hardness of approximately 100 HV0.2 for MS300 steel. Kang et al. [18] in contrast only observed a slight increase in hardness of 50 HV (350 to 400 HV) when adding 15 wt.-% WC to maraging steel. Gu et al. [19] also investigated the addition of WC to an iron-based matrix. Their results also show an

improved wear resistance, which is partially attributed to a novel microstructure and the interface of the carbide with the matrix. These observations are also in accordance with the previously discussed results.

Shi et al. found that the size of WC particles significantly affected crack formation and bonding in Inconel IN718 [20]. Different particles with a medium size of 21 µm, 10.5 µm, and 5.25 µm were used. It was observed that smaller particles favored a finer microstructure as well as a more homogeneous distribution of internal stresses within the specimens.

Grünenwald et al. investigated the effects of laser surface alloying on the material hardness and wear behavior of case-hardening steel 16MnCr5 by adding carbon and tungsten. While increasing carbon content led to increased hardness, wear resistance was only improved until a threshold value of carbon content of approximately 0.8 wt.-%. They also observed that with increasing tungsten contents, the wear rate was constantly reduced. However, pore and crack susceptibility increased for excessive tungsten contents above 20 wt.-% [21].

From literature review, it is seen that carbon-enhancement of steels is rarely performed for PBF-LB/M materials. This can be attributed to reduced weldability of steels for higher carbon content. Thus, improving material hardness is generally achieved by following conventional processing routes including resource-intensive carburizing and heat treatment steps. In PBF-LB/M, WC particles are more commonly used for improving wear properties compared to the base material.

The following work aims at investigating the effect of different potential hardening mechanisms for increasing the material hardness of case-hardening steels during the additive manufacturing process. By this, energy-intensive heat treatment strategies could be avoided. Two different approaches are followed: on the one hand, CB nanoparticles are added for increasing the total carbon content within the material as the martensitic hardness is typically characterized by the amount of carbon. Therefore, carbon content will be increased by adding carbon nanoparticles. On the other hand, the addition of hard particles gives the opportunity for significantly improving material hardness and wear resistance when embedded into the matrix material. In both cases, the interdependencies are mostly unknown for low-alloyed steels such as 16MnCr5. The aim of this experiment is to find upper limits for the maximum concentration for the addition of carbon and WC particles while still possessing a good processability. Based on these results, energy-consuming post carburizing and ideally heat treatment steps could potentially be avoided. The latter, however, would require the processing of ready-to-use components with sufficient high material hardness in the as-built state. Target hardness should exceed 56 HRC, which is equivalent to approximately 615 HV.

2 Materials and methods

In the presented work, different in situ approaches are investigated for improving the material hardness. First, pure 16MnCr5 powder is processed for determination of an adequate processing window as well as a benchmark for achievable hardness of the base material. In a second step, the influence of both carbon and tungsten carbide addition on material properties is investigated. Different carbon and tungsten carbide concentrations and their respective influence are examined. By means of optical microscopy and pixel brightness analysis, relative part density as well as defect formation is determined. Energy-dispersive X-ray (EDX) measurements are performed for analyzing tungsten distribution within the specimen. Additionally, dispersing effects and connectivity zone of these tungsten carbides are studied. In the next step, material hardness for different specimens is investigated. Finally, samples for wear analysis by means of pin-on-disc tests are manufactured. Our goal is to manufacture ready-to-use samples that possess material properties similar to conventionally carburized and hardened 16MnCr5. The methodological approach is presented in Fig. 1.

In the first step, a processing window for the nearly defect-free ($\rho_{rel} > 99.7\%$) fabrication of unmodified 16MnCr5 specimens is determined. Powder material was supplied by Nanoval GmbH, Berlin, Germany. Subsequent particle analysis was performed at FIT AG (Lupburg,

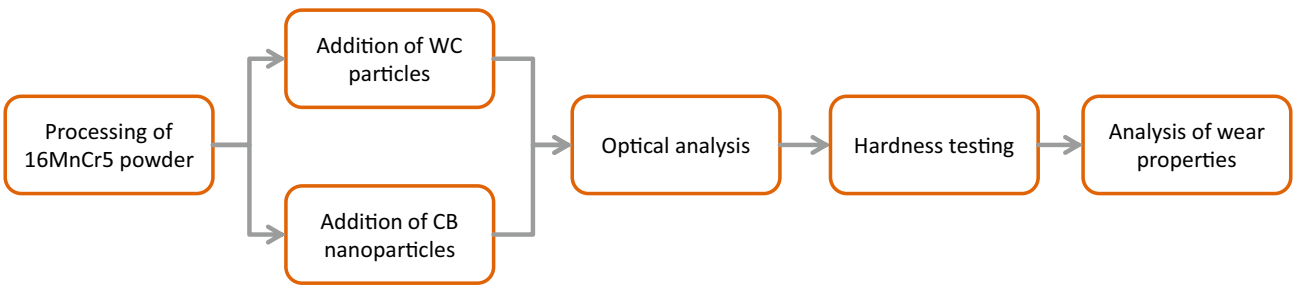

Fig. 1 Methodological approach for in situ material modification and subsequent analysis of this research work

Germany) using a CamsizerX2 (Microtrac Retsch GmbH, Haan, Germany). Characteristic particle size d_{10}, d_{50}, and d_{90} were determined to be 17.23 µm, 27.86 µm, and 40.69 µm, respectively. Experiments are performed on a commercially available AconityMINI (Aconity GmbH, Herzogenrath, Germany). The machine is characterized by a maximum build envelope of Ø 140 × 200 mm^3 and is equipped with a 1 kW single mode fiber laser ($\lambda = 1070$ nm). All experiments were performed in a reduced build envelope of Ø 55 mm with no additional platform pre-heating. Argon was utilized as shielding gas. Typical remaining oxygen content in the machine was below 500 ppm.

Key process parameters such as laser power and scanning speed are varied within test samples. Investigated laser power P_L was varied from 250 to 350 W in steps of 50 W. Scanning speed v_s was modified in steps of 100 mm/s from 500 to 900 mm/s. Hatch distance h, layer thickness H, and spot size were set constant to 120 µm, 50 µm, and 120 µm, respectively. Contour laser power $P_{L,C}$ and contour scanning speed $v_{s,c}$ were chosen at 250 W and 900 mm/s, respectively. These parameter ranges were selected based on common literature values for the processing of low-alloyed steels. As specimen, geometry cubes with an edge length of 6 × 6 × 6 mm^3 were manufactured in all tests. Even though transferability to large-scale applications is not provided in this work and thus needs further investigation, these samples are used as an indicator for potentially achievable material properties.

Based on the most promising processing window for the manufacturing of 16MnCr5 specimens, a parameter range for the fabrication of CB- and WC-enhanced 16MnCr5 was determined. Carbon black nanoparticles were added in different concentrations leading to a total C content in the powder material of 0.28 wt.-%, 0.44 wt.-%, and 0.52 wt.-%, respectively. The last carbon concentration was chosen as experiments showed that a slightly higher carbon content than 0.4 wt.-% in the solid would be suitable considering potential post-process heat treatment strategies as well as tempering at around 200 °C. Previously determined best parameter combinations for the fabrication of 16MnCr5 specimens were used as an indication and were varied further. Carbon black nanoparticles of type N550 were procured from Harold Schold & Co. GmbH, Partenstein, Germany. Carbon concentration both in powder and in solidified material was determined using an ELEMENTRAC CS-i carbon and sulfur analyzer produced by ELTRA GmbH, Haan, Germany.

For WC addition, different concentrations of 2.5, 5, and 10 wt.-% were admixed to 16MnCr5 base material prior to fabrication. WC microparticles of type DS 250 were provided by H.C. Starck GmbH, Goslar, Germany. Since the effect of WC-particles on processability is unknown, a wider parameter range was studied. All powders were mixed using an automatic periodic tumbling unit and are mixed for at least 2 h prior to processing.

Optical analysis is performed to evaluate the homogeneity of the powder mixture as well as determining potentially process-hindering defects. For carbon addition, attached CB nanoparticles can be found distributed over the entire surface of 16MnCr5 powder after tumbling, as shown in Fig. 2.

In some places, smaller agglomerations of these particles can be observed. Performing Hall-flowmeter tests showed that flowability of these powder materials decreased slightly from 17.28 to 21.81 s for 0.44 wt.-% C. Second, WC particles were added to 16MnCr5. An exemplary SEM image is shown in Fig. 3.

In contrast to the carbon-enriched powder, larger agglomerations of WC particles can be found on the surface of the base material. These accumulations might act obstructively

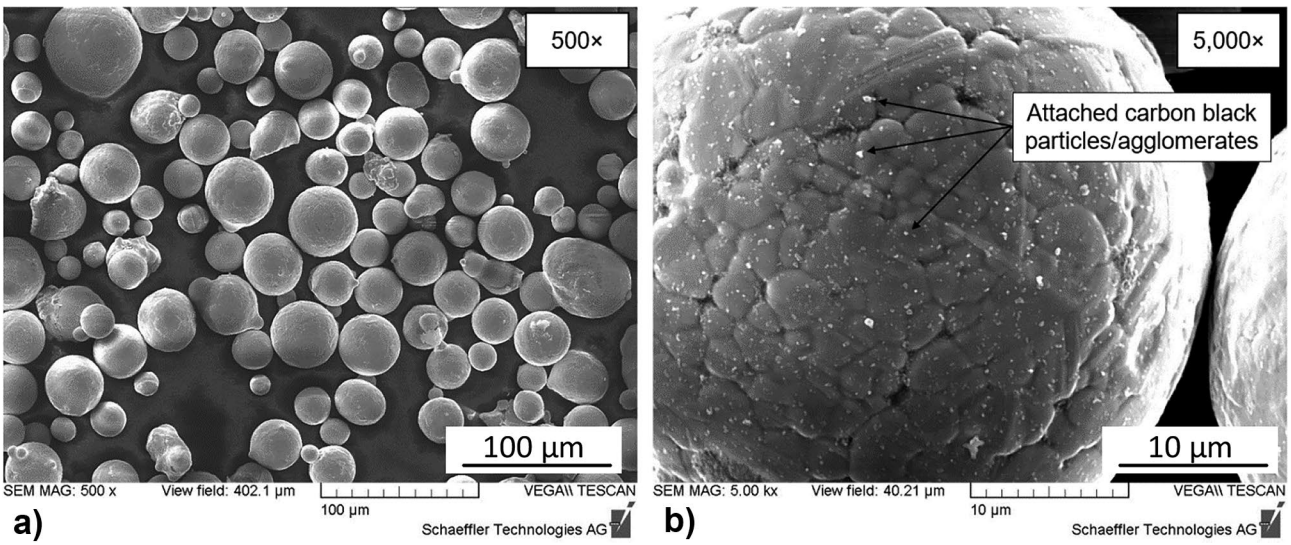

Fig. 2 SEM images of a 16MnCr5 and carbon black powder mixture at 500 × magnification (**a**) and 5,000 × magnification (**b**)

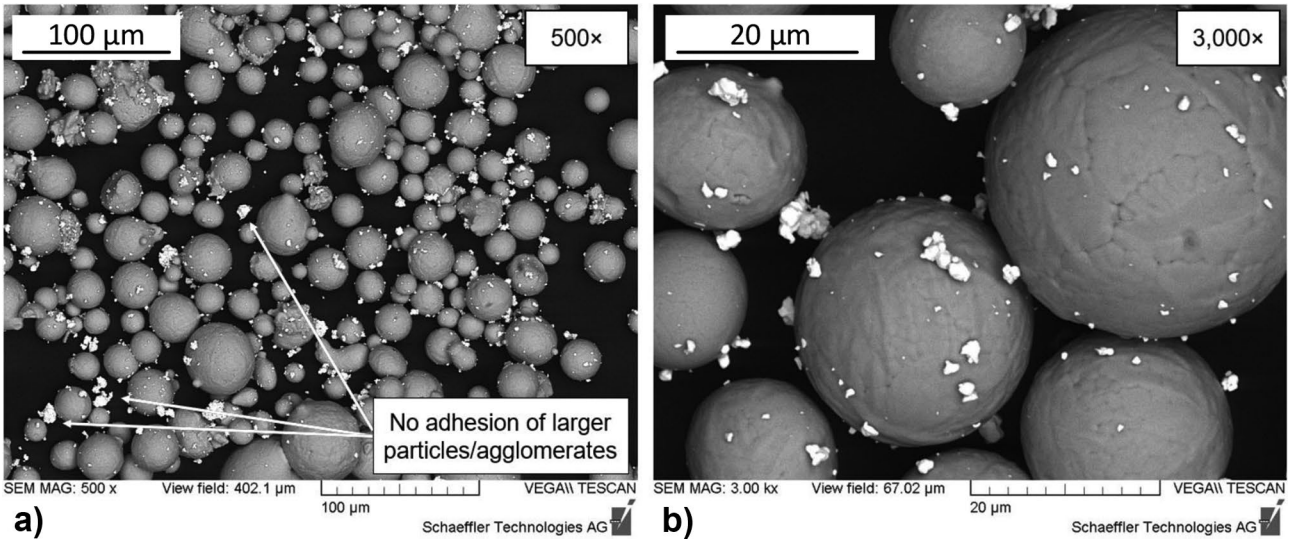

Fig. 3 SEM images of a 16MnCr5 and WC powder mixture at 500× magnification (**a**) and 3000× magnification (**b**)

while processing due to their irregular shape, leading to hooking effects during powder supply. This can also be seen during Hall-flowmeter testing as the investigated powder mixtures do not flow through the capillary. However, recoating of powder during PBF-LB/M process was possible. Furthermore, it can be observed that larger particles did not adhere to the surface of the base material. This is the result of insufficient adhering forces due to too large particle size. During processing, this could result in WC losses during powder supply or inhomogeneous WC distribution within the manufactured specimen. Additional images of the WC particles can be found in the Appendix of this work (Fig. 20).

Table 1 lists the investigated process parameters and their range for the corresponding experiments using the different powder mixtures.

After processing, all manufactured specimens are analyzed in a metallographic laboratory. This procedure includes powder analysis before processing as well as the investigation on manufactured samples. Test cubes are embedded at 150 °C in a resin matrix for optical analysis, and built-up direction is from left to right in all cases. For this, all samples need to be grinded and subsequently polished to 1 µm using a diamond suspension. Relative part density is determined using magnified (25× and 50×) images of cross-sections that are evaluated manually using GIMP (magn. 25×) or (magn. 50×) by use of an analysis module in the Image Management System (Imagic Bildverarbeitung AG). These images are binarized based on a determined threshold value, thus separating defect-free regions from defect-prone regions. Influence of WC-particles on microstructure is determined using scanning electron microscopes (SEM) of types TESCAN MIRA3 and TESCAN VEGA (TESCAN ORSAY Holding, a.s., Czech Republic).

Thirdly, hardness testing was performed on embedded cross-sections using a Qness Q10 A + microhardness tester (ATM Qness GmbH, Germany). Material hardness is tested according to Vickers with a test load of 5 kp (HV5) supporting comparison of manufactured samples. Nine points in the inner region of the manufactured specimens were measured per sample. Three cubes were built for every validated parameter set. Furthermore, material hardness of wear specimens was determined along build direction. For case-hardened specimens, hardness profile is determined using HV1.

Analysis of tribological material properties of additively manufactured samples is performed by means of pin-on-disc tests using an SRV 4 tribometer (Optimol Instruments

Table 1 Investigated process parameters

Parameter	16MnCr5	16MnCr5 + CB	16MnCr5 + WC
Laser power P_L	250–350 W	250–300 W	250–350 W
Scanning speed v_s	500–900 mm/s	500–900 mm/s	500–900 mm/s
Hatch distance h	120 µm	120 µm	120 µm
Layer thickness H	50 µm	50 µm	50 µm
Focal diameter d_f	120 µm	120 µm	120 µm
Contour laser power $P_{L,C}$	250 W	250 W	250 W
Contour scanning speed $v_{s,c}$	900 mm/s	900 mm/s	900 mm/s

Table 2 Selected parameters for pin-on-disc testing

Parameter	Value
Contact force (normal force)	180 N
Testing period	1 h
Velocity	0.05 m/s
Lubrication	FVA 3
Temperature	Ambient

Prüftechnik GmbH, Germany). These investigations aim at qualitative comparison of different alloying systems, thus deriving most promising compositions for improving wear resistance in the as-built state. Testing discs with the diameter of 35 mm and a height of 8 mm were built using the best parameter combinations for pure 16MnCr5, 0.44 wt.-% carbon in 16MnCr5, and 2.5 wt.-% WC in 16MnCr5. Manufactured discs were machined to the final diameter of 31 ± 0.1 mm and height of 4 mm. As pin, a cylindrical roll of type ZRB5 × 10 made from conventional bearing steel was used. The length and diameter of this pin were 10 and 5 mm, respectively. Testing conditions for tribological analysis are listed in Table 2.

By continuously measuring friction force while maintaining a constant contact force, the coefficient of friction is determined. Furthermore, roughness measurement on worn disc surfaces allows the estimation of wear loss. This supports at least a qualitative analysis of the performance of different material systems.

3 Results and discussion

In the following section, the results on optical analysis, hardness measurement, and wear testing are provided for unmodified base material 16MnCr5, carbon black-enriched 16MnCr5, and WC-reinforced 16MnCr5.

Laser power in W	Scanning speed in mm/s: 500	600	700	800	900
350	99,146%	99,837%	99,938%	99,916%	99,900%
300	99,576%	99,850%	99,944%	99,956%	99,898%
250	99,903%	99,941%	99,962%	99,919%	99,793%

Fig. 5 Illustration of the relative part density (determined by IMS) depending on the applied processing parameters during PBF-LB/M for one exemplary specimen each using 50 × magnification

3.1 Optical analysis

This section aims at presenting results on the part density analysis by means of optical imaging. Results are divided into base material 16MnCr5, carbon black–modified 16MnCr5, and tungsten carbide–modified 16MnCr5.

3.1.1 Base material 16MnCr5

First, results on relative density analysis for different in situ alloyed materials are presented. Unmodified 16MnCr5 base material is used as benchmark for further comparison. Higher laser powers lead to an increased amount in pores within the material. Cross-sections for additively manufactured samples with high and low laser power can be seen in Fig. 4. Here, an increased amount of defects is obvious for a laser power of 350 W and a scanning speed of 500 mm/s (Fig. 4a) compared to a power of 250 W and scanning speed of 600 mm/s (Fig. 4b).

Furthermore, a higher number of pores can be found in the outer regions of the manufactured specimens. This is the result of non-optimized contour parameters which could potentially result in pores due to deep penetration welding. Contour porosity could potentially be countered

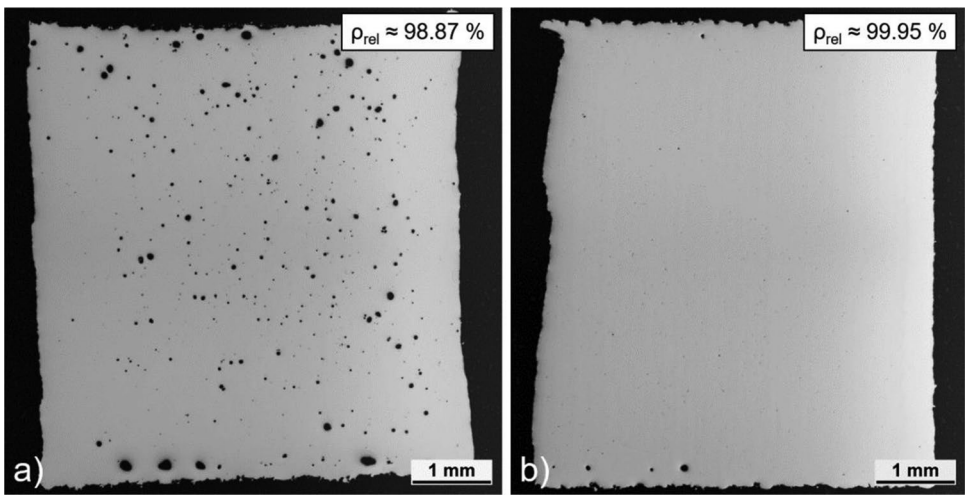

Fig. 4 Cross-section and relative part density (determined by GIMP) of additively manufactured 16MnCr5 specimen for parameters $P_L = 350$ W and $v_s = 500$ mm/s (**a**) and $P_L = 250$ W and $v_s = 600$ mm/s (**b**)

by optimizing the parameter set by, e.g., increasing the scanning speed to reduce the energy input.

Increase in porosity can be attributed to higher laser powers evaporating elements within the matrix material. These defects might also be the consequence of deep penetration welding as shielding gas is entrapped inside the solidified layer. This is the case for instable and thus collapsing keyholes during welding. The identified process window and the corresponding relative part densities for further parameter combinations are illustrated in Fig. 5.

A constant decrease in relative part density with increasing laser powers is obvious. However, increasing the scanning speed for higher laser powers leads to reduced porosity in the final specimen as total energy decreases. Based on determined relative part density, the process window for further experiments with CB-addition is constricted to laser powers between 250 and 300 W as well as scanning speeds in the range of 600 to 900 mm/s. These best results are also similar to Kamps [5], Schmitt et al. [8], and Bartels et al. [7], who all have found a relative part density above 99.9%.

3.1.2 Carbon black–modified 16MnCr5

The following subsection focuses on the addition of different carbon black concentrations to base material 16MnCr5. Similar to processing of the base material, a comparison of parameter combinations resulting in the lowest and highest relative part density is presented. For a measured C content of 0.28 wt.-%, relative part densities between 99.72% (a, $P_L = 250$ W, $v_s = 600$ mm/s) and 99.88% (b, $P_L = 300$ W, $v_s = 700$ mm/s) can be determined using previously well-suited parameter combinations, as shown in Fig. 6.

Increased carbon content in the material requires an increased laser power for the fabrication of nearly defect-free specimens. Nevertheless, for a carbon content of 0.28 wt.-%, specimens can be manufactured with satisfying part densities. In the next step, the addition of further 0.16 wt.-% C is investigated, leading to a total of 0.44 wt.-% in the material. Again, a defect-free fabrication of samples is possible. Relative part densities of up to 99.89% can be achieved as illustrated in Fig. 7.

When comparing to the specimens with a total carbon content of 0.28 wt.-%, no clear decrease in porosity can be found. The pores in the center of the material, however, possess a larger size. Finally, specimens with a total carbon concentration of 0.52 wt.-% in the powder were manufactured additively. Figure 8 presents the results for the most and least porous cross-sections.

In contrast to lower carbon contents, an increased porosity is found for the worst parameter combination investigated. This shows that the potential process window shrinks for higher carbon concentrations, which could be expected as the defect-affinity increases. The increase in porosity compared to preliminary experiments on processing the unmodified 16MnCr5 powder can be attributed to both a higher energy input due to the carbon black nanoparticles and the higher defect affinity of carbon-enriched steels. Next, carbon content was measured both for the pre-mixed powder material and for manufactured test samples using the ELEMENTRAC CS-i analyzer. It was observed that the carbon content in the powder was typically higher by about 10% compared to the content of manufactured specimens. This trend observed throughout all carbon-enriched powders is listed in Table 3.

Losses between powder and specimen can possibly result from adhesion on the surface of the glass container after tumbling and during the powder supply during the process.

3.1.3 Tungsten carbide–modified 16MnCr5

The second investigated approach for in-situ modification is the addition of WC-microparticles to unmodified 16MnCr5 base material. By adding these carbides, an increase in wear resistance is targeted. However, analyzing the corresponding

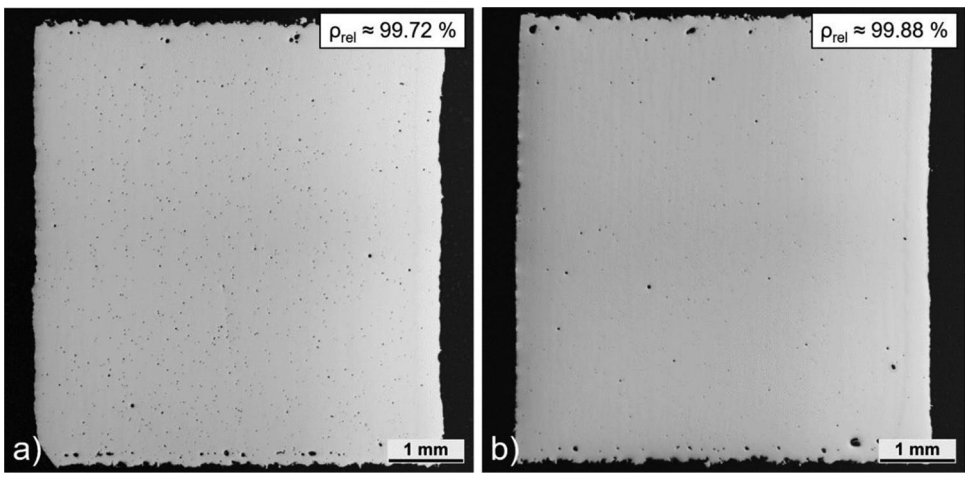

Fig. 6 Most (**a**) and least (**b**) porous cross-sections of 0.28 wt.-% carbon black–modified 16MnCr5 test cubes used for density measurements, process parameters: $P_L = 250$ W, $v_s = 600$ mm/s (**a**) and $P_L = 300$ W, $v_s = 700$ mm/s (**b**)

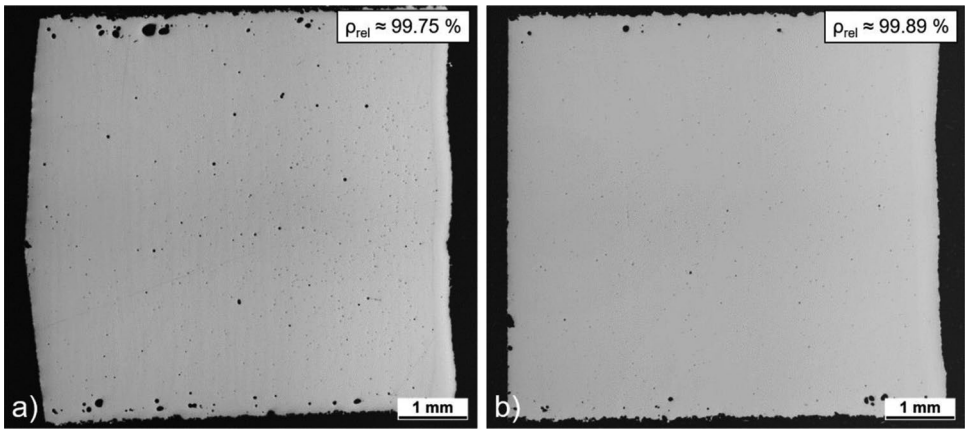

Fig. 7 Most (**a**) and least (**b**) porous cross-sections of 0.44 wt.-% carbon black–modified 16MnCr5 test cubes used for density measurements, process parameters: $P_L = 250$ W, $v_s = 900$ mm/s (**a**) and $P_L = 250$ W, $v_s = 650$ mm/s (**b**)

relative part density is more complicated compared to carbon addition as polished cross-sections show darker zones around WC particles, which appear like defects within the sample, as can be seen in Fig. 9. An automated determination of the relative part density is not feasible as pores cannot be distinguished from the embedded carbides. Therefore, information on the relative part density is omitted at this stage. To assess whether the dark spots are pores or carbides, a more in-depth analysis of the microstructure including SEM and EDX imaging of these cross-sections is required.

As the presence of these WC particles appears to be highly dependent on the energy input, it can be assumed that these particles are either partly or completely solved within the matrix material. For a higher energy input, less of these dots can be found (see Fig. 9a). Using a larger magnification reveals the differences between pores and WC particles within the material, as illustrated in Fig. 10.

Here, a small but bright dot, which could either be a WC carbide or oxidized particles, can be identified within the center of the majority of the black spots. As these spots are both irregularly shaped and surrounded by a darker bonding region, it is assumed that these dots are WC particles. This is due to the WC particles possessing an irregular shape compared to the base powder material. Pores, on the other hand, possess a more spherical shape than the WC particles. A similar differentiation of pores and WC-particles was already presented by Kang et al. [18]. In a next step, EDX line scans are performed for measuring the W content of these potential WC particles within matrix. This supports the assumption that these darker sections within the specimen are the consequence of bonded WC particles and not pores or other defects like oxidation. An exemplary EDX line scan of the tungsten concentration in two different directions is shown in Fig. 11.

EDX analysis shows that these brighter regions within the material are characterized by an increased W peak. Furthermore, a drastic fall in Fe content is detectable. This supports the assumption that not all dark spots in Fig. 12 are defects such as pores or cracks within the specimen. Furthermore, the diffusion zone of these WC particles within the 16MnCr5 matrix needs to be analyzed. SEM images also show asymmetrical diffusion zones of these WC particles as well as elongated diffusion zones, in addition to spherical zones as shown in Fig. 11, within the matrix. These effects can be seen in Fig. 12.

This elongated diffusion zone can also be referred to as a W tail, which was already reported by Schaak et al. in previous work [22]. Additional EDX line scans of this tungsten tail are

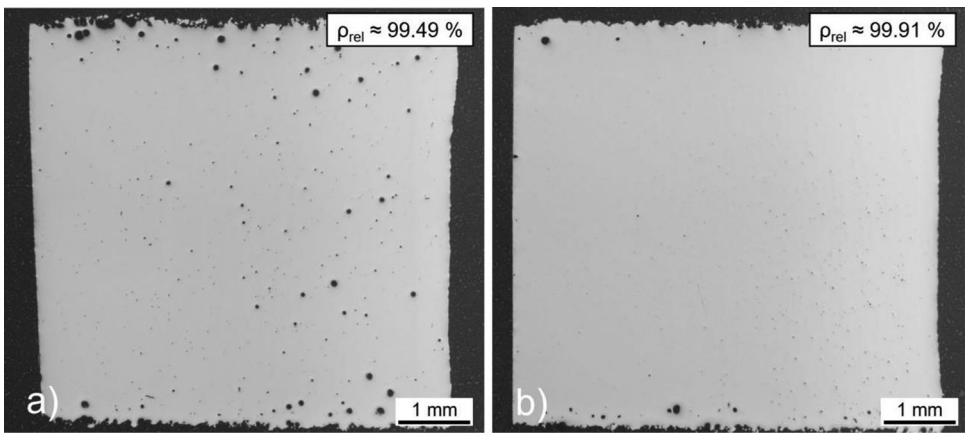

Fig. 8 Most (**a**) and least (**b**) porous cross-sections of 0.52 wt.-% carbon black–modified 16MnCr5 test cubes used for density measurements, process parameters: $P_L = 300$ W, $v_s = 500$ mm/s (**a**) and $P_L = 250$ W, $v_s = 700$ mm/s (**b**)

Table 3 Carbon content in powder material and additively manufactured specimens

Powder mixture	Powder	Specimen
16MnCr5	0.177 ± 0.002	–
0.28 wt.-% C	0.279 ± 0.004	0.259 ± 0.002
0.44 wt.-% C	0.445 ± 0.006	0.400 ± 0.004
0.52 wt.-% C	0.528 ± 0.004	0.448 ± 0.011

presented in the Appendix (Fig. 21), proving that the brighter region is the consequence of tungsten within the material.

Finally, SEM analysis of the diffusion zone of WC particles was performed. Our goal was to investigate the occurrence of potential defects after solidification. Exemplary images of two WC particles within the 16MnCr5 matrix are presented in Fig. 13.

Here, the formation of a carbide network starting from the embedded WC particles can be observed. The carbide network appears to form with a preferred direction within the specimen. However, further investigation on the development of this network structure is necessary for fully understanding its propagation. Furthermore, bonding defects surrounding the WC particle can be found consistently. These defects are characterized by darker spots that form both directly at the WC particle and in the surrounding diffusion zone. One potential reason for these defects is insufficient wetting behavior of the WC particles within the matrix in the molten state. One potential approach for minimizing bonding defects is the use of Co-coated WC particles, allowing a better wetting of the added particles within the matrix. However, additional research needs to be performed for fully understanding the origin of this defect formation. Besides the micro-scale bonding defects near individual particles, it can be concluded that the addition of 2.5 wt.-% WC to 16MnCr5 base material still allows the fabrication of nearly defect-free specimen. An increase of pores in the outer regions of the specimens is evident.

Furthermore, addition of 5 wt.-% and 10 wt.-% WC to unmodified 16MnCr5 has been investigated. Here, a significant increase in defects, which includes gas porosity and crack formation, can be found after processing, even for all investigated parameter sets. Exemplary cross-sections of WC-modified 16MnCr5 are shown in Fig. 14.

In both cases, crack formation can be identified in the outer edges of the specimen. With increasing WC content (10 wt.-%), crack tendency in the center of the specimens also increases (see Fig. 14b). Here, the cracks appear to spread between the pores which originate from the embedded carbides. Similar effects were observed by Chen et al. [23] even for lower carbide contents. Further microstructure is investigated by means of SEM for determining the dilution zone of the WC particles, as depicted in Fig. 15.

In contrast to modification with 2.5 wt.-% WC, a more pronounced carbide network can be found in the area surrounding the added particles. However, presumably due to insufficient wetting behavior, an increased amount of WC particles, and a harder matrix material, crack formation in the region of WC particles drastically increases. These cracks probably result from internal stresses occurring during processing and form during cooling and solidification of the melt pool. This crack formation could possibly be avoided by integrating a high-temperature platform heating at least for a WC content of 5 wt.-%. Another potential solution for avoiding this crack formation lies in using even smaller particles in the sub-micron scale, as it was reported by Chen et al. [24].

In summary, processing of WC-enriched base material is possible for low contents of 2.5 wt.-%. For higher contents, defect-affinity drastically increased as crack formation was initiated.

3.2 Hardness analysis

Material hardness was determined for different carbon and tungsten carbide concentrations in the final specimens.

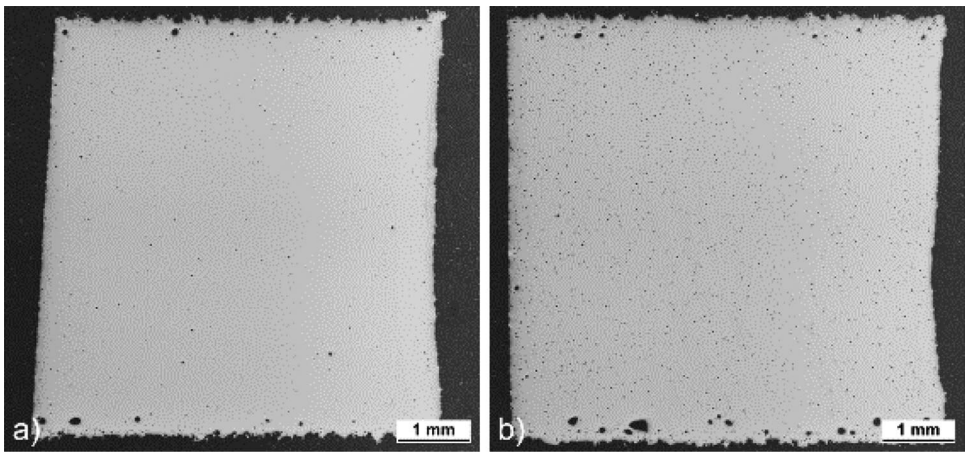

Fig. 9 Cross-sections of 2.5 wt.-% WC-modified 16MnCr5 test cubes with (**b**) and without (**a**) dispersed WC particles visible, process parameters: $P_L = 350$ W, $v_s = 600$ mm/s (**a**) and $P_L = 300$ W, $v_s = 900$ mm/s (**b**)

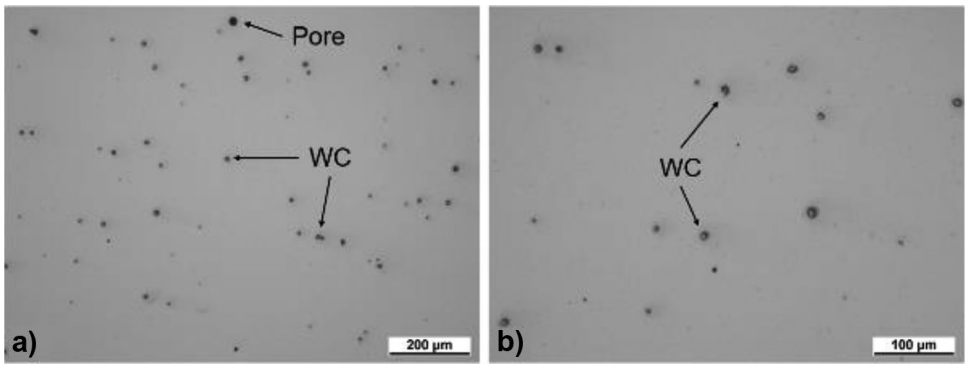

Fig. 10 Microscope analysis of WC-enhanced 16MnCr5 with dispersed WC particles at magnification of 100-times (**a**) and 200-times (**b**)

Furthermore, samples with a carbon content of 0.52 wt.-% were also heat-treated prior to indentation measurement. Determined material hardness for different carbon-modified materials is shown in Fig. 16.

Additively manufactured 16MnCr5 specimens are characterized by a mean material hardness of 337 HV5 for the favored parameter set. Hardness of the conventionally fabricated and case-hardened reference system was determined to be 602 ± 9 HV5 for a carbon content of 0.4% in the case. Average material hardness for CB-modified base material was determined to be 375 HV5 for 0.28 wt.-% and 436 HV5 for 0.44 wt.-%, respectively.

Further increasing the carbon content to 0.52 wt.-% in the powder, which is equivalent to a carbon content of approximately 0.45 wt.-% in the specimen after PBF-LB/M, leads to a material hardness of 458 ± 24 HV5 in the as-built state. After austenitization at 860 °C for 30 min and subsequent quenching, these specimens possess an indentation hardness of 725 ± 7 HV5, which falls to 617 ± 3 HV5 after a subsequent tempering step at 200 °C with a holding time of 2 h. This temperature was selected as it is commonly used for quenched and tempered specimens. The observed drop in material hardness supports the assumption that the martensitic phase is dominant after heat treatment, as other

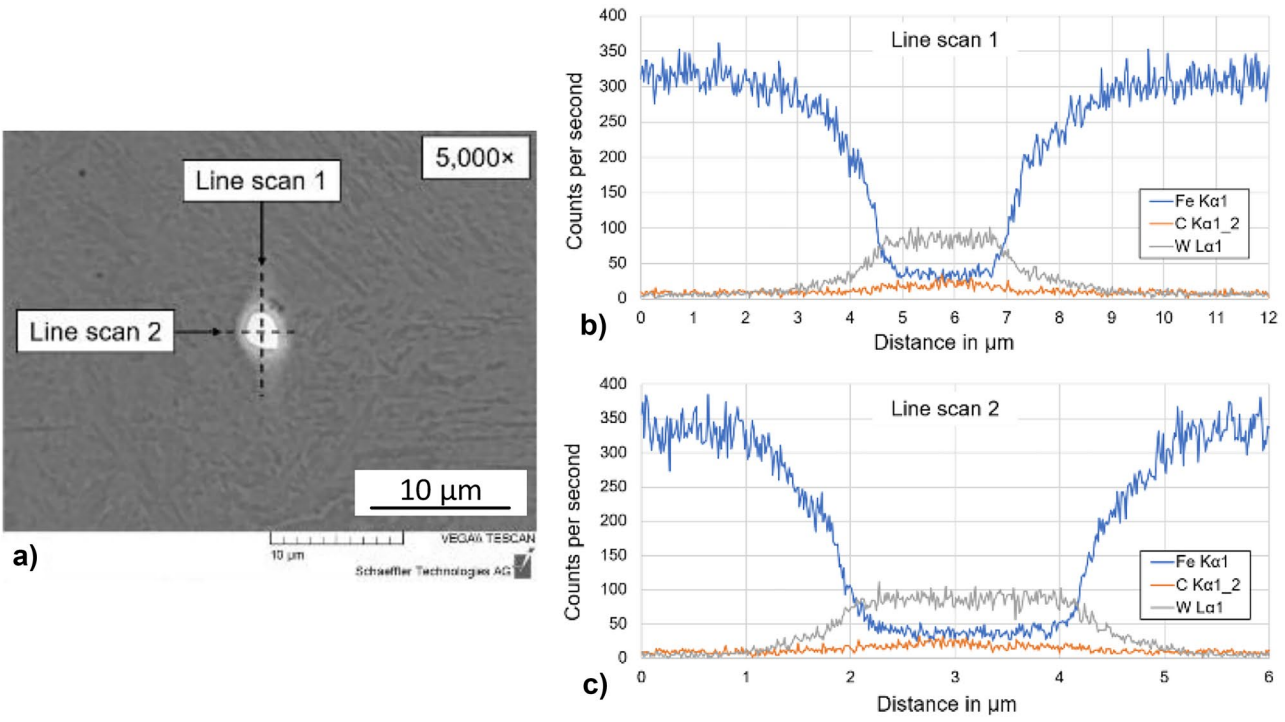

Fig. 11 SEM images of dispersed WC particle within the etched base material (**a**) as well as EDX line scans for determining the elemental composition (**b**, **c**)

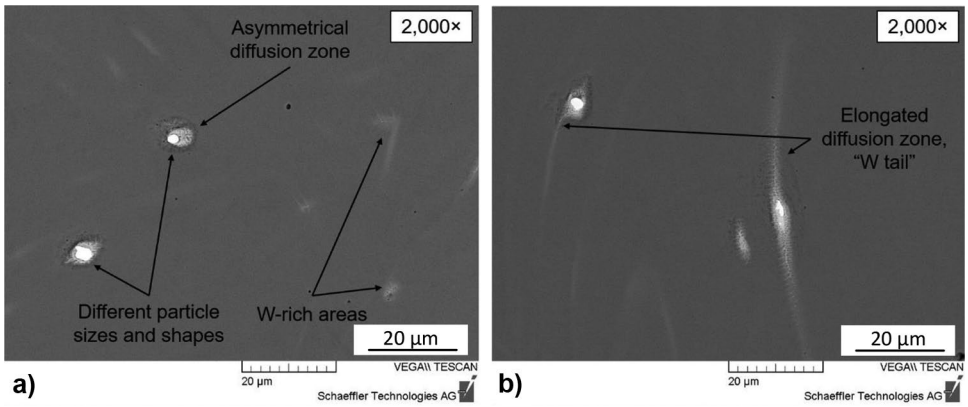

Fig. 12 SEM images of WC particles with asymmetrical diffusion zones (**a**) and elongated W tails (**b**)

phases, e.g., bainite, possess a higher tempering stability. Comparing the results of the material hardness with the ones presented by Hutchinson et al. [25] supports the assumption that a primarily martensitic phase is present after hardening, as the hardness values are similar. At this point, it is evident that solely increasing the carbon content of the powdery material does not result in a sufficiently increased material hardness. This can be attributed to the process intrinsic heat treatment leading to a continuous tempering of lower layers, resulting in reduced material hardness compared to the theoretically achievable one. Therefore, additional XRD analysis was performed which show that the content of retaining austenite was approximately 4% for manufactured specimens. Considering the high hardness of martensite, this leads to the assumption that a microstructure possessing a lower hardness must underlie. Etched cross-sections of carbon black–modified 16MnCr5 are displayed in Fig. 17.

From the presented images, no clear increase in dark needle formation, which could potentially represent an enhanced martensite formation, is detectable. This supports the assumption that the present microstructure is not solely martensitic in the as-built state. Furthermore, the addition of CB-nanoparticles might lead to a finer microstructure, which is characterized by smaller martensitic needles with increasing carbon contents. This would correlate with the observations made by Reinert et al. [26] that carbon nanotubes and nanoparticles result in grain refinement. The finer grain then favors an increase in material hardness, as shown in the studies by Hall [27]. Coupled with an improved martensitic hardness due to an increased carbon content, the rise in material hardness can be explained. Further analysis on the average grain size needs to be performed. This, however, falls within the scope of future investigations. The obtained results lead to two main findings: On the one hand, specimens from a carbon-enriched 16MnCr5 can be manufactured nearly defect-free, showing the possibility to avoid a post-process chemical heat treatment for increasing the carbon content. On the other hand, however, heat treatment is still required for achieving a desirable material hardness.

In the next step, material hardness of WC-enhanced 16MnCr5 specimens was determined. Obtained results for different WC concentrations are depicted in Fig. 18.

Firstly, material hardness is constantly increasing with higher WC concentrations. A rise in hardness of approximately 80 HV5 per additional 2.5 wt.-% WC compared

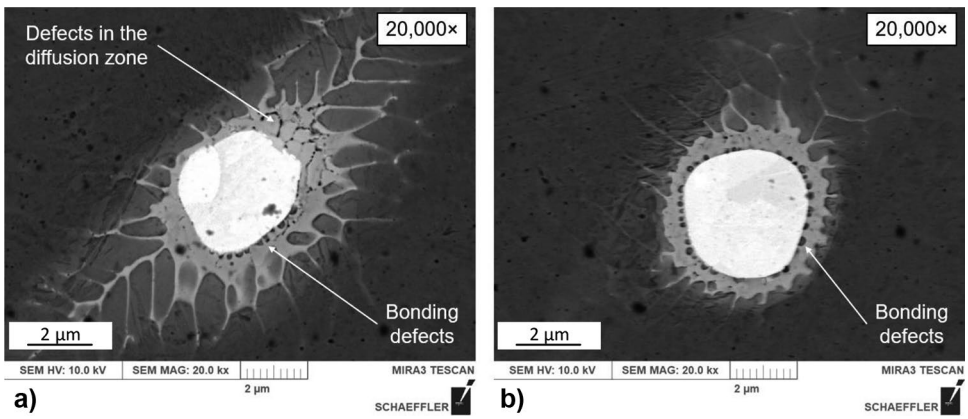

Fig. 13 SEM images of individual particles containing mainly defects in the diffusion zone (**a**) and bonding defects (**b**)

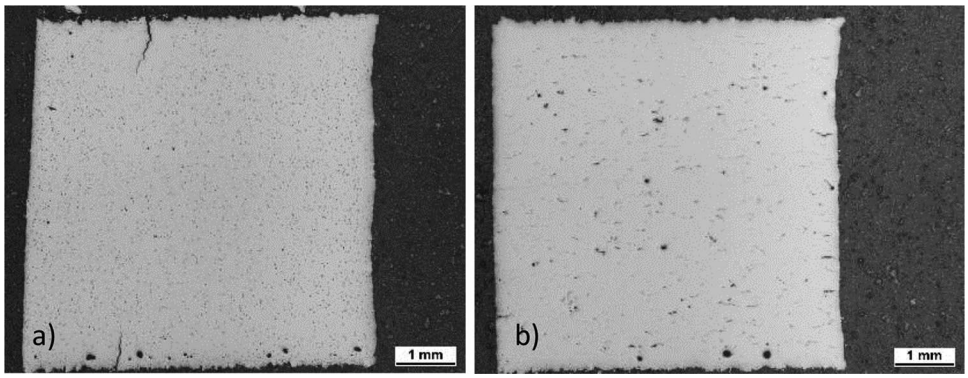

Fig. 14 WC-modified 16MnCr5 base material with 5 wt.-% WC (**a**) and 10 wt.-% WC (**b**)

to the base material can be assumed. This is in accordance with the results presented by [17], who reported an increase by approximately 100 HV for 2 wt.-% WC. Furthermore, in comparison to C-addition, a significant increase in material hardness can be determined already in the as-built state. This could be attributed to the comparably high hardness of WC particles compared to the base material, dispersion hardening effects, or other hardening mechanisms. Standard deviations also tend to increase drastically for larger WC contents. One possible reason for this is the increasing number of defects within the sample.

3.3 Wear analysis

Finally, qualitative wear analysis tests were performed for determining wear rate of manufactured test specimens. Conventionally fabricated and case-hardened 16MnCr5 samples were used as reference system. Furthermore, additively manufactured and case-hardened specimens as well as in situ modified samples with enhanced carbon or WC content were studied. For comparability, roughness values R_a (mean arithmetic roughness) and R_z (maximum height of a specified profile) and R_t (maximum roughness entire sample) are determined. Measurement points (b) as well as corresponding roughness in µm (a) for different material systems are presented in Fig. 19.

System 4, which was manufactured conventionally and subsequently carburized to a carbon content of approximately 0.4% in the case, was set as a reference value. After 1 h of testing, measured R_z value is 0.40 ± 0.02 µm. For unmodified 16MnCr5, the roughness R_z was determined to be around 2.4 ± 0.59 µm. As-built specimens of system 2 (16MnCr5 with a total of 0.42 wt.-% C) result in a significantly higher maximum height of the profile of almost 1.9 ± 0.16 µm. This increase can be attributed to the comparably low hardness in the as-built state. In contrast, specimens with added WC (system 3) show significantly improved wear behavior ($R_z = 0.8 \pm 0.16$ µm) compared to carbon-enriched specimens (system 2). The material hardness in the as-built state is similar for both WC-enriched and CB-enriched material. Therefore, this decreased surface roughness can be attributed to the more wear-resistant carbide network within the test disc. Presented results show the potential of carbide addition, already in the range of 2.5 wt.-%, for improving the wear resistance of additively manufactured samples from case-hardening steels. Here, compared to pure 16MnCr5, a reduction in roughness by factor 3 was realized. However, even as both system 2 and system

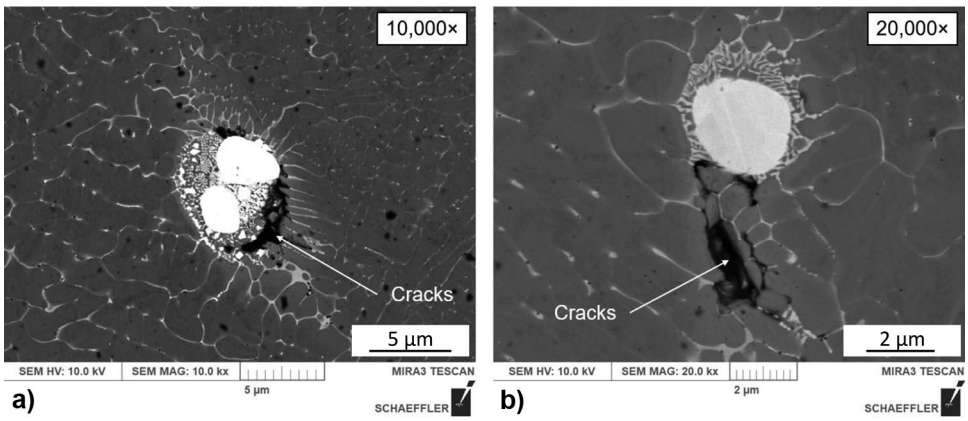

Fig. 15 SEM images of WC particles in a 10 wt.-% WC specimen at 10,000× (**a**) and 20,000× magnification (**b**)

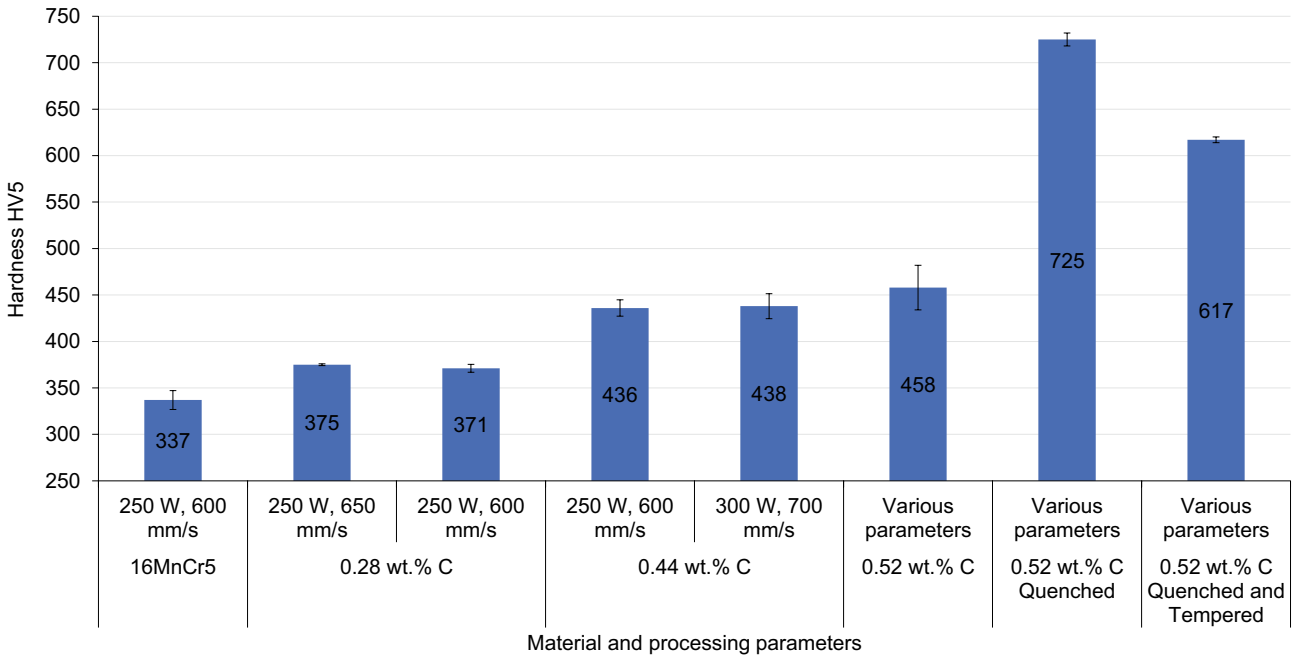

Fig. 16 Mean hardness of C-modified 16MnCr5 at different concentrations and processing parameters in as-built and heat-treated conditions

3 possess similar hardness, wear rate for WC-enriched specimens is reduced by more than 50%. Considering that hardness of WC-enhanced 16MnCr5 (437 ± 2 HV5) compared to C-enriched 16MnCr5 (458 ± 3 HV5) is comparable, it can be concluded that wear resistance is not primarily affected by material hardness. This was already observed by Gore and Gates in 1997 when they found that cast irons in the as-built state possessed a lower wear rate against a dry sand rubber wheel compared to carbon-reduced cast iron. However, changing the material of the wheel to steel resulted in opposite results. This is similar to the findings of this work as material hardness is not the sole indicator of a material wear rate [28]. Further studies by Tjong [29] have also shown that a moderate addition of 5 wt.-% TiB2 to stainless steel already resulted in a significantly reduced wear loss.

Analysis of μ shows a lower coefficient of friction after 60 min of testing for conventionally manufactured and case-hardened samples ($\mu = 0.036$) compared to additively fabricated ones. For carbon-enriched 16MnCr5, coefficient of fiction was determined to be around 0.66, which is similar to the one of the unmodified base materials. WC addition resulted in the lowest coefficient of frictions of approximately 0.030. This reduced coefficient of friction could be another potential indicator for the significantly improved wear performance of WC-modified specimens. Due to the possibility of nearly defect-free fabrication, the addition of WC-particles to 16MnCr5 base material in low concentrations allows for both a significant increase in material hardness and wear resistance. However, even longer testing periods are required for analyzing the removal of hard particles out of the ductile matrix material.

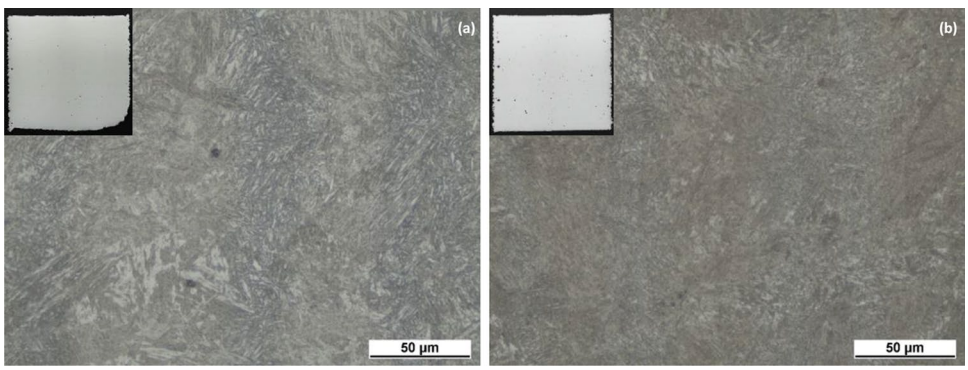

Fig. 17 Etched cross-sections of unmodified (**a**) and carbon black modified to 0.44 wt.-% C (**b**)

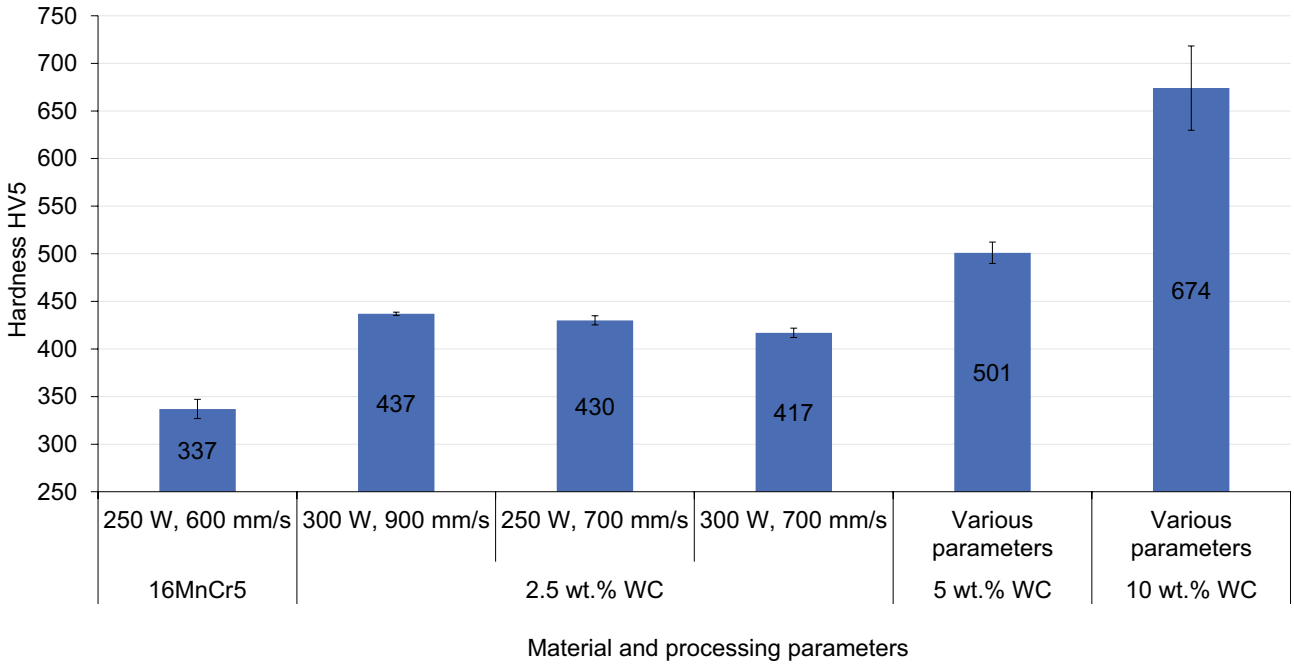

Fig. 18 Mean hardness of WC-modified 16MnCr5 at different concentrations and processing parameters

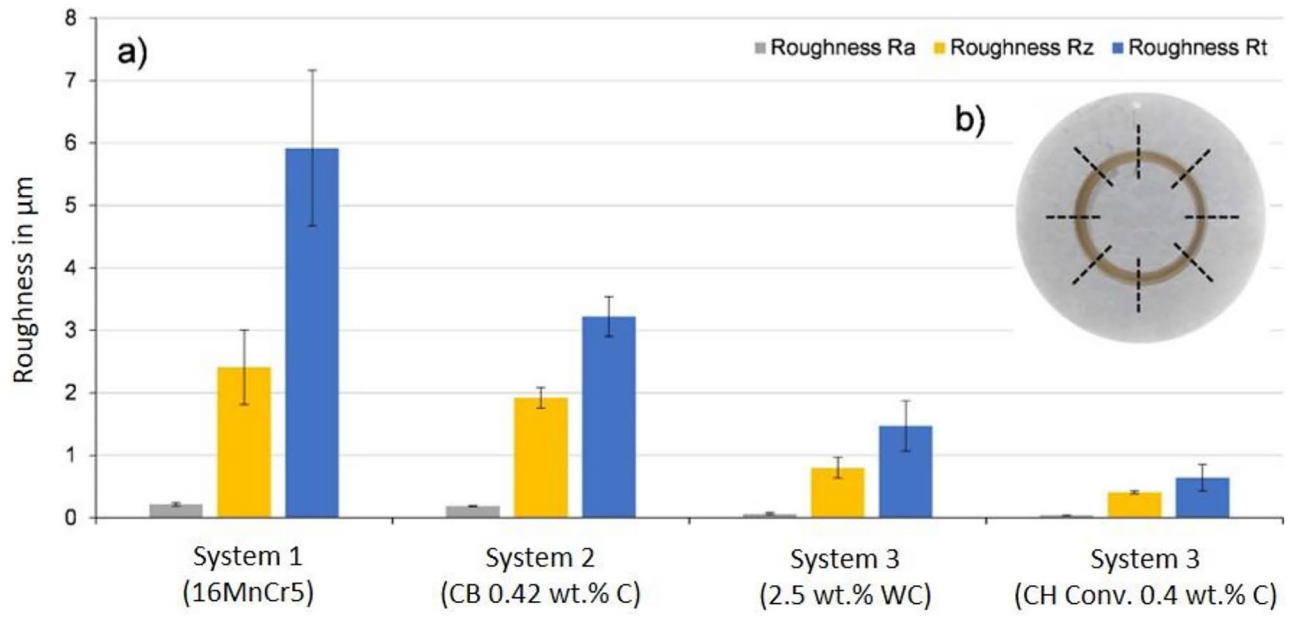

Fig. 19 Mean roughness for different wear samples tested for different material systems (**a**) and measurement points on a worn disc (**b**)

4 Conclusions

In the presented work, in situ material modification using low-alloyed case-hardening steel as base material and carbon black nanoparticles as well as tungsten carbide microparticles as additional alloying component was investigated. Both C- and WC-enriched 16MnCr5 steels were processed successfully using the PBF-LB/M process. In the following, the key findings are summarized:

- The processing of low-alloyed case-hardening steels with carbon contents of up to 0.52 wt.-% is possible by means of PBF-LB/M
- Increasing the carbon content only slightly improves the material hardness in the as-built state, therefore demanding a post-process heat treatment
- Applying a conventional heat treatment proves that the required material hardness for industrial applications of above 615 HV can be achieved
- Carburizing heat treatment strategies for increasing the carbon content could be replaced in the future as materials with an increased carbon content can already be processed nearly defect-free by means of PBF-LB/M
- The addition of WC particles resulted in an increased material hardness and drastically improved wear resistance even for small concentrations in the as-built state
- Carbide reinforcing of the material provides a significant potential for tailoring the wear resistance of additively manufactured specimens as the wear resistance is increased by the factor of two for similar hardness values compared to the as-built material

Based on these results, future work will focus on the combined addition of carbon black and carbide hard particles to further improve the wear resistance of the material. Furthermore, the presented approach can be applied to manufacture highly complex products like gears using a combination of the PBF-LB/M process for generating the main body and the DED-LB/M process for tuning the wear resistance of the product.

Appendix

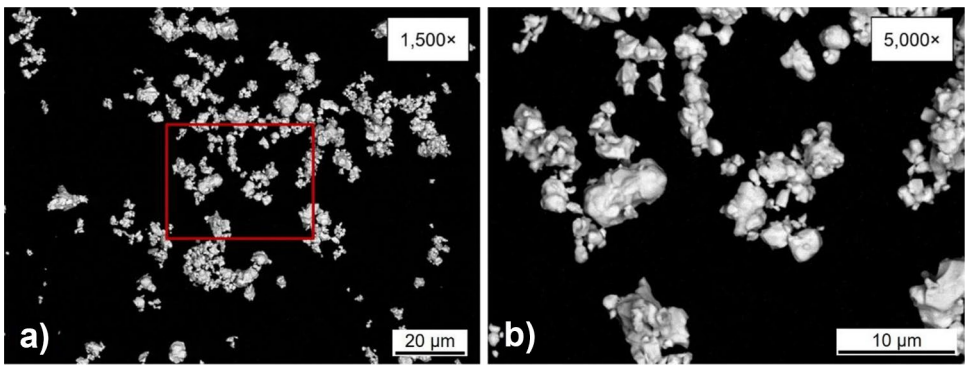

Fig. 20 SEM images of WC particles at 1,500× (**a**) and 5000× (**b**) magnification

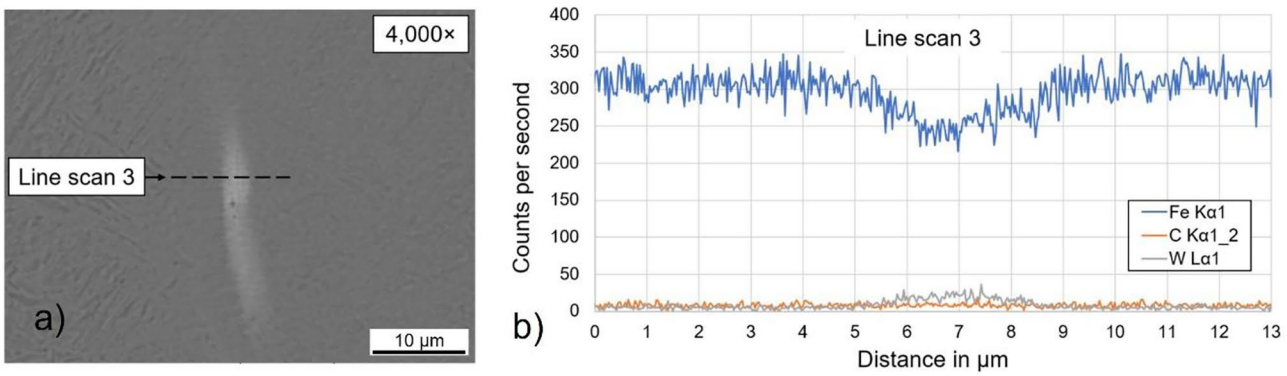

Fig. 21 Bright shimmering tail within WC modified 16MnCr5 (**a**) and the corresponding EDX line scan proving the presence of tungsten (**b**)

Acknowledgements The authors gratefully acknowledge the support provided by the Erlangen Graduate School in Advanced Optical Technologies.

Author contribution The authors have provided an equal contribution to the drafting of the paper.

Funding Open Access funding enabled and organized by Projekt DEAL. The work was supported by the Schaeffler Hub for Advanced Research at Friedrich–Alexander University Erlangen–Nürnberg (SHARE at FAU). This research was also supported by the German Research Foundation (DFG), Collaborative Research Center 814, subproject A5.

Availability of data and material The raw/processed data required to reproduce these findings cannot be shared at this time as the data also forms part of an ongoing study.

Declarations

Ethics approval The authors respect the ethical guidelines of the journal.

Consent to participate Not applicable.

Consent for publication Not applicable.

Competing interests The authors declare no competing interests.

References

1. Liedtke D (2008) Merkblatt 452 Einsatzhärten. Stahl-Informations-Zentrum Ausgabe
2. Palaniradja K, Alagumurthi N, Soundararajan V (2006) Optimization of process variables in gas carburizing—an experimental investigation with AISI 3310 steel material. Mater Manuf Process 21(Heft 1, S):111–113. https://doi.org/10.1080/AMP-200060671
3. Qian M, Xu W, Brandt M et al (2016) Additive manufacturing and postprocessing of Ti-6Al-4V for superior mechanical properties. MRS Bullet 41(Heft 10, S):775–784. https://doi.org/10.1557/mrs.2016.215
4. Song B, Zhao X, Li S et al (2015) Differences in microstructure and properties between selective laser melting and traditional manufacturing for fabrication of metal parts: a review. Front Mech Eng 10 (2015)(Heft 2, S):111–125. https://doi.org/10.1007/s11465-015-0341-2
5. Kamps T (2018) Leichtbau von Stirnzahnrädern aus Einsatzstahl mittels Laserstrahlschmelzen. Universitätsbibliothek der TU München, München
6. Schmitt M, Schlick G, Seidel C et al (2018) Examination of the processability of 16MnCr5 by means of laser powder bed fusion. Procedia CIRP 74:76–81. https://doi.org/10.1016/j.procir.2018.08.041
7. Bartels D, Klaffki J, Pitz I et al (2020) Investigation on the case-hardening behavior of additively manufactured 16MnCr5. Metals 10(Heft 4, S):536. https://doi.org/10.3390/met10040536
8. Schmitt M, Kamps T, Siglmüller F et al (2020) Laser-based powder bed fusion of 16MnCr5 and resulting material properties. Additive Manuf 35(S):101372. https://doi.org/10.1016/j.addma.2020.101372
9. Aumayr C, Platl J, Zunko H et al (2020) Additive manufacturing of a low-alloyed engineering steel. BHM Berg- und Hüttenmännische Monatshefte 165(Heft 3, S):137–142. https://doi.org/10.1007/s00501-020-00966-3
10. Yang M, Sisson RD (2020) Carburizing heat treatment of selective-laser-melted 20MnCr5 steel. J Mater Eng Perform 173(Heft 1, S)20. https://doi.org/10.1007/s11665-020-04564-9
11. Zumofen L, Kirchheim A, Dennig H-J (2020) Laser powder bed fusion of 30CrNiMo8 steel for quenching and tempering: examination of the processability and mechanical properties. Progr Additive Manuf 5(Heft 1, S)75–81. https://doi.org/10.1007/s40964-020-00121-x
12. Wanke K, Schramm K (1963) Stahlhärtung. Fachbuch für die Wärmebehandlung von Eisenlegierungen. Grundlagen, Technoloige, Prüfung. VEB Verlag Technik, Berlin
13. Bischof C, Nitsch G, Scheitler C et al (2016) Laser beam melting of water atomized iron base alloy FE-4800 with in-situ alloying of carbon nanoparticles. Proceedings of the 17th Annual Conference of the Rapid Product Development Association of South Africa
14. Huber F, Bischof C, Hentschel O et al (2019) Laser beam melting and heat-treatment of 1.2343 (AISI H11) tool steel – microstructure and mechanical properties. Mater Sci Eng: A 742(S) 109–115. https://doi.org/10.1016/j.msea.2018.11.001
15. Schmitt M, Gottwalt A, Winkler J et al (2021) Carbon particle in-situ alloying of the case-hardening steel 16MnCr5 in laser powder bed fusion. Metals 11 (Heft 6, S):896. https://doi.org/10.3390/met11060896
16. Hentschel O, Siegel L, Scheitler C et al (2018) Processing of AISI H11 tool steel powder modified with carbon black nanoparticles for the additive manufacturing of forging tools with tailored mechanical properties by means of laser metal deposition (LMD). Metals 8(Heft 9, S):659. https://doi.org/10.3390/met8090659
17. Yan X, Chen C, Zhao R et al (2019) Selective laser melting of WC reinforced maraging steel 300: Microstructure characterization and tribological performance. Surf Coat Technol 371:355–365. https://doi.org/10.1016/j.surfcoat.2018.11.033
18. Kang N, Ma W, Heraud L et al (2018) Selective laser melting of tungsten carbide reinforced maraging steel composite. Addit Manuf 22:104–110. https://doi.org/10.1016/j.addma.2018.04.031
19. Gu D, Ma J, Chen H et al (2018) Laser additive manufactured WC reinforced Fe-based composites with gradient reinforcement/matrix interface and enhanced performance. Compos Struct 192:387–396. https://doi.org/10.1016/j.compstruct.2018.03.008
20. Shi Q, Gu D, Lin K et al (2018) The role of reinforcing particle size in tailoring interfacial microstructure and wear performance of selective laser melting WC/Inconel 718 composites. J Manuf Sci Eng 140(Heft 11, S):74. https://doi.org/10.1115/1.4040544
21. Grünenwald B, Bischoff E, Shen J et al (1992) Laser surface alloying of case hardening steel with tungsten carbide and carbon. Mater Sci Technol 8(Heft 7, S):637–644. https://doi.org/10.1179/mst.1992.8.7.637
22. Schaak C, Kleszczynski S, Tillmann W et al (2019) Investigation of LBM-processed bimodal powder mixtures of the nickel base alloy HX and WC–Co. Progr Additive Manuf 4(Heft 1, S):43–54. https://doi.org/10.1007/s40964-018-0058-y

23. Chen H, Gu D, Zhang H et al (2021) Novel WC-reinforced iron-based composites with excellent mechanical properties synthesized by laser additive manufacturing: Underlying role of reinforcement weight fraction. J Mater Process Technol 289(S):116959. https://doi.org/10.1016/j.jmatprotec.2020.116959
24. Chen H, Gu D, Deng L et al (2021) Laser additive manufactured high-performance Fe-based composites with unique strengthening structure. J Mater Sci Technol 89:242–252. https://doi.org/10.1016/j.jmst.2020.04.011
25. Hutchinson B, Hagström J, Karlsson O et al (2011) Microstructures and hardness of as-quenched martensites (0.1–0.5%C). Acta Materialia 59(Heft 14, S):5845–5858. https://doi.org/10.1016/j.actamat.2011.05.061
26. Reinert L, Suarez S, Müller T et al (2017) Carbon nanoparticle-reinforced metal matrix composites: microstructural tailoring and predictive modeling. Adv Eng Mater 19(Heft 5, S):1600750. https://doi.org/10.1002/adem.201600750
27. Hall EO (1954) Variation of hardness of metals with grain size. Nature 173(Heft 4411, S):948–949. https://doi.org/10.1038/173948b0
28. Gore GJ, Gates JD (1997) Effect of hardness on three very different forms of wear. Wear 203–204:544–563. https://doi.org/10.1016/S0043-1648(96)07414-5
29. Tjong S (2000) Abrasion resistance of stainless-steel composites reinforced with hard TiB2 particles. Composites Sci Technol 60(Heft 8, S):1141–1146. https://doi.org/10.1016/S0266-3538(00)00008-7

Contribution to the Goal of this Work:

Results on the in-situ modification of case-hardening steels with elemental carbon and WC particles are presented. Elemental carbon nanoparticles can be successfully added to increase the carbon concentration of the workpiece. However, higher carbon concentrations promote pore formation and thus negatively affect the processability of the material. Even though case-hardening steels with carbon concentrations of around 0.45 wt.-% in the solid can be processed successfully, the resulting as-built hardness falls below the defined threshold of around 615 HV1. Correspondingly, an ex-situ hardening is still necessary to achieve the demanded hardness both in the quenched (725 HV1) and quenched and tempered state (617 HV1, 200 °C). Furthermore, the addition of WC particles to form an MMC was investigated. It was found that the processing strategy plays an important role when adding hard particles. High energy inputs lead to a dissolving or partial melting of the WC particles while lower energy inputs result in a fine and homogeneous dispersion within the matrix of the case-hardening steel. Furthermore, the crack tendency rises with increasing WC concentrations. Low WC concentrations (2.5 wt.-%) are characterised by only minor bonding defects between the particles and the matrix. Higher WC concentrations (≥ 5 wt.-%) lead to a pronounced carbide network originating from the embeddes WC particles and macroscopic cracks throughout the specimen. Even though the targeted hardness could only be achieved for the highest WC concentration (10 wt.-%, 674 HV1), a positive impact on the wear resistance was already observed for low WC concentrations. At the same material hardness of around 430 HV1, the addition of WC particles helped to reduce the wear of the material by the factor of two. Correspondingly, the contribution to RQ3 is that sufficiently hard materials can be generated in PBF-LB/M when premixing case-hardening steels with C or WC. Carbon-modified specimens can be processed at the absence of cracks but require an ex-situ hardening to achieve a sufficiently high hardness. Consequently, the carburisation heat treatment step can be spared. WC specimens possess a sufficient hardness but are characterised by a promoted crack tendency. Based on these findings, the WC concentration in PBF-LB/M should not exceed 2.5 wt.-% while the C concentration should be around 0.4 wt.-% and a combined addition appears promising.

Since DED-LB/M is characterised by lower cooling rates, the in-situ modification with C and WC will be analysed in the next step for this process. The reduced cooling rates in combination with the heat accumulation during build-up should be favourable to avoid undesired crack formation and might allow for the use of higher C or WC concentrations.

6.3 In-situ Alloying with Carbon for flexible Hardness Depths in DED-LB/M

Title: Influence of Carbon Content on the Material Properties of Low-alloyed Steel Bainidur AM [P15]

Journal: Additive Manufacturing in Multidisciplinary Cooperation and Production, Springer Tracts in Additive Manufacturing, Springer

DOI to Web-version: https://doi.org/10.1007/978-3-031-37671-9_10

Authors: Dominic Bartels, Tobias Novotny, Michael Schmidt

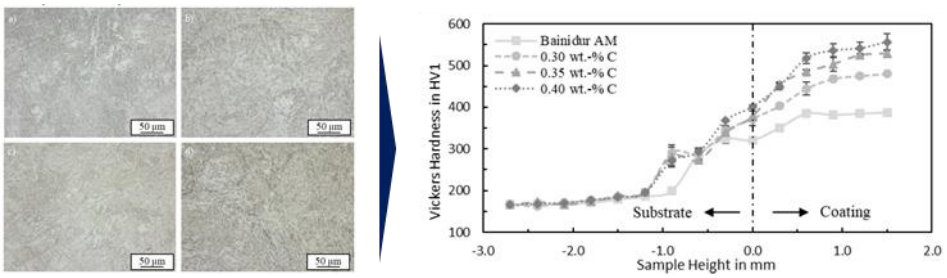

Motivation and Key Findings:

Carbon is the main alloying element for improving the material hardness of most steels since it supports the formation of hard martensite. The DED-LB/M process allows for a fast switching between different powder materials to modify the chemical composition of a material on-the-fly. Correspondingly, the flexibility of DED-LB/M supports the generation of graded structures with tailorable material properties. This work presents investigations on the correlations between carbon concentration and resulting material properties of carbon-reinforced case-hardening steels. The **highlights** are:

- Influence of varying carbon concentration on the material properties of case-hardening steels processed by DED-LB/M
- Linear correlation between carbon concentration and material hardness due to an almost complete transformation into martensite
- Potential for tailoring flexible case-hardening depths through the variation of the layer numbers

Chapter 10
Influence of Carbon Content on the Material Properties of Low-Alloyed Steel Bainidur AM

Dominic Bartels, Tobias Novotny, and Michael Schmidt

Abstract Low-alloyed steels are used in various application fields like gearing and bearing technology. The hardenability of these steels is mainly determined by the carbon content, which increases the strength of the martensitic phase. Since low-alloyed steels typically possess a low carbon content below 0.2 wt.%, an additional post-process heat treatment in a carbon-rich atmosphere is necessary to increase the carbon concentration in the product's case. Another potential approach for improving the strength of the part's surface is provided by applying additive manufacturing processes like laser-based directed energy deposition (DED-LB/M). Powder-based DED-LB/M supports in-situ alloying since multiple powder hoppers can be used for supplying the different powder materials. By adding e.g., carbon or hard particles, the hardness and wear resistance of the part can be tailored to the needs of the final application. However, to exploit the potentials of in-situ alloying for the deposition of optimized structures, the influence of the chemical composition, especially the carbon content, on the resulting material properties needs to be known. Within this work, the low-alloyed steel Bainidur AM (0.23 wt.% C) is processed by means of DED-LB/M. Furthermore, elemental carbon nanoparticles are added to increase the total carbon concentration up to 0.3 wt.%, 0.35 wt.%, and 0.4 wt.% within the powder. Multiple layers are manufactured to investigate the underlying material properties. The relative part density is only barely affected by the different carbon contents. Furthermore, the increased carbon content did not result in an increased crack tendency. Light optical microscopy reveals a primarily martensitic microstructure for all carbon contents. The material hardness increases linearly with increasing carbon concentration. Whereas the hardness of the unmodified Bainidur AM falls

D. Bartels (✉) · T. Novotny · M. Schmidt
Institute of Photonic Technologies (LPT), Friedrich-Alexander-Universität Erlangen-Nürnberg (FAU), Konrad-Zuse-Straße 3/5, 91052 Erlangen, Germany
e-mail: dominic.bartels@lpt.uni-erlangen.de

D. Bartels · M. Schmidt
Erlangen Graduate School in Advanced Optical Technologies (SAOT), Friedrich-Alexander-Universität Erlangen-Nürnberg (FAU), Paul-Gordan-Straße 6, 91052 Erlangen, Germany

I. Drstvensek et al. (eds.), *Additive Manufacturing in Multidisciplinary Cooperation and Production*, Springer Tracts in Additive Manufacturing,
https://doi.org/10.1007/978-3-031-37671-9_10

in the range of just below 400 HV1, a maximum hardness of around 560 HV1 was observed for a carbon content of 0.4 wt.%.

Keywords DED-LB/M · Low-alloyed steels · Carbon concentration · Coating · Bainidur AM

10.1 Introduction

Low-alloyed case-hardening steels like 16MnCr5, 20MnCr5, or 18CrNi8 are used in different fields of application due to their material properties [1]. Their alloy design results in good processability across different manufacturing technologies at the expense of material hardness. This can be attributed to a low con-centration of carbon and nitrogen, which are considered major drivers of hardenability in steels. The chemical composition of this class of steels supports the carbon and nitrogen diffusion at elevated temperatures, which is beneficiary for hardening these materials in a subsequent step [2]. Carburizing and nitrating heat treatments require long holding times at high temperatures. Correspondingly, these processes are mostly used for large batches of e.g., gears, shafts, or bearings. The fabrication of smaller lot sizes, however, is not necessarily economically efficient. Furthermore, the conventional case-hardening process is limited regarding the spatially-resolved carburizing of the parts. To tailor the carbon diffusion, the specimens need to be e.g., covered to avoid excessive carbon concentrations in the shell/case of the product [3].

Additive manufacturing technologies like directed energy deposition (DED-LB/M) are mainly used for the fabrication of small lot sizes since the long processing times are associated with high costs-per-part. However, the flexibility regarding material use and local processing allows for the tailoring of surfaces by e.g., selectively increasing the carbon content [4] or adding hard phase particles [5].

In the past, DED-LB/M has been used for the processing of different materials, ranging from aluminum alloys [6] over titanium alloys [7] to high-strength steels [8] and even duplex stainless steels [9]. Low-alloyed steels, however, have received comparatively little research attention. Bartels et al. [10] studied the influence of different process parameters on the resulting material properties of the low-alloyed steel Bainidur AM. A wide parameter window could be identified for the processing of these steels by means of DED-LB/M. Furthermore, first investigations on increasing the hardness by adding hard phase particles have been performed [11]. In contrast to DED-LB/M, case-hardening steels like 16MnCr5 or 20MnCr5 have already been researched more thoroughly in laser powder bed fusion (PBF-LB/M) [12–14]. The additively manufactured steels possess a high relative part density and do not possess cracks when processed by means of PBF-LB/M. Furthermore, the underlying microstructure can be identified as at least partially bainitic. First studies also investigated the in-situ modification of the material properties by carbon [15, 16] and tungsten carbide [16] addition.

Hentschel et al. [4] added carbon black nanoparticle concentrations of up to 0.5 wt. % to tool steel AISI H11 prior to processing the powder blends by means of DED-LB/M. They found that crack-free specimens could be manufactured for total carbon contents of up to approximately 0.6 wt.%. The material hardness increased continuously for higher carbon content, which was attributed to the higher strength of the martensitic phase. This approach appears feasible for experimentally determining the limits of carbon addition to low alloy steels for the DED-LB/M process. Goal of this work is to study the influence of different carbon concentrations on the resulting material properties of the low-alloyed steel Bainidur AM. The carbon content is increased continuously to analyze the resulting microstructure and the corresponding material hardness.

10.2 Materials and Methods

Low-alloyed steel Bainidur AM with a particle size range from 45 to 90 µm was used for performing the experiments. A Camsizer was further used for determining the particle size distribution of the steel powder. D_{10}, D_{50}, and D_{90} values of the Bainidur AM powder are 58.8 µm, 80.8 µm, and 100.4 µm, respectively.

For generating the powder blends, carbon black nanoparticles (Type: N550 carbon black, Harald Scholz GmbH, Germany) with a carbon content of approximately 99% were used. The particle size varies between 50 and 100 nm according to the supplier. All powder materials (Bainidur AM and carbon nanoparticles) were dried in a vacuum furnace at 110 °C for 12 h prior to mixing. Powder mixtures with a total mass of 300 g were prepared. The carbon concentration of the base powder was determined using an elemental analyzer of type CS (ELTRA GmbH, Germany). A carbon content of 0.23 wt.% was determined for Bainidur AM. Three additional powder mixtures were generated with total carbon contents of 0.3 wt.% (+0.07 wt.%), 0.35 wt.% (+0.12 wt.%), and 0.4 wt.% (+0.17 wt.%) were generated. First, the base material Bainidur AM was filled into a glass container. Next, the required amount of carbon black was added until the desired carbon content was achieved. The powder blend was stirred using a spoon to avoid undesired agglomerations at the surface of the glass. After that, the powder blend was mixed for two hours using a turbula mixing unit.

DED-LB/M experiments were performed on an ERLAS 50,237 DED machine (ERLAS GmbH, Germany). The machine is equipped with a 4 kW diode laser with a characteristic wavelength ranging from 940 to 963 nm (Type: LDF 4000–4, Laserline GmbH, Germany). Laser spot size can be adjusted between 1 and 3 mm using a zoom optic.

16MnCr5 steel plates (200 × 200 x 15.3 mm^3) were used as substrates for all experiments (Abrams Steel GmbH, Germany). The process parameters were selected based on previous investigations using the low-alloyed steel Bainidur AM [10]. Throughout the experiments, all parameters, except for the chemical composition of the powder material, were kept constant. The process parameters are listed in Table 10.1.

Table 10.1 Process parameters for manufacturing the specimens by means of DED-LB/M

Process parameter	Value
Laser Power [W]	600
Feed Rate [mm/min]	400
Laser Spot Size [mm]	1.5
Weld Track Width [mm]	1.5
Powder Mass Flow [g/min]	2.98 ± 0.02
Avg. layer height [mm]	0.45

Shielding and carrier gas flow were set to 20 L/min and 4 L/min, respectively. Argon of type 4.6 was used for both gas flows. The powder material was supplied using a three-jet nozzle. Four-layered specimens with an edge-length of 10 mm were manufactured. The core of the specimen was generated using a meander-shape strategy. An overlap of 50% was chosen between the single weld tracks that form the final geometry. Afterwards, the four contour tracks were deposited along each edge of the specimen. The build direction was rotated by 90 °C after the deposition of each layer.

After fabrication, all samples were analyzed in a metallographic laboratory. The specimens were cut in half before cold mounting. Samples were further prepared by grinding and polishing with a 1 µm diamond suspension. Images of the polished cross-sections were generated by means of optical light microscopy to assess the relative part density and crack formation. Furthermore, the material hardness was determined on these cross-sections using an indentation tester. The hardness was measured every 300 µm and at least five times per layer. After the hardness measurements were performed, the samples were etched using a 3%-Nital solution to reveal the microstructure. Again, optical light microscopy was used to analyze the cross-sections within the different regions of the specimens.

10.3 Results and Discussion

The results section is divided into three sub-sections. First, the macroscopic relative part density and etching behavior is addressed. The microstructural properties in different regions of the specimen are presented in a second step. Finally, the underlying material hardness is shown for the different carbon concentrations.

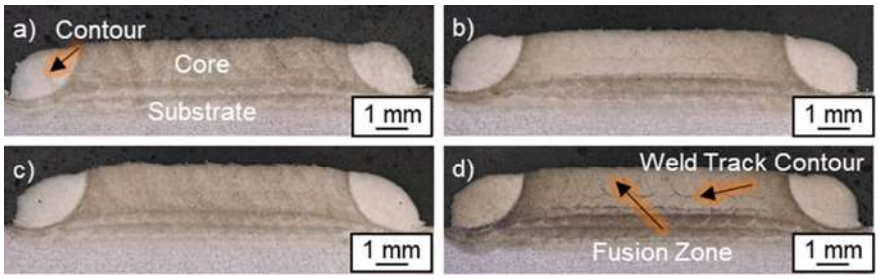

Fig. 10.1 Cross-sections of the additively manufactured structures for **a** unmodified Bainidur AM, **b** 0.3 wt.% C, **c** 0.35 wt.% C, and **d** 0.4 wt.% C

10.3.1 Macroscopic Structure of the Specimens

In the first step, the cross-sections of the specimens were analyzed regarding relative part density and internal defects like cracks and larger pores. The images of the etched cross-sections are presented in Fig. 10.1.

All specimens possess a high relative part density exceeding 99.9%. Noticeable pores were only found in the contour track. Furthermore, no cracks were formed even for the higher carbon concentrations. This shows that a good part quality can be achieved despite the high cooling rates and the increased carbon content. Furthermore, the geometrical part properties like part height or weld track geometry did not change significantly.

Each specimen can be divided into three main regions: core, contour, and substrate. The microstructure of the substrate is mostly unaffected, except for the heat-affected zone. Within the core region, the DED-LB/M-specific weld tracks can be identified. The boundary of these weld tracks appears mostly whitish after etching, which might indicate the presence of retained austenitic. Finally, the contour tracks are characterized by a bright etching. This region was exposed to a faster cooling during build-up due to the ambient atmosphere. Since the contour was always manufactured at the end of one layer, no in-situ heat treatment from adjacent weld tracks is present.

10.3.2 Microstructural Part Properties

The microstructure was analyzed in two different regions of each specimen. This includes the dilution zone between substrate and cladding (see Fig. 10.2) as well as the core region close to the surface (see Fig. 10.3) of the additively manufactured structure. Figure 10.2 shows the microstructure that is formed in the dilution zone of the specimens.

A similar microstructure can be observed in the dilution zone for all carbon concentrations. The structure appears predominantly lath-like with some shares of

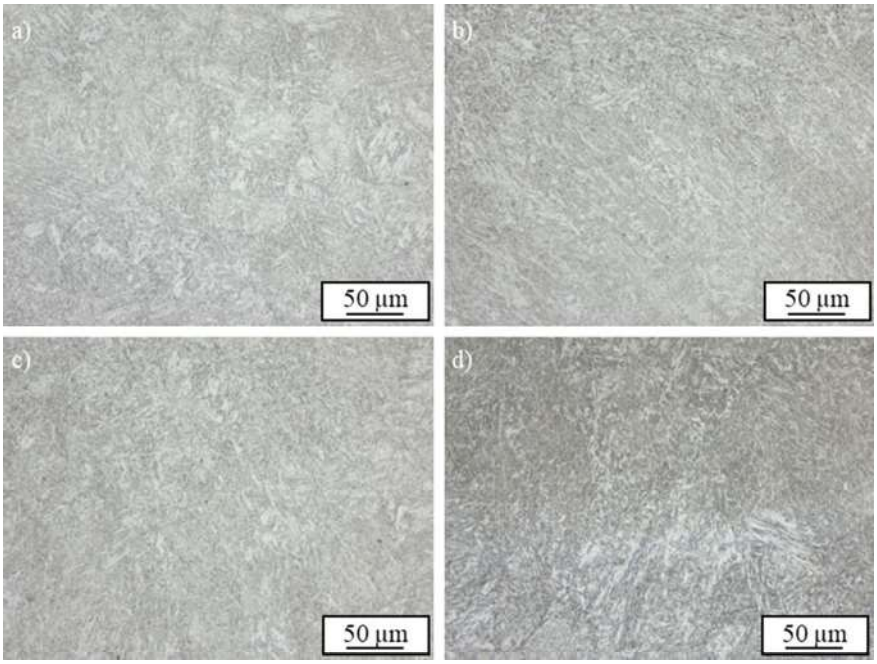

Fig. 10.2 Etched cross-section of the dilution zone for **a** unmodified Bainidur AM, **b** 0.3 wt.% C, **c** 0.35 wt.% C, and **d** 0.4 wt.% C

white blocks. These blocks are most likely austenite that was not completely transformed during cooling. Furthermore, the weld boundaries possess a slightly different structure than the fusion zone of the weld tracks. The weld track boundaries appear brighter due to the white and blueish structures. In contrast, the fusion zone of the specimens is characterized by browner etching response.

Moving towards the top region of the specimen, a change in microstructure can be observed. Figure 10.3 shows the images for the different carbon concentrations.

Here, a change from the lath-like structure towards a more granular-like structure can be observed. This granular structure is permeated with fine needles, which are characteristic for martensite. Furthermore, the microstructure tends to be refined with increasing carbon concentration. This might be attributable to the carbon black nanoparticles, which could act as nucleation agents during solidification.

10.3.3 Material Hardness

Finally, the material hardness was determined for the different carbon concentrations. The hardness was measured within each layer as well as within the substrate and the dilution zone. Three samples were analyzed per parameter combination. Figure 10.4

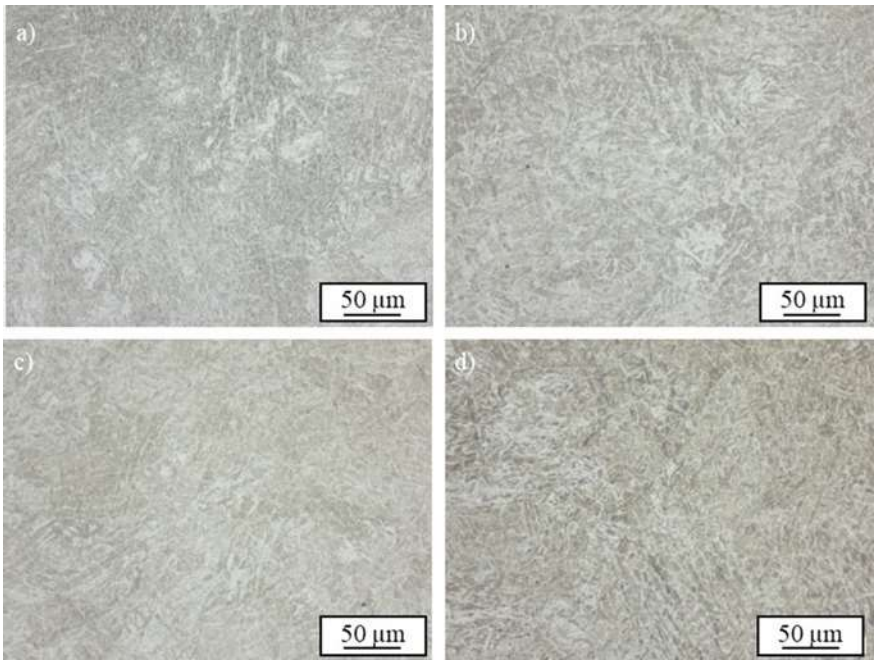

Fig. 10.3 Etched cross-section of the top regions for **a** unmodified Bainidur AM, **b** 0.3 wt.% C, **c** 0.35 wt.% C, and **d** 0.4 wt.% C

shows the material hardness for the different carbon concentrations. The unmodified base material Bainidur AM is characterized by the lowest material hardness. At the surface of the specimen, an average hardness of around 390 HV1 was obtained. Increasing the carbon content to 0.3 wt.% C leads to an increase in hardness up to 460 HV1. An even higher carbon content of 0.35 wt.% C results in a hardness of around 510 HV1. The highest hardness of around 560 HV1 was determined for the highest carbon concentration (0.4 wt.% C). This hardness rise can be explained by the higher hardness of the martensite for larger carbon contents.

Furthermore, the material hardness also increases in the dilution zone for higher carbon concentrations. This is due to both mixing effects and the energy input in this region. Since the carbon content of the base material is lower than that of the coating in all cases, the mixing results in a higher hardness of the dilution zone. Furthermore, the penetration depth of the laser results in a local melting of the material as well as the formation of the corresponding heat-affected zone. This also results in an increased material hardness in this region, even though the carbon concentration is most likely the same as in the substrate. Finally, the experimentally obtained hardness is compared with the theoretically achievable one. The as-built hardness as well as the maximum theoretical hardness are shown in Table 10.2.

The hardness values of the martensitic-hardened specimens were extracted from literature [17, 18]. It can be seen that the material hardness falls short of what is

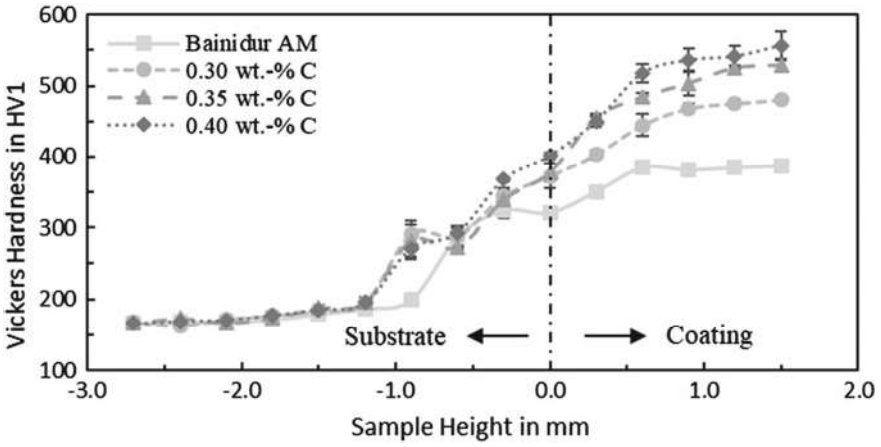

Fig. 10.4 Material hardness of the coatings deposited with different carbon concentrations

Table 10.2 Experimentally determined hardness for Bainidur AM and its powder blends with different carbon concentrations. The theoretical material hardness was approximated based on the work of Gerber and Wyss using a 95% and 99% transformation [17, 18]

Powder Blend	Hardness as-built [HV1]	Hardness, 95% transformed [HV1]	Hardness, 99% transformed [HV1]
Bainidur AM	390	420 to 430	450 to 470
0.30 wt.% C	460	480 to 490	500 to 520
0.35 wt.% C	510	520 to 530	550 to 570
0.40 wt.% C	560	560 to 570	600 to 620

theoretically achievable. The hardness of Bainidur AM in the as-built state should be approximately 470 HV1 for a hardened specimen. This can be attributed to several effects. First, and most likely, the microstructure is not transformed completely into martensite. This is associated with a decrease of the hardness due to retained austenite and other low-strength phases. Second, the in-situ heat treatment during DED-LB/M reduces the hardness by tempering the initially martensitic microstructure. This tempering is caused by adjacent weld tracks and by the processing of subsequent layers. Third, the heat accumulation during build-up increases the lower transformation temperature to which the molten material is cooled. The transformation is therefore performed differently in e.g., lower and higher regions of the specimens. This assumption is supported by the different etching behaviors in the top regions and the ones close to the substrate.

10.4 Conclusion

This work shows the influence of different carbon concentrations on the material properties of the low-alloyed steel Bainidur AM processed by means of DED-LB/M. Defect-free specimens could be manufactured both for the base material and for carbon concentrations of up to 0.4 wt.%. Different microstructures were observed within the dilution zone and the coated structure due to the different chemical compositions and cooling conditions. The microstructure analysis is supported by hardness measurements. The material hardness rises almost linearly with increasing carbon concentrations. Depending on the carbon content, structures with a material hardness of as much as 560 HV1 could be generated successfully. The hardness of the DED-LB/M specimens approximates the theoretically achievable hardness for martensite when roughly 95% of the austenite was transformed. Future work will focus on the processing of powder blends with even higher carbon ratios and the simultaneous admixture of hard phase particles like tungsten carbide to further improve the hardness and wear resistance.

Acknowledgements The authors would like to thank the German Federal Ministry for Economic Affairs and Energy for funding the joint project HyConnect (FKZ: 03LB3010*), within the framework of which the present investigations were carried out. We also thank the Deutsche Forschungsgemeinschaft DFG for the grant 359757317. Furthermore, the authors would like to thank the Deutsche Edelstahlwerke Specialty Steel GmbH & Co. KG and Schaeffler Technologies AG & Co. KG for their support. The authors gratefully acknowledge the support provided by the Erlangen Graduate School in Advanced Optical Technologies.

Funding This work was funded by the German Federal Ministry for Economic Affairs and Energy for funding the joint project HyConnect (FKZ: 03LB3010*).

Data Availability Statement The data is available upon on request.

References

1. Schatt, W. (ed): Konstruktionswerkstoffe des Maschinen- und Anlagenbaues: 131 Tabellen (Dt. Verl. für Grundstoffindustrie; Wiley-VCH, Stuttgart, [Weinheim], 2001)
2. Grosch, J., Bartz, W.J.: Einsatzhärten: Grundlagen - Verfahren - Anwendung - Eigenschaften einsatzgehärteter Gefüge und Bauteile: Grundlagen - Verfahren - Anwendung - Eigenschaften einsatzgehärteter Gefüge und Bauteile (Expert, Tübingen, 2019)
3. Davis, J.R.: Surface hardening of steels: Understanding the basics: understanding the basics (ASM International, Materials Park, OH, 2002)
4. Hentschel, O., Siegel, L., Scheitler, C., Huber, F., Junker, D., Gorunow, A., Schmidt, M.: Metals **8**, 659 (2018)
5. Benarji, K., Ravi kumar, Y., Jinoop, A.N., Paul, C.P., Bindra, K.S.: J. Mater. Eng. Perform. **30**, 6732 (2021)
6. Javidani, M., Arreguin-Zavala, J., Danovitch, J., Tian, Y., Brochu, M.: J Therm Spray Tech **26**, 587 (2017)
7. Azarniya, A., Colera, X.G., Mirzaali, M.J., Sovizi, S., Bartolomeu, F., St Weglowski, M., Wits, W.W., Yap, C.Y., Ahn, J., Miranda, G., Silva, F.S., Madaah, H.R., Hosseini, Ramakrishna, S., Zadpoor, A.A.: J. Alloys Compounds **804**, 163 (2019)

8. Hentschel, O., Scheitler, C., Fedorov, A., Junker, D., Gorunov, A., Haimerl, A., Merklein, M., Schmidt, M.: J. Laser Appl. **29**, 22307 (2017)
9. Maier, A., Munk, A., Kühl, A., Rühr, M., Hentschel, O., Kaufmann, F., Schrauder, J., Roth, S., Schmidt, M.: Procedia CIRP **111**, 241 (2022)
10. Bartels, D., Hentschel, O., Dauer, J., Burgmayr, W., Schmidt, M.: Lasers in Manufacturing (LiM) 2021 (2021)
11. Bartels, D., Rohdenburg, J., Mohr, A., Rothfelder, R., Schmidt, M.: Procedia CIRP **111**, 237 (2022)
12. Schmitt, M., Schlick, G., Seidel, C., Reinhart, G.: Procedia CIRP **74**, 76 (2018)
13. Robatto, L., Rego, R., Mascheroni, J., Kretzer, A., Criscuolo, I., Borille, A.: Procedia CIRP **108**, 873 (2022)
14. Aumayr, C., Platl, J., Zunko, H., Turk, C.: Berg Huettenmaenn Monatsh **165**, 137 (2020)
15. Schmitt, M., Gottwalt, A., Winkler, J., Tobie, T., Schlick, G., Stahl, K., Tetzlaff, U., Schilp, J., Reinhart, G.: Metals **11**, 896 (2021)
16. Bartels, D., Novotny, T., Hentschel, O., Huber, F., Mys, R., Merklein, C., Schmidt, M.: Int J Adv Manuf Technol **120**, 1729 (2022)
17. Liedtke, D.: Mat.-wiss. u. Werkstofftech. **34**, 86 (2003)
18. Gerber, W., Wyss, U.: Von Roll Mitteilungen **7**, 13 (1948)

Contribution to the Goal of this Work:

Different carbon concentrations were added to the case-hardening steel Bainidur AM prior to processing by means of DED-LB/M to investigate the influence on the resulting material properties. Carbon concentration of up to 0.4 wt.-% can be processed at the absence of cracks and larger pores. A linear increase of the hardness depending on the carbon concentration was observed for the DED-LB/M specimens. Furthermore, the material hardness mirrors an almost complete transformation of around 95 % of the austenite into martensite for all investigated carbon concentrations. At a carbon concentration of 0.4 wt.-%, the hardness surpasses 550 HV1, which is the threshold that defines the case-hardening depth. Within these investigations, four layers needed to be deposited to surpass the threshold for the CHD of 550 HV1. It was also found that the surface hardness approximates its maximum since only minor hardness differences are evident between layer three and four. Correspondingly, it can be assumed that the hardness remains at this level. Using higher carbon concentrations in the bonding zone or modified processing strategies that result in reduced mixing effects are possible solutions to reduce the minimum amount of layer required. It was furthermore observed that the microstructure of the main body is only barely affected by the heat input during the deposition of the cladding. The core of the workpiece still possesses its as-delivered material hardness, indicating that no fundamental microstructural transformations are present. With regard to RQ4, it is now possible to generate parts with flexible case-hardening depths by means of DED-LB/M. Processing case-hardening steels with 0.4 wt.-% of carbon allows to tailor the case-hardening depth by depositing more or less layers to the surface of a part. The microstructure of the deposited coating is predominantly martensitic while the microstructure of the main body is mostly unaffected. Correspondingly, this work lays the foundation for the later combined addition of carbon and tungsten carbide particles in DED-LB/M.

The next step focusses on the influence of different WC concentrations on the resulting material properties of case-hardening steels. For PBF-LB/M, it was already found that the hardness rises almost linearly with increasing WC concentrations. Transferring this knowledge to DED-LB/M, the addition of WC particles could prove promising for tailoring the hardness by increasing the WC concentration while simultaneously improving the wear resistance of the material through the formation of an MMC.

6.4 In-situ Reinforcement with Tungsten Carbide for Tailored Surface Hardness in DED-LB/M

Title: Laser Metal Deposition of Carbide-reinforced low-alloyed steel Bainidur AM [P7]

Journal: Procedia CIRP 111, Elsevier

DOI to Web-version: https://doi.org/10.1016/j.procir.2022.08.057

Authors: Dominic Bartels, Jonathan Rohdenburg, Andreas Mohr, Richard Rothfelder, Michael Schmidt

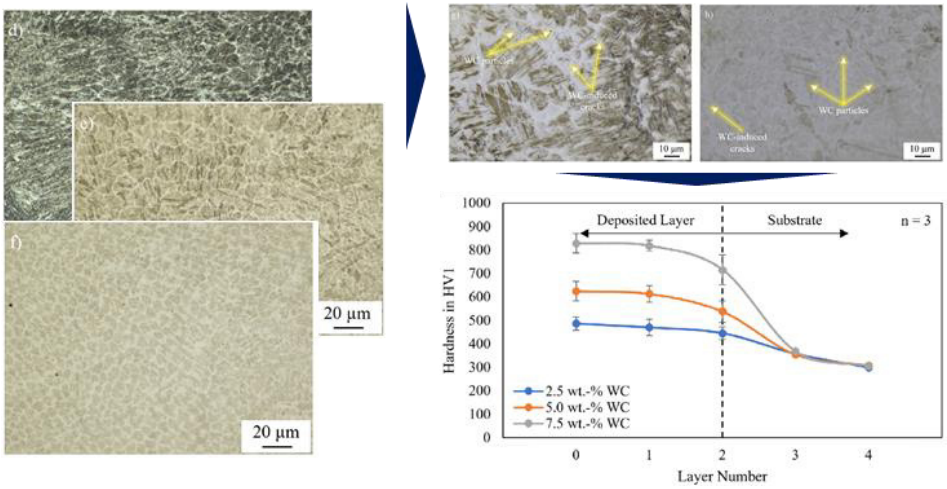

Motivation and Key Findings:

Carbide-reinforced structures improve the wear resistance of a material significantly and are therefore preferred over martensitic-hardened steels. However, the addition of too high hard particle concentrations can lead to bonding defects and crack formation. This work presents investigations on the influence of different WC concentrations on the resulting material properties. The **highlights** are:

- Influence of varying WC concentrations and processing strategies on the processability of case-hardening steels
- Mostly linear correlation between WC concentration and material hardness
- Formation of cracks originating at the grain boundaries for WC concentrations exceeding 5 wt.-%

Available online at www.sciencedirect.com

ScienceDirect

Procedia CIRP 111 (2022) 237–240

www.elsevier.com/locate/procedia

12th CIRP Conference on Photonic Technologies [LANE 2022], 4-8 September 2022, Fürth, Germany

Laser Metal Deposition of Carbide-reinforced low-alloyed steel Bainidur AM

Dominic Bartels[a,b], Jonathan Rohdenburg[a], Andreas Mohr[c], Richard Rothfelder[a,b], Michael Schmidt[a,b]

[a]*Institute of Photonic Technologies (LPT), Friedrich-Alexander-Universität Erlangen-Nürnberg, Konrad-Zuse-Straße 3/5, 91052 Erlangen, Germany*
[b]*Erlangen Graduate School in Advanced Optical Technologies (SAOT), Paul-Gordan-Straße 6, 91052 Erlangen, Germany*
[c]*Deutsche Edelstahlwerke Speciality Steel GmbH & Co. KG, Oberschlesienstraße 16, 47807 Krefeld, Germany*

* Corresponding author. Tel.: +49091318564101; fax: +49091318523234. *E-mail address:* Dominic.bartels@lpt.uni-erlangen.de

Abstract

Case-hardening steels are typically exposed to a post-process carburization or nitriding chemical heat treatment. Laser-based directed energy deposition (DED-LB\M) provides the possibility of substituting this case-hardening step through applying a wear resistant coating. The powder-based process allows for the addition of hard phase particles to the feedstock powder for generating advantageous coatings compared to e.g., solely carburized surfaces. Within this work, the addition of WC hard phase carbides to the low-alloyed steel Bainidur AM is investigated. It is found that the metal matrix is strengthened when adding the WC carbides. Depending on the carbide content and processing strategy, different material hardness through dispersion and partial solving of the carbides are present. Furthermore, a correlation between the applied processing strategy and the material hardness is identified as higher laser power e.g., favor a stronger mixing with the softer substrate.

Keywords: Laser Metal Deposition; Directed Energy Deposition (DED-LB/M); Bainidur AM; Low-alloyed Steel; Carbide reinforcement; WC; Tungsten Carbide

1. Introduction

Low-alloyed steels are commonly used in gearing and bearing applications due to their excellent formability in the as-delivered condition. For the later use, chemical post-process heat treatments like carburization or nitriding are applied to improve the material properties, namely the hardness and corresponding the wear resistance [1]. Additive manufacturing technologies like powder bed fusion using a laser beam (PBF-LB/M) also provide enormous potential in fabricating highly sophisticated products with specific geometries [2,3]. Laser-based processes also support the formation of an ultrafine grain [4] due to the extremely high cooling rates [5]. However, due to crack susceptibility, carbon-rich steels are hard to process. Correspondingly, the material hardness is often insufficient for the mentioned fields of application. Exposing additively manufactured products to e.g., a carburizing or quenching heat treatment results in an at least partial destruction of the underlying fine microstructure [6].

To maintain the process-specific microstructural properties, adjusted manufacturing approaches are needed for generating a hard and wear-resistant case. One potential way of increasing the hardness and wear resistance is provided by laser metal deposition (DED-LB/M). The high flexibility of this process allows for the local reinforcement of the material surface where needed. Hentschel et al. have studied the influence of carbon nanoparticle addition on the properties of tool steel 1.2343 [7]. An increase in material hardness was observed with increasing carbon contents. However, this came at the cost of a poorer processability at too high carbon concentrations. Another way of improving the surface hardness is provided by carbide or oxide addition. Ostolaza et al. have added WC particles in different concentrations to Stellite 6 carrier powder [8]. A continuous hardness increase was observed for higher WC concentrations, peaking in a maximum hardness of around

2212-8271
10.1016/j.procir.2022.08.057

700 HV for a WC ratio of 40 %. Benarji et al. studied the influence of different WC concentrations on the mechanical properties, namely hardness, of stainless steel 316L [9]. Again, an increase in material hardness was observed for higher amounts of WC hard phase particles. The wear resistance of the modified material was more than twice as high as the one of base material 316L. Previous studies by Bartels et al. have also shown that the addition of WC particles is beneficial in increasing the wear resistance of low-alloyed steels [10]. It was found that at similar hardness values the wear rate of WC-reinforced steel is way lower compared to a solely carbon-enriched material.

Goal of this work is to investigate the influence of different WC concentrations on the microstructure formation, defect-tendency, and material hardness of the low-alloyed steel Bainidur AM. Hard particles are known to strengthen the matrix and enhance the wear resistance of the product. Thus, the long-term aim is to substitute conventionally used chemical heat treatments like carburization for adjusting the surface hardness of additively manufactured specimens from low-alloyed steel. One potential advantage of this is that the underlying potentially favorable or fine microstructure of the main body can be maintained during either coating or repair processes.

2. Experimental Approach

Two-layer coatings of a carbide-reinforced low-alloyed steel were manufactured by means of DED-LB/M. Low-alloyed case-hardening steel Bainidur AM (Deutsche Edelstahlwerke, Germany) was used as the base material for the investigations. The nominal grain size of the powder ranged from 45 to 90 µm according to the supplier. WC particles (fisher size: 0.63 µm) were used in three different concentrations (2.5, 5.0, and 7.5 wt.-%) to modify the Bainidur AM base material. The hard phase particles were provided by abcr GmbH (Germany). WC is characterized by an approximate hardness of 2400 HV [11] and possess a melting point around 2,870 °C. Powder mixtures (300 g in total) were made with different carbide concentrations. The powders were mixed using a dry-coating tumbling unit for 2 h. Table 1 lists the powder mixtures and the corresponding carbon content which has been calculated based on the supplier's information.

Table 1: Properties of the powder mixtures used for the experiments.

Powder Mixture	Mass in g Bainidur AM	Mass in g WC	Weight-% Carbon
Bainidur AM	300 g	0 g	0.23 %
2.5 wt.-% WC	292.5 g	7.5 g	0.38 %
5.0 wt.-% WC	285 g	15.0 g	0.52 %
7.5 wt.-% WC	277.5 g	22.5 g	0.67 %

To remove larger powder agglomerates the powder mixtures were sieved using a stainless steel sieve with a mesh size of 150 µm. The experiments were performed on an ERLASER UNIVERSAL 50349 (ERLAS GmbH, Germany) DED machine equipped with a 4 kW diode laser and a zoom optic for adjusting the size of the laser spot.

Throughout the experiments, powder feeding parameters and shielding gas flow were maintained constant. Laser power and feed rate were varied to analyze the influence of different energy inputs on the underlying hardening effect. Higher laser powers result in larger melt pools due to an increased energy input. The feed rate was varied to (a) generate structures with a higher build height and (b) to assess the influence of different average melt pool temperatures on the material properties [12]. Table 2 lists the applied process parameters.

Table 2: Process parameters applied for manufacturing the specimens.

Process Parameter	Value and Unit
Feed Rate	200, 400, 600 mm/min
Laser Power	600, 800, 1000 W
Shielding Gas Flow	20.0 L/min
Carrier Gas Flow	4.0 L/min
Disc Rotational Speed	0.6 rpm

Two-layered specimens with an edge length of 10 mm (x- and y-direction) were manufactured additively. This structure was generated using a meander build-up strategy. Finally, this core structure was followed by contour tracks around the four edges. The second layer was rotated clockwise by 90 °. Layer height was set based on the single layer height A fine balance was used to determine the powder mass flow experimentally. Therefore, the powder material was transported into a closed box for two minutes at least three times. The average powder mass flow was calculated based on this information.

After manufacturing, the samples were cut into two halves and embedded using a cold-embedding resin. All specimens were grinded and polished. The hardness was measured at least six times in each layer using an indentation tester of type KB30S (Hegewald & Peschke, Germany). To avoid influences of the previous indentation point on the material hardness, a distance between 1 mm was chosen along x-direction. The offset in z-direction (among build direction) was set according to the average layer height (for further information please check [13]). In the next step, the cross-sections were etched using a 3-% Nital solution to promote the microstructure. Images of these cross-sections were taken using and optical light microscope to assess defects, presence of carbides, and microstructure formation.

3. Results

In the first step, the powder mass flow of the three different powder materials was determined. The average mass flow slightly decreased from 2.79 ± 0.01 g/min (2.5 wt.-% WC) over 2.78 ± 0.03 g/min (5 wt.-% WC) to 2.63 ± 0.01 g/min (7.5 wt.-% WC). This reduction in powder mass flow can be attributed to the poorer flowability of the milled WC particles. Due to the irregular shape, in combination with the small particle size, a reduced flowability is probable.

Fig. 1 a) to c) exemplary presents the cross-sections of additively manufactured Bainidur AM specimens with different carbide concentrations ranging from 2.5 wt.-% to 7.5 wt.-% for comparable process parameters. All samples could be fabricated for the investigated parameter window

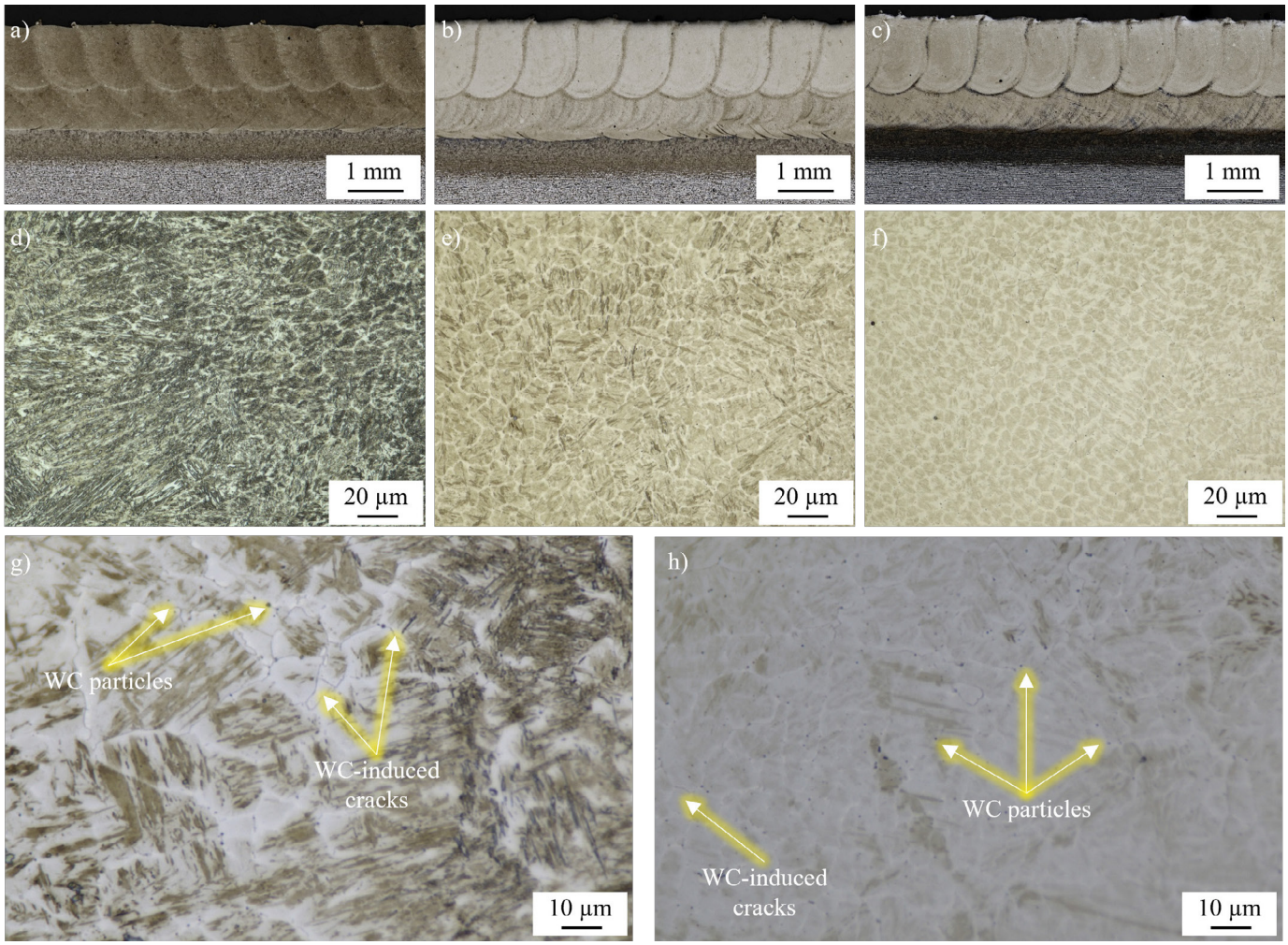

Fig. 1: Microstructure of specimens manufactured with (a, d) 2.5 wt.-%, (b, e) 5 wt.-%, and (c. f) 7.5 wt.-% WC using P = 600 W, v = 400 mm/min. Cracks at the grain boundaries for specimens manufactured with 7.5 wt.-% WC and (g) 600 W, 400 mm/min (h) 600 W, 600 mm/min.

without greater part defects like large pores or cracks.

Furthermore, a similar cellular microstructure was found in the fusion zone of the top layer for all specimens, as shown in Fig. 1 d) to f). Increasing the carbide content resulted in a finer microstructure (Fig. 1 f), which can be attributed to the small carbide particles acting as nucleation agents. Similar effects were also reported for other materials like Inconel 718 strengthened with TiC micro-particles [14].

Further analysis of the microstructure indicates that the WC particles are not completely dissolved during DED-LB/M but remain as hard phases, as shown in Fig. 1 g) and h). It can also be seen that high carbide concentrations (7.5 wt.-% WC) resulted in crack formation and favored crack growth along the grain boundaries. Even though these cracks are only barely existent, poorer long-term properties are expected [15].

To assess the influence of the different carbide concentrations on the mechanical properties, the material hardness was determined. The main processing parameters were maintained constant to minimize the influencing factors on the resulting hardness. Figure 2 presents the obtained hardness values for three different WC concentrations exemplary processed with the same parameter set. The average hardness of Bainidur AM was found to vary between 390 and 410 HV. Increasing the WC concentration resulted in an improved material hardness. Thereby, the hardness continuously increased for a higher number of WC particles. Maximum hardness values of around 840 HV were observed for a WC ratio of 7.5 wt.-%, which are superior to the ones obtained for in-situ modified 16MnCr5 with carbon (up to 0.8 wt.-%) [16]. Furthermore, a reduced material hardness was observed in the bonding zone. This can be attributed to mixing effects at the substrate's boundary which lead to a decreased hardness compared to the applied coating. Overall, the obtained results correlate well with other works that studied the directed energy deposition of WC-reinforced steels [8,9].

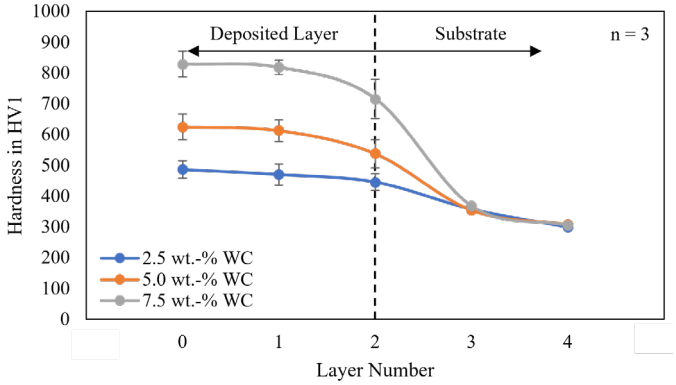

Fig. 2: Material hardness for different WC concentrations (2.5, 5.0, and 7.5 wt.-%), manufactured using P = 600 W, v = 400 mm/min.

In the next step, the influence of different processing parameters on the material hardness was investigated for a WC concentration of 5 wt.-%. This content was selected as no cracks were found at the grain boundaries. Fig. 4 presents the results on the determined hardness.

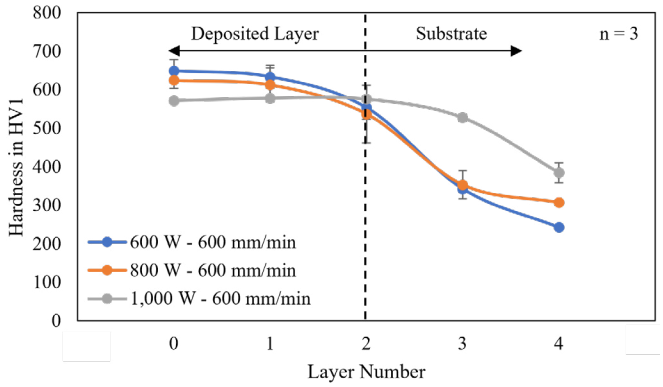

Fig. 3: Experimentally determined material hardness for 5 wt.-% WC specimens manufactured with different energy inputs (P = 600 to 1,000 W) using a feed rate of 400 mm/min.

Depending on the applied process parameters, hardness values ranging from 570 HV1 (P = 1,000 W) to 650 HV1 (P = 600 W) could be observed. The decrease in hardness with increasing laser powers can be attributed to the increased energy input and the corresponding enlarged size of the diffusion zone. This correlates well with the determined hardness in the bonding zone and the substrate. Here, the higher laser powers results in a harder transition zone, which is the consequence of mixing the applied coating with the base material. Regarding the feed rate, no significant influence could be identified as the hardness varied between 630 HV1 and 650 HV1 in the top layer of the coating for different feed rates (compare Fig. 2 and Fig. 3). Increased feed rates, however, result in a thicker coating. This might be helpful in reducing the thermal input into the substrate.

4. Conclusion

The underlying work presents investigations on the suitability of different WC particle concentrations for reinforcing the metal matrix of the low-alloyed steel Bainidur AM. Three different carbide concentrations were studied regarding their effect on the processability. Furthermore, the influence of the applied processing conditions on the obtained material hardness was investigated. Hardness values as high as 840 HV were obtained. However, the increased number of hard particles favored crack formation along the grain boundaries. Therefore, too high carbide concentrations are undesirable for highly loaded products as a premature failure could occur. Future investigations will focus on identifying suitable processing strategies so that high carbide concentrations can be processed without a promoted crack tendency. The dispersion of the hard phase carbides also leads to the assumption that the generated coatings possess an improved wear resistance compared to solely carburized specimens, which will be scope of future investigations.

Acknowledgements

The authors like to thank the BMWi for funding the project “HyConnect - Ressourcenminimale Fertigung durch hybride und hochvernetzte Prozesse” within the scope of the “Technologietransfer-Programm Leichtbau”. Furthermore, we would like to thank the Deutsche Edelstahlwerke Speciality Steel GmbH for providing the powder material. The authors gratefully acknowledge the support provided by the Erlangen Graduate School in Advanced Optical Technologies.

References

[1] Davis JR. Surface Hardening of Steels: Understanding the Basics. Materials Park: A S M International; 2002.
[2] Kumar LJ, Pandey PM, Wimpenny DI (eds.). 3D Printing and Additive Manufacturing Technologies. Singapore: Springer Singapore; 2019.
[3] Lachmayer R, Lippert RB (eds.). Additive Manufacturing Quantifiziert: Visionäre Anwendungen und Stand der Technik. 1st ed. Berlin, Heidelberg: Springer Berlin Heidelberg; 2017.
[4] Zhang D, Feng Z, Wang C, Wang W, Liu Z, Niu W. Comparison of microstructures and mechanical properties of Inconel 718 alloy processed by selective laser melting and casting. Materials Science and Engineering: A 2018;724:357–67.
[5] Scipioni Bertoli U, Guss G, Wu S, Matthews MJ, Schoenung JM. In-situ characterization of laser-powder interaction and cooling rates through high-speed imaging of powder bed fusion additive manufacturing. Materials & Design 2017;135:385–96.
[6] Deirmina F, Peghini N, AlMangour B, Grzesiak D, Pellizzari M. Heat treatment and properties of a hot work tool steel fabricated by additive manufacturing. Materials Science and Engineering: A 2019;753:109–21.
[7] Hentschel O, Siegel L, Scheitler C, Huber F, Junker D, Gorunow A et al. Processing of AISI H11 Tool Steel Powder Modified with Carbon Black Nanoparticles for the Additive Manufacturing of Forging Tools with Tailored Mechanical Properties by Means of Laser Metal Deposition (LMD). Metals 2018;8(9):659.
[8] Ostolaza M, Arrizubieta JI, Cortina M, Lamikiz A. Study of the reinforcement phase dilution into the metal matrix in functionally graded Stellite 6 and WC metal matrix composite by Laser Metal Deposition. Procedia CIRP 2020;94:330–5.
[9] Benarji K, Ravi kumar Y, Jinoop AN, Paul CP, Bindra KS. Effect of WC Composition on the Microstructure and Surface Properties of Laser Directed Energy Deposited SS 316-WC Composites. J. of Materi Eng and Perform 2021;30(9):6732–42.
[10] Bartels D, Novotny T, Hentschel O, Huber F, Mys R, Merklein C et al. In situ modification of case-hardening steel 16MnCr5 by C and WC addition by means of powder bed fusion with laser beam of metals (PBF-LB/M). Int J Adv Manuf Technol 2022.
[11] Kieffer R, Benesovsky F. Hartstoffe. Vienna: Springer Vienna; 1963.
[12] Thawari N, Gullipalli C, Chandak A, Gupta T. Influence of laser cladding parameters on distortion, thermal history and melt pool behaviour in multi-layer deposition of stellite 6: In-situ measurement. Journal of Alloys and Compounds 2021;860:157894.
[13] Bartels D, Hentschel O, Dauer J, Burgmayr W, Schmidt M. Processing of low-alloyed case-hardening steel Bainidur AM by means of DED-LB/M. In: Lasers in Manufacturing (LiM) 2021; 2021.
[14] Kong D, Dong C, Ni X, Zhang L, Man C, Zhu G et al. Effect of TiC content on the mechanical and corrosion properties of Inconel 718 alloy fabricated by a high-throughput dual-feed laser metal deposition system. Journal of Alloys and Compounds 2019;803(1):637–48.
[15] Wycisk E, Solbach A, Siddique S, Herzog D, Walther F, Emmelmann C. Effects of Defects in Laser Additive Manufactured Ti-6Al-4V on Fatigue Properties. Physics Procedia 2014;56:371–8.
[16] Schmitt M, Gottwalt A, Winkler J, Tobie T, Schlick G, Stahl K et al. Carbon Particle In-Situ Alloying of the Case-Hardening Steel 16MnCr5 in Laser Powder Bed Fusion. Metals 2021;11(6):896.

Contribution to the Goal of this Work:

Hard particles like tungsten carbide are promising for tailoring not only the material hardness but also the wear resistance due to their inherent high hardness. This work reports findings on the influence of different WC concentrations on the resulting material properties of case-hardening steels. It was found that the material hardness rises almost linearly with increasing WC concentration. Correspondingly, the hardness can be tailored between around 500 HV1 (2.5 wt.-% WC) and 840 HV1 (7.5 wt.-% WC). The peak hardness values obtained of the highest WC concentration are similar to the ones of conventionally case-hardened specimens (see Section 6.1). An almost linear correlation between WC concentration and material hardness was observed, with the small WC microparticles (≈ 1 µm) enhancing grain-refinement at the highest concentrations. However, too high WC concentrations in the range of 7.5 wt.-% promote the formation of microcracks at the grain boundaries. Even though those cracks are rather microthan macroscopic, these defects might still affect the long-term properties. The main contributions to RQ4 are that, based on the almost linear correlation between WC concentration and hardness, it is possible to tailor the final surface hardness of the workpiece by adjusting the WC concentration. To avoid an undesired and premature failure of the workpiece due to crack formation, the WC concentration should be lower than 7.5 wt.-% when reinforcing the material with small WC microparticles.

Reasonable carbon and WC concentrations have been identified within the works in Section 6.3 and Section 6.4. Based on these findings, a combined addition of carbon (total: 0.4 wt.-%) and tungsten carbide (5 wt.-%) will be followed in the next section with the goal of deriving an optimised chemical composition for the in-situ modification of case-hardening steels in DED-LB/M. Furthermore, the influence of the different additives on the microstructural and macroscopic material properties is investigated. The goal is to achieve a surface hardness comparable to case-hardened specimens investigated within Section 6.1.

6.5 Development of a Wear-resistant Coating deposited through DED-LB/M

Title: Development of a novel wear-resistant WC-reinforced coating based on the case-hardening steel Bainidur AM for the substitution of carburizing heat treatments [P14]

Journal: Journal of Materials Research and Technology, Elsevier

DOI to Web-version: https://doi.org/10.1016/j.jmrt.2023.07.200

Authors: Dominic Bartels, Mikael Fallqvist, Miriam Heise, Johannes Vetter, Michael Schmidt, Pavel Krakhmalev

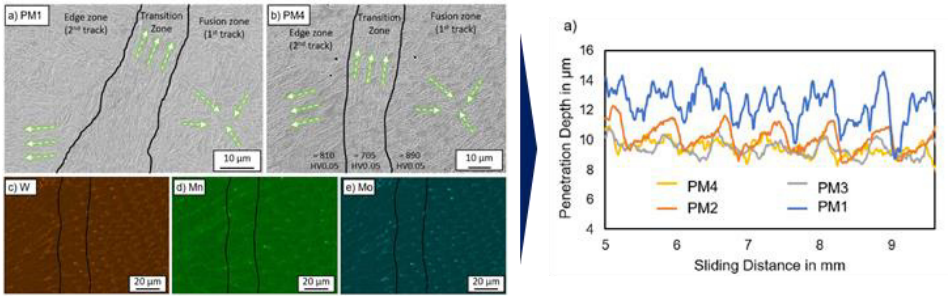

Motivation and Key Findings:

Section 6.3 and Section 6.4 show the potential of the individual addition of carbon and tungsten carbide for tailoring the material properties. However, knowledge on their joint influence on the microstructure formation as well as the associated wear resistance of the material is still lacking. This is necessary since the sole addition of WC particles results in a promoted crack tendency while the effect of carbon on the wear resistance is smaller compared to the one of WC particles. Correspondingly, the influence of the combination of these different additives on the material properties was studied systematically in this work. The **highlights** are:

- Influence of C and WC on microstructure formation and material properties in case-hardening steels revealing an exceptional material hardness
- Correlation between element distribution within weld tracks and local material hardness for reinforced case-hardening steels
- Recommendation for the deposition strategy during DED-LB/M to avoid excessive wear due to inhomogeneous material hardness

Available online at www.sciencedirect.com

jmr&t Journal of Materials Research and Technology

journal homepage: www.elsevier.com/locate/jmrt

Development of a novel wear-resistant WC-reinforced coating based on the case-hardening steel Bainidur AM for the substitution of carburizing heat treatments

Dominic Bartels [a,b,*], *Mikael Fallqvist* [c], *Miriam Heise* [a], *Johannes Vetter* [a,b], *Michael Schmidt* [a,b], *Pavel Krakhmalev* [c]

[a] *Institute of Photonic Technologies (LPT), Friedrich-Alexander-Universität Erlangen-Nürnberg (FAU), Konrad-Zuse-Straße 3/5, 91052 Erlangen, Germany*

[b] *Erlangen Graduate School in Advanced Optical Technologies (SAOT), Friedrich-Alexander-Universität Erlangen-Nürnberg (FAU), Paul-Gordan-Straße 6, 91052 Erlangen, Germany*

[c] *Department of Engineering and Physics, Karlstad University, SE-651 88 Karlstad, Sweden*

ARTICLE INFO

Article history:
Received 3 June 2023
Accepted 24 July 2023
Available online 26 July 2023

Keywords:
DED-LB/M
Wear resistance
Coating
Bainidur AM
Case-hardening steel
Additive manufacturing

ABSTRACT

Laser-based directed energy deposition of metals (DED-LB/M) supports the synthesis of functional materials with tailored properties and performance through in-situ modification of the alloying composition within the processing zone. In this investigation, a low-alloyed steel was modified stepwise to analyse the influence of carbon and tungsten carbide (WC) addition on the resulting material properties. A moderate carbon concentration of 0.4 wt.-% improved the average hardness (520 HV0.5). WC particles on the other hand were dissolved within the matrix and resulted in a fine microstructure with high hardness (780 HV0.5). A combined addition of carbon and WC led to the highest material hardness (840 HV0.5). Scratch tests showed that the wear resistance rises with increasing hardness but is improved the most by the addition of hard particles. Furthermore, these tests revealed an anisotropic abrasive wear resistance which correlates with the direction of the weld tracks. Loading the material parallel to the weld track direction led to a homogeneous wear. When the material is scratched perpendicularly to the weld tracks, an inhomogeneous wear with periodic characteristics occurred. The periodicity can be explained by the different microstructural characteristics and hardness at the transition zone between adjacent weld tracks deposited in DED-LB/M. For all materials, the transition between two weld tracks was characterized by a columnar microstructure with low microhardness while the adjacent weld tracks possessed a finer microstructure and higher microhardness. These microstructural differences were mirrored in scratch testing since wear peaks can be observed at the transition zone between two weld tracks.

* Corresponding author. Konrad-Zuse-Straße 3/5, 91052 Erlangen, Germany.
E-mail address: Dominic.bartels@lpt.uni-erlangen.de (D. Bartels).

https://doi.org/10.1016/j.jmrt.2023.07.200

1. Introduction

Case-hardened steels are commonly used for gears and bearings applications. The low carbon content of this class of materials results in an excellent processability for different production technologies like forming, forging, and welding. However, the low carbon contents limits the hardenability of this group of materials. A special heat treatment, which is referred to as case-hardening, is necessary to improve the hardenability of these materials. This heat treatment comprises of either carburisation or nitriding followed by a subsequent hardening operation to improve the surface hardness. The limitations of carburizing are that the process is time consuming and that thin-walled parts might distort [1]. Long holding times make this process unappealing for the fabrication of small batch sizes. Furthermore, it was found that solely martensitic structures are disadvantageous regarding the wear resistance of a material [2]. Speaking of wear resistance, wear and tear of products alone can be responsible for economic costs of up to 4% of the national gross domestic product [3]. The case-hardening of low-alloyed steels primarily results in a martensitic microstructure since almost all carbon is entrapped within the martensite [4]. Tempering these products is often necessary to improve the ductility of the workpiece. Regarding wear resistance, secondary phases like carbides are preferred to a solely martensitic microstructure. To form secondary carbides like vanadium carbide (VC) or tungsten carbide (WC), high tempering temperatures exceeding 500 °C are required [5]. However, these carbide-forming elements are typically either absent or only present in minor ratios within case-hardening steels. Their absence hinders the effect of precipitation of secondary carbides, thus limiting the wear resistance of the final part. Therefore, alternatives to a solely carbon-reinforcement are needed to improve the part properties of case-hardening steels even further.

Laser-based directed energy deposition (DED-LB/M) provides a promising alternative to case-hardening for tailoring the surface hardness of a product [6]. The flexible processing in DED-LB/M allows to generate three-dimensional structures, repair worn surfaces, or deposit wear-resistant claddings to highly loaded surfaces. Since multiple powder materials can be used simultaneously in DED-LB/M, it is possible to locally adjust the chemical composition of the final workpiece [7]. This high flexibility opens the possibility of applying coatings on freeform surfaces with tailored properties where needed. One potential field of application is to substitute the carburizing product for large parts that are only manufactured in small batch sizes. In doing so, long holding times during carburisation can be avoided. The large potentials of the DED-LB/M process for repair applications also enable the refurbishment of locally worn investment goods. Using the DED-LB/M for repair applications requires the generation of hard surfaces with similar material hardness as the previously carburised material. Knowing the before-mentioned disadvantages of solely martensitic-hardened products from case-hardening steels, further alloying elements can be added to improve key properties like wear resistance or hardness. Incorporating e.g., tungsten can help to improve the material properties of steels through solid-solution strengthening as well as the high-temperature resistance [8]. However, the processing of the main material can always be seen as a prerequisite for a targeted tailoring of the final material properties. The processing of case-hardening steels by means of DED-LB/M has been investigated in preliminary investigations recently [9–11]. As-built case-hardening steels are characterized by a bainitic-martensitic microstructure, which is the consequence of the high cooling rates of the process and the thermal cycle.

Another key advantage of the DED-LB/M process is that oxides [12] and hard particles like TiC, VC [13], or WC can be added to improve the wear resistance of the material. This in-situ particle reinforcement has proven beneficiary in the past for improving the hardness of the underlying material through the formation of e.g., a metal-matrix-composite (MMC). Grünewald et al. [14] studied the laser surface alloying of a conventional case-hardening steel with elemental carbon and tungsten carbide. They have found that the additional alloying elements helped to improve both the hardness and the wear resistance of the material. Bartels et al. [15] have also shown that reinforcement of 16MnCr5 through WC addition in PBF-LB/M results in superior wear properties compared to the addition of carbon. Shi et al. [16] identified small tungsten carbide particles with a size of around 5 μm to be beneficial regarding improvement of the wear resistance. The improved material properties were mainly attributed to the formation of a fine dendritic microstructure. Furthermore, preliminary investigations reported the beneficial effect of WC microparticles on the material hardness of case-hardening steels when processed by DED-LB/M [17]. It was found that the hardness rises almost linearly with increasing WC concentrations, showing the potential for specifically tailoring the surface hardness of a workpiece through altering the total WC content. Rezaee Hajideh and Farahani [18] have shown that a similar trend is also accountable when depositing a SiC-reinforced In718 cladding on tool steels.

Motivated by the fundamentals of the case-hardening process chain, this work aims at presenting an alternative processing route for the generation of a wear-resistant surface through DED-LB/M. The goal was to identify the influence of elemental carbon and WC particles on the resulting microscopic and macroscopic material properties of a case-hardening steel. This includes the microstructure formation, element distribution, surface hardness, and abrasive wear resistance. The base material is modified in-situ to improve the final part properties. The carbon concentration of the case-hardening steel Bainidur AM (≈0.23 wt.-% C) is increased to 0.4 wt.-% to surpass the threshold hardness of 550 HV1 that is required when speaking of the case-hardening depth. Additionally, the influence of tungsten carbide on the material properties is studied. These hard particles are added to improve the wear resistance of the material. In the final step, a combined addition of C and WC is performed to generate an optimized material system with the aim of substituting cost- and energy-intensive carburizing or nitriding processes. Especially the addition of WC is promising since WC-reinforced specimens are known for an improved wear resistance. The investigations of this work will then provide an alternative process for the generation of wear-resistant coatings by means of DED-LB/M. Furthermore, since the coating is based on a case-hardening steel, the findings of this

work can perspectively be used for the local repair of worn surfaces of e.g. previously carburised specimens.

2. Materials and methods

A 5-axis ERLAS 50237 DED-LB/M machine (ERLAS GmbH, Germany) was used for generating the coatings. This machine is equipped with a 4 kW diode laser of type Laserline LDF 4000-4 (Laserline GmbH, Germany). The characteristic wavelength lies between 940 and 963 nm. A zoom optics can be used for varying the laser spot size between 1 and 3 μm. The low-alloyed case-hardening steel Bainidur AM (Deutsche Edelstahlwerke Speciality Steel GmbH, Krefeld, Germany) is used as powder material. Table 1 presents the chemical composition of the material Bainidur AM.

An average particle size distribution between 45 and 90 μm was selected for performing the DED experiments. For modifying Bainidur AM, carbon black (C) nanoparticles (ECKA Granules, Fürth, Germany) and tungsten carbide (WC) particles (abcr GmbH, Haan, Germany) were selected. The carbon nanoparticles are around 20 nm [19] in size while the WC particles are characterized by a fisher size of 0.63 μm according to the supplier's certificate. Fig. 1 shows scanning electron microscopy (SEM) images of the used powder materials. Bainidur AM particles are characterized by a mainly spherical shape with minor share of non-spherical, elliptical particles. Particle size distribution was determined using a Camsizer X2 (Microtrac Retsch GmbH, Germany). The experimentally determined d_{10}, d_{50}, and d_{90} values are 58.8 μm, 80.8 μm, and 100.4 μm, respectively. The carbon black nanoparticles adhere very well to the surface and are distributed homogeneously along the surface. In contrast, the WC particles possess poorer adhesion to the substrate of the Bainidur AM particles. This can be explained by the larger size and the asymmetry of these particles compared to the smaller carbon black nanoparticles. However, no larger agglomerations of these particles were identified after mixing.

2.1. Powder mixing

In addition to the base material, three different powder mixtures were investigated. The first powder mixture was solely modified by addition of carbon nanoparticles to reach an average carbon content of approximately 0.4 wt.-% C in the powder. Powder mixture two was characterized by the sole addition of 5 wt.-% WC. Goal of these two powder mixtures was to assess the influence of the respective additives on the material properties. For the third powder mixture (0.4 wt.-% C and 5 wt.-% WC), both carbon nanoparticles and WC particles were added. The different materials are summarized in Table 2.

All powders were dried in a vacuum furnace at 110 °C for 12 h prior to mixing to avoid undesired agglomerations during mixing. A powder blend of 300 g was prepared for the different mixtures. The different powder materials were added into a glass with a volume of 750 ml. All glasses were cleaned using isopropanol and dried before adding the powder. First, the Bainidur AM powder material was added into the glass. After that, the carbon nanoparticles were added. WC particles were added in the final step. After the addition of the respective additive (C and WC), the powder blend was premixed using a spoon. All glasses were then tumbled for 2 h in a tumbling mixing unit. The carbon content was determined after mixing using a CS elemental analyser (Eltra GmbH, Haan, Germany).

2.2. Sample manufacturing

Two-layered specimens were manufactured using the DED machine. 16MnCr5 substrates (Abrams Stahl GmbH, Germany) with an edge length of 200 mm in x- and y-direction and a thickness of 15 mm were used for the DED-LB/M experiments. All samples were manufactured using a laser power of 600 W. The feed rate and laser spot size were set to 400 mm/min and 1.5 mm, respectively. To deposit the cladding within the focal plane of the powder nozzle and the laser processing optics, a stand-off working distance of 16 mm was defined. Argon gas of purity 4.6 was used both as carrier and shielding gas. The respective gas flows were 4.0 L/min (carrier gas) and 20 L/min (shielding gas). A uniform track width of 1.5 mm was defined for the experiments. For hatching of these single tracks, a hatch distance of 750 μm was chosen to provide an overlap of 50%. The core of the structure was fabricated using an alternating, meander-shaped deposition strategy. The core was followed by four contour tracks that were applied around the four edges of the rectangular geometry. The orientation of the deposited layer was turned by 90° for the second layer.

These rectangular specimens were fabricated in two different sizes. Investigations regarding hardness and microstructure were performed on specimens with an edge length of 10 mm. Building on this, a larger geometry was manufactured for scratch testing with an edge length of 40 mm. The average layer height was 0.45 mm independent of the size of the structure since the key process parameters were maintained constant. Manufacturing two-layered specimens resulted in a coating height of 0.9 mm. After fabrication, the specimens were polished to a uniform part height of 0.65 mm for subsequent analysis. This step was performed to assure that the material properties are assessed at comparable positions within the specimen.

2.3. Microstructure and hardness analysis

The 10 × 10 mm^2 specimens were cut into two halves and embedded using an epoxy resin. After the resin was cured, the samples were grinded and polished down to 1 μm using a diamond paste. These cross-sections were then analysed

Table 1 – Chemical composition of the powder material Bainidur AM according to the supplier's certificate.

Batch	Element Concentration in wt.-%									
	C	Si	Mn	P	S	Cr	Mo	Ni	V	Fe
DED	0.23	0.7	1.2	<0.02	<0.02	1.0	0.9	<0.3	<0.15	bal.

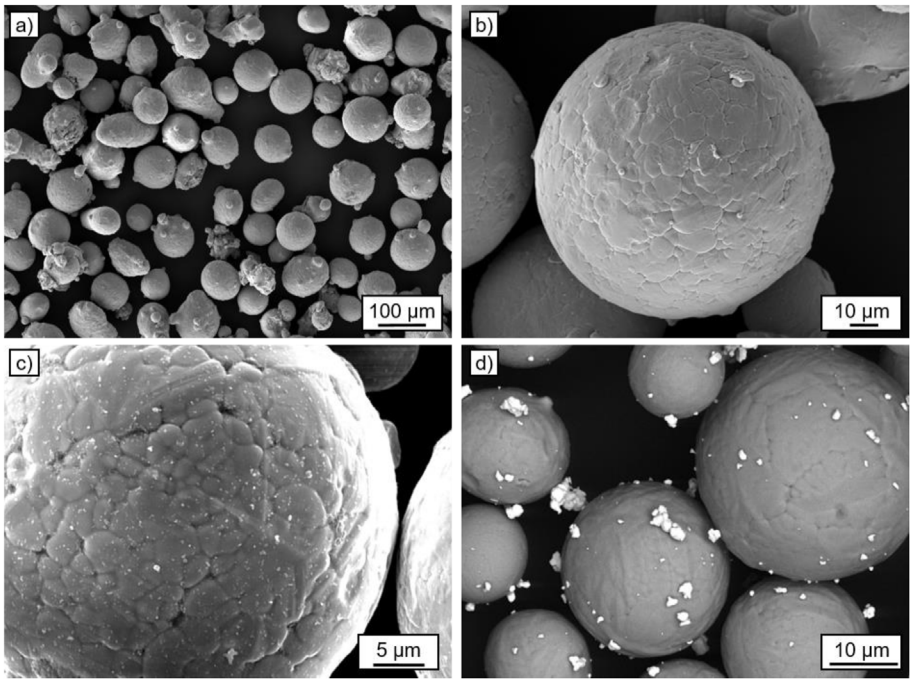

Fig. 1 – SEM images of (a and b) Bainidur AM, (c) Bainidur AM mixed with carbon, and (d) Bainidur AM mixed with WC.

using optical light microscopy (Olympus BX53 M, Evident Europe GmbH, Germany) to identify defects such as larger pores or cracks. Furthermore, the material hardness was determined using an indentation tester of type KB30S (KB Prüftechnik, Germany). Measurement rows were defined to investigate the hardness (test load resembling HV0.5) 150 µm below the surface of the coating. Ten measurement points were defined within this layer. The distance between each measurement point within one layer was set to 0.2 mm. Offset between two layers was set to 200 µm. After analysing the material hardness, the samples were etched using a 3% Nital solution to reveal the microstructure. Again, optical light microscopy was used for studying the cross-sections. However, this time the focus was placed on analysing the microstructure and the phase formation. The austenite content of the materials after DED-LB/M was determined using an X-ray diffractometer (Malvern Panalytical Empyrean) with the HighScore software. Furthermore, additional micro-hardness measurement (HV0.05) were performed at the overlaps between two weld tracks to determine the material hardness with a high resolution. Furthermore, the commercially available software JMatPro v13.2 (Sente Software Ltd., United Kingdom) was used for the calculation of material properties like solidification behaviour.

2.4. *Scratch testing*

To evaluate abrasion resistance and investigate changes in abrasion mechanisms, scratch resistance tests were carried out. The investigations were done using a micro scratch tester (Anton Paar Revetest) equipped with a Rockwell C diamond conical indenter, 120° angle with a tip radius of 200 µm. The tests were performed in an increased load (linear load increase 0–75 N), and in a constant 40 N load modes. Scratch length was of 10 mm in both cases. Increased load tests were evaluated to identify critical loads at which transition from ploughing to wedge formation takes place. Constant load tests were performed to quantify wear and friction in dependence of the material. Penetration depth, coefficient of friction, and acoustic emissions were recorded during all tests. The experiments were carried out parallel and perpendicular to the deposited tracks. Characterization of wear mechanisms and transitions in abrasion modes (ploughing, wedge formation, and cutting/chip formation) were done with the field-emission gun scanning electron microscope FE-SEM JEOL JSM-7000 F. Characterization of the small-scaled specimens (10×10 mm^2) was performed using an SEM of type Merlin Gemini 2 (Carl Zeiss AG, Germany). The SEM is equipped with an EDS detector of type X-Mas (Oxford Instruments, United

Table 2 – Chemical compositions of the different powder mixtures. *The total carbon concentration in wt.-% assumes that the WC particles (6.09 wt.-% C) are completely dissolved during DED-LB/M.

Abbreviation	Powder Mixture	Carbon in wt.-%	WC in wt.-%	Total Carbon in wt.-%*
PM1	Bainidur AM	0.23 wt.-%	–	0.23 wt.-%
PM2	Bainidur AM with 0.4 wt.-% C	0.40 wt.-%	–	0.40 wt.-%
PM3	Bainidur AM with 5 wt.-% WC	0.23 wt.-%	5 wt.-%	0.53 wt.-%
PM4	Bainidur AM with 0.4 wt.-% C and 5 wt.-% WC	0.40 wt.-%	5 wt.-%	0.70 wt.-%

Kingdom), which was used for recording the element mappings within this work.

3. Results and discussion

The results section is divided into three subsections. First, the relative part density as well as the underlying microstructure is analysed by means of optical microscopy. Hardness measurements were performed in the second step to determine the influence of the different alloying elements on the surface hardness. Finally, scratch tests were performed to study the wear resistance and defect formation of the different materials PM1 to PM4 under constant and progressive load.

3.1. *Microstructure formation and material hardness*

The relative density and microstructure of the specimens was assessed based on polished and etched cross-sections. Fig. 2 shows the cross-sections of the different coatings that were generated by means of DED-LB/M. All DED-LB/M structures were free of cracks and larger pores. This is essential when aiming at using these material systems for hard-facing applications. The macroscopic structure of the specimens can be divided into three different regions for all materials (exemplary shown in Fig. 2g): (1) centre of 1st weld track, (2) transition zone, and (3) edge of 2nd weld track.

The transition zone between two weld tracks is characterized by a different etching response. PM1 and PM2 possessed a lath-like structure, which could resemble a fine martensitic or a bainitic-martensitic microstructure. This type of microstructure is reasonable due to the high cooling rates associated with the DED-LB/M process and was previously obtained for multilayer specimens from case-hardening steels [11]. The Microstructure of PM2 and PM3 is quite similar, fine lath martensite is observed in both materials (see Fig. 2g and h). The differences were identified regarding the colour of the etching. When adding tungsten, material PM3, a brighter etching, which is most likely due to dissolved tungsten, is obvious. The microstructure of PM4 material modified with both carbon and WC is different. The cellular dendritic structure is clearly observed in Fig. 2h.

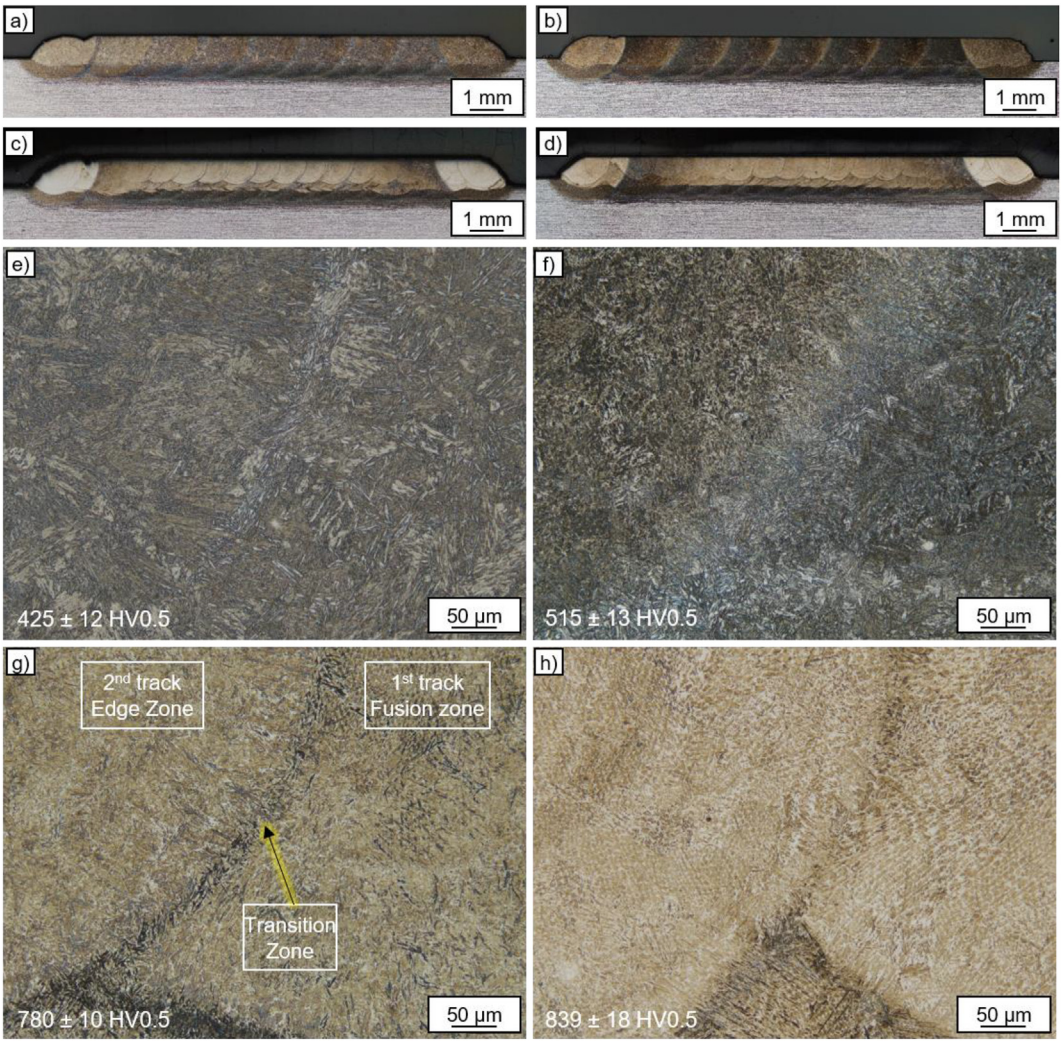

Fig. 2 – Cross-sections of the deposited coatings after mechanical polishing for (a, e) PM1, (b, f) PM2, (c, g) PM3, and (d, h) PM4.

Differences in microstructure are well explained by thermodynamic calculations. Fig. 3 shows the solidification path simulated for all four materials. It is seen that in PM1, PM2, and PM3 the crystallization starts with the formation of δ-ferrite. The volume fraction of δ-ferrite in PM1 reaches about 60 vol.-%, then by the peritectic reaction (liquid + δ-ferrite → austenite) austenite is formed. In PM2 and PM3 materials, the amount of primarily solidified δ-ferrite is lower, 22 and 27 vol.-% in PM2 and PM3 respectively.

Based on the microscopy observations, it can be concluded that austenite grains were larger in PM1 material and therefore martensite laths formed upon cooling are also coarser. In PM4 material δ-ferrite is not formed during solidification, instead, pure austenitic crystallization takes place. In this case, cellular dendrites of austenite are formed directly from the liquid. Usually, they are decorated with a network of segregated elements with lower diffusivity. When this structure is subjected to martensitic transformation during cooling, very fine martensite is commonly formed within cells [20]. It is worth noting that the absolute values of phase volume fractions and transformation temperatures should be used with caution as the calculation was done with some assumptions, which do not perfectly obey the non-equilibrium solidification conditions experimentally in DED process.

Analysing the material hardness revealed a continuous increase of the material hardness for the different powder blends. PM1 was characterized by the lowest material hardness (425 ± 12 HV0.5). Adding elemental carbon (PM2) increased the hardness up to 515 ± 13 HV0.5. The higher hardness can be attributed to a higher hardness of the martensite due to the higher carbon concentration. In contrast to the sole carbon modification, the addition of WC led to a significantly higher surface hardness of 780 ± 10 HV0.5. A combined addition of C and WC resulted in the highest hardness of the material in the range of 839 ± 18 HV0.5. Considering the overall carbon concentration of the materials (see Table 2), a non-linear hardness increase was observed for the WC-modified materials. One potential explanation might be that the addition of the WC-microparticles promoted grain-refining effects. A finer grain would result in an improved material hardness, which is commonly observed in DED-LB/M of steels [24]. Furthermore, grain boundary strengthening mechanisms were already observed in the past by Yin et al. [25], which could explain the improved hardness compared to the solely carbon-modified material. The obtained hardness is similar to conventionally carburised and hardened specimens from case-hardening steels. 16MnCr5 samples manufactured by means of laser-based powder bed fusion possess a hardness of around 800 HV1 after hardening [21,22]. Another work by Yang and Sisson [23] reported hardness values of around 850 HV, which are similar to the ones achieved within this work. However, the main advantage of the presented DED-LB/M technology lies in

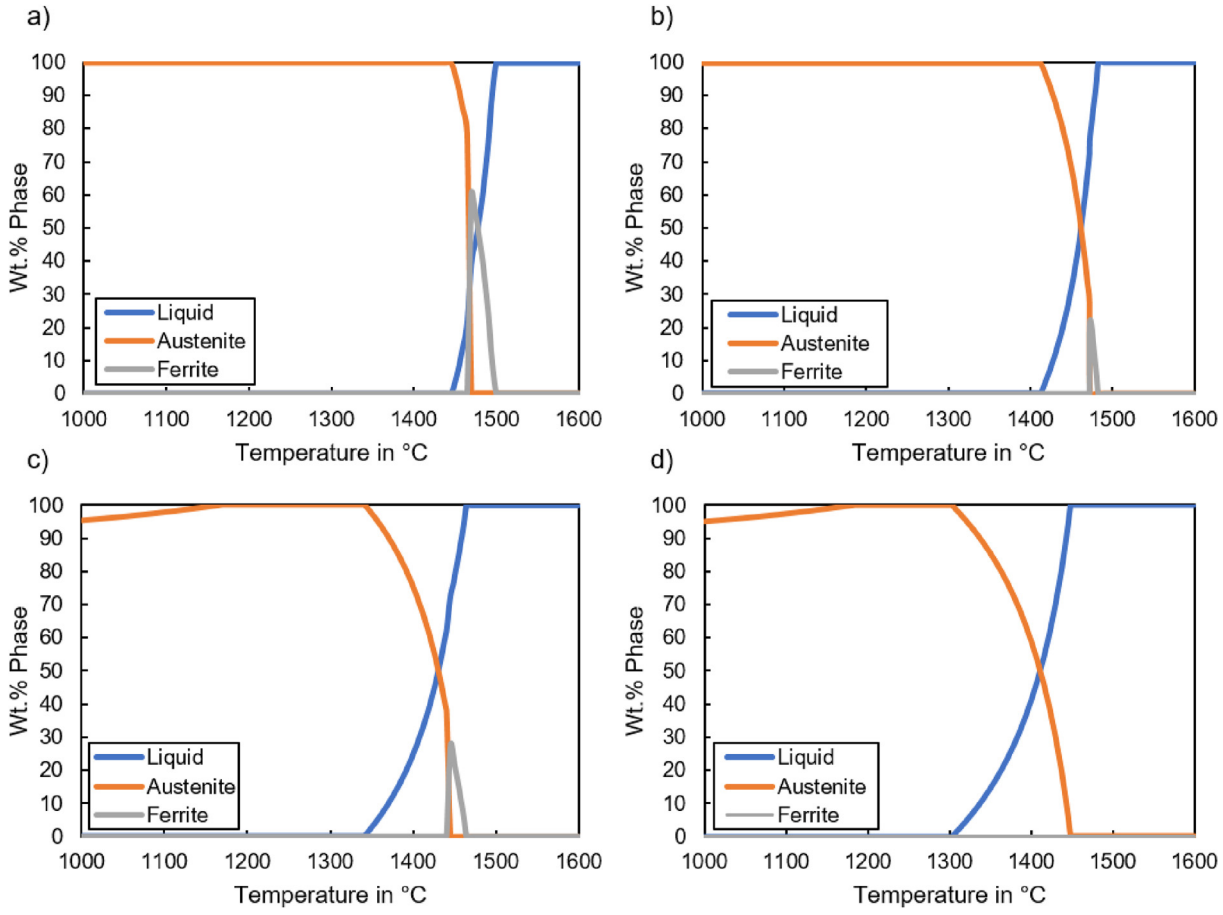

Fig. 3 – Solidification of the different materials (a) PM1, (b) PM2, (c) PM3, and (d) PM4. The diagrams were calculated using the software JMatPro.

the flexible modification of the case-hardening depth. Increasing the number of layers allows for the generation of coatings with variable hardness depths – without the need for excessive carburisation or nitriding times.

XRD measurements were performed to determine the retained austenite content for the four materials. It was found that the retained austenite content increased from PM1 (~9%) over PM2 (~11%) and PM3 (~24%) to PM4 (~30%). The increased retained austenite contents indicate that the carbon of the WC particles is at least released during solidification and affects the transformation kinetics of the material. Correspondingly, both martensite as well as bainite start and finish temperature were affected by the higher carbon concentrations upon cooling [26]. The presented hardness observations are kind of contradictory as the PM4 material with the highest content of retained austenite possess highest hardness (~30%) of 839 ± 18 HV0.5. This phenomenon can be explained if differences in microstructure and morphology of martensite, and possible effect of solid-solution strengthening by W are taken into account. Effect of W on hardness is clear, having quite similar microstructure, PM3 material has remarkably higher hardness of 780 ± 10 HV0.5 comparing to 515 ± 13 HV0.5 observed in PM2. Additionally, changes in solidification path lead to substantial changes in martensite morphology, and the finest martensite structure was observed in PM4 material (see Fig. 4).

In the next step, the cross-sections were analysed by means of SEM. Fig. 4 presents the SEM images for the different materials after DED-LB/M. PM1 and PM2 were characterized by a lath-like martensitic microstructure. This structure is reasonable since the high cooling rates in DED-LB/M favour the formation of martensite. PM3 and PM4 also possessed a lath-like structure. However, this time, the structure was entrapped and thereby more densely packed and finer compared to the material without additional WC particles. This microstructure suggests that the solidification conditions are different for the group without WC (PM1 and PM2) and the group with WC (PM3 and PM4) due to the elevated carbon and tungsten concentration of the materials.

Furthermore, no embedded WC particles were identified within the matrix. The absence of these particles indicates that these particles were either dissolved or molten during DED-LB/M. However, due to the high melting points of tungsten carbide at around 2900 °C, melting of the WC particles is not very likely. Nevertheless, it cannot be excluded that shares of the WC particles, especially very small particles, were molten during DED-LB/M. The fine microstructure validates the assumption that the increased hardness of the WC-modified materials was further boosted by fine-grain hardening.

Additional SEM analysis was performed at the transition zone between the two weld tracks for the different materials. Fig. 5 shows exemplary SEM images of the cross-sections for PM1 and PM4. The SEM images reveal the differences of the three previously introduced regions within the specimens. Associated with these regions was an altered orientation of the grain direction, independent of the used additives. The centre of the first weld track did not possess a preferred grain orientation. Even though this region is close to the transition zone, this represents the centre of the previous weld track due to the meander-shaped deposition strategy. The lack of a preferential direction can be attributed to the growth mechanisms. During solidification and cooling, the grains grow preferably from the weld track boundaries towards the centre, resulting in longish grains. In the centre, the grains grew from the different directions of the weld track boundaries and came together, which explains the more random orientation in this region. The transition zone can be identified as the third region. Here, the grains were oriented straight towards the surface of the coating, which can be explained by the growth along the direction of the highest thermal gradient.

Associated with these different grain growth mechanisms might be an altered element distribution within the specimens.

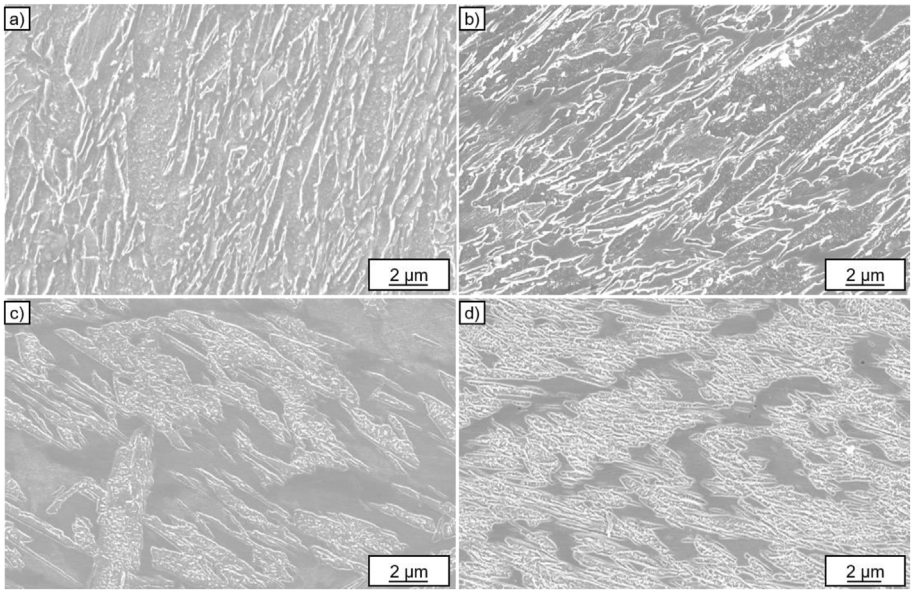

Fig. 4 – SEM images of the cross-sections for (a) PM1, (b), PM2, (c) PM3, and (d) PM4. The images were taken in the centre of the weld tracks.

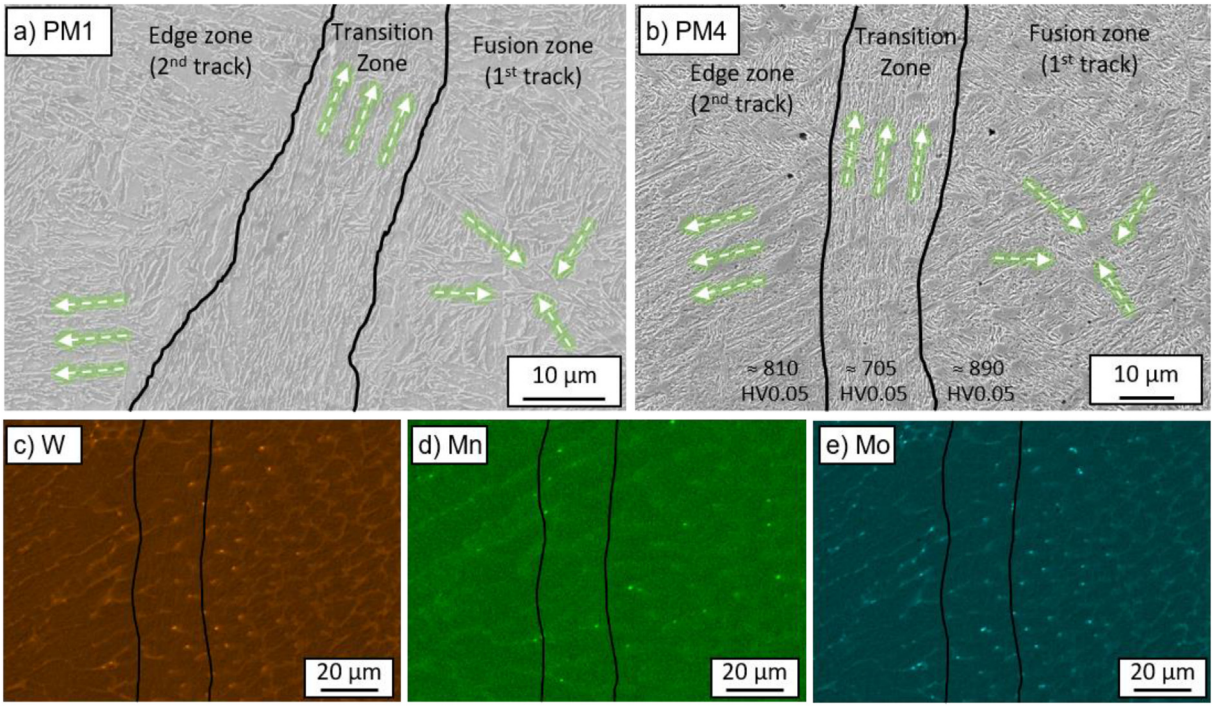

Fig. 5 – SEM images of the cross-section in the transition zone between two weld tracks of (a) PM1 and (b) PM4. (c, d, and e) present EDS mappings of the different alloying elements W, Mn, and Mo for PM4, based on the SEM image (b).

Therefore, SEM EDS mappings were performed at the weld track boundaries to determine the distribution of the elements within the matrix. Fig. 5b–e shows an SEM image as well as the corresponding EDS mapping for the elements tungsten, manganese, and molybdenum of PM4. The mappings reveal that all these elements were distributed preferably at the cell boundaries of the material, independent of the orientation and morphology of the microstructure. Almost no W and Mn were identified within the transition zone between the two weld tracks. This impoverishment of these elements resulted in a material hardness of 705 HV0.05 in this transition zone. In contrast to the transition zone, the 1st weld track was characterized by finely distributed W and Mo at the grain boundaries. This distribution indicates that the tungsten carbides were dissolved, which was also observed in [27]. Since the mappings for Mn, Mo, and W are partially overlapping, it is reasonable to assume that mixed carbides of these elements were formed during DED-LB/M. The presence of W and Mo led to a high material hardness of around 890 HV0.05 in the centre of the weld track. For the second weld track (edge zone), W and Mo were also precipitated at the grain boundaries. However, this time W and Mo were distributed more longish along the grain growth direction. Associated with this longish distribution was a reduced hardness of around 810 HV0.05. The findings indicate that tungsten is beneficial since it improves the material hardness compared to regions characterized by less tungsten. It is therefore reasonable to assume additional strengthening mechanisms through the addition of the (dissolved) WC particles [25,28]. However, the different distributions of the tungsten within the metal matrix might present some weak points within the material as reported for TiC-reinforced material [29]. In contrast to W and Mo, Mn was distributed relatively homogeneously within the metal matrix. This leads to the assumption that additional Mn could be helpful for homogenizing the material properties of laser-deposited coatings in the future through strengthening the transition zone.

3.2. *Wear resistance*

In the final step, the wear resistance of the material is studied. The different modes *Constant Load* and *Progressive Load* were investigated. By applying a constant load, periodic effects that appear regularly during load can be determined more precisely. The *Progressive Load* mode allows to determine the influence of the additives on wear characteristics like ploughing.

3.2.1. *Scratch testing under constant load*

Tests at constant load of 40 N were performed to quantify wear and friction behaviour of the tested materials in dependence on material composition. In preliminary investigations, the influence of the scratch direction on the wear behaviour was studied. The scratch direction was oriented perpendicular and parallel to the deposition direction of the coating. Following this approach, the influence of the adjacent weld track boundaries on the wear resistance was assessed, which might become important when designing tailored coatings. Fig. 6 shows the progress of the penetration depth for PM4 when scratching perpendicular and parallel to the deposition direction. The penetration depth remained mostly constant when scratching parallel to the welding direction. Only minor deviations were identified with increased sliding distance. This linear progression can be explained by the nearly homogeneous material properties along a single weld track. When changing the orientation towards a perpendicular scratching direction, periodically repeated peaks

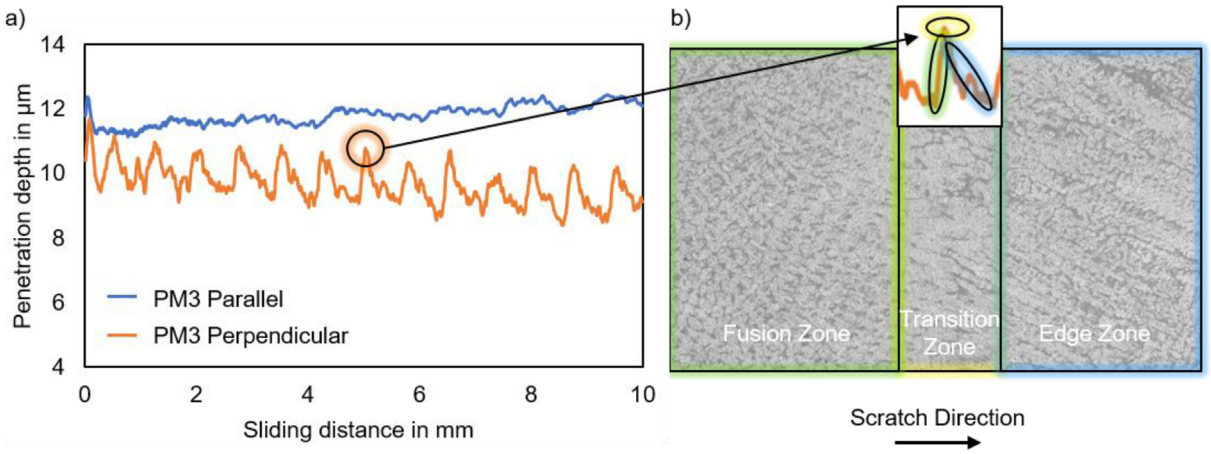

Fig. 6 – (a) Penetration depth of scratch testing in perpendicular and parallel direction as well as (b) SEM images of the transition region for screening investigations for PM3.

and valleys were identified. The distance between two peaks was roughly 0.75 mm. This distance equals the hatch distance that was defined for the DED-LB/M experiments. The penetration depth between two peaks decreased slowly and gradually. After a certain distance of roughly 0.75 mm, the penetration depth increased again. The second peak of this penetration depth was typically similar to the previous peak. This increase in penetration depth was attributed to the weld track boundaries, as shown in Fig. 6b.

One potential explanation for this is the lower wear resistance of this region due to the altered microstructural characteristics like grain size and grain direction. This assumption is supported by the reduced hardness around the transition zone (see Fig. 5). When aiming at upscaling the presented coating process, it is recommended to use larger laser spot sizes. Using larger spot sizes most likely helps to achieve a wider difference between the peaks and valleys within the weld track. An increasing distance helps to reduce the number of the periodic peaks. However, it needs to be considered that larger melt pool sizes will affect the cooling rates [30]. Slight process modifications might thereby be required to obtain similar part properties. Based on these findings, the upcoming scratch tests were performed perpendicular to the weld tracks. This direction was chosen since a precise scratching along the middle region of a weld track is hardly possible. Fig. 7 illustrates typical scratch test diagram (penetration depth and friction coefficient) obtained for a constant load of 40 N.

A periodic waviness was visible for all specimens when analysing both the friction and depth data. Considering the periodicity of the penetration depth, some variations could be observed when modifying the powder material. The additives affect the absorptivity and correspondingly the temperature of the melt pool [31]. These higher temperatures will lead to larger melt pool sizes. Nevertheless, periodicity of about 750–800 µm was observed in this investigation for all materials, which indicates that the addition of C and WC did not change shape of molten pool severely.

The highest penetration depth was observed for the base material PM1. Furthermore, this material is also characterized by a large discrepancy between the minimum and maximum penetration depth. A better wear behaviour was determined for the carbon-reinforced material PM2. However, the peak-to-valley values were still high, indicating that an inhomogeneous

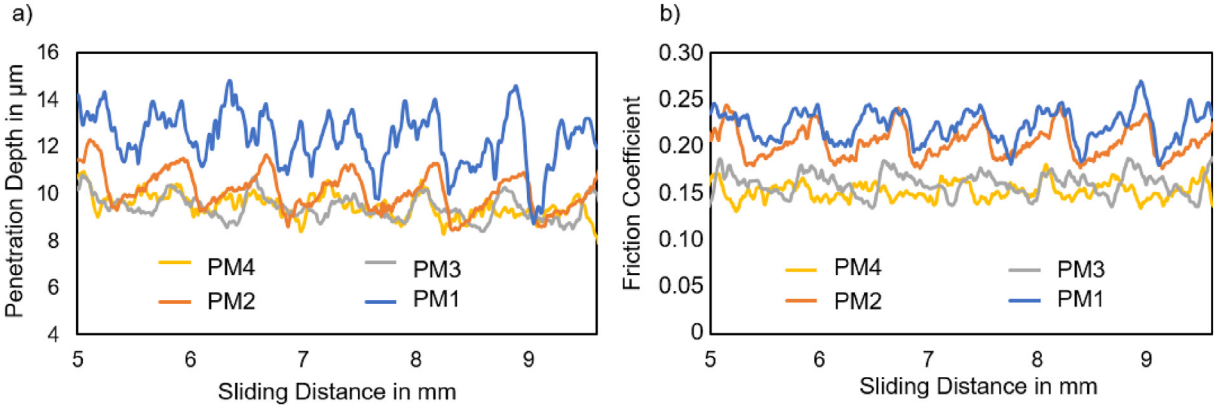

Fig. 7 – (a) Penetration depth and (b) friction coefficient determined for the different powder materials through scratch testing.

wear of the workpiece would take place during use. WC-reinforced materials PM3 and PM4 possessed better wear resistance. A slight decrease of the penetration depth was observed for PM4 compared to PM3. PM4 was also associated with a decrease of the difference between the maximum and minimum penetration depth was observed. It can be concluded that the higher hardness of the base material is beneficiary to avoid excessive wear. Furthermore, the maximum differences in penetration depth were almost completely countered through a combined addition of C and WC in PM4. Similar trends are mirrored in the coefficient of friction for the different materials. In general, a higher hardness was associated with a lower coefficient of friction. This is in accordance with the findings in [32], who also reported a reduced coefficient of friction for WC-reinforced stainless steels.

3.2.2. *Scratch testing under progressive load*

In the next step, scratch tests were performed perpendicular to the weld track direction using a progressive load. Fig. 8 illustrates penetration depth and friction coefficient obtained from the increasing load scratch test for all materials as well as an exemplary presentation of the surface after scratching.

It can be seen that material PM1 possessed the highest penetration depth and the highest coefficient of friction. PM2 was characterized by an increased abrasion resistance due to the higher hardness of the martensite. A higher effect was observed when adding 5 wt.-% WC to the base powder. As for the experiments performed under a constant load, a combined addition of C and WC (PM4) did not lead to a remarkable improvement of the overall abrasion resistance compared to PM3. The penetration depth and friction coefficient of materials PM3 and PM4 are quite similar. However, the PM4 was characterized by a more homogeneous wear since peak-to-valley values were reduced due to a harder transition between two weld tracks. It is further seen for all materials that the penetration depth was unstable at low loads due to the surface roughness of the specimens. When the load increased and was sufficient to smoothen the roughness, friction and depth values stabilized and showed monotonic increase with an increase in normal load. At about 20 N load some periodic waviness was observed and this waviness was visible until the load reached 75 N. In all tests, a transition from ploughing to wedge formation was observed, Fig. 8 (c, d – SEM of typical groove at that state). Loads and penetration depths at which these transitions were observed are summarized in Table 3.

Abrasive wear resistance is described well with the Archard's equation, which establishes a dependence between wear loss V, hardness of soft material H and normal load L.

$$\text{Wear loss } V \propto P_d \propto k\frac{LS}{H}$$

In this equation S is the sliding distance and k = 1/K is the wear coefficient. In the present investigation, the total wear at a selected load is directly proportional to the penetration depth Pd via geometry of the indenter, and therefore, the wear resistance is proportional to the inversed penetration depth. This equation can be used to analyse abrasion resistance of materials as a function of normal load, hardness or sliding distance. Fig. 9 illustrates penetration depth vs. load behaviour of the investigated materials. For each material, the

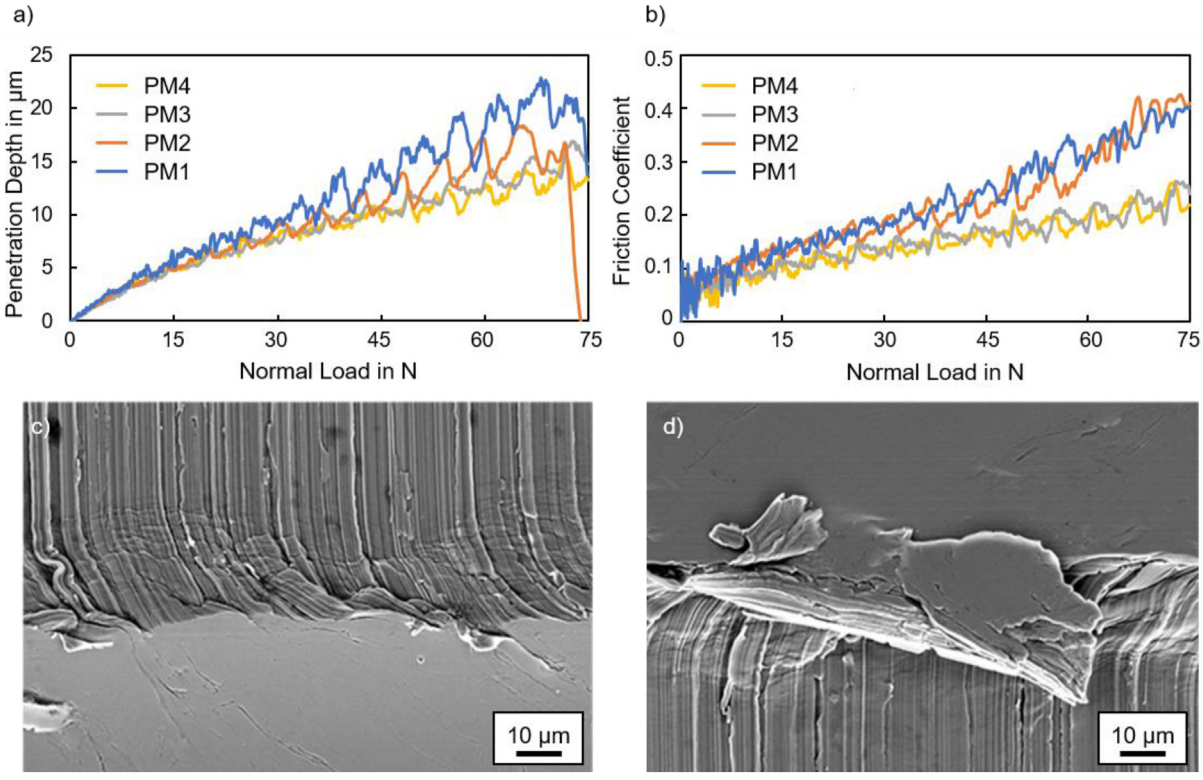

Fig. 8 – (a) Penetration depth and (b) friction coefficient determined under progressive load. (c) Shows the characteristic wear track for moderate loads while (d) portrays an exemplary wedge formation.

Table 3 – Summary of wear properties obtained through scratch testing.

Material	Surface Roughness S_a, μm	Onset of wedge formation N	Wear coefficient (Slope)	Mean COF (Constant Load)	Mean Penetration Depth (Constant Load)	Mean Penetration Depth (Increasing Load)
PM1	0.63 ± 0.03	50	0.325	0.23	13.7	21.6
PM2	0.26 ± 0.01	59	0.251	0.20	11.3	18.1
PM3	0.31 ± 0.01	71	0.196	0.16	9.8	15.5
PM4	0.31 ± 0.01	73	0.146	0.15	9.3	13.7

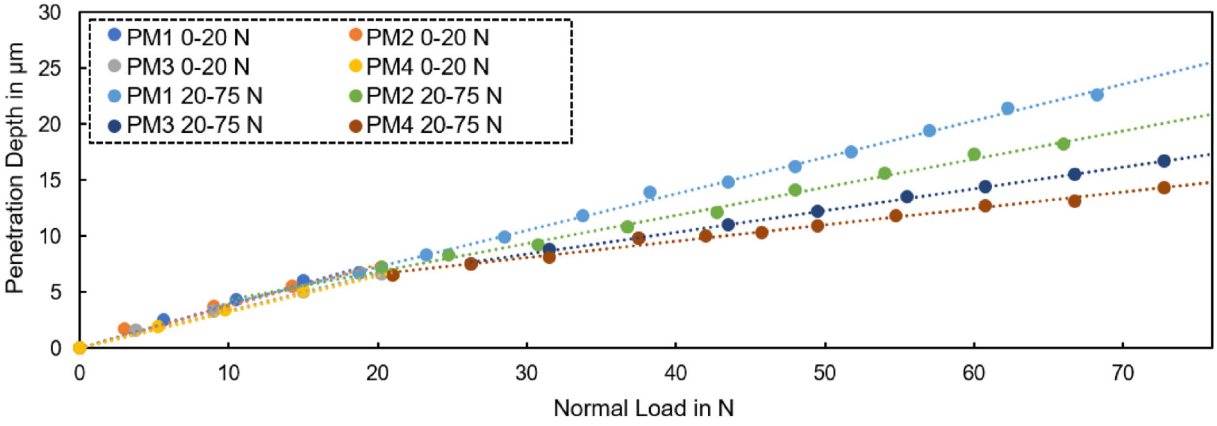

Fig. 9 – Correlation between penetration depth and load for the different materials.

highest value of Pd was selected. The selection was done in the close neighbourhood to the chosen load and was extracted from the curves. This value was then used to describe the total wear. According to the equipment manufacturer, accuracy of these measurements is ±0.5 nm in z-direction. The diagram shows that the linear dependence proposed by the Archard's equation is only accurate after a certain load has been surpassed. All materials had some kind of run-in period at low loads, when the specimen surface roughness was flattened, and the penetration depth did not exceed the surface roughness of the specimen. At about 20 N the indent was in full contact with the tested material and the ploughing abrasive wear was observed. This part of the diagram linearly depends on the load. Higher loads resulted in higher penetration depth, which in turn was associated with higher wear losses [33,34]. Ploughing abrasive wear regime, as presented in Table 1, changed to the wedge formation after 50, 59, 71, and 73 N loads for materials PM1, PM2, PM3, and PM4 respectively. This transition, nevertheless, was not very pronounced and no slope change on the diagrams is observed (see Fig. 9).

This behaviour could be explained by taking the differences in microstructure of the tested materials into account. XRD observations showed that the materials PM3 and PM4 had high amount of retained austenite while still demonstrating a higher hardness and abrasive wear resistance at the same time. Similar observations have been reported in [35]. At an increase in load, larger volume of the material was deformed around the indent, which could have resulted in a deformation-induced transformation of retained austenite into the harder martensitic phase [36]. Freshly transformed martensite is hard and therefore has higher abrasive wear resistance. A similar effect was observed at abrasive resistance tests on high carbon steel with high content of Si [37].

In general, deeper penetration depths were also linked to a higher coefficient of friction. A pronounced depth means that a big part of the diamond tip radius is ploughing the material while a shallow penetration depth resulted in ploughing by the outermost part of the tip. The latter one means that the ploughing area, i.e. the segment of the tip radius, is big in relation to the depth. For the deeper penetration depths, the ploughing area is smaller in relation to the depth. However, the load carrying area is not changing in the same way, which means that the quota between ploughing area and the normal area is higher for the deeper depths – i.e. the theoretical friction coefficient increases with increasing deformation depth. This will be obtained at higher load as well as for softer materials [38,39]. This was seen in the present study where the hardest material showed the lowest friction and the softest material showed the highest friction. In addition, the friction coefficient was seen to increase with increasing load.

4. Conclusions

This work presents findings on the in-situ modification of case-hardening steels in DED-LB/M to substitute the ex-situ case-hardening process. Thereby, the influence of different constituents like carbon and tungsten carbide particles on the microstructure formation, material hardness, and wear resistance of the low-alloyed steel Bainidur AM were studied. All materials could be processed without larger defects such as pores or cracks. This indicates that despite of the additional

constituents a sophisticated material could be generated by means of DED-LB/M. The key findings of this work are:

- The hardness and the microstructure of the material depends on the region within the deposited coating. While the centre of the weld tracks are characterized by a fine microstructure with a non-preferred grain orientation, the edges of the weld tracks as well as the transition zone between two tracks are characterized by a preferred grain orientation.
- Associated with the different grain orientations is a lower (for a targeted grain orientation) or higher (for a non-targeted grain orientation) material hardness, which is then again mirrored in the wear properties.
- WC particles are dissolved during DED-LB/M. EDS mappings reveal tungsten and molybdenum at the grain boundaries which affect the material hardness in these regions.
- The highest hardness of around 840 HV0.5 observed for a combined addition of C and WC leads to a surface hardness that exceeds the one of additively manufactured and case-hardened specimens reported in literature.
- Regarding the wear resistance, the addition of WC particles is preferred since tungsten-induced strengthening effects lead to a higher material hardness and delay critical wear mechanisms like ploughing to higher loads.
- The deposition direction needs to be considered when depositing a coating since loads that are applied perpendicular to the deposition direction promote an inhomogeneous wear. It is recommended to take this anisotropic behaviour into account already during the design process to assure a homogeneous wear.

Future work will focus on additional tailoring of these coatings, e.g. through the addition of Mn, as well as the comparison with conventional reference materials in test stands to determine e.g., fatigue properties of the additively generated claddings. Associated with these reference tests comes the need for the development of advantageous heat treatment strategies that are suited for this novel material system.

Funding

The authors like to thank the BMWi for funding the project “HyConnect – Ressourcenminimale Fertigung durch hybride und hochvernetzte Prozesse” (FKZ: 03LB3010*) within the scope of the “Technologietransfer-Programm Leichtbau”.

Data availability statement

The data that support the findings of this study are available from the corresponding author upon reasonable request.

Declaration of competing interest

The authors declare that they have no known competing financial interests or personal relationships that could have appeared to influence the work reported in this paper.

Acknowledgements

The authors like to thank the BMWi for funding the project “HyConnect – Ressourcenminimale Fertigung durch hybride und hochvernetzte Prozesse” within the scope of the “Technologietransfer-Programm Leichtbau.” Furthermore, the authors would like to thank the Deutsche Edelstahlwerke Speciality Steel GmbH for providing the powder material. We would like to thank the Deutsche Forschungsgemeinschaft (DFG) for funding the DED-LB/M machine with the grant 359757317. The authors gratefully acknowledge the support provided by the Erlangen Graduate School in Advanced Optical Technologies. Further acknowledgement is addressed to the Swedish KK-foundation, project number 6069, for financial support. We acknowledge financial support by Deutsche Forschungsgemeinschaft and Friedrich-Alexander-Universität Erlangen-Nürnberg within the funding programme “Open Access Publication Funding”.

REFERENCES

[1] Baek J, Cho Y, Kim D, Lee K. Plasma carburizing process for the low distortion of automobile gears. Surf Coating Technol 2000;131(1–3):568–73. https://doi.org/10.1016/S0257-8972(00)00777-5.
[2] Shah M, Das Bakshi S. Three-body abrasive wear of carbide-free bainite, martensite and bainite-martensite structure of similar hardness. Wear 2018;402–403:207–15. https://doi.org/10.1016/j.wear.2018.02.020.
[3] Patnaik A, Singh T, Kukshal V. Tribology in materials and manufacturing - wear, friction and lubrication. InTech; 2021.
[4] Parrish G. Carburizing: microstructures and properties. Materials Park, OH: ASM International; 1999.
[5] Dudova N, Kaibyshev R. On the precipitation sequence in a 10%Cr steel under tempering. ISIJ Int 2011;51(5):826–31. https://doi.org/10.2355/isijinternational.51.826.
[6] Wilms MB, Pirch N, Gökce B. Manufacturing oxide-dispersion-strengthened steels using the advanced directed energy deposition process of high-speed laser cladding. Prog Addit Manuf 2022. https://doi.org/10.1007/s40964-022-00319-1.
[7] Han J, Zhang G, Chen X, Cai Y, Luo Z, Zhang X, et al. High strength Ti alloy fabricated by directed energy deposition with in-situ Cu alloying. J Mater Process Technol 2022;310:117759. https://doi.org/10.1016/j.jmatprotec.2022.117759.
[8] Narita T, Ukai S, Ohtsuka S, Inoue M. Effect of tungsten addition on microstructure and high temperature strength of 9CrODS ferritic steel. J Nucl Mater 2011;417(1–3):158–61. https://doi.org/10.1016/j.jnucmat.2011.01.060.
[9] Bartels D, Hentschel O, Dauer J, Burgmayr W, Schmidt M. Processing of low-alloyed case-hardening steel Bainidur AM by means of DED-LB/M. In: Lasers in manufacturing. LiM; 2021. p. 2021.
[10] Bartels D, Lattre-Hertel A von, Novotny T, Mohr A, Hill H, Merklein C, et al. Directed energy deposition of low-alloyed steels: an insight on microstructural and mechanical properties. steel research int 2023:2200925. https://doi.org/10.1002/srin.202200925.
[11] Ebrahimnia M, Xie Y, Chi C. Effect of cladding parameters on microstructure and defects in direct laser metal deposition of 24CrNiMo steel. J Laser Appl 2021;33(1):12007. https://doi.org/10.2351/7.0000214.
[12] Doñate-Buendia C, Streubel R, Kürnsteiner P, Wilms MB, Stern F, Tenkamp J, et al. Effect of nanoparticle additivation on

the microstructure and microhardness of oxide dispersion strengthened steels produced by laser powder bed fusion and directed energy deposition. Procedia CIRP 2020;94:41–5. https://doi.org/10.1016/j.procir.2020.09.009.
[13] Gualtieri T, Bandyopadhyay A. Additive manufacturing of compositionally gradient metal-ceramic structures: stainless steel to vanadium carbide. Mater Des 2018;139:419–28. https://doi.org/10.1016/j.matdes.2017.11.007.
[14] Grünenwald B, Bischoff E, Shen J, Dausinger F. Laser surface alloying of case hardening steel with tungsten carbide and carbon. Mater Sci Technol 1992;8(7):637–44. https://doi.org/10.1179/mst.1992.8.7.637.
[15] Bartels D, Novotny T, Hentschel O, Huber F, Mys R, Merklein C, et al. In situ modification of case-hardening steel 16MnCr5 by C and WC addition by means of powder bed fusion with laser beam of metals (PBF-LB/M). Int J Adv Manuf Technol 2022;120(3–4):1729–45. https://doi.org/10.1007/s00170-022-08848-3.
[16] Shi Q, Gu D, Lin K, Chen W, Xia M, Dai D. The role of reinforcing particle size in tailoring interfacial microstructure and wear performance of selective laser melting WC/inconel 718 composites. J Manuf Sci Eng 2018;140(11). https://doi.org/10.1115/1.4040544.
[17] Bartels D, Rohdenburg J, Mohr A, Rothfelder R, Schmidt M. Laser metal deposition of carbide-reinforced low-alloyed steel Bainidur. AM. Procedia CIRP 2022;111:237–40. https://doi.org/10.1016/j.procir.2022.08.057.
[18] Rezaee Hajideh M, Farahani M. Direct laser metal deposition cladding of IN718 on DIN 1.2714 tool steel reinforced by the SiC nanoparticles. J Mater Res Technol 2023;23:2020–30. https://doi.org/10.1016/j.jmrt.2023.01.107.
[19] Hentschel O, Siegel L, Scheitler C, Huber F, Junker D, Gorunow A, et al. Processing of AISI H11 tool steel powder modified with carbon black nanoparticles for the additive manufacturing of forging tools with tailored mechanical properties by means of laser metal deposition (LMD). Metals 2018;8(9):659. https://doi.org/10.3390/met8090659.
[20] Krakhmalev P, Kazantseva N. Microstructure of L-PBF alloys. In: Fundamentals of laser powder bed fusion of metals. Elsevier; 2021. p. 215–43.
[21] Schmitt M, Kamps T, Siglmüller F, Winkler J, Schlick G, Seidel C, et al. Laser-based powder bed fusion of 16MnCr5 and resulting material properties. Addit Manuf 2020;35:101372. https://doi.org/10.1016/j.addma.2020.101372.
[22] Bartels D, Klaffki J, Pitz I, Merklein C, Kostrewa F, Schmidt M. Investigation on the case-hardening behavior of additively manufactured 16MnCr5. Metals 2020;10(4):536. https://doi.org/10.3390/met10040536.
[23] Yang M, Sisson RD. Carburizing heat treatment of selective-laser-melted 20MnCr5 steel. J Mater Eng Perform 2020;29(6):3476–85. https://doi.org/10.1007/s11665-020-04564-9.
[24] Zhang K, Wang S, Liu W, Shang X. Characterization of stainless steel parts by laser metal deposition shaping. Mater Des 2014;55:104–19. https://doi.org/10.1016/j.matdes.2013.09.006.
[25] Yin X, Zhai Q, Zhang Q, Wang K, Meng L, Ma Z, et al. Effect of tungsten particles on microstructure and properties of 316 L stainless steel manufactured by selective laser melting. J Manuf Process 2021;68:210–21. https://doi.org/10.1016/j.jmapro.2021.05.039.
[26] van Bohemen SMC. Bainite and martensite start temperature calculated with exponential carbon dependence. Mater Sci Technol 2012;28(4):487–95. https://doi.org/10.1179/1743284711Y.0000000097.
[27] Fetni S, Enrici TM, Niccolini T, Tran HS, Dedry O, Duchêne L, et al. Thermal model for the directed energy deposition of composite coatings of 316L stainless steel enriched with tungsten carbides. Mater Des 2021;204:109661. https://doi.org/10.1016/j.matdes.2021.109661.
[28] Fazliana F, Aqida SN, Ismail I. Effect of tungsten carbide partial dissolution on the microstructure evolution of a laser clad surface. Opt Laser Technol 2020;121:105789. https://doi.org/10.1016/j.optlastec.2019.105789.
[29] Wang XH, Song SL, Qu SY, Zou ZD. Characterization of in situ synthesized TiC particle reinforced Fe-based composite coatings produced by multi-pass overlapping GTAW melting process. Surf Coating Technol 2007;201(12):5899–905. https://doi.org/10.1016/j.surfcoat.2006.10.042.
[30] Akbari M, Kovacevic R. An investigation on mechanical and microstructural properties of 316LSi parts fabricated by a robotized laser/wire direct metal deposition system. Addit Manuf 2018;23:487–97. https://doi.org/10.1016/j.addma.2018.08.031.
[31] Doñate-Buendía C, Gu D, Schmidt M, Barcikowski S, Korsunsky AM, Gökce B. On the selection and design of powder materials for laser additive manufacturing. Mater Des 2021;204:109653. https://doi.org/10.1016/j.matdes.2021.109653.
[32] Chakraborty A, Singh JK, Sen D, Pityana S, Manna I, Krishna S, et al. Microstructures, wear and corrosion resistance of laser composite surfaced austenitic stainless steel (AISI 304 SS) with tungsten carbide. Opt Laser Technol 2021;134:106585. https://doi.org/10.1016/j.optlastec.2020.106585.
[33] Hutchings IM, Shipway P. Tribology: friction and wear of engineering materials. Oxford: Butterworth-Heinemann, an imprint of Elsevier; 2017.
[34] zum Gahr K-H. Wear by hard particles. Tribol Int 1998;31(10):587–96. https://doi.org/10.1016/S0301-679X(98)00079-6.
[35] Pöhl F, Hardes C, Theisen W. Deformation behavior and dominant abrasion micro mechanisms of tempering steel with varying carbon content under controlled scratch testing. Wear 2019;422–423:212–22. https://doi.org/10.1016/j.wear.2019.01.073.
[36] Zhou TP, Wang CY, Wang C, Cao WQ, Chen ZJ. Austenite stability and deformation-induced transformation mechanism in cold-rolled medium-Mn steel. Mater Sci Eng, A 2020;798:140147. https://doi.org/10.1016/j.msea.2020.140147.
[37] Brykov MN, Akrytova TO, Osipov MJ, Petryshynets I, Puchy V, Efremenko VG, et al. Abrasive wear of high-carbon low-alloyed austenite steel: microhardness, microstructure and X-ray characteristics of worn surface. Materials 2021;14(20):6159. https://doi.org/10.3390/ma14206159.
[38] Lee K, Marimuthu KP, Kim C-L, Lee H. Scratch-tip-size effect and change of friction coefficient in nano/micro scratch tests using XFEM. Tribol Int 2018;120:398–410. https://doi.org/10.1016/j.triboint.2018.01.003.
[39] Vencl A, Manić N, Popovic V, Mrdak M. Possibility of the abrasive wear resistance determination with scratch tester. Tribol Lett 2010;37(3):591–604. https://doi.org/10.1007/s11249-009-9556-x.

Contribution to the Goal of this Work:

The combined addition of elemental carbon and tungsten carbide particles to improve the material hardness of case-hardening steels was investigated in this manuscript. Defect-free structures with a surface hardness exceeding 800 HV can be generated by means of DED-LB/M for a carbon content of 0.4 wt.-% and a WC concentration of 5 wt.-%. This hardness even surpasses the one obtained for additively manufactured and carburised specimens that were obtained in Section 6.1. During processing, the WC particles are dissolved and are no longer present as hard and embedded particles within the matrix. The consequence is a predominantly martensitic microstructure with high shares of retained austenite of up to 30 %. These retained austenite ratios depend on the reinforcing materials and increase significantly with the addition of WC. Even though high contents of retained austenite were measured, an exceptionally high surface hardness was determined, which is uncharacteristic. However, the single weld tracks that form the final component need to be distinguished in harder (fusion zone) and softer (weld track boundary) regions. The softer regions are characterised by longer grains with a preferred growth direction while the harder regions possess finer grains without a preferential grain orientation. Furthermore, the softer regions are almost completely absent of carbide forming elements that might help to increase the hardness and thus reduce the wear rate. In contrast to the soft regions, precipitated tungsten can be identified within the hard regions. Softer regions are consequently characterised by a higher abrasive wear while harder regions are associated with a lower wear. This difference becomes critical when loading the workpiece perpendicular to the deposition direction of the weld tracks. Adding hard WC particles helps to homogenise the wear within the entire specimen, even when crossing multiple single weld tracks. The main contribution to RQ4 is that hard particles like WC should be introduced not only to reduce but also homogenise the wear rate of additively manufactured case-hardening steels. Even though hardness differences within the single weld tracks are still evident, the wear resistence is positively affected. Furthermore, the coating deposition strategy should be selected accordingly so that the surface of the workpiece is loaded parallel and not perpendicular to the weld track direction.

Figure 22 summarises the key findings of Section 6.2 to 6.5 regarding the in-situ modification of case-hardening steels with elemental carbon and tungsten carbide particles. Overall, thresholds were identified at which an

almost defect-free processing of modified case-hardening steels was possible in PBF-LB/M and DED-LB/M. Furthermore, the associated material properties were analysed for the different reinforcement approaches.

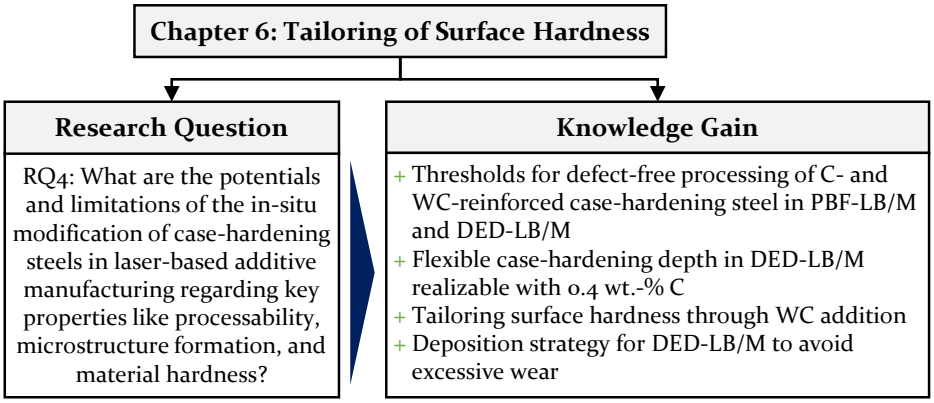

Figure 22: Summary of the key findings with regard to RQ4.

The hardness in PBF-LB/M can exceed 700 HV1 when modifying the material in-situ with carbon and hardening the specimen afterwards. When using DED-LB/M, an even higher hardness of above 800 HV1 can be obtained. The underlying material hardness in both processes is correspondingly sufficiently high for the use of the materials in different applications such as bearings, gears, or tooling. These findings show that it is possible to achieve a sufficiently high surface hardness by modifying the material already in-situ, meaning that post-process carburising heat treatments could be spared in the future.

7 Summary and Conclusion

Within this work, the processing of case-hardening steels using the laser-based AM technologies PBF-LB/M and DED-LB/M was investigated. The overarching goal was to explain the correlations between processing strategy, material composition, and the resulting material properties. By a thorough characterisation of the as-built properties of case-hardening steels, a fundamental understanding on the underlying microstructure was generated for small-scaled specimens manufactured by means of PBF-LB/M and DED-LB/M. It was furthermore shown that the thermal history is a decisive lever that affects the resulting material properties of case-hardening steels by altering the key mechanism responsible for microstructure transformation when fabricating large-scaled parts. However, it is possible to minimise the influence of the heat accumulation on the resulting part properties by tailoring the process strategy through a reduction of the energy input. Furthermore, the influence of different ex-situ and in-situ strategies on the hardenability was shown. It was found that the in-situ material modification by the addition of carbon and tungsten carbide allows to generate parts with a sufficiently high surface hardness while still possessing a reasonable processability. The key findings of this work are:

- The resulting microstructure in small-scaled specimens is bainite-dominated with shares of martensite and retained austenite. PBF samples are characterised by a lower and upper bainitic microstructure in the fusion and heat-affected zone, respectively. DED specimens possess a more upper bainitic microstructure. However, independent of the applied laser-based AM process, the additively generated parts are characterised by an excellent temperature stability upon tempering and a comparable material hardness of around 405 HV1 (RQ1).
- Building large-scaled parts in PBF-LB/M promotes heat accumulation along build direction due to the layerwise energy input. This heat accumulation affects the microstructure in different regions within the parts due to an altered transformation. In lower regions, the austenite is almost fully transformed into bainite with shares of martensite and austenite. With increasing part height, the amount of retained austenite increases, indicating an incomplete transformation into degenerated upper bainite and large shares of austenite plates. Moving towards even higher regions leads to a reversal of this trend, resulting in a granular bainitic microstructure with a reduced austenite content and a similar material hardness as in the bottom region. This effect was found to be

energy-input-dependent and can be postponed by lowering the energy input or introducing additional inter-layer times during build-up (RQ2).

- Additively manufactured specimens possess a better case-hardenability compard to conventionally manufactured specimens, which is due to the finer microstructure. Both the peak hardness (+ 10 %) and the case-hardening depth (+ 15 %) are higher for additively manufactured parts. The improved case-hardenability can be used either as safety factor during product design or for reducing the carburisation time (RQ3).
- In-situ modification of case-hardening steels can be performed successfully in PBF-LB/M and DED-LB/M. Specimens with up to 0.4 wt.-% carbon can be processed successfully using both processes. However, differences can be identified when adding WC particles. The identified thresholds for WC addition were 2.5 wt.-% (PBF-LB/M) and 5 wt.-% (DED-LB/M), respectively. Higher WC concentrations support crack formation due to the formation of a pronounced carbide network. In PBF-LB/M, low energy inputs result in a fine dispersion while higher enery inputs lead to melting of the WC particles. In contrast to PBF-LB/M, the majority of the particles is dissolved in DED-LB/M (RQ4).
- Coatings based on reinforced case-hardening steels are characterised by different microstructures in the centre and in the boundary region of the weld track. Associated with these inhomogeneities is a varying material hardness within the single tracks that form the coating. Correspondingly, the wear rate is fluctuating when loading the specimen perpendicular to the weld track deposition direction. It is therefore recommended to either deposit the weld track parallel to the later load direction, to apply a heat treatment for dissolving the weld track boundaries, or to use larger laser spot sizes to reduce the amount of these interfaces (RQ4).

The presented investigations reveal the potentials of sparing the time-consuming carburising heat treatment from the conventionally established process chain by in-situ alloying and in-situ particle reinforcement. It is possible to process carbon-modified case-hardening steels using PBF-LB/M at the absence of cracks and pores. By introducing WC particles, the wear resistance can further be improved compared to martensitic-hardened materials. The potentials of DED-LB/M are even more significant since it can be used for flexibly tailoring the surface properties while even maintaining the underlying microstructure of the main body. Based on these findings, a combination of PBF-LB/M and DED-LB/M appears promising for the fabrication of sophisticated parts with integrated structures (PBF-LB/M) and the deposition of tailored surface coatings (DED-LB/M).

Bibliography

[1] *Vollset, S.E.; Goren, E.; Yuan, C.-W. et al.:* Fertility, mortality, migration, and population scenarios for 195 countries and territories from 2017 to 2100: a forecasting analysis for the Global Burden of Disease Study. *In:* Lancet (London, England), Vol. 396 (2020), Iss. 10258, pp. 1285-1306. https://doi.org/10.1016/S0140-6736(20)30677-2.

[2] *United Nations:* The 17 Goals. Department of Economic and Social Affairs, https://sdgs.un.org/goals [Zugriff am: 07.03.2023].

[3] *United Nations:* Progress towards the Sustainable Development Goals – Report of the Secretary-General, 2020.

[4] *Kron, T. (Hrsg.):* Individualisierung und soziologische Theorie. VS Verlag für Sozialwissenschaften, Wiesbaden, 2000.

[5] *Despeisse, M.; Ford, S.:* The Role of Additive Manufacturing in Improving Resource Efficiency and Sustainability. *In: Umeda, S.; Nakano, M.; Mizuyama, H. et al.* (Hrsg.): Advances in Production Management Systems: Innovative Production Management Towards Sustainable Growth, IFIP Advances in Information and Communication Technology. Springer International Publishing, Cham, 2015, S. 129-136.

[6] *Mosallanejad, M.H.; Niroumand, B.; Aversa, A. et al.:* In-situ alloying in laser-based additive manufacturing processes: A critical review. *In:* Journal of Alloys and Compounds 872 (2021), S. 159567. https://doi.org/10.1016/j.jallcom.2021.159567.

[7] *Das, S.:* Physical Aspects of Process Control in Selective Laser Sintering of Metals. *In:* Advanced Engineering Materials 5 (2003), Heft 10, S. 701-711. https://doi.org/10.1002/adem.200310099.

[8] *Svetlizky, D.; Das, M.; Zheng, B. et al.:* Directed energy deposition (DED) additive manufacturing: Physical characteristics, defects, challenges and applications. *In:* Materials Today 49 (2021), S. 271-295. https://doi.org/10.1016/j.mattod.2021.03.020.

[9] *Bleck, W.; Moeller, E. (Hrsg.):* Handbuch Stahl – Auswahl, Verarbeitung, Anwendung, Hanser eLibrary, Hanser, München, 2018.

[10] *Nutting, J.; Baker, R.G.:* The Microstructure of Metals, Institute of Metals, Monograph and Report Series, Institute of Metals, 1965.

[11] *Iron and Steel Institute:* The Journal of the Iron and Steel Institute. The Institute, Pennsylvania State University, 1879.

[12] *Halle, J.S.; Perret, J.J.:* Präktische Anweisung alle Stahlarten zu kennen, zu härten, anzulassen, und vernünftig zu bearbeiten: zum Gebrauch der mechanischen Künstler, sonderlich der Künstler in Stahl : nach des gekrönten Preisschrift des Herrn Perrets. bey Friedrich Maurer, 1783.

[13] *Bain, E.C.:* Functions of the Alloying Elements in Steel. American Society for Metals, 1939.

[14] *Papp, J.F.; United States. Bureau of Mines:* Chromium, Nickel, and Other Alloying Elements in U.S.-produced Stainless and Heat-resisting Steel, Information circular, U.S. Department of the Interior, Bureau of Mines, 1991.

[15] *Majert, H.:* Der Einfluß verschiedener Legierungselemente auf die Härtbarkeit der Kohlenstoffstähle. Stahleisen, 1933.

[16] *Gerber, W.; Wyss, U.:* Die Härtbarkeit und die Vergütbarkeit der Stähle. Roll Mitteilungen, 1948.

[17] *Ludlum Steel Company:* High Speed, Carbon and Alloy Tool Steels: Non-corrosive Iron and Steel. The Company, 1924.

[18] *Callister, W.D.; Rethwisch, D.G.:* Materials science and engineering – An introduction. John Wiley & Sons, Inc, Hoboken, NJ, 2018.

[19] *Totten, G.E. (ed.):* Steel Heat Treatment Handbook. Marcel Dekker, New York, 1997.

[20] *Éntin, R.I.:* Transformation of austenite on cooling. *In:* Metal Science and Heat Treatment 9 (1967), Heft 10, S. 791-797. https://doi.org/10.1007/BF00652823.

[21] *Saunders, E.R.:* A study of martensite formation. Cincinnati University, 1941.

[22] *Vaidyanathan, S.:* The Shaping of Brittle Solids. University of California, 1969.

[23] *Society of Manufacturing Engineers:* Troubleshooting manufacturing processes – Adapted from the Tool and Manufacturing Engineers Handbook ; a reference book for manufacturing engineers, managers, and technicians. Society of Manufacturing Engineers. Society of Manufacturing Engineers, Dearborn, Mich., 1988.

[24] *Stout, R.D.; Doty, W.:* Weldability of Steels. Welding Research Council, 1971.

[25] *Gilath, I.; Signamarcheix, J.M.; Bensussan, P.:* A comparison of methods for estimating the weld-metal cooling rate in laser welds. *In:*

Journal of Materials Science 29 (1994), Heft 12, S. 3358-3362. https://doi.org/10.1007/BF00356685.

[26] *Migliore, L.R.:* Laser materials processing, Manufacturing engineering and materials processing no. 46, Marcel Dekker, Inc., New York, Basel, Hong Kong, 1996.

[27] *Cottrell, C.:* Austenite Transformation Characteristics in Relation to Hard-zone Cracking in Welded Low-alloy Steels – Part II - Determination of Continuous-Cooling Transformation Diagrams for a Manganese-Molybdenum Steel Containing Different Amounts of Hydrogen. British Welding Research Association, BWRA-FM-8/89, British Welding Research Association, 1953.

[28] *Hultgren, A.:* Isothermal Transformation of Austenite and Partitioning of Alloying Elements in Low Alloy Steels, Kungl. Svenska vetenskapsakademiens handlingar, Almaqvist & Wiksell, 1953.

[29] *Okazaki, A.; Lowde, R.D.:* An explanation of the "martensite start"-"martensite finish" temperature interval. *In:* Solid State Communications 43 (1982), Heft 7, S. 503-506. https://doi.org/10.1016/0038-1098(82)90063-1.

[30] *Vander Voort, G.F. (ed.):* Atlas of time-temperature diagrams for irons and steels. ASM International, Materials data series, ASM International, Metals Park, Ohio, 1991.

[31] *Iron and Steel Institute:* Physical Properties of Martensite and Bainite – : Report of the Proceedings of the Joint Conference Organized by the British Iron and Steel Research Association and the Iron and Steel Institute and Held at Scarborough, on 10, 11, and 12 May 1965, Iron and Steel Institute. Special report, Iron and Steel Institute, 1965.

[32] *Saunders, N.; Miodownik, A.P.:* CALPHAD (calculation of phase diagrams) – A comprehensive guide, Pergamon Materials Serv.Volume 1, Pergamon, Oxford, 1998.

[33] *Davis, J.R. (ed.):* Tool materials. ASM International, ASM specialty handbook, ASM International, Materials Park, Ohio, 1995.

[34] *Frankel, H.E.:* Fatigue Properties of High Strength Steels. *In:* Trans. ASM 52 (1960), S. 257-276.

[35] *Jacques, P.J.; Delannay, F.; Ladrière, J.:* On the influence of interactions between phases on the mechanical stability of retained austenite in transformation-induced plasticity multiphase steels. *In:* Metallurgical and Materials Transactions A 32 (2001), Heft 11, S. 2759-2768. https://doi.org/10.1007/s11661-001-1027-4.

[36] *Cochrane, R.W.; Ström-Olsen, J.O.:* Rapidly quenched metals 6 – Proceedings of the Sixth International Conference on Rapidly Quenched Metals, Montréal, August 3-7, 1987. Elsevier Applied Science; Sole distributor in the USA and Canada, Elsevier Science Pub. Co, London, 1988.

[37] *Bergh, D.A.:* The Effect of Time on the Isothermal Decomposition of Retained Austenite in Case Carburized Low Alloy Steels in the Range 450 to 800 Degrees Fahrenheit. Michigan State College of Agriculture and Applied Science. Department of Chemical and Metallurgical Engineering, 1948.

[38] *Baker, R.G.:* The tempering of 2.25Cr%-1%Mo steel after quenching and normalizing. *In:* J. Iron Steel Inst. 192 (1959), Heft 3, S. 257-268.

[39] *Zhang, Z.:* An atlas of continuous cooling transformation (CCT) diagrams applicable to low carbon low alloy weld metals. CRC Press, Boca Raton, 2020.

[40] *Qingbin, L.; Hong, L.:* Experimental study of the laser quenching of 40CrNiMoA steel. *In:* Journal of Materials Processing Technology 88 (1999), 1-3, S. 77-82. https://doi.org/10.1016/S0924-0136(98)00381-1.

[41] *Zare, A.; Ekrami, A.:* Influence of martensite volume fraction on tensile properties of triple phase ferrite–bainite–martensite steels. *In:* Materials Science and Engineering: A 530 (2011), S. 440-445. https://doi.org/10.1016/j.msea.2011.09.108.

[42] *British Iron and Steel Research Association:* Atlas of Isothermal Transformation Diagrams of B.S. En Steels, Special report (Iron and Steel Institute), Iron and Steel Institute, 1949.

[43] *Stickels, C.A.:* Carbide refining heat treatments for 52100 bearing steel. *In:* Metallurgical Transactions 5 (1974), Heft 4, S. 865-874. https://doi.org/10.1007/BF02643140.

[44] *Sidoroff, C.:* Analyse microstructurale et modélisation des évolutions dimensionnelles de l'acier 100Cr6: structures martensitique et bainitique, Lyon, INSA, 2002.

[45] *Bhadeshia, H.K.D.H.:* Bainite in Steels – Transformations, Microstructure and Properties, Book / Institute of Materials no. 504, Institute of Materials, London, 1992.

[46] *SUGIMOTO, K.; YU, B.; MUKAI, Y. et al.:* Microstructure and Formability of Aluminum Bearing TRIP-Aided Steels with Annealed Martensite Matrix. *In:* ISIJ International 45 (2005), Heft 8, S. 1194-1200. https://doi.org/10.2355/isijinternational.45.1194.

[47] *Deutsche Edelstahlwerke GmbH:* Selecting Materials – for Punching and Forming Tools and the Heat Treatment thereof. *In:* 2013, August, **2013**.

[48] *Klocke, F.; Brecher, C.:* Zahnrad- und Getriebetechnik – Auslegung - Herstellung - Untersuchung - Simulation. Carl Hanser Verlag. CARL HANSER Verlag GMBH & [Place of publication not identified], 2016.

[49] 281:2007: Rolling bearings — Dynamic load ratings and rating life. ISO, Ausgabe Februar 2007.

[50] *Krauss, G.:* Martensite in steel: strength and structure. *In:* Materials Science and Engineering: A 273-275 (1999), S. 40-57. https://doi.org/10.1016/S0921-5093(99)00288-9.

[51] *Motallebi, R.; Mirzadeh, H.:* Tailoring the mechanical properties of austempered low-carbon ferritic–bainitic/martensitic dual-phase steel. *In:* Archives of Civil and Mechanical Engineering 23 (2023), Heft 1. https://doi.org/10.1007/s43452-022-00572-9.

[52] *Engqvist, H.; Jacobson, S.; Axén, N.:* A model for the hardness of cemented carbides. *In:* Wear 252 (2002), 5-6, S. 384-393. https://doi.org/10.1016/S0043-1648(01)00866-3.

[53] *Grange, R.A.:* The Temperature Range of Martensite Formation. *In:* Transactions of the American Institute of Mining and Metallurgical Engineers 167 (1946), S. 467-501.

[54] *Messler, R.W.:* Joining of materials and structures – From pragmatic process to enabling technology. Butterworth-Heinemann, Amsterdam, 2004.

[55] *Sharma, R.C.:* Principles of heat treatment of steels. New Age International, New Delhi, 1996.

[56] *Burns, J.L.; Moore, T.L.; Archer, R.S.:* Quantitative Hardenability. *In:* Transactions of American Society for Metals 26 (1938), Heft 1.

[57] *Jaffe, L.D.; Hollomon, J.H.; WATERTOWN ARSENAL LABS MA.:* Effect of Tempering Treatment Upon Physical Properties of Martensite Tempered to a Fixed Hardness. Defense Technical Information Center, 1945.

[58] *Zhao, Y.; Xiang, Z.; Tan, Y. et al.:* Microstructure Transformation on Pre-Quenched and Ultrafast-Tempered High-Strength Multiphase Steels. *In:* Materials (Basel, Switzerland), Vol. 12 (2019), Iss. 3. https://doi.org/10.3390/ma12030396.

[59] *Honda, K.:* Die Theorie der Stahlhärtung. *In:* Archiv für das Eisenhüttenwesen 1 (1928), Heft 8, S. 527-536. https://doi.org/10.1002/srin.192800229.

[60] *Jhingan, A.K.; University of California, Berkeley. Department of Materials Science; Mineral Engineering:* Tempered Martensite Embrittlement in Medium Carton Steels. University of California, Berkeley, 1983.

[61] *Banerjee, B.R.; Capenos, J.M.; Hauser, J.J.:* Grain-Boundary Carbides in High-Speed Tool and Hot-Work Die Steels. ASTM International, 1966.

[62] *Garcia-Mateo, C.:* Bainite and Martensite: Developments and Challenges. MDPI, Basel, 2020.

[63] *Takahashi, M.; Bhadeshia, H.K.D.H.:* Model for transition from upper to lower bainite. *In:* Materials Science and Technology 6 (1990), Heft 7, S. 592-603. https://doi.org/10.1179/026708390790191521.

[64] *Bhadeshia, H.; Honeycombe, R.:* Steels – Microstructure and Properties, Fourth Edition, Engineering professional collection, Elsevier Science and Technology Books, Inc [Place of publication not identified], 2017.

[65] *Cui, X.; Zhang, S.; Wang, Z.Y. et al.:* Microstructure and fatigue behavior of 24CrNiMo low alloy steel prepared by selective laser melting. *In:* Materials Science and Engineering: A 845 (2022), S. 143215. https://doi.org/10.1016/j.msea.2022.143215.

[66] *Lapouge, P.; Dirrenberger, J.; Coste, F. et al.:* Laser heat treatment of martensitic steel and dual-phase steel with high martensite content. *In:* Materials Science and Engineering: A 752 (2019), S. 128-135. https://doi.org/10.1016/j.msea.2019.03.016.

[67] *Bhadeshia, H.:* The lower bainite transformation and the significance of carbide precipitation. *In:* Acta Metallurgica 28 (1980), Heft 8, S. 1103-1114. https://doi.org/10.1016/0001-6160(80)90093-0.

[68] *Bhadeshia, H.K.D.H.; Edmonds, D.V.:* The bainite transformation in a silicon steel. *In:* Metallurgical and Materials Transactions A 10 (1979), Heft 7, S. 895-907. https://doi.org/10.1007/BF02658309.

[69] *Honeycombe, R.W.K.; Pickering, F.B.:* Ferrite and bainite in alloy steels. *In:* Metallurgical Transactions 3 (1972), Heft 5, S. 1099-1112. https://doi.org/10.1007/BF02642441.

[70] *Bhadeshia, H.K.D.H.:* Bainite in steels – Transformations, microstructure and properties, Book // Institute of Materials no. 735, IOM Communications, London, 2001.

[71] *Ohmori, Y.; Ohtani, H.; Kunitake, T.:* Tempering of the Bainite and the Bainite/Martensite Duplex Structure in a Low-Carbon Low-Alloy Steel. *In:* Metal Science 8 (1974), Heft 1, S. 357-366. https://doi.org/10.1179/msc.1974.8.1.357.

[72] *Irvine, K.J.; Pickering, F.B.:* Low-Carbon Bainitic Steels. *In:* Journal of the Iron and Steel Institute 184 (1957), Heft 12, S. 292-309.

[73] *Bormann, A.:* Serielle, induktive Wärmebehandlung laserstrahlgeschweißter Feinbleche Ausgabe 2004.

[74] *Bush, M.; Kelly, P.:* Strengthening mechanisms in bainitic steels. *In:* Acta Metallurgica 19 (1971), Heft 12, S. 1363-1371. https://doi.org/10.1016/0001-6160(71)90074-5.

[75] *Kang, J.; Zhang, F.C.; Yang, X.W. et al.:* Effect of tempering on the microstructure and mechanical properties of a medium carbon bainitic steel. *In:* Materials Science and Engineering: A 686 (2017), S. 150-159. https://doi.org/10.1016/j.msea.2017.01.044.

[76] *Kafadar, G.; Kalkanli, A.; Özdemir, A.T. et al.:* Effect of Isothermal Transformation Treatment and Tempering on the Microstructure and Hardness of a Medium C and High Si Steels. *In:* ISIJ International 61 (2021), Heft 5, S. 1679-1687. https://doi.org/10.2355/isijinternational.ISIJINT-2020-419.

[77] *Apple, C.A.; Krauss, G.:* The Effect of Carbide-forming Elements on the Structure and Mechanical Properties Produced by Cyclic Transformation. Department of Metallurgy and Materials Science, Lehigh University, 1969.

[78] *Davis, J.R. (ed.):* Heat-resistant materials. ASM International, ASM speciality handbook, ASM International, Materials Park, 1999.

[79] *Abe, F.:* Strengthening Mechanisms in Creep of Advanced Ferritic Power Plant Steels Based on Creep Deformation Analysis. *In: Weng, Y.; Dong, H.; Gan, Y.* (Hrsg.): Advanced Steels. Springer Berlin Heidelberg, Berlin, Heidelberg, 2011, S. 409-422.

[80] *Miyahara, H.; Bravo, S.V.; Yamamoto, K. et al.:* Solute Concentration and Carbides Formation for Steel Milling Rolls. *In:* ISIJ International 49 (2009), Heft 7, S. 1075-1079. https://doi.org/10.2355/isijinternational.49.1075.

[81] *Scott, H.:* Relation of the High-temperature Treatment of High-speed Steel to Secondary Hardening and Red Hardness, Scientific papers of the Bureau of Standards, U.S. Government Printing Office, 1920.

[82] *Bu, F.Z.; Wang, X.M.; Chen, L. et al.:* Influence of cooling rate on the precipitation behavior in Ti–Nb–Mo microalloyed steels during continuous cooling and relationship to strength. *In:* Materials Characterization 102 (2015), S. 146-155. https://doi.org/10.1016/j.matchar.2015.03.005.

[83] *Voigt, R.C.; Loper Jr, C.R.:* Study of heat-affected zone structures in ductile cast iron. *In:* WELDING J 62 (1983), Heft 3, S. 82.

[84] *Khrushchev, M.M.; Babichev, M.A.; National Science Foundation et al.:* Resistance to Abrasive Wear and the Hardness of Metals, NSF-tr, U.S. Atomic Energy Commission, Technical Information Service, 1953.

[85] *zum Gahr, K.-H.:* Microstructure and Wear of Materials, Tribology series no. 10, Elsevier, Amsterdam [u.a.], 1987.

[86] *Coronado, J.J.; Caicedo, H.F.; Gómez, A.L.:* The effects of welding processes on abrasive wear resistance for hardfacing deposits. *In:* Tribology International 42 (2009), Heft 5, S. 745-749. https://doi.org/10.1016/j.triboint.2008.10.012.

[87] *Galgali, R.K.; Ray, H.S.; Chakrabarti, A.K.:* Wear characteristics of TiC reinforced cast iron composites Part 1 – Adhesive wear. *In:* Materials Science and Technology 14 (1998), Heft 8, S. 810-815. https://doi.org/10.1179/mst.1998.14.8.810.

[88] ISO 683-3:2022: Für eine Wärmebehandlung bestimmte Stähle, legierte Stähle und Automatenstähle. DIN EN, Ausgabe 2022.

[89] *Ohno, T.; Fujita, M.; Nishida, K. et al.:* Molybdenum-saving case hardening steel. *In:* SAE transactions (1982), S. 445-455.

[90] *Barthelmes, H.:* Handbuch Industrial Engineering – Vom Markt zum Produkt. Hanser, München, 2013.

[91] *Badger, H.R.:* Heat Treatment of Steel: Hardening, Tempering, Case-Hardening (Classic Reprint). 1kg Limited, 2016.

[92] *Hoffmann, H.; Neugebauer, R.; Spur, G.:* Handbuch Umformen, Handbuch der Fertigungstechnik, Hanser, München, 2012.

[93] *Çetinkaya, C.; Arabaci, U.:* Flash butt welding application on 16MnCr5 chain steel and investigations of mechanical properties. *In:*

Materials & Design 27 (2006), Heft 10, S. 1187-1195. https://doi.org/10.1016/j.matdes.2005.02.002.

[94] *Grosch, J.; Bartz, W.J.:* Einsatzhärten – Grundlagen - Verfahren - Anwendung - Eigenschaften einsatzgehärteter Gefüge und Bauteile, Kontakt & Studiumv. 356, Expert, Tübingen, 2019.

[95] *Parrish, G.:* Carburizing – Microstructures and properties. ASM International, Materials Park, OH, 1999.

[96] *Whipple, W.J.:* The carburization of steels of" Krupp" analysis. Carnegie Institute of Technology. Dudley Know Library, 1936.

[97] *Liedtke, D.:* Merkblatt 452 – "Einsatzhärten", Düsseldorf, Germany, 2008.

[98] 2639:2002: Stahl - Bestimmung und Prüfung der Einsatzhärtetiefe. ISO, Ausgabe April 2003.

[99] *Rudnev, V.; Loveless, D.; Cook, R.L. et al.:* Handbook of Induction Heating, Manufacturing engineering and materials processing, CRC Press, Boca Raton, FL, 2002.

[100] *Laubscher, R.F.:* Advanced Gear Manufacturing and Finishing – Classical and Modern Processes. Elsevier Science Publishing Co, 2017.

[101] *Hippenstiel, F.; Bleck, W.; Clausen, B. et al.:* Innovative Einsatzstähle als massgeschneiderte Werkstofflösung zur Hochtemperaturaufkohlung von Getriebekomponenten. Diskussion, 2002.

[102] *Davies, A.C.:* The Science and Practice of Welding: Volume 1, The Science and Practice of Welding, Cambridge University Press, 1992.

[103] *Burbank, J.; Woydt, M.:* Comparison of slip-rolling behaviour between 20MnCr5 gear steel, 36NiCrMoV1-5-7 hot working tool steel and 45SiCrM06 spring steel. *In:* Wear 328-329 (2015), S. 28-38. https://doi.org/10.1016/j.wear.2015.01.024.

[104] *Lupi, S.; Forzan, M.; Aliferov, A.:* Induction and Direct Resistance Heating – Theory and Numerical Modeling. Springer International Publishing, Cham, 2015.

[105] 52900:2021: Additive manufacturing — General principles — Fundamentals and vocabulary. Ausgabe 2021.

[106] *Gebhardt, A.:* Additive Fertigungsverfahren – Additive Manufacturing und 3D-Drucken für Prototyping - Tooling - Produktion. Carl Hanser Verlag GmbH & Co. KG, München, 2017.

[107] *Gibson, I.:* Additive Manufacturing Technologies – 3D Printing, Rapid Prototyping, and Direct Digital Manufacturing, Springer

eBook Collection Engineering, Springer New York, New York, NY, 2015.

[108] *Bian, L.; Shamsaei, N.; Usher, J.M. (eds.):* Laser-based additive manufacturing of metal parts – Modeling, optimization, and control of mechanical properties, Advanced and Additive Manufacturing Series, CRC Press, Boca Raton, Florida, 2018.

[109] *Deininger, M.:* Additive Fertigungsverfahren. Selektives Lasersintern, Fused Deposition Modeling, Electron Beam Melting, Stereolithografie, Polygrafie, Schicht-Laminat-Verfahren. GRIN Verlag, München, 2020.

[110] *Breuninger, J.; Becker, R.; Wolf, A. et al.:* Generative Fertigung mit Kunststoffen – Konzeption und Konstruktion für Selektives Lasersintern, SpringerLink Bücher, Springer Berlin Heidelberg; Imprint; Springer, Berlin, Heidelberg, 2013.

[111] *Yang, L.; Hsu, K.; Baughman, B. et al.:* Additive Manufacturing of Metals: The Technology, Materials, Design and Production, Springer Series in Advanced Manufacturing, Springer International Publishing, Cham, 2017.

[112] *Yadroitsev, I.; Yadroitsava, I.; Du Plessis, A. et al. (eds.):* Fundamentals of laser powder bed fusion of metals, Additive manufacturing materials and technologies, Elsevier, Amsterdam, 2021.

[113] *Möller, M.L.B.:* Prozessmanagement für das Laser-Pulver-Auftragschweißen, Light Engineering für die Praxis, Springer Berlin Heidelberg; Springer Vieweg, Berlin, Heidelberg, 2021.

[114] *Lachmayer, R.; Lippert, R.B.; Kaierle, S. (Hrsg.):* Additive Serienfertigung – Erfolgsfaktoren und Handlungsfelder für die Anwendung. Springer Berlin Heidelberg, Berlin, Heidelberg, 2018.

[115] *SLM Solutions Group AG:* SLM®280 – SLM®280 Technical Specifications, https://www.slm-solutions.com/products-and-solutions/machines/slm-280/ [Zugriff am: 03.03.2023].

[116] *Aconity GmbH:* AconityMIDI – Machine Description, 2023, https://aconity3d.com/products/aconity-midi/ [Zugriff am: 03.03.2023].

[117] *Rombouts, M.; Kruth, J.P.; Froyen, L. et al.:* Fundamentals of Selective Laser Melting of alloyed steel powders. *In:* CIRP Annals 55 (2006), Heft 1, S. 187-192. https://doi.org/10.1016/S0007-8506(07)60395-3.

[118] *Górny, M.; Tyrała, E.:* Effect of Cooling Rate on Microstructure and Mechanical Properties of Thin-Walled Ductile Iron Castings. *In:* Journal of Materials Engineering and Performance 22 (2013), Heft 1, S. 300-305. https://doi.org/10.1007/s11665-012-0233-0.

[119] *Mercelis, P.; Kruth, J.-P.:* Residual stresses in selective laser sintering and selective laser melting. *In:* Rapid Prototyping Journal 12 (2006), Heft 5, S. 254-265. https://doi.org/10.1108/13552540610707013.

[120] *Kempen, K.; Thijs, L.; Vrancken, B. et al.:* Producing Crack-Free, High Density M2 HSS Parts by Selective Laser Melting: Pre-Heating the Baseplate Ausgabe 2013.

[121] *Edin, E.; Svahn, F.; Åkerfeldt, P. et al.:* Rapid method for comparative studies on stress relief heat treatment of additively manufactured 316L. *In:* Materials Science and Engineering: A 847 (2022), S. 143313. https://doi.org/10.1016/j.msea.2022.143313.

[122] *Sun, S.; Teng, Q.; Xie, Y. et al.:* Two-step heat treatment for laser powder bed fusion of a nickel-based superalloy with simultaneously enhanced tensile strength and ductility. *In:* Additive Manufacturing 46 (2021), S. 102168. https://doi.org/10.1016/j.addma.2021.102168.

[123] *Yap, C.Y.; Chua, C.K.; Dong, Z.L. et al.:* Review of selective laser melting: Materials and applications. *In:* Applied Physics Reviews 2 (2015), Heft 4, S. 41101. https://doi.org/10.1063/1.4935926.

[124] *Schmitt, M.; Schlick, G.; Seidel, C. et al.:* Examination of the processability of 16MnCr5 by means of laser powder bed fusion. *In:* Procedia CIRP 74 (2018), S. 76-81. https://doi.org/10.1016/j.procir.2018.08.041.

[125] *Davidson, K.; Singamneni, S.:* Selective Laser Melting of Duplex Stainless Steel Powders: An Investigation. *In:* Materials and Manufacturing Processes 31 (2016), Heft 12, S. 1543-1555. https://doi.org/10.1080/10426914.2015.1090605.

[126] *Saewe, J.; Gayer, C.; Vogelpoth, A. et al.:* Feasability Investigation for Laser Powder Bed Fusion of High-Speed Steel AISI M50 with Base Preheating System. *In:* BHM Berg- und Hüttenmännische Monatshefte 164 (2019), Heft 3, S. 101-107. https://doi.org/10.1007/s00501-019-0828-y.

[127] *Zhang, H.; Xu, W.; Xu, Y. et al.:* The thermal-mechanical behavior of WTaMoNb high-entropy alloy via selective laser melting (SLM): experiment and simulation. *In:* The International Journal of Advanced Manufacturing Technology 96 (2018), 1-4, S. 461-474. https://doi.org/10.1007/s00170-017-1331-9.

[128] *Todd, M.K.:* High value manufacturing – Advanced research in virtual and rapid prototyping : proceedings of the 6th International Conference on Advanced Research and Rapid Prototyping, Leiria, Portugal, 1-5 October, 2013. CRC Press/Balkema, Leiden, The Netherlands, 2014.

[129] *Mazumder, J.; Choi, J.; Nagarathnam, K. et al.:* The direct metal deposition of H13 tool steel for 3-D components. *In:* JOM 49 (1997), Heft 5, S. 55-60. https://doi.org/10.1007/BF02914687.

[130] *Taminger, K.M.B.; Hafley, R.A.:* Electron Beam Freeform Fabrication: A Rapid Metal Deposition Process. *In: ,* 2003.

[131] *Mahamood, R.M.:* Laser Metal Deposition Process of Metals, Alloys, and Composite Materials, Engineering Materials and Processes, Springer International Publishing; Imprint; Springer, Cham, 2018.

[132] *Marchese, G.; Garmendia Colera, X.; Calignano, F. et al.:* Characterization and Comparison of Inconel 625 Processed by Selective Laser Melting and Laser Metal Deposition. *In:* Advanced Engineering Materials 19 (2017), Heft 3, S. 1600635. https://doi.org/10.1002/adem.201600635.

[133] *Giordano, L.; Ramous, E.; Ferraro, F. et al.:* Comparison of stellite hardfacing by laser and traditional techniques. *In:* High Temperature Technology 2 (1984), Heft 4, S. 213-216. https://doi.org/10.1080/02619180.1984.11753265.

[134] *Ahn, D.-G.:* Directed Energy Deposition (DED) Process: State of the Art. *In:* International Journal of Precision Engineering and Manufacturing-Green Technology 8 (2021), Heft 2, S. 703-742. https://doi.org/10.1007/s40684-020-00302-7.

[135] *Hentschel, O.; Siegel, L.; Scheitler, C. et al.:* Processing of AISI H11 Tool Steel Powder Modified with Carbon Black Nanoparticles for the Additive Manufacturing of Forging Tools with Tailored Mechanical Properties by Means of Laser Metal Deposition (LMD). *In:* Metals 8 (2018), Heft 9, S. 659. https://doi.org/10.3390/met8090659.

[136] *Huber, F.; Bischof, C.; Hentschel, O. et al.:* Laser beam melting and heat-treatment of 1.2343 (AISI H11) tool steel – microstructure and mechanical properties. *In:* Materials Science and Engineering: A 742 (2019), S. 109-115. https://doi.org/10.1016/j.msea.2018.11.001.

[137] *Kempen, K.; Vrancken, B.; Buls, S. et al.:* Selective Laser Melting of Crack-Free High Density M2 High Speed Steel Parts by Baseplate Preheating. *In:* Journal of Manufacturing Science and Engineering 136 (2014), Heft 6. https://doi.org/10.1115/1.4028513.

[138] *Wang, J.; Chen, C.; Zhang, M.:* Effect of Mo and Tempering Treatment on the Microstructural Evolution and Mechanical Properties of M2 High-Speed Steel Prepared by Laser-Directed Energy Deposition. *In:* steel research international 92 (2021), Heft 11, S. 2100225. https://doi.org/10.1002/srin.202100225.

[139] *Laeng, J.; Stewart, J.G.; Liou, F.W.:* Laser metal forming processes for rapid prototyping - A review. *In:* International Journal of Production Research 38 (2000), Heft 16, S. 3973-3996. https://doi.org/10.1080/00207540050176111.

[140] *Vilar, R.:* Laser Alloying and Laser Cladding. *In:* Materials Science Forum 301 (1999), S. 229-252. https://doi.org/10.4028/www.scientific.net/msf.301.229.

[141] *Banerjee, R.; Collins, P.C.; Genç, A. et al.:* Direct laser deposition of in situ Ti–6Al–4V–TiB composites. *In:* Materials Science and Engineering: A 358 (2003), 1-2, S. 343-349. https://doi.org/10.1016/S0921-5093(03)00299-5.

[142] *Pei, Y.; Hosson, J.* de: Functionally graded materials produced by laser cladding. *In:* Acta Materialia 48 (2000), Heft 10, S. 2617-2624. https://doi.org/10.1016/S1359-6454(00)00065-3.

[143] *Carroll, B.E.; Otis, R.A.; Borgonia, J.P. et al.:* Functionally graded material of 304L stainless steel and inconel 625 fabricated by directed energy deposition: Characterization and thermodynamic modeling. *In:* Acta Materialia 108 (2016), S. 46-54. https://doi.org/10.1016/j.actamat.2016.02.019.

[144] *Li, W.; Karnati, S.; Kriewall, C. et al.:* Fabrication and characterization of a functionally graded material from Ti-6Al-4V to SS316 by laser metal deposition. *In:* Additive Manufacturing 14 (2017), S. 95-104. https://doi.org/10.1016/j.addma.2016.12.006.

[145] *Scipioni Bertoli, U.; Wolfer, A.J.; Matthews, M.J. et al.:* On the limitations of Volumetric Energy Density as a design parameter for Selective Laser Melting. *In:* Materials & Design 113 (2017), S. 331-340. https://doi.org/10.1016/j.matdes.2016.10.037.

[146] *Li, Y.; Gu, D.:* Thermal behavior during selective laser melting of commercially pure titanium powder: Numerical simulation and experimental study. *In:* Additive Manufacturing 1-4 (2014), S. 99-109. https://doi.org/10.1016/j.addma.2014.09.001.

[147] *Mohr, G.; Scheuschner, N.; Hilgenberg, K.:* In situ heat accumulation by geometrical features obstructing heat flux and by reduced inter layer times in laser powder bed fusion of AISI 316L stainless steel. *In:*

Procedia CIRP 94 (2020), S. 155-160. https://doi.org/10.1016/j.procir.2020.09.030.

[148] *Mohr, G.; Altenburg, S.J.; Hilgenberg, K.:* Effects of inter layer time and build height on resulting properties of 316L stainless steel processed by laser powder bed fusion. *In:* Additive Manufacturing 32 (2020), S. 101080. https://doi.org/10.1016/j.addma.2020.101080.

[149] *Mohr, G.; Sommer, K.; Knobloch, T. et al.:* Process Induced Preheating in Laser Powder Bed Fusion Monitored by Thermography and Its Influence on the Microstructure of 316L Stainless Steel Parts. *In:* Metals 11 (2021), Heft 7, S. 1063. https://doi.org/10.3390/met11071063.

[150] *Wang, X.; Keya, T.; Chou, K.:* Build Height Effect on the Inconel 718 Parts Fabricated by Selective Laser Melting. *In:* Procedia Manufacturing 5 (2016), S. 1006-1017. https://doi.org/10.1016/j.promfg.2016.08.089.

[151] *Denlinger, E.R.; Heigel, J.C.; Michaleris, P. et al.:* Effect of inter-layer dwell time on distortion and residual stress in additive manufacturing of titanium and nickel alloys. *In:* Journal of Materials Processing Technology 215 (2015), S. 123-131. https://doi.org/10.1016/j.jmatprotec.2014.07.030.

[152] *Heigel, J.C.; Michaleris, P.; Reutzel, E.W.:* Thermo-mechanical model development and validation of directed energy deposition additive manufacturing of Ti–6Al–4V. *In:* Additive Manufacturing 5 (2015), S. 9-19. https://doi.org/10.1016/j.addma.2014.10.003.

[153] *Kamps, T.:* Gear wheel manufacture via selective laser melting Ausgabe 2014.

[154] *Kamps, T.:* Leichtbau von Stirnzahnrädern aus Einsatzstahl mittels Laserstrahlschmelzen. Technische Universität München, München, 2018.

[155] *Schmitt, M.; Kamps, T.; Siglmüller, F. et al.:* Laser-based powder bed fusion of 16MnCr5 and resulting material properties. *In:* Additive Manufacturing 35 (2020), S. 101372. https://doi.org/10.1016/j.addma.2020.101372.

[156] *Aumayr, C.; Platl, J.; Zunko, H. et al.:* Additive Manufacturing of a Low-alloyed Engineering Steel. *In:* BHM Berg- und Hüttenmännische Monatshefte 165 (2020), Heft 3, S. 137-142. https://doi.org/10.1007/s00501-020-00966-3.

[157] *Wei, M.; Chen, S.; Xi, L. et al.:* Selective laser melting of 24CrNiMo steel for brake disc: Fabrication efficiency, microstructure evolution, and properties. *In:* Optics & Laser Technology 107 (2018), S. 99-109. https://doi.org/10.1016/j.optlastec.2018.05.033.

[158] *Schmitt, M.; Kempter, B.; Inayathulla, S. et al.:* Influence of Baseplate Heating and Shielding Gas on Distortion, Mechanical and Case hardening Properties of 16MnCr5 fabricated by Laser Powder Bed Fusion. *In:* Procedia CIRP 93 (2020), S. 581-586. https://doi.org/10.1016/j.procir.2020.03.089.

[159] *Schmitt, M.; Gerstl, F.; Boesele, M. et al.:* Influence of Part Geometry and Feature Size on the Resulting Microstructure and Mechanical Properties of the Case Hardening Steel 16MnCr5 processed by Laser Powder Bed Fusion. *In:* Procedia CIRP 104 (2021), S. 726-731. https://doi.org/10.1016/j.procir.2021.11.122.

[160] *Yang, M.; Sisson, R.D.:* Carburizing Heat Treatment of Selective-Laser-Melted 20MnCr5 Steel. *In:* Journal of Materials Engineering and Performance 29 (2020), Heft 6, S. 3476-3485. https://doi.org/10.1007/s11665-020-04564-9.

[161] *Mukherjee, M.; Kundu, J.; Balla, V.K. et al.:* Microstructure and properties of parts manufactured by directed energy deposition of water-atomized low-alloy steel powders. *In:* Materials Science and Engineering: A 814 (2021), S. 141232. https://doi.org/10.1016/j.msea.2021.141232.

[162] *Zhao, X.; Lv, Y.; Dong, S. et al.:* The martensitic strengthening of 12CrNi2 low-alloy steel using a novel scanning strategy during direct laser deposition. *In:* Optics & Laser Technology 132 (2020), S. 106487. https://doi.org/10.1016/j.optlastec.2020.106487.

[163] *Zhou, Y.; Chen, S.; Chen, X. et al.:* The evolution of bainite and mechanical properties of direct laser deposition 12CrNi2 alloy steel at different laser power. *In:* Materials Science and Engineering: A 742 (2019), S. 150-161. https://doi.org/10.1016/j.msea.2018.10.092.

[164] *Cao, L.; Chen, S.; Wei, M. et al.:* Effect of laser energy density on defects behavior of direct laser depositing 24CrNiMo alloy steel. *In:* Optics & Laser Technology 111 (2019), S. 541-553. https://doi.org/10.1016/j.optlastec.2018.10.025.

[165] *Ebrahimnia, M.; Xie, Y.; Chi, C.:* Effect of cladding parameters on microstructure and defects in direct laser metal deposition of 24CrNiMo steel. *In:* Journal of Laser Applications 33 (2021), Heft 1, S. 12007. https://doi.org/10.2351/7.0000214.

[166] *Zhao, X.; Dong, S.; Yan, S. et al.:* The effect of different scanning strategies on microstructural evolution to 24CrNiMo alloy steel during direct laser deposition. *In:* Materials Science and Engineering: A 771 (2020), S. 138557. https://doi.org/10.1016/j.msea.2019.138557.

[167] *Kang, X.; Dong, S.; Men, P. et al.:* Microstructure evolution and gradient performance of 24CrNiMo steel prepared via laser melting deposition. *In:* Materials Science and Engineering: A 777 (2020), S. 139004. https://doi.org/10.1016/j.msea.2020.139004.

[168] *Zhou, L.; Chen, S.; Jia, W. et al.:* Effects of preheating-ultrasonic synergistic on the microstructure and strength-ductility of 24CrNiMoY alloy steel by laser directed energy deposition. *In:* Materials Science and Engineering: A 863 (2023), S. 144463. https://doi.org/10.1016/j.msea.2022.144463.

[169] *Wang, Q.; Zhang, S.; Zhang, C. et al.:* A high strength low alloy steel fabricated by direct laser deposition. *In:* Vacuum 161 (2019), S. 225-231. https://doi.org/10.1016/j.vacuum.2018.12.030.

[170] *Rothfelder, R.; Lanzl, L.; Selzam, J. et al.:* Vibrational Microfeeding of Polymer and Metal Powders for Locally Graded Properties in Powder-Based Additive Manufacturing. *In:* Journal of Materials Engineering and Performance 30 (2021), Heft 12, S. 8798-8809. https://doi.org/10.1007/s11665-021-06271-5.

[171] *Foerster, J.; Michatz, M.; Binder, M. et al.:* Electrostatic powder attraction for the development of a novel recoating system for metal powder bed-based additive manufacturing. *In:* Journal of Electrostatics 115 (2022), S. 103641. https://doi.org/10.1016/j.elstat.2021.103641.

[172] *Griffith, M.L.; Harwell, L.D.; Romero, J.T. et al.:* Multi-material processing by LENS. *In: :* 1997 International Solid Freeform Fabrication Symposium, 1997.

[173] *Chmielewska, A.; Wysocki, B.; Buhagiar, J. et al.:* In situ alloying of NiTi: Influence of laser powder bed fusion (LBPF) scanning strategy on chemical composition. *In:* Materials Today Communications 30 (2022), S. 103007. https://doi.org/10.1016/j.mtcomm.2021.103007.

[174] *Huber, F.; Bartels, D.; Schmidt, M.:* In-Situ Alloy Formation of a WMoTaNbV Refractory Metal High Entropy Alloy by Laser Powder Bed Fusion (PBF-LB/M). *In:* Materials (Basel, Switzerland), Vol. 14 (2021), Iss. 11. https://doi.org/10.3390/ma14113095.

[175] *Schmitt, M.; Gottwalt, A.; Winkler, J. et al.:* Carbon Particle In-Situ Alloying of the Case-Hardening Steel 16MnCr5 in Laser Powder Bed

Fusion. *In:* Metals 11 (2021), Heft 6, S. 896. https://doi.org/10.3390/met11060896.

[176] *Huber, F.; Rasch, M.; Schmidt, M.:* Laser Powder Bed Fusion (PBF-LB/M) Process Strategies for In-Situ Alloy Formation with High-Melting Elements. *In:* Metals 11 (2021), Heft 2, S. 336. https://doi.org/10.3390/met11020336.

[177] *Anstätt, C.; Seidel, C.; Reinhart, G.:* Fabrication of 3D-multimaterial parts by laser beam based powder bed fusion. *In:* Proceedings of the solid freeform fabrication SFF (2017).

[178] *Huber, F.; Papke, T.; Kauffmann, C. et al.:* Systematic exploration of the L-PBF processing behavior and resulting properties of β-stabilized Ti-alloys prepared by in-situ alloy formation. *In:* Materials Science and Engineering: A 818 (2021), S. 141374. https://doi.org/10.1016/j.msea.2021.141374.

[179] *Chen, M.; van Petegem, S.; Zou, Z. et al.:* Microstructural engineering of a dual-phase Ti-Al-V-Fe alloy via in situ alloying during laser powder bed fusion. *In:* Additive Manufacturing 59 (2022), S. 103173. https://doi.org/10.1016/j.addma.2022.103173.

[180] *Hassanin, A.E.; Silvestri, A.T.; Napolitano, F. et al.:* In Situ Alloying through Laser-Powder Bed Fusion of a 60%Inconel718-40%Cu Powders Mixture. *In:* Metallography, Microstructure, and Analysis (2023). https://doi.org/10.1007/s13632-023-00942-6.

[181] *Li, B.; Han, C.; Lim, C.W.J. et al.:* Interface formation and deformation behaviors of an additively manufactured nickel-aluminum-bronze/15-5 PH multimaterial via laser-powder directed energy deposition. *In:* Materials Science and Engineering: A 829 (2022), S. 142101. https://doi.org/10.1016/j.msea.2021.142101.

[182] *Sing, S.L.; Huang, S.; Goh, G.D. et al.:* Emerging metallic systems for additive manufacturing: In-situ alloying and multi-metal processing in laser powder bed fusion. *In:* Progress in Materials Science 119 (2021), S. 100795. https://doi.org/10.1016/j.pmatsci.2021.100795.

[183] *Huebner, J.; Kata, D.; Rutkowski, P. et al.:* Grain-Boundary Interaction between Inconel 625 and WC during Laser Metal Deposition. *In:* Materials (Basel, Switzerland), Vol. 11 (2018), Iss. 10. https://doi.org/10.3390/ma11101797.

[184] *Springer, H.; Baron, C.; Szczepaniak, A. et al.:* Efficient additive manufacturing production of oxide- and nitride-dispersion-strength-

ened materials through atmospheric reactions in liquid metal deposition. *In:* Materials & Design 111 (2016), S. 60-69. https://doi.org/10.1016/j.matdes.2016.08.084.

[185] *Doñate-Buendía, C.; Frömel, F.; Wilms, M.B. et al.:* Oxide dispersion-strengthened alloys generated by laser metal deposition of laser-generated nanoparticle-metal powder composites. *In:* Materials & Design 154 (2018), S. 360-369. https://doi.org/10.1016/j.matdes.2018.05.044.

[186] *Kang, N.; Ma, W.; Li, F. et al.:* Microstructure and wear properties of selective laser melted WC reinforced 18Ni-300 steel matrix composite. *In:* Vacuum 154 (2018), S. 69-74. https://doi.org/10.1016/j.vacuum.2018.04.044.

[187] *Everett, R.K.; Arsenault, R.J.:* Metal Matrix Composites: Mechanisms and properties, Metal Matrix Compounds, Academic Press, 1991.

[188] *Grünenwald, B.; Bischoff, E.; Shen, J. et al.:* Laser surface alloying of case hardening steel with tungsten carbide and carbon. *In:* Materials Science and Technology 8 (1992), Heft 7, S. 637-644. https://doi.org/10.1179/mst.1992.8.7.637.

[189] *AlMangour, B.; Baek, M.-S.; Grzesiak, D. et al.:* Strengthening of stainless steel by titanium carbide addition and grain refinement during selective laser melting. *In:* Materials Science and Engineering: A 712 (2018), S. 812-818. https://doi.org/10.1016/j.msea.2017.11.126.

[190] *Huebner, J.; Kata, D.; Kusiński, J. et al.:* Microstructure of laser cladded carbide reinforced Inconel 625 alloy for turbine blade application. *In:* Ceramics International 43 (2017), Heft 12, S. 8677-8684. https://doi.org/10.1016/j.ceramint.2017.03.194.

[191] *Liu, S.; Li, Y.; Wang, Y. et al.:* Selective laser melting of WC-Co reinforced AISI 1045 steel composites: microstructure characterization and mechanical properties. *In:* Journal of Materials Research and Technology 19 (2022), S. 1821-1835. https://doi.org/10.1016/j.jmrt.2022.05.158.

[192] *van Acker, K.; Vanhoyweghen, D.; Persoons, R. et al.:* Influence of tungsten carbide particle size and distribution on the wear resistance of laser clad WC/Ni coatings. *In:* Wear 258 (2005), 1-4, S. 194-202. https://doi.org/10.1016/j.wear.2004.09.041.

[193] *Shi, Q.; Gu, D.; Lin, K. et al.:* The Role of Reinforcing Particle Size in Tailoring Interfacial Microstructure and Wear Performance of Selective Laser Melting WC/Inconel 718 Composites. *In:* Journal of

Manufacturing Science and Engineering 140 (2018), Heft 11. https://doi.org/10.1115/1.4040544.

[194] *Song, L.; Zeng, G.; Xiao, H. et al.:* Repair of 304 stainless steel by laser cladding with 316L stainless steel powders followed by laser surface alloying with WC powders. *In:* Journal of Manufacturing Processes 24 (2016), S. 116-124. https://doi.org/10.1016/j.jmapro.2016.08.004.

[195] *Zhou, X.; Su, D.; Wu, C. et al.:* Tensile Mechanical Properties and Strengthening Mechanism of Hybrid Carbon Nanotube and Silicon Carbide Nanoparticle-Reinforced Magnesium Alloy Composites. *In:* Journal of Nanomaterials 2012 (2012), S. 1-7. https://doi.org/10.1155/2012/851862.

[196] *Han, Q.; Gu, Y.; Huang, J. et al.:* Selective laser melting of Hastelloy X nanocomposite: Effects of TiC reinforcement on crack elimination and strength improvement. *In:* Composites Part B: Engineering 202 (2020), S. 108442. https://doi.org/10.1016/j.compositesb.2020.108442.

[197] *Molobi, E.; Sacks, N.; Theron, M.:* Crack mitigation in laser engineered net shaping of WC-10wt%FeCr cemented carbides. *In:* Additive Manufacturing Letters 2 (2022), S. 100028. https://doi.org/10.1016/j.addlet.2022.100028.

[198] *Mussatto, A.; Groarke, R.; Vijayaraghavan, R.K. et al.:* Laser-powder bed fusion of silicon carbide reinforced 316L stainless steel using a sinusoidal laser scanning strategy. *In:* Journal of Materials Research and Technology 18 (2022), S. 2672-2698. https://doi.org/10.1016/j.jmrt.2022.03.170.

Own publications referring to this work

[P1] Bartels D., Klaffki J., Pitz I., Merklein C., Kostrewa F., Schmidt M.: Investigation on the case-hardening behavior of additively manufactured 16MnCr5. In: Metals 10 (2020), Art.Nr.: 536.

[P2] Papke T., Bartels D., Schmidt M., Merklein M., Gerhard D., Baumann J., Pitz I.: Additive Fertigung für industrielle Anwendungen - Entwicklung einer Auswahlsystematik für Bauteile zur Generierung funktionalen Mehrwerts mittels additiver Fertigung. In: Industrie 4.0 Management: Gegenwart und Zukunft industrieller Geschäftsprozesse 2020 (2020), S. 50-54.

[P3] Bartels D., Hentschel O., Dauer J., Burgmayr W., Schmidt M.: Processing of low-alloyed case-hardening steel Bainidur AM by means of DED-LB/M. Lasers in Manufacturing (LiM) 2021 (München, 21. Juni 2021 - 24. Juni 2021).

[P4] Papke T., Bartels D., Hofmann H., Mys R., Schmidt M., Merklein M.: Additive Fertigung eines hybriden Planetenträgers. In: Zeitschrift für wirtschaftlichen Fabrikbetrieb 116 (2021), S. 478-482.

[P5] Bartels D., Novotny T., Hentschel O., Huber F., Mys R., Merklein C., Schmidt M.: In situ modification of case-hardening steel 16MnCr5 by C and WC addition by means of powder bed fusion with laser beam of metals (PBF-LB/M). In: International Journal of Advanced Manufacturing Technology (2022).

[P6] Bartels D., Novotny T., Mohr A., van Soest F., Hentschel O., Merklein C., Schmidt M.: PBF-LB/M of Low-Alloyed Steels: Bainite-like Microstructures despite High Cooling Rates. In: Materials 15 (2022), S. 6171.

[P7] Bartels D., Rohdenburg J., Mohr A., Rothfelder R., Schmidt M.: Laser Metal Deposition of Carbide-reinforced low-alloyed steel Bainidur AM. In: Procedia CIRP 111 (2022), S. 237-240.

[P8] Kreß M., Bartels D., Schmidt M., Merklein M.: Material Characterization of Hybrid Components Manufactured by Laser-Based

Directed Energy Deposition on Sheet Metal Substrates. The 25th International Conference on Material Forming (ESAFORM 2022) (Braga, 27. April 2022 - 29. April 2022).

[P9] Bartels D., von Lattre-Hertel A., Novotny T., Mohr A., Hill H., Merklein C., Schmidt M.: Directed Energy Deposition of Low-Alloyed Steels: An Insight on Microstructural and Mechanical Properties. In: Steel Research International (2023), S. 2200925.

[P10] März R., Hafenecker J., Bartels D., Schmidt M., Merklein M.: Numerical investigation on the deep drawing of sheet metals with an additively applied coating. The 26th International ESAFORM Conference on Material Forming (Kraków, 19. April 2023 - 21. April 2023). In: Lukasz Madej, Mateusz Sitko, Konrad Perzynsk (Hrsg.): Material Forming 2023.

[P11] Papke T., Hafenecker J., Römisch D., März R., Hentschel O., Bartels D., Schmidt M., Merklein M.: Alternating Additive Manufacturing and Forming - An Innovative Manufacturing Approach. In: Journal of Manufacturing and Materials Processing 7 (2023), S. 1-21.

[P12] Bartels D., Albert M.E., Nahr F., Schmidt M.: On the Influence of Volumetric Energy Density and Inter-Layer Time on the Material Properties of Case-Hardening Steels. Alloys 2023, 2, 168–183.

[P13] Bartels D., Novotny T., Albert M., Mohr A., van Soest F., Hill H., Merklein C. and Schmidt, M: Effect of Volumetric Energy Density and Part Height on the Material Properties of Low-Alloyed Steels Manufactured by Laser-Based Powder Bed Fusion of Metals. Adv. Eng. Mater. (2023), 2300009.

[P14] Bartels D., Fallqvist, M., Heise, M., Schmidt M., Krakhmalev, P.: Development of a novel wear-resistant WC-reinforced coating based on the case-hardening steel Bainidur AM for the substitution of carburizing heat treatments, Journal of Materials Research and Technology, Volume 26, 2023, Pages 186-198, ISSN 2238-7854.

[P15] Bartels D., Novotny T., Schmidt M.: Influence of Carbon Content on the Material Properties of Low-Alloyed Steel Bainidur AM. In: Drstvensek, I., Pal, S., Ihan Hren, N. (eds) Additive Manufacturing in Multidisciplinary Cooperation and Production. Springer Tracts in Additive Manufacturing. Springer, Cham, 2024.

Students' theses referring to this work

[S1] Klaffki, Julian; Bartels, Dominic; Schmidt, Michael: *Untersuchung verschiedener Prozessstrategien zur Verbesserung der Oberflächenhärte des Einsatzstahls 16MnCr5 in der Additiven Fertigung*. Bachelorarbeit (2019), Erlangen

[S2] Baumann, Maximilian; Bartels, Dominic; Schmidt, Michael: *Characterization of minimal contour resolution geometries and surplus angles for the additive manufactur-ing of 16MnCr5 specimens*. Projektarbeit (2019), Erlangen

[S3] Novotny, Tobias; Bartels, Dominic; Merklein, Carsten; Schmidt, Michael: *In-situ modification and subsequent processing of additively manufactured case hardening steel 16MnCr5 for improved hardness and wear resistance*. Projektarbeit (2020), Erlangen

[S4] Burgmayr, Wolfgang; Bartels, Dominic; Schmidt, Michael: *Untersuchung der in-situ Legierungsbildung bei der Verarbeitung von niedriglegierten Einsatzstählen mittels Laserpulverauftragschweißen*. Masterarbeit (2020), Erlangen

[S5] Dauer, Jonas; Bartels, Dominic; Schmidt, Michael: *Experimentelle Entwicklung eines höherfesten Beschichtungssystems für das DED-LB/M auf Basis des niedriglegierten Einsatzstahles Bainidur AM*. Bachelorarbeit (2021), Erlangen

[S6] Novotny, Tobias; Bartels, Dominic; Merklein, Carsten; Schmidt, Michael: *Investigation of the process-specific microstructure formation and corresponding mechanical properties of Bainidur AM in PBF-LB/M*. Masterarbeit (2021), Erlangen

[S7] Rohdenburg, Jonathan; Bartels, Dominic; Schmidt, Michael: *Influence of carbide reinforcing on the microstructural and mechanical proper-ties of low-alloyed steels*. Bachelorarbeit (2022), Erlangen

[S8] Albert, Moritz; Bartels, Dominic; Schmidt, Michael: *Untersuchung der Gefügeausbildung bei der additiven Fertigung von Einsatzstählen mittels PBF-LB/M*. Bachelorarbeit (2022), Erlangen

Kurzzusammenfassung

Einsatzstähle weisen aufgrund ihrer guten Schweißbarkeit sowie der Möglichkeit zur Härtesteigerung durch das nachgelagerte Einsatzhärten ein hohes Potenzial auf, um hochfeste Produkte mittels Additiver Fertigung zu erzeugen. In der vorliegenden Arbeit wurde die Verarbeitung von Einsatzstählen mittels Laserstrahlschmelzen (PBF-LB/M) und Laserpulverauftragschweißen (DED-LB/M) untersucht, sowie die resultierenden Materialeigenschaften charakterisiert. Analog zur konventionellen Prozesskette wurde das Einsatzhärten additiv gefertigter Probekörper analysiert und deren Übertragbarkeit bewertet. Dabei zeigt sich, dass additiv hergestellte Bauteile eine verbesserte Einsatzhärtbarkeit aufweisen, welche auf die Vorzüge der Feinkornhärtung zurückzuführen sind. Parallel dazu wurden Untersuchungen zur Substitution des Einsatzhärtens durch Modifikation der Pulvermaterialien vor der Additiven Fertigung durchgeführt. Die Zugabe von Kohlenstoff und Wolframkarbid beim PBF-LB/M erlaubt es, Produkte mit ausreichend hoher Härte (> 620 HV) bei verbesserter Verschleißbeständigkeit nach dem Härten herzustellen. Um zusätzlich die Härteoperation zu ersetzen, wurden die Potenziale des DED-LB/M zur Erzeugung hochfester Beschichtungen (> 800 HV) aufgezeigt. Der Einsatz des DED-LB/M erlaubt eine flexbile Einstellung der Bauteilhärte und potenziell der Verschleißbeständigkeit der Werkstückoberfläche. Auf Basis dieser Ergebnisse wurde eine alternative Prozesskette für die Additive Fertigung von Einsatzstählen abgeleitet.

Abstract

The good weldability associated with the possibility to improve the surface hardness through carburisation make case-hardening steels appealing for the generation of high-strength products by means of laser-based additive manufacturing. Within this work, the processing of these steels and the resulting material properties were investigated for laser powder bed fusion (PBF-LB/M) and directed energy deposition (DED-LB/M). The case-hardening of additively manufactured specimens was analysed according to the conventional process chain. Additively manufactured specimens are characterized by an improved hardenability, which was assigned to fine-grain hardening effects. Furthermore, alternative process routes were investigated for substituting the case-hardening process by modifying the powder materials that are used for PBF-LB/M and DED-LB/M. The addition of carbon and tungsten carbide supports the generation of parts by PBF-LB/M with a surface hardness exceeding 620 HV and an improved wear resistance after hardening. Furthermore, the potentials of DED-LB/M were revealed, allowing for the direct generation of materials with a high surface hardness (> 800 HV) without the need of a post-process heat treatment. The flexibility of DED-LB/M allows for a targeted tailoring of the surface hardness and potentially the wear resistance of a material. Based on these findings, an alternative process chain was derived for the additive manufacturing of case-hardening steels.